Binding forces in metallo-supramolecular coordination compounds

Dissertation

zur Erlangung des akademischen Grades

doctor rerum naturalium

(Dr. rer. nat.)

im Fach: Physik

Spezialisierung: Experimentalphysik

eingereicht an der

Mathematisch-Naturwissenschaftlichen Fakultät

der Humboldt-Universität zu Berlin

von

Dipl.-Chem. Manuel Gensler

Präsidentin der Humboldt-Universität zu Berlin
Prof. Dr.-Ing. habil. Dr. Sabine Kunst

Dekan der Mathematisch-Naturwissenschaftlichen Fakultät
Prof. Dr. Elmar Kulke

Gutachter/innen:
1. Prof. Dr. Jürgen P. Rabe
2. Prof. Dr. Hans-Ulrich Reißig
3. Prof. Dr. Christoph A. Schalley

Tag der mündlichen Prüfung: 03.03.2017

Zusammenfassung

Multivalente Wechselwirkungen sind in diversen biomolekularen und supramolekularen Systemen anzutreffen. Gewöhnlich werden sie durch ihre thermische Stabilität charakterisiert, beispielsweise durch Messung der durchschnittlichen Lebensdauer oder der Gleichgewichtskonstanten. In biologisch relevanten Anwendungsfällen ist jedoch auch die mechanische Stabilität wichtig. Diese ist einerseits durch die Reißkraft und andererseits durch die Reißlänge gekennzeichnet; auch auf der Ebene einzelner Moleküle. Ein System mit großer Reißlänge (Verformbarkeit) weist zwar eine geringere Reißkraft auf, kann aber besser auf äußere Einflüsse ohne Bindungsbruch reagieren. Daher besteht ein zunehmendes Interesse an Modellen, die Vorhersagen über die mechanische Stabilität multivalenter Wechselwirkungen erlauben.

Einzelmolekül-Kraftspektroskopie ist eine nützliche Methode, um den Reißprozess nichtkovalenter Wechselwirkungen zu studieren. Im Rahmen dieser Dissertation wurde eine umfangreiche Studie an mono- und bivalenten Pyridinen, komplexiert und verbunden durch Cu^{2+} und Zn^{2+}, durchgeführt. Die bivalenten Pyridine wurden mit unterschiedlich flexiblen Rückgratstrukturen entworfen (flexibel, teilflexibel, steif). Überraschenderweise wurde ein anderer Trend für die Verformbarkeiten gemessen (Verformbarkeit: flexibles > steifes > teilflexibles Rückgrat). Durch Vergleich von experimentellen Daten mit *ab-initio* Berechnungen, konnte ein komplexer Reißmechanismus vorgeschlagen werden. In diesem spielte die wässrige Umgebung eine entscheidende Rolle. Insbesondere waren wasserverbrückte Zwischenprodukte Ursache einer vergleichsweise großen Verformbarkeit: Das bivalente System mit teilflexiblem Rückgrat, koordiniert durch Cu^{2+}, riss bei 0.30 ± 0.01 nm. Dies konnte mit einem gleichzeitigen Reißen beider Bindungen erklärt werden. Eine ähnliche Reißlänge von 0.33 ± 0.01 nm wurde auch für das monovalente System mit Cu^{2+} gemessen. Die beiden anderen Systeme wurden nach 0.51 ± 0.03 nm (steifes Rückgrat) und 1.12 ± 0.07 nm (flexibles Rückgrat) voneinander getrennt, was auf zweistufige Prozesse hindeutete. Diese große Verformbarkeit führte zu vergleichsweise kleinen Reißkräften und obwohl das flexible System thermisch stabiler war, brach es sogar leichter als das monovalente System. Mit Zn^{2+} konnten nur monovalente Wechselwirkungen detektiert werden, was auf die konkurrierenden Stapelwechselwirkung der Pyridine zurückgeführt wurde.

Im Rahmen dieser Dissertation konnte zum ersten Mal der große Einfluss des Rückgrats auf die mechanische Stabilität gezeigt werden. Obwohl die Art der

Wechselwirkung in allen drei bivalenten Systemen gleich war, variierten die Reißkräfte über einen großen Bereich. Mit dem Modellsystem aus Koordinationsverbindungen von Pyridinen mit Cu^{2+} und variierbarem Rückgrat wurde ein Baukasten entwickelt, der für weiterführende Untersuchungen an der mechanischen Stabilität von bi- und multivalenten Verbindungen nützlich sein wird und kompatibel mit biologisch relevanten wässrigen Lösungsmitteln ist. Neben der Flexibilität des Rückgrats, sind auch der Abstand der Reaktionspartner, sterische und allosterische Effekte spannende Parameter für zukünftige Untersuchungen.

Abstract

Multivalent interactions are ubiquitous in biomolecular and supramolecular systems. They are commonly characterized by their thermal stability in terms of average bond lifetime or equilibration constant. However when exposed to biologically relevant environment, mechanical stabilities become relevant as well. Those are characterized by a balanced interplay between rupture forces and rupture length, also on the level of single-molecules. A system with high rupture length (malleability) has a lower rupture force, but can more easily adopt to external constraints without rupture. Thus it is of ever-increasing interest to find appropriate models that allow predictions on the malleability of multivalent interactions.

Single-molecule force spectroscopy (SMFS) is a powerful tool to study the rupture process of non-covalent interactions. In the present thesis, a comprehensive study on the mechanical stability of bivalent pyridine coordination compounds with the metal ions Cu^{2+} and Zn^{2+} was performed. Surprisingly, three different backbone flexibilities (high, intermediate, low) did not correlate with the measured malleabilities (malleability: high > low > intermediate flexible backbone). Theoretical calculations using *ab-initio* calculations revealed more complex underlying rupture mechanisms due to the aqueous environment. Hydrogen bound complexes were formed and important intermediate structures that strongly increased malleabilities: Both interactions of the intermediate flexible bivalent system with Cu^{2+} broke simultaneously at a high rupture length of 0.30 ± 0.01 nm. A similar length of 0.33 ± 0.01 nm was measured for the monovalent system with Cu^{2+}. The bivalent ligands with low and high flexibility showed even larger rupture lengths of 0.51 ± 0.03 nm and 1.12 ± 0.07 nm, respectively, which was attributed to stepwise bond rupture processes. Due to the balanced interplay, their corresponding rupture forces were reduced. For the very flexible interaction they even dropped below those of the monovalent interaction (although exhibiting a higher thermal stability). With Zn^{2+}, only the monovalent interaction was formed due to a competing stacking interaction between the pyridines themselves.

In this thesis it was shown for the first time, that rupture forces can be tuned over a broad range just by changing the connecting backbone structure and not the type of interaction. The developed approach of using Cu^{2+} pyridine coordination compounds with various backbone structures is a rich toolkit to study the balanced interplay between mechanical and thermal stability also in systems of higher valency as a function of backbone flexibility, distance of interaction partners, steric

match/mismatch, and allosteric multivalency in biologically relevant aqueous solvents.

Contents

„Geschrieben steht: Im Anfang war der *Sinn*.
Bedenke wohl die erste Zeile,
Daß deine Feder sich nicht übereile!
Ist es der *Sinn*, der alles wirkt und schafft?
Es sollte stehn: Im Anfang war die *Kraft*!“

Johann Wolfgang von Goethe (1749 − 1832), Faust I

1. Introduction

In this thesis, we are studying the mechanical stability of single-molecular interactions. Here, typical forces are on the piconewton scale. Some mechanical properties are similar to the observations made in the macroscopic world, some are very different. An illustrative example that has been analyzed on various scales is the foot of a Tokay gecko. Its foot adheres with a typical adhesive force of 10 N.[1] From a macroscopic point of view, adhesive forces are characterized by a characteristic critical force of rupture f_c. If forces are below f_c, the gecko feet will stay adhered to the surface. The gecko will not fall off the surface spontaneously just by waiting. However he is able to remove his foot at much lower force by a peeling movement.[2] The mechanical stability of adhesion is strongly dependent on the rupture mechanism. Taking a closer look, each gecko foot is equipped with 5000 hairs (setae), which are subdivided into 100 − 1000 spatulae at their tips. Those are approximately 200 nm in size and still show a narrow distribution of f_c = 10.8 ± 1.0 nN when pulled off from glass.[3] Taking an even closer look on the interaction of single molecules, there is no critical force anymore. Now, already at zero external forces, the thermal energy is sufficient to break non-covalent interactions within seconds or even milliseconds. This is illustrated in figure 1a. According to the Arrhenius law, the average bond lifetime (inverse of the thermal off-rate constant) decreases exponentially with applied load. The activation energy barrier E_a of non-covalent interactions (mono- or bivalent) is close to the thermal energy k_BT. In the gecko spatulae, several bonds act cooperatively in a polyvalent way. As a result, the effective activation barrier increases and interactions that are exposed to low forces are stable for minutes, days or years.

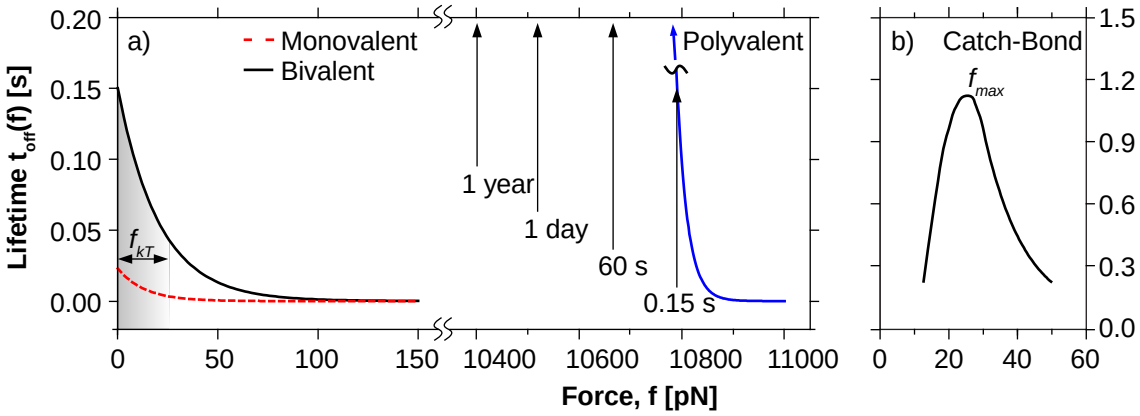

Figure 1: a) Arrhenius-type lifetime plots for the mono- and bivalent interactions of Zn-porphyrin with C_{60}[4] and the polyvalent interaction of one gecko spatula with a glass surface. The latter exhibits

lifetimes of more than a year below constant forces of 10.4 nN. The thermal force $f_{kT} = k_B T/\Delta x$ is sketched for 298 K and $\Delta x = 0.2$ nm. b) A catch-bond behavior is characterized by an initial lifetime increase. Beyond a certain threshold force f_{max}, the Arrhenius-type decrease is recovered.[5]

As illustrated in figure 1b, additional effects that are not known from the macroscopic world may occur on the level of single-molecules. For example, the average lifetime of the interaction between P-selectin and the P-selectin glycoprotein ligand-1 increases up to a force of 25 pN (catch-bond behavior) and then decreases exponentially (slip-bond behavior).[5,6] This interaction is relevant in the inflammatory immune response and participates in the attachment of leukocytes to endothelial cells within the blood stream – an environment where macroscopic forces are transferred to the single bonds.[7]

The mechanical stability of single-molecular interactions is highly relevant in natural systems and material sciences. A famous example for natural systems is the mechanical activation of the ultralarge protein “von Willebrand Factor” (*VWF*). At hemorrhage, the flow profile in blood vessels is changed leading to higher shear flows at the injury. Thereby the *VWF* in the blood stream is affected by larger tensile forces, its conformation changes and a binding site for platelets is exposed: an important step in hemostasis.[8] In material sciences, knowledge of the single-molecular behavior leads to a better understanding and tunability of macroscopic properties. For example, polymer chains and crosslinked networks behave as an entropic spring. This allows reversible deformation of materials, yielding resilience. In contrast weak, non-covalent interactions within a polymer behave as shock absorbers. Corresponding materials absorb energy and deform plastically without fracture, yielding toughness. In the muscle protein *I27* both properties are combined, yielding both, resilient and tough mechanical properties.[9,10] Only recently, artificial elastomeric proteins were successfully cast into solid materials mimicking the mechanical properties of *I27*: toughness, extensibility, and resilience.[11]

1. How to apply, quantify and evaluate forces on single-molecules?

Forces acting on tethers such as polymers are transferred throughout the molecule. Breakage occurs preferentially at weakest interactions, for example non-covalent bonds within a covalent chain. This property is used in ultrasonic-induced mechanochemistry, where the reaction center is first coupled to two polymeric chains. Due to the relative movement of solvent inside an ultrasonic bath, the polymeric chains and the reaction center are exposed to external forces. This

method can be scaled up from catalytic to synthetic scale as shown for the dis- and conrotatory ring opening in cyclobutadien in between two chains of PEG.[12] In a similar way, macroscopic compressive forces can be transferred through a polymer matrix to single-molecules.[13]

Quantification of forces applied to single-molecules is possible by means of glass microneedles[14], magnetic[15] or optical tweezers[16], and the scanning force microscope (SFM). All those and similar techniques are summarized under the term single-molecule force spectroscopy (SMFS). Measurements are usually performed at various pulling speeds, yielding a dynamic force spectrum (DFS) that exhibits the most probable rupture forces *f** as a function of loading rates *lr* (the velocity of force ramp with time).

Since the first publications of SFM based SMFS in 1994,[17,18] lots of biological and supramolecular systems have been analyzed for their rupture behavior. A major advance was made by Evans, who combined models on force-induced bond dissociation (particularly by Zhurkov[19,20] and Bell[21,22]) and applied them to SMFS in a concise theory with some easy-to-use methods for data analysis (KBE model, figure 2).[23] According to equation (1) $f^*(\ln(lr))$ is characterized by two characteristic parameters:

- $k_{off}(0\ \mathrm{pN})$: The thermal off-rate constant in the forceless state, inverse proportional to the average bond lifetime $t_{off}(0\ \mathrm{pN})$.
- Δx: The rupture length, defined as the distance between bound and transition state in a cross-section of the potential energy diagram along the direction of applied force (sometimes interpreted as bond stretching, which is misleading).

$$f^*(lr) = \frac{k_B T}{\Delta x} \ln\left(\frac{\Delta x}{k_B T} \frac{lr}{k_{off}(0pN)}\right) \tag{1}$$

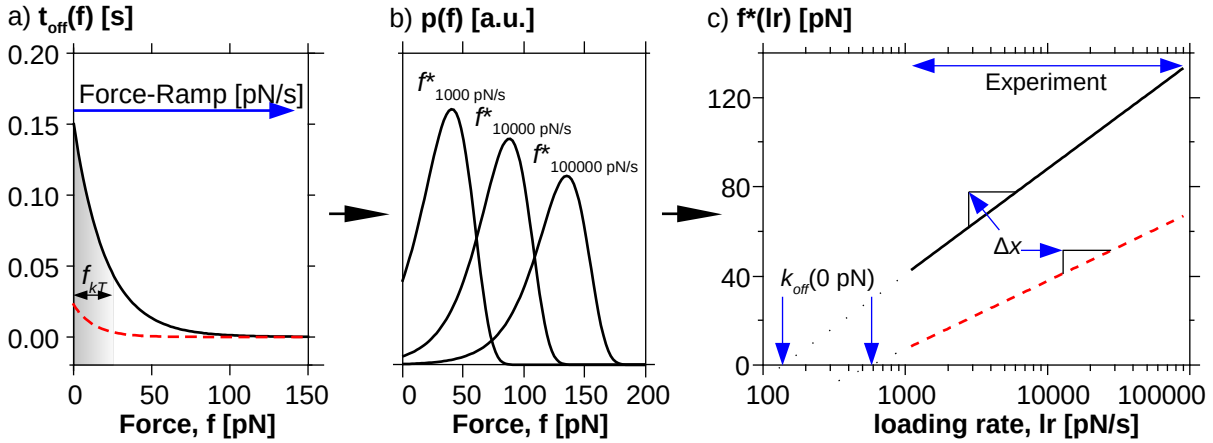

Figure 2: Basic principles of SMFS illustrated for the mono- (dashed lines) and bivalent (continuous lines) interaction of Zn^{2+}-porphyrin with C_{60}[4]. a) Both bonds with force dependent average lifetime $t_{off}(f)$ are ramped at various loading rates [pN/s]. b) Rupture force probability distributions $p(f)$ at higher loading rates are characterized by higher most probable rupture forces f^*. c) The log-linear relationship of both values is called dynamic force spectrum. A fit according to the KBE model equation (1) yields the rupture length Δx from the inverse slope and the thermal off-rate constant k_{off}(0 pN) from the extrapolated crossing with the f^* = 0 pN axis.[23]

SMFS is unique for being a direct measurement of interaction forces at constant velocity (force-ramp mode) or thermal lifetimes at constant forces (force-clamp mode, possible for interactions with higher average lifetimes)[24]. Additionally the thermal off-rate constant (k_{off}(0 pN)) and the rupture length Δx are accessible. The first parameter is also measurable by ensemble methods, the second parameter accessible by theoretical calculations[25] or geometrical considerations such as deformation of-[26] or dethreading from a binding pocket [27]. Additionally, specific signatures in force-distance diagrams may be used to discriminate between different types of interaction. This was used to fully map the mechanical response of transmembrane proteins β_2AR[28] and rhodopsin[29] with seven distinct segments, each.

Summarizing, there are several techniques available to apply forces to single molecules in a quantitative way. All these techniques may be used to measure dynamic force spectra, yielding additional information from the KBE model, which is also called standard model in DFS.

2. What is a stable bond?

From an energetic point of view, the activation energy barrier E_a of a stable bond should be much higher than the thermal energy k_BT. According to Arrhenius' equation (2) this results in higher average bond lifetimes t_{off}, or lower thermal off-rate constants k_{off} (thermal stability).

$$t_{off} = A \exp\left(\frac{E_a}{k_B T}\right) = k_{off}^{-1} \quad (2)$$

Here, A is the pre-exponential factor. As mentioned above, the stability under the influence of external forces is another feature relevant in biological and artificial systems. According to Zhurkov and Bell equation (2) translates to equation (3) under the influence of external force f and rupture length Δx.

$$t_{off}(f) = A \exp\left(\frac{E_a - f\,\Delta x}{k_B T}\right) = k_{off}(f)^{-1} \quad (3)$$

Thus an interaction with high E_a should also be more resistant to applied forces (higher mechanical stability). This theory explains SMFS experiments on systems with similar Δx, but different E_a (figure 3):

- Red arrow: The hydrophobic interaction of the pincer complex $ZnPor_2$[4] is less stable than the host-guest system with cation-π interactions + H-bonding[30,31], which is again less stable than the tetravalent hydrogen bond in UPy_2[32].
- Green arrow: Also the first rupture step in strept(avidin) with biotin, which is identified as a network of various hydrogen bonds and hydrophobic interactions, [27] is mechanically and thermally weaker than the PSGL-1 interaction[33], that is mediated by salt bridges (a combination of hydrogen bonding and electrostatic interactions).[7] The currently largest known rupture force for a non-covalent interaction is due to an extensive contact area consisting of a hydrophobic center, surrounded by a polar ring and charged residues at the rim protecting the hydrophobic center (Dockerin + Cohesin).[34]

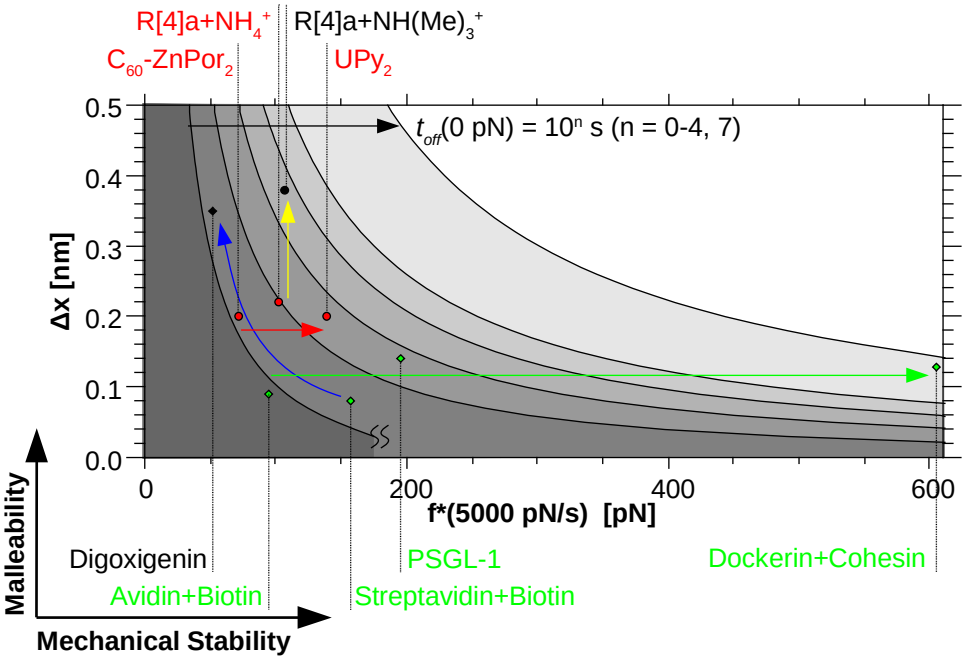

Figure 3: Mechanical stability is a result of high thermal stability (t_{off}(0 pN)) or low malleability. Continuous lines are KBE model plots of most probable rupture forces (f^*) at a loading rate of 5000 pN/s against the rupture length (equation 1) for different average lifetimes. In supramolecular (red circles and arrow, top) and biological interactions (green diamonds and arrow, bottom) of similar malleabilities Δx, increased t_{off} lifetimes yield higher f^*. In contrast, higher malleability Δx at similar t_{off} lifetime (black diamond and blue arrow) leads to lower mechanical stability.

Besides E_a, also the rupture length Δx (malleability) should be an important parameter as it strongly influences the effective energy barrier reduction in the Zhurkov and Bell model (equation 3). In figure 3 this trend is shown for two host-guest systems: Yellow arrow, Resorc[4]arene and NH_4^+ compared to Resorc[4]arene and $NH(Me)_3^+$. Although the latter has a significantly larger average bond lifetime t_{off} (54 ± 21 vs. 1.0 ± 0.8 s), both f^* are around 100 pN (at lr = 5000 pN/s). The reason is a much higher malleability for the methylated guest, attributed to the larger van der Waals diameter of 0.6 nm compared to 0.3 nm for the ammonium guest.[30] Another example are the first rupture steps in streptavidin + biotin and digoxigenin + antibody (blue arrow). Both show the same average lifetime of t_{off} = 0.2 s. But the digoxigenin interaction is purely hydrophobic[35], thus more malleable than the interaction of biotin, which is dominated by hydrogen bonds, and breaks at a much lower f^* (50 vs. 160 pN).

Thus the mechanical stability of a single-molecular interaction is characterized by a balanced interplay between most probable rupture force f^* and malleability Δx. This interplay is comparable to the macroscopic force-displacement relationship, where

mechanical work is the product of a constant force *f* along a displacement Δ*x*: A principle, the Tokay gecko makes use of in peeling his foot off from surfaces.

3. Which influence has multivalency on the stability-malleability relationship?

A frequent motif in both, biochemistry[36] and supramolecular chemistry[37], is multivalency. Here, two partners interact with each other through a multitude of interactions. Those interactions may be similar (homomultivalent) or different from each other (heteromultivalent).[38] Multivalency benefits from reversibility, self-sorting, or self-correction of weak monovalent units on the one hand and a remarkable overall kinetic or thermodynamic stability on the other hand.[39] Directed multivalent interactions (H-bonds, coordination bonds, ion-bridges) may additionally be influenced by malleable isotropic interactions (hydrophobic, electrostatic), charge or strain distribution upon the first binding (allosteric effects), or the solvent environment.

To date, there is much data available on mechanical rupture of polyvalent interactions, especially between β-sheets in proteins. In some reviewing[40–43] and theoretical articles[44,45] those results have been summarized in order to discover force-clamp motifs in proteins. In figure 4, the balanced interplay between most probable rupture force *f** and malleability Δ*x* is shown for parallel aligned primary β-sheets in proteins. In this context, “primary” defines that both interconnected β-sheets are N- and C-terminal in the protein sequence, hence directly exposed to the applied forces. Two motifs with very different behavior are highlighted: Proteins with a zipper-motif (green diamonds, Δ*x* = 1.5-2.0 nm) and proteins with a shear-motif (red circles, Δ*x* = 0.1-0.5 nm)[42,43]. This means, also polyvalent systems follow the Zhurkov and Bell model.

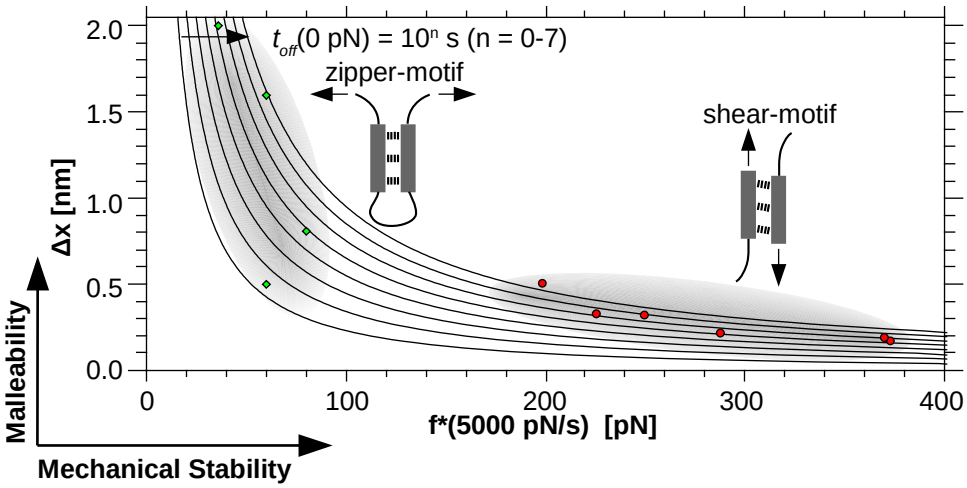

Figure 4: Balanced interplay between malleability and mechanical stability in the unfolding of parallel aligned primary β-sheets in zipper (green diamonds) and shear configuration (red circles).[42,43] Both clamp motifs show very different mechanical stabilities due to their different malleability. Proteins are: (zipper from top to bottom) PAS-B, VCAM1, T4 lysozyme, and ddFLN4, (shear from left to right) SUMO 1, SUMO 2, EcPOTRA 2, Protein L, Ubiquitin, and Protein G.

Besides the two main motifs, the subgroup in shear-configuration is not yet understood. For example, malleability does not correlate with the number of hydrogen bounds between primary β-sheets, but rather with the overall number of inter-residue contacts.[43] Thus it seems to play a role, how the clamp motif is cooperatively stabilized by the whole protein structure.[40] To separate the influences of polyvalency and complex environment, supramolecular systems are powerful models.[46,47] Here, specific ligand design and modification can be used to study selected parameters such as type of interaction, steric interference and backbone flexibility. Only recently, even a supramolecular model for protein folding was presented.[48]

On the level of mono- and bivalent supramolecular model systems, we[I)] are only aware of two comparative studies.[4,49] As illustrated in figure 5, Zhang et al. utilized the interaction between a pair of Zn^{2+}-porphyrin tweezers and a C_{60}-fullerene in aqueous environment. Both types of interaction were nicely distinguishable from each other. The distribution of rupture forces in the bivalent system showed a distinct second maximum at approximately twice f^*_{mono}. The authors attributed this peak to correlated bivalent bond rupture f^*_{bi}. When one of the tweezers arms was absent, the

I) This thesis was written by a single author. I also performed all the experiments and data analysis, but have chosen the first person plural throughout the work as it is common practice in scientific publications.

second maximum disappeared. Using the KBE model and DFS, they calculated a shorter rupture length (Δx_{bi} = 0.20 ±0.02 nm compared to Δx_{mono} = 0.31 ± 0.03 nm) and higher average lifetime ($t_{off,bi}$ = 0.15 ± 0.03 s compared to $t_{off,mono}$ = 0.023 ±0.003 s) for the bivalent interaction. Thus bivalency increased thermal and mechanical stability. Gomez-Casado et al. measured the same trend on mono-, bi- and trivalent host-guest systems, which they identified as a non-cooperative (additive) effect.[49] Additive multivalency in a bivalent system is due to a larger effective local concentration of the remaining interaction after the first one has formed.

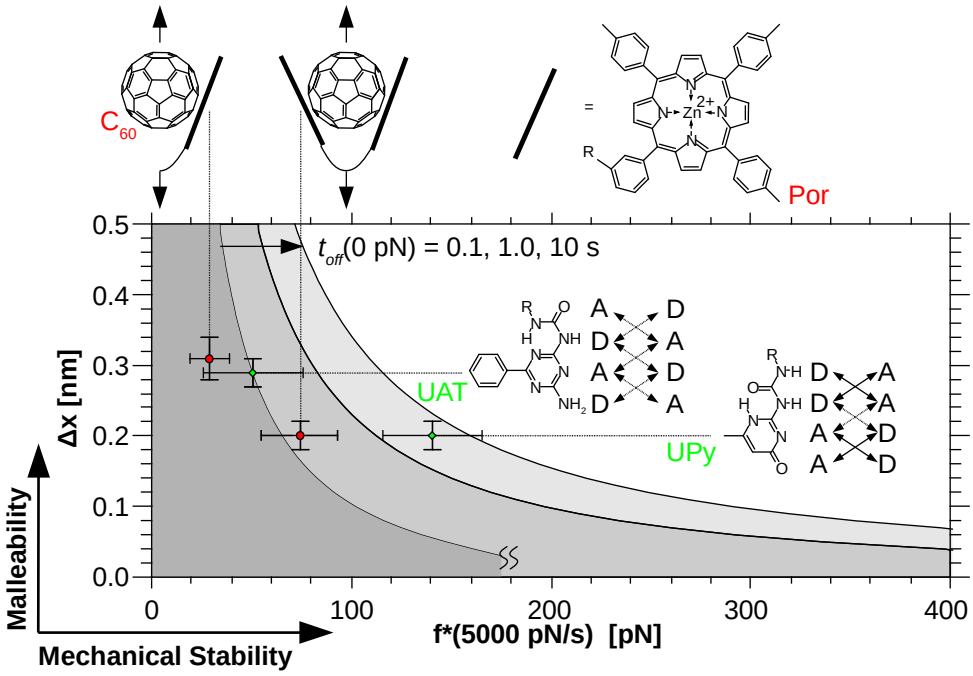

Figure 5: Balanced interplay between malleability and mechanical stability in the mono- and bivalent complexes of Zn^{2+}-porphyrin (Por) with C_{60}[4] (red circles) and two tetravalent hydrogen arrays with different configuration of donor (D) and acceptor (A) sites (green diamonds, in the sketches symmetric reaction partners are omitted for clarity).[32] UPy-UPy is characterized by four attractive secondary interactions (continuous two-sided arrows) and two repulsive ones (dotted two-sided arrows). UAT-UAT exhibits six repulsive secondary interactions.[50] Error bars for f*(5000 pN/s) are estimated from published uncertainties of Δx and k_{off}(0 pN) according to the variance formula.

An even larger multivalent effect is possible, when the first interaction influences the binding free energy at another site, which is called allosteric cooperativity. Allosteric cooperativity was studied by Embrechts et al. using two tetravalent systems in hexadecane.[32,51,52] As sketched in figure 5, UAT is characterized by a donor-acceptor-donor-acceptor (DADA) configuration, while UPy shows a DDAA sequence of hydrogen bonds. The DDAA configuration had a shorter rupture length

(Δx_{DDAA} = 0.20 ±0.02 nm compared to Δx_{DADA} = 0.29 ± 0.02 nm) and showed a more than tenfold higher average bond lifetime ($t_{off,DDAA}$ = 3.9 ± 0.9 s compared to $t_{off,DADA}$ = 0.10 ±0.08 s). This correlated with dimerization constants K_{dim} found in NMR studies ($K_{dim,DDAA} > 10^6\,M^{-1}$[50] compared to $K_{dim,DADA} = 10^4\,M^{-1}$[53]) and can be attributed to attractive secondary interactions between neighboring hydrogen bonds with similar orientation.[50,54] Thus in addition to the effective local concentration, also allosteric effects may increase thermal and mechanical stability.

Comparing the work from Schröder et al.[55] with the results of Embrechts et al.[32] mentioned above, we discovered another example for the balanced interplay between malleability and mechanical stability. The authors applied SMFS to four hydrogen bonds connecting the rims of a pair of capsules. In contrast to UPy and UAT, the hydrogen bonds had larger lateral separations from each other reducing the allosteric effects above. However, one solvent molecule of p-Xylene was incorporated as guest into the aggregate leading to a heteromultivalent system of four directed and one isotropic interaction. DFS uncovered a higher average bond lifetime for the capsules than for UAT, which was expected due to the additional host-guest interaction. However the rupture length was significantly larger ($\Delta x_{capsule}$ = 0.56 ± 0.08 nm), which resulted in a lower mechanical stability over the whole range of probed loading rates. In other words, this system translated higher thermal stability into malleability instead of mechanical stability. Unfortunately the rupture mechanism was not studied. The typically accepted range of H-bonds is only 0.25 nm[56], which suggests a stepwise rupture process with hydrogen bond rupture followed by breakage of the host-guest interaction. This would be similar to a zipper-type of bond rupture in larger systems. (Note that in a SMFS experiment jumps of less than a few nanometers cannot be resolved due to the thermal noise oscillation of the soft cantilevers utilized here.)

In summary, mechanical rupture of a multivalent system may occur stepwise (zipper-motif) or simultaneously (shear-motif). For two systems with similar thermal stability, the first motif leads to higher malleability, but lower mechanical stability. Allosteric effects increase both, thermal and mechanical stability.

4. Goals of the Present Thesis

It was known, that the mechanical stability of a multivalent interaction is determined by its rupture motif and malleability. However the systems compared above differed

in various parameters such as degree of valency (2, 4, 4+1, poly), type of interaction and backbone structure. Our goal was to design a flexible model system that would allow us to analyze the effects mentioned above separately from each other. In this thesis we focused on the backbone structure as promising parameter. Experimental[57] and theoretical[58] studies on bivalent systems have shown that a rigid backbone increases the thermal stability. As soon as the first interaction has been formed, the second one is pre-organized (high effective concentration). Additionally, the entropic loss due to formation of the second partner is lower for rigid spacer structures.[38]

The type of interaction between both interaction partners was chosen to be compatible with biologically relevant aqueous environments. A non-covalent interaction allows repeated force-distance experiments with one modified SFM cantilever probe. Both properties are fulfilled by pyridine and its coordination compounds, which are ubiquitous in natural products[59] and widely used in the design of supramolecular compounds.[60] The thermal stabilities of pyridine complexes with metal ions are well characterized and ranked in the Irving-Williams-Series.[60–62] Experimental studies have shown that this series also holds true for the mechanical stability.[63] Thus the type of metal ion is an additional parameter, widening the variability of a pyridine model system.

Consequently, we designed and synthesized the pyridine coordination complexes sketched in figure 6 with high (**2a**), intermediate (**2b**), and low (**2c**) backbone rigidity. All three bivalent systems were compared to the monovalent interaction of (**1**). Polymeric spacers were utilized to ensure non-equilibrium conditions at force-induced bond rupture,[64] and to facilitate separation from non-specific interactions as well as simultaneous bond rupture[65]. The thiol group was coupled to gold coated cantilever probes and surfaces, respectively.

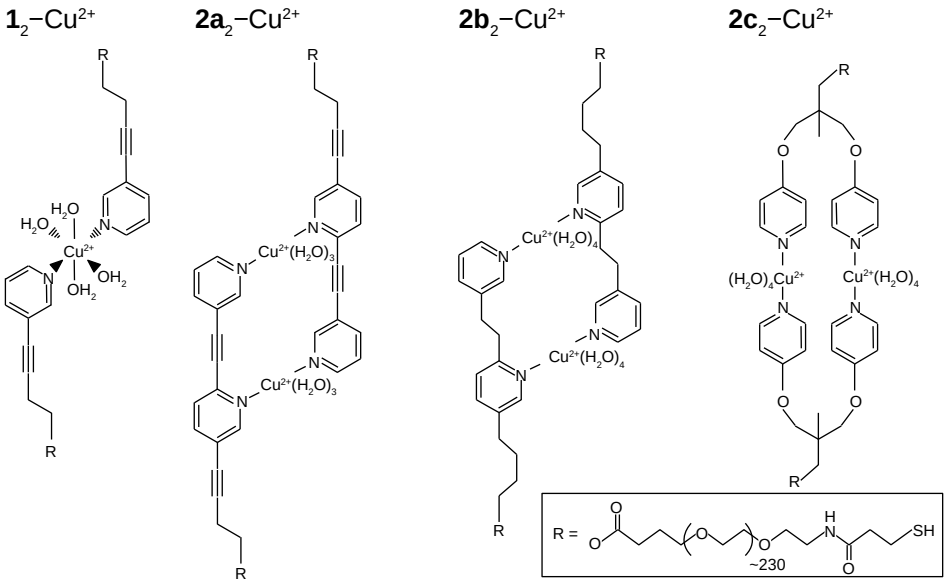

Figure 6: Schemes of mono (**1**) and bivalent (**2a**, **2b**, **2c**) pyridines designed and synthesized in this thesis, in their coordinated form to Cu^{2+} in aqueous environment. The octahedral coordination sphere with trans-configuration illustrated for **1**$_2$−Cu^{2+} was taken from the crystal structure[66] of $[Cu(py)_2(H_2O)_4]^{2+}$ and is also suggested for compounds **2b**$_2$−Cu^{2+} and **2c**$_2$−Cu^{2+}. Structural DFT optimizations for **2a**$_2$−Cu^{2+} indicated a first coordination sphere with only three water ligands, each, due to steric reasons.[67]

In the following chapter 2.1, the concept of multivalency will be detailed with a focus on binding energy. In the context of supramolecular model systems with known valency, this is more useful than the alternative approach using equilibration constants. We will show, that rebinding increases the average bond lifetime t_{off}, thus the mechanical stability f^* of multivalent systems. Chapter 2.2 will describe the methodology of SMFS and its recent advances. In two sub-chapters we will discuss, under which circumstances rupture occurs under equilibrium or non-equilibrium conditions and give a recent application, where a SFM instrument and the balanced interplay between mechanical stability and malleability was used for a specific arrangement of molecules with a precision better than 10 nm. A proper and interlaboratory comparable calibration procedure is essential in SFM based SMFS. Thus chapter 2.3 will give an overview of techniques and motivate our choice of using the thermal noise method. Afterwards the force-extension behavior of polymeric tethers will be discussed (chapter 2.4). The polymer utilized in this thesis, PEG, has been studied in detail by SMFS and exhibits a distinct behavior in aqueous solvents. Here, the water molecules are able to bridge ether groups within one chain. In chapter 2.5, the KBE model will be derived and discussed in detail. We will also

present and discuss more elaborate models using advanced potential energy diagrams such as the Dudko, Hummer, Szabo (DHS) model.

Key issue in SMFS is discrimination between specific and non-specific interactions. In the materials and methods chapter 3, we will present our optimized procedure to extract specific data from the raw measurements and to calculate the KBE model parameters rupture length (Δx) and thermal off-rate constant ($k_{off}(0\ pN)$). The chapter also includes a description of the theoretical constraint geometries simulate external forces (COGEF) model, utilized by our cooperation partners.

In the results and discussions, we will present our approach to gain reproducible results (specific interactions) by a proper characterization of the modification process, detection of simultaneous bond rupture and making use of the known PEG contour length (double tether approach) (chapter 4.1). Then we will focus on SMFS measurements using our model systems as shown in figure 6. Detailed analysis will reveal a complex mixture of pyridine metal complexes and metal free interactions. Using blank experiments in pure water, we will characterize the metal free interactions (chapter 4.2.1). As a result we will be able to distinguish those from the intended interactions of our pyridines with Zn^{2+} and Cu^{2+} (chapter 4.2.2). The weaker metal center Zn^{2+} was able to form a monovalent complex with **1**, but no bivalent complex with **2a**. Thus we changed to the stronger metal center Cu^{2+}, which was coordinated by all thee bivalent ligands **2a**, **2b**, and **2c**, but not by a trivalent one also tested in this thesis. Then we will discuss possible additional conformations (chapter 4.2.3) and influences of tilted pulling (chapter 4.2.4). Finally we will take the COGEF results into consideration and purpose detailed rupture mechanisms, which include explicit water from the environment. They are very different for all three backbone structures, yielding high mechanical stability for $\mathbf{2b}_2{-}Cu^{2+}$ and large malleability for $\mathbf{2c}_2{-}Cu^{2+}$ (chapter 4.3). Ultimately we will give conclusions and perspectives (chapter 5).

“In the future we may have a device to measure the position of each and every atom in our body. Will we fully understand its function? Not before we measure the forces as well.”

Daniel J. Müller (* 1965), Scanning Probe Microscopy & Optical Tweezers in Life Sciences on 14./15.10.2009

2. Fundamentals

2.1. Multivalency

A multivalent interaction is characterized by various interactions between two partners, similar to a zipper (figure 7a). A single zipper tooth can be opened at low force F_{zipper}, such as in the sequential unzipping at malfunction of the bottom stop. Simultaneous opening of all teeth in a zipper requires a much higher force ($F_{sim} \gg F_{zipper}$). On the molecular level, multivalent interactions are ubiquitous. Many biochemical examples are cited in the review by Whitesides et al.[39], some supramolecular examples are given in the review by Stoddard et al.[37] In figure 7b, the inflammatory immune response is sketched. Endothelial cells near a center of inflammation expose selectins on their surface. Leukocyte cells are able to interact with those ligands in a multivalent manner, thereby they slow down and start to roll. Migration through endothelial cells yields extravasation to the source of inflammation.[7,68] In this example a multivalent type of interaction is strong enough to avoid detachment from the leukocyte (F_{sim}), while sequential bond rupture at the rim of the interaction (F_{zipper}) enables the rolling movement.

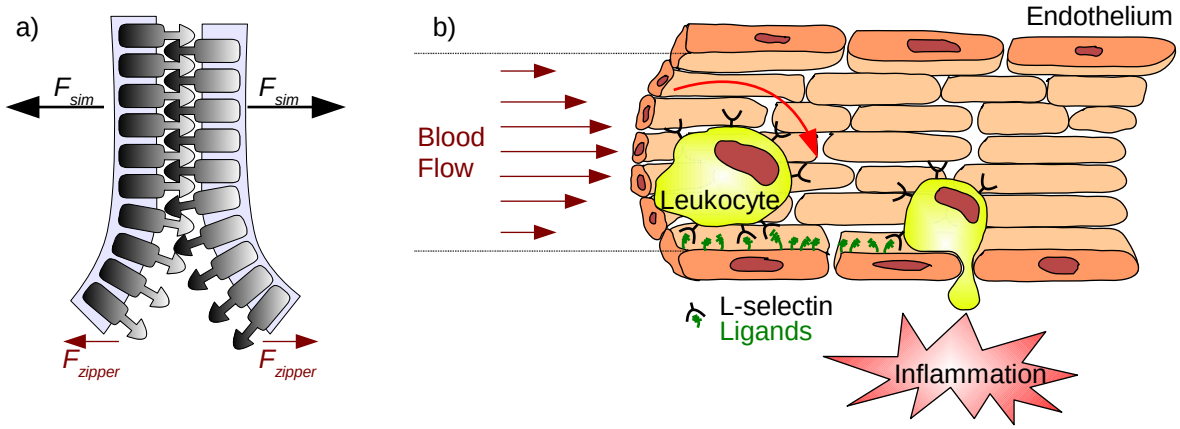

Figure 7: Cooperative rupture of interactions in a multivalent system requires a much higher force than sequential bond breakage. a) A zipper is a macroscopic system, which is much more prone to sequential opening in zipper configuration than to simultaneous opening ($F_{sim} \gg F_{zipper}$). b) The interaction between leukocytes and endothelial cells is characterized by multiple L-selectin and L-selectin ligand interactions. The blood flow applies enough force to allow sequential bond rupture in zipper configuration, leading to a rolling movement. The force is not sufficient to break up all interactions simultaneously in order to detach the leukocyte.[7,68]

The term multivalency is comparable to the terms avidity in biochemistry[39] or chelate cooperativity[69] in supramolecular chemistry. The latter originates from the chelate effect,[70] which describes an increased interaction strength towards a central atom or

molecule when the ligand is able to form multiple interactions. Later this term was generalized to the binding between two partners with multiple interaction sites.[71] Chelate cooperativity should not be confused with allosteric cooperativity. Here, binding of the first interaction partner changes the binding propensity of another site. A famous example is the binding of oxygen to tetravalent hemoglobin, where binding to one interaction site induces a conformational change in the other binding sites mediated by the protein backbone. As a result, oxygen has a higher affinity to partially oxygenated hemoglobin.[72] However all oxygen molecules are separate ligands, thus this is not a multivalent system. Multivalency is often accompanied by allosteric cooperativity, for example due to conjugated π-systems in the backbone[73] or secondary interactions between neighboring hydrogen bonds[50].

2.1.1. Degree of Cooperativity

Usually the binding free energy of a multivalent system ΔG_{multi} is different from the sum of the corresponding monovalent interactions ΔG_{mono}. For a homomultivalent system of N interacting partners, the degree of cooperativity α is defined by equation (4). There are three types to be distinguished: synergistic ($\alpha > 0$), additive ($\alpha = 1$), and interfering ($\alpha < 0$).[39] K_{multi} and K_{mono} are the corresponding equilibration constants.

$$\alpha = \frac{\Delta G_{multi}}{N \Delta G_{mono}} = \frac{\ln\left(K_{multi}\right)}{\ln\left(K_{mono}^{N}\right)} \tag{4}$$

The disadvantage of this concept is, that the degree of multivalency N needs to be known. This is usually the case in well defined supramolecular systems, but not in biological systems. For example, multivalent interactions frequently connect interaction partners such as cells, viruses or bacteria with flexible structure and varying numbers of interaction. If binding free energies ΔG_{mono} are low, N is only an average value due to a fluctuating network of unbound and rebound interactions. Therefore Whitesides et al. introduced an enhancement factor β, which is defined as ratio between multivalent and monovalent equilibration constants.[39]

$$\beta = \frac{K_{multi}}{K_{mono}} \tag{5}$$

Also additive ($\alpha = 1$) or interfering ($\alpha < 1$) systems can show large multivalent enhancements β. In contrast to α, the enhancement factor β is a measure of how useful a multivalent interaction is.[38] Two other concepts frequently applied to multivalent systems are the effective concentration (C_{eff}, equation 6) and effective

molarity (*EM*, equation 7). Effective concentrations are estimated from physical geometries of complexes, while effective molarities represent the ratio of intra- and intermolecular association rates.[46]

$$K_{multi} = b\,K_{mono}^{N}\,C_{eff}^{N-1} \tag{6}$$

$$EM = \left(\frac{K_{multi}}{b\,K_{mono}^{N}} \right)^{1/(N-1)} \tag{7}$$

The symmetry number *b* is a statistical factor that equals the number of different, but indistinguishable atomic arrangements. It can be calculated from the compound symmetry or directly by counting the number of possible configurations.[74] If $b\,EM\,K^{N}_{mono} \ll 1$, the partially bound intermediate is more stable (enabling intermolecular polymerization), if $b\,EM\,K^{N}_{mono} \gg 1$ the multivalent interaction is preferred.[69]

In this thesis we were predominantly interested in the rupture mechanism of well defined model systems. Thus in the following we will focus on the degree of cooperativity and energetic representations. In an additive system, the multivalent binding free energy is the sum of all corresponding monovalent interactions. In synergetic or interfering systems, there is a negative or positive difference ΔG_x.

$$\Delta G_{multi} = \sum_{N} \Delta G_N + \Delta G_x \tag{8}$$

ΔG_x contains various chelate cooperativity effects due to the bridging backbone system:[37,38,75]

1. Less translational and rotational **entropic** penalty upon binding (This entropic penalty has already been payed in the synthesis upon bridging interaction partners with the backbone.)
2. Degeneracy of atomic arrangements *b*, increasing binding **entropy** by $RT \ln(1/b)$
3. Loss in conformational **entropy** of the backbone upon binding
4. Backbone strain (**enthalpic** penalty) due to non-optimal spacial orientation of interaction partners
5. Less binding free **energy** between interaction partners due to steric constraints

6. Reorganization of the solvent (**entropic** and **enthalpic** penalties as well as gains are possible)

The first two effects (1 and 2) increase, the subsequent three (3, 4, and 5) decrease chelate cooperativity when compared to the monovalent interaction. In an additive system, those effects cancel each other out. In a synergetic system, the increasing effects surpass the interfering ones. Consequently the perfect-fit model sketched in figure 8 is a frequently applied model for highest synergy. Due to optimal backbone lengths and configuration, there is only a loss in conformational entropy (effects 4 and 5 are negligible). Rigid backbones further decrease the entropic penalty (effect 1). A nice example is the ladder formation of zinc-porphyrin nanorods with 1,4-Diazabicyclo[2.2.2]octane (DABCO). Anderson et al. synthesized[76] and analyzed[77] this system by by ^{1}H-NMR and UV-Vis titration analysis in chloroform and toluene. The binding free energies show a remarkably linear increase upon ladder elongation n with slopes of $\Delta G_t/n$ = -58.1 ± 0.2 (toluene) and $\Delta G_c/n$ = -54.5 ± 0.4 kJ/mol (chloroform). The monovalent binding free energies are $\Delta G_{t,mono}/n$ = -55.3 ± 0.3 (toluene) and $\Delta G_{c,mono}/n$-49.6 ± 0.3 kJ/mol (chloroform), leading to y-axis intersections at $\Delta G_t(n = 0)$ = 3.7 ± 0.9 (toluene) and $\Delta G_c(n = 0)$ = 6.4 ± 1.5 kJ/mol (chloroform). The authors attribute $\Delta G(n = 0)$ to entropic penalties of ladder initiation,[77] due to solvent reorganization (effect 6). Further binding shows synergistic multivalency as $\Delta G_x < 0$ due to the high preconfiguration of interaction partners. In the present thesis, we had the same considerations upon designing the bivalent nanorod **2a**.

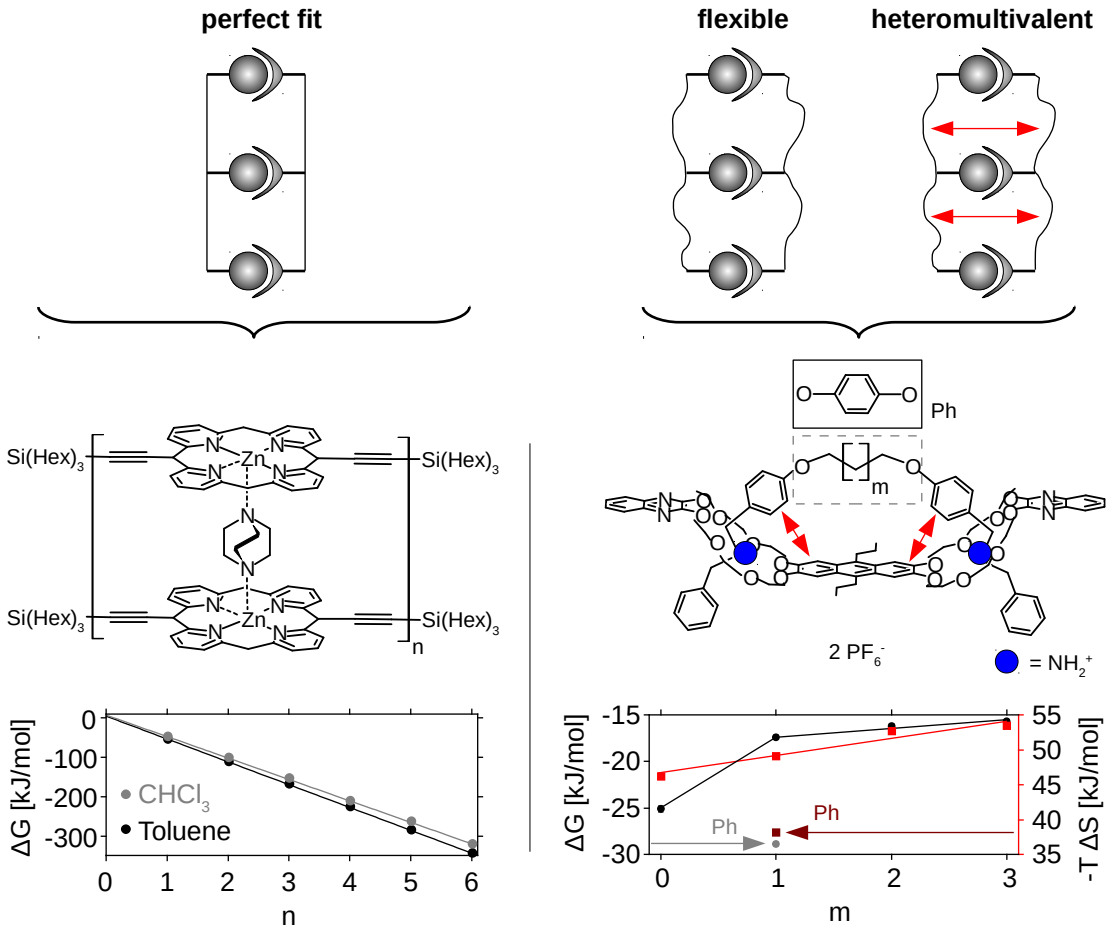

Figure 8: left) Chelate cooperativity is maximized in perfect fit systems, such as in the sketched supramolecular ladder between Zn^{2+}-porphyrin nanorods with 1,4-Diazabicyclo[2.2.2]octan. Here, each additional interaction decreases the binding free energy (ΔG) by the same value, larger than the monovalent binding free energy. This effect is solvent dependent. Error bars are included, but smaller than the data points.[77] right) Chelate cooperativity is less pronounced in flexible systems, such as in the sketched bivalent crown-ether. Upon backbone elongation (m), the entropic penalty ($-T\,\Delta S$) increases in a linear fashion (red line). In contrast the binding free energies show a strong decrease from $m = 0$ to $m = 1$ due to the non-innocent backbone. For $m = 0$, the system is actually heteromultivalent with additional π-π-stacking interactions (red arrows).[73] This effect is even more pronounced for the guest with an additional phenyl group (Ph).[78] Error bars are included, but smaller than data points.

Considering synthetic chemistry, perfect fit systems are limited to only a small amount of possible rigid backbone connections such as alkines, benzenes, or adamantanes. This is the reason why flexible backbone structures such as alkanes or ethylene oxides are much more frequently used. Jiang et al. performed a systematic isothermal titration calorimetry study using flexible connections of different lengths on the bivalent host-guest systems sketched in figure 8.[73] Crystal structure analysis revealed an optimal fit for the shortest chain length with $m = 0$. The binding free energy of the corresponding complex was $\Delta G_{m=0} = -25.1 \pm 0.3$ kJ/mol

and less than twice the monovalent binding energy of ΔG_{mono} = -15.0 ± 0.3 kJ/mol (interfering as $\Delta G_x < 0$). For systems of higher backbone length, interactions got increasingly adverse (black circles). However they did not cross the -15 kJ/mol barrier, where monovalent binding would be favored over the bivalent interaction. Thus the bivalent complex showed interfering multivalency, with higher loss in conformational entropy (red squares) for longer, flexible linker structures. However the extraordinary large energy penalty from $m = 0$ to $m = 1$ cannot be explained by this effect alone, as $-T\Delta S$ was linearly decaying. A closer investigation of the crystal structure for $m = 0$ also revealed an optimal stacking configuration between the two phenyl groups in the guest with the anthracene moiety in the host (red arrows, 0.35 nm distance). In other words, the spacer was not an innocent spectator, but lead to additional interactions in heteromultivalent system of two host-guest and two π-π-stacking interactions.[73] In a subsequent publication the authors successfully increased this effect by introducing a phenyl group (Ph) into the backbone, leading to an overall binding free energy of ΔG_{Ph} = -27.6 kJ/mol (gray circle) that even exceeded the entropic effect (dark red square) due to higher backbone rigidity.[78]

In addition to the effects of chelate cooperativity discussed above, allosteric cooperativity was found in the host-guest systems of Jiang et al. Both effects were distinguished from each other, using double mutant cycle analysis such as sketched in figure 9.[79,80] Here, both interaction partners are needed in their connected and separated form, yielding four different types of interaction: **A**, **B**, **C**, and **D**. In the following hypothetical chemical equilibration, all host-guest interactions appear on both sides of the equilibration.

$$\mathbf{B} + \mathbf{C} \rightleftharpoons \mathbf{A} + \mathbf{D}$$

For example, binding of one crown-ether by a positively charged guest in **C** influenced the second one due to the coupling anthracene unit.[73] Indeed, both binding free energies ΔG_1 in **B** and **C** were similar, but ΔG_2 was approximately 1 kJ/mol lower in **C** than in **B** (figure 9). In a double mutant cycle, those allosteric influences are canceled out and $\Delta\Delta G$ is solely due the chelate cooperativity and a possibly non-innocent backbone.

$$\Delta\Delta G = \Delta G_A + \Delta G_D - \Delta G_B - \Delta G_C \tag{9}$$

The corresponding value of $\Delta\Delta G$ = 3.2 ± 0.9 kJ/mol was smaller than the binding free energy difference ΔG_x = 4.9 ± 0.4 kJ/mol. Thus the allosteric cooperativity was

also interfering and its magnitude indeed approximated the 1 kJ/mol due to the electronic coupling in the guest molecule or **C**. The remaining free energy of 3.2 kJ/mol was due to chelate cooperativity as discussed above in mixture with heteromultivalent effects, only occurring in **A**.

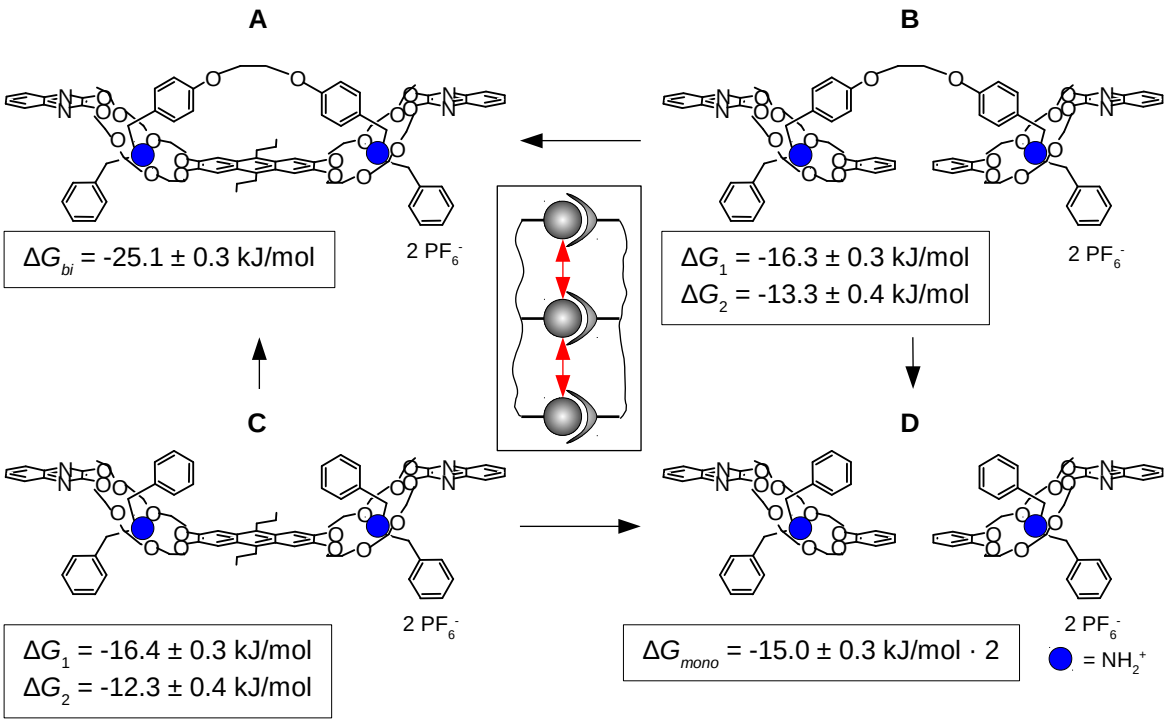

Figure 9: Double mutant cycles allow separation of chelate cooperativity and allosteric cooperativity (red arrows in the central scheme).[73,79,80] They require four separate measurements (ITC, ^{1}H-NMR, etc.) to determine binding free energies of complexes **A**, **B**, **C**, and **D**. Now, the hypothetical reaction of reorganization **B** + **C** ⇌ **A** + **D** is analyzed as written in the text.

2.1.2. Mechanical Stability

As illustrated in figure 7 above, the mechanical stability of systems with high valency, such as in the inflammatory immune response, is similar to the behavior in macroscopic systems: A stepwise (zipper-type) rupture mechanism allows rupture at low forces, a simultaneous rupture requires much larger forces ($F_{sim} \gg F_{zipper}$). This behavior was also found in experiments on the unfolding processes of protein structures. As shown in figure 4, clamp motifs of pairwise β-sheets have a high mechanical stability in shear-configuration (yielding simultaneous bond rupture), but a low mechanical stability in zipper-type configuration. Less is known about the rupture mechanisms in systems of low valency. To date such systems have been only sparsely studied, namely bivalent C_{60}-porphyrin tweezers,[4] tetravalent hydrogen

bonds with additional allosteric cooperativity,[32] and mono-, bi-, and trivalent adamantane/β-cyclodextrins.[49]

As mentioned in the introduction, the Kramers Bell Evans (KBE) or standard model in SMFS (chapter 2.5),[81] attributes the mechanical stability of interactions (most probable rupture force f^*) to a balanced interplay between thermal stability (activation energy barrier E_a or thermal off-rate constant k_{off}) and malleability (rupture length Δx). In their study on adamantane/β-cyclodextrin systems, Gomez-Casado et al. measured a similar malleability, but increasing thermal stability: monovalent < bivalent < trivalent.[49] They explained this increase using the concept of effective concentration C_{eff}. For a bivalent system equation (10) yields the equilibration constant K_{bi} as a function of C_{eff}, K_{mono} and a symmetry factor b:

$$K_{bi} = b K_{mono}^2 C_{eff} \ . \tag{10}$$

In figure 10, the general reaction scheme is shown. The symmetry factor b equals the number of different, but chemically indistinguishable products. For a bivalent interaction of symmetric partners two possible final configurations (red) are possible and $b = 2$.[74]

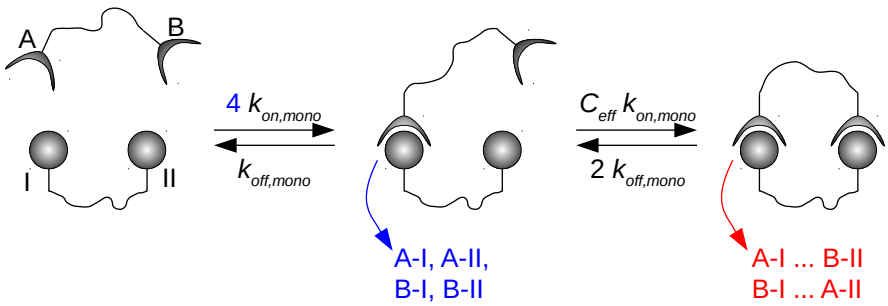

Figure 10: Binding between bivalent ligands is characterized by four possible configurations in the first reaction step (blue). In the second step, only one possible interaction remains, yielding two identical interactions for A-I and B-II as well as for A-II and B-I (red). The second step is influenced by the effective concentration, a parameter depending on backbone flexibility and match.[49]

Comez-Casado et al. used the following derivation to describe the bivalent interaction in figure 10 in terms of thermal off-rate constant $k_{off,bi}$, a parameter accessible by the KBE model.[49] In a cooperative system, the second binding step ($C_{eff}\, k_{on,mono}$) is expected to be much faster than the first one ($4\ k_{on,mono}$). This means, the first step is rate determining and the second may be neglected:

$$k_{on,bi} = 4\, k_{on,mono} \tag{11}$$

Using $K = k_{on}/k_{off}$ and equation (11) they got:

$$K_{bi} = \frac{k_{on,bi}}{k_{off,bi}} = 4\frac{k_{on,mono}}{k_{off,bi}} \quad (12)$$

Equation (10) may be rewritten as (only one K_{mono} was expanded):

$$K_{bi} = bK_{mono}\frac{k_{on,mono}}{k_{off,mono}}C_{eff} \quad (13)$$

Combining equations (11), (12), and $b = 2$ they received:

$$k_{off,bi} = 2\frac{k_{off,mono}}{K_{mono}C_{eff}} \quad (14)$$

This means, a high chelate cooperativity of effective concentration C_{eff} (strong rebinding effect) yields a low thermal off-rate constant $k_{off,bi}$ or thermally stable interaction. For the analyzed adamantane/β-cyclodextrine interactions, K_{mono} and C_{eff} had also been measured in isothermal titration and surface plasmon resonance experiments ($4.6\ 10^4$ l/mol and 0.2 mol/l), yielding $k_{off,bi} = 2.2\ 10^{-4}\ k_{off,mono}$.[82] This result from bulk measurements was close to the experimental value from the single-molecule experiment ($k_{off,bi} = 1.0\ 10^{-4}\ k_{off,mono}$), where both thermal off-rate constants had been determined from the KBE model. Thus equation (14) and the rebinding effect also quantitatively explained the increased thermal stability of the bivalent system.

In the present thesis we compared the mechanical stability of three bivalent systems with different backbone structures. Due to different backbone flexibility we aimed to change the effective concentrations, however similar thermal off-rate constants were measured. Instead the malleability was different, yielding a broad range of mechanical stabilities.[67,83] Comparing mono- and bivalent interactions, the thermal off-rate constant decreased by a factor of 10, indicating some rebinding effect. This rebinding was, however, not significantly influenced by the backbone flexibility.

2.1.3. Additional Effects

In addition to the influences described above, multivalent systems may be influenced by a variety of effects. Consequently the multivalent effect is still not fully understood and prediction of properties challenging. For example, a combined double mutant cycle and molecular mechanics analysis of the benzene bridged guest in figure 8, unveiled additional chelate interactions of the free, unbound ligand with the counter

ions from the solvent.[78] A selection of further effects, relevant in biological systems and surfaces, is sketched in figure 11.[36] Also template directed synthesis,[84] synergistic catalysis[85] and multivalent machines[37] are active fields of research on multivalent systems. Recently, chemically modified thermally reduced graphene oxides allowed first studies on flexible 2-dimensional multivalent binders.[86]

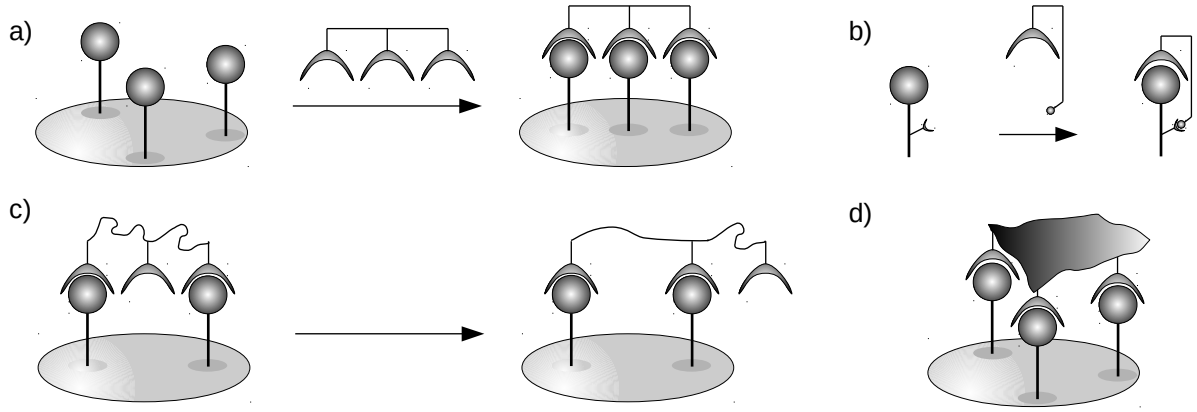

Figure 11: A selection of additional effects in multivalent interactions: a) Membrane ligands in a supported lipid bilayer are able to translocate in two dimensions. Here, clustering is possible.[36] b) Certain receptors allow additional binding to subsites.[36] c) Statistical rebinding allows for dynamic networks of bound- and unbound states. This effect is especially pronounced in case of a large excess of one interaction partner.[36] d) Flexible 2-dimensional sheets are able to follow complex surface geometries of larger partners such as viruses or bacteria.[86]

2.2. Single-Molecule Force Spectroscopy

The scanning force microscope (SFM), presented by Binning, Quate and Gerber in 1986[87], soon evolved into one of the most important high-resolution imaging methods overcoming the diffraction limit of light microscopic devices.[88,89] In 1994 for the first time an SFM was used to measure forces between single-molecules: Independent from each other, the groups of Gaub[17] and Colton[18] analyzed the mechanical stability of the streptavidin-biotin interaction. Since then, single-molecule force spectroscopy (SMFS) quickly evolved and found its application in various areas of science. Especially biomolecular systems are of large interest, because the cellular machinery is force affected or even force driven.[90] Also supramolecular interactions are frequently studied. They are model systems to gain fundamental information on force-induced bond rupture, which may be compared with biomolecular systems or applied in the design of mechanoresponsive materials. Here, reactive groups are activated by external forces on the material. These groups, preferentially of catalytic activity, are potential centerpieces of autonomous self-healing materials.[13]

In an SMFS experiment, the SFM cantilever is used as force sensor.[91] In the low-deflection regime, its vertical bending directly correlates with the applied force. Using very soft cantilever probes, also forces in the range of non-covalent interactions get accessible. In comparison to common probes for intermittent contact applications (2 - 42 N/m), here spring constants are in the range of 6 - 600 mN/m and deliver sufficiently high deflection values of 0.8 - 0.08 nm already at the thermal noise level (using T = 298 K and equation 27).

In order to probe specific interactions, the cantilever, the surface, or both are modified giving adhesion signals in the retract part of the force-distance cycle. A typical SMFS experiment is sketched in figure 12. To date, signals of various shapes have been identified and studied, such as peaks originating from direct tip-sample contact[92] (figure 12b), sawtooth signals from polymeric spacers such as PEG[93](figure 12c) or the *I27* domain of titin[94], and plateaus from continuous detachment processes such as the stepwise desorption of polyalanine from hydrophobic diamond surfaces[95,96] or pulling of membrane tethers[97] (figure 12d). Melting of 3-point fixed DNA at 65 pN[98] or RNA at slightly lower forces[99], structural transition of 4-point fixed DNA at 110 pN[100], and DNA slippage[101] are characterized by a sawtooth with intermediate plateau.

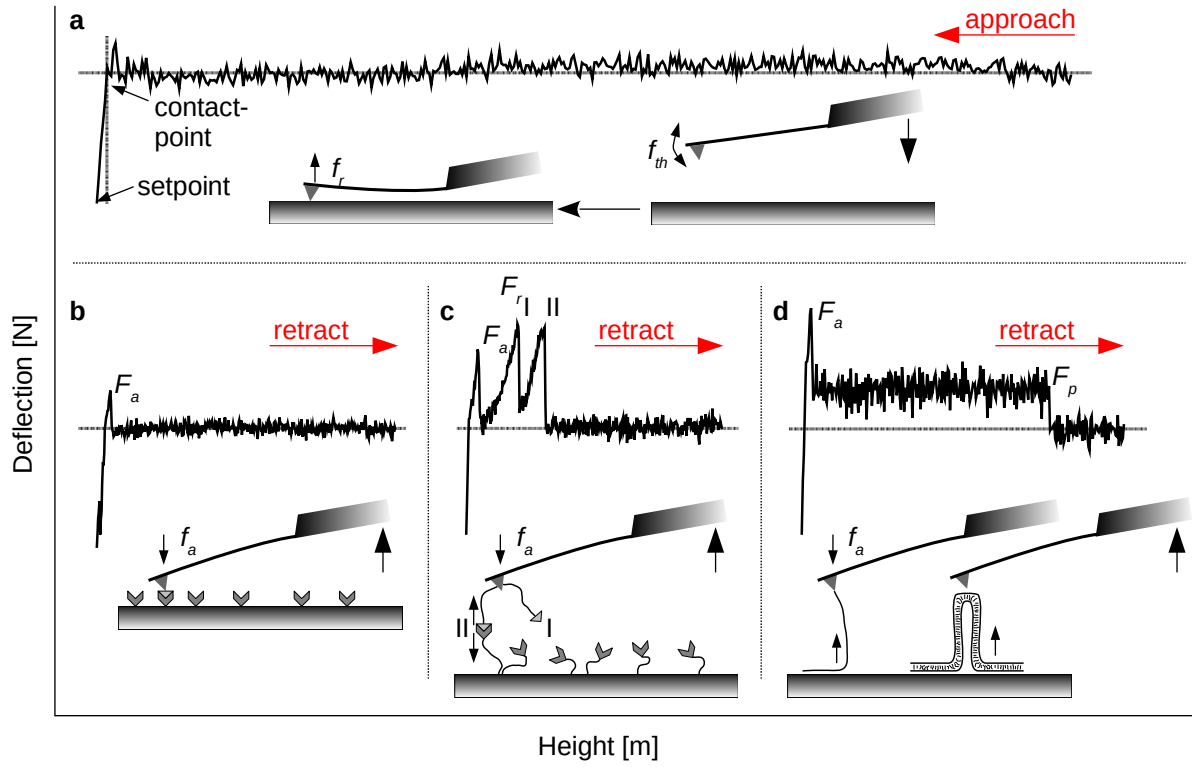

Figure 12: In a typical SMFS experiment, the vertical deflection of a calibrated cantilever is plotted against the relative position of the z-piezo (height signal, usually in a closed-loop setup to exclude piezo hysteresis effects). a) During the approach, the cantilever is oscillating around a baseline due to thermal noise and hydrodynamic effects. When the tip hits the surface at the “contact point”, the deflection instantaneously increases due to the repulsive force f_r. The shape of this part is a measure of the elastic surface properties. See also Wang et al. for further details about JKR, DMT and Hertzian models as they are not further discussed in this thesis.[102] b) After reaching the setpoint, the cantilever is retracted. Usually the first signal is due to the tip-sample interaction at the contact point with a maximum, called adhesion force of F_a. c) To discriminate multiple rupture events from single-molecule signals, the polymeric tether approach is often utilized. Here the deflection-height diagram shows additional sawtooth signals (I broke in advance of II). Their peak height is the rupture force F_r. d) Some mechanical processes yield a plateau with force F_p rather than a sharp signal. a)-d) are scaled arbitrary to emphasize characteristic features.

According to Newton‘s third law, stationary forces are propagated through all elements of the system. For example, when using polymeric tethers to probe a single-molecular interaction such as shown in figure 12c, the same vertical force component acts on the cantilever (or the force sensor), all bonds in the tether molecules and the interactions that were used to modify tip and surface. All parts need to be much more stable than the single-molecular interaction of interest. Fortunately, non-covalent interactions have rupture forces that are much lower than those of covalent interactions. To date, the strongest non-covalent interactions

known are the protein complexes between XMod stabilized Dockerin and Cohesin (600 – 750 pN)[34] and the trimeric titin-telethonin complex (700 pN)[103]. Both rupture forces are only half as large as the mechanical stabilities of covalent interactions.

SMFS experiments are much more challenging, when the interaction of interest is covalent. Even if the experiment is properly designed and the interaction of interest is the weakest part, rupture of a covalent bond is an irreversible process. The SFM cantilever modification is used up after only a few force-distance cycles and it gets difficult to obtain statistically significant amounts of rupture events. Therefore it is still not fully understood, under which mechanism covalent bonds break in an SMFS experiment. In the initial work from Grandbois et al. in 1999[104], single polysaccharide chains were attached to surfaces by silane (glass-O-Si-C-saccharide) or thiol bonds (gold-Au-S-C-saccharide). Different rupture forces of 2.0 ± 0.3 nN for the silane coupled and 1.4 ± 0.3 nN for the gold coupled chain were measured. The underlying mechanisms were heavily discussed in the literature:

a. Silane: Initial DFT and KBE model approximations suggested that the Si-C bond shows the lowest resistance against forces and preferentially brakes due to the applied forces[105]. This is in contradiction to a recent experimental work by Clausen-Schaumann and coworkers. Their results rather indicate force-induced catalytic bond hydrolysis involving the aqueous solvent. Here the Si-O or possible C-O bonds are most sensitive to forces,[106] which is also supported by theoretical calculations.[107,108]

b. Gold: The lower force resistance of thiol-gold coupled systems compared to silane attachment indicated a breakage involving the Au-S bond. However in 2002 molecular dynamics simulations in the group of Marx showed, that also Au-Au interactions reorient under force, forming a “gold-wire” transition state. The rupture force of an Au-Au bond in such a wire was calculated to be 1.2 nN, well matching the experimental value.[107]

The measurable range of forces in SMFS spans over three orders of magnitude. In the low force regime, it is limited by the thermal noise oscillation of the cantilever. According to the equipartition theorem, $\Delta f = \sqrt{k_B T / 2 \cdot k_c}$ yields an average displacement of Δf = 3.5 pN for k_c = 6 mN/m probes, and of Δf = 35 pN for k_c = 600 mN/m ones. In the high force regime, the largest cantilever deflection that is still measurable and of linear bending behavior is limiting. Stiffer cantilevers allow

measurements of higher forces and also covalent interactions are accessible. The overall range of forces includes up to three different regimes of polymer deformation.[109] In figure 13 two representative force-distance plots of PEG in chloroform and water are shown:

1. Entropic elasticity: Up to ~50 pN, the resistance against pulling is entropic.[110] In this regime both force-distance curves are linear as expected for Gaussian chains[111].
2. Supramolecular reorganization: Above ~50 pN up to ~300 pN, force-distance curves show a non-linear transition into regime three. Here, non-covalent interactions are broken. For example, ds-DNA is over- and unwound[14], nicked ds-DNA is molten[98] and PEG in water looses its secondary gauche in favor of a trans conformation[93]. Also most host-guest interactions and supramolecular systems (such as those analyzed in this work) break in this force regime.
3. Bond angle deformation: Beyond ~300 pN, force-distance profiles in protic and aprotic solvents exhibit an asymptotic behavior.[112] Here, bond angle torsion and deformation are dominating processes. Both extensible WLC and FJC models include this high-force regime by means of an elasticity term K_s (chapter 2.4).

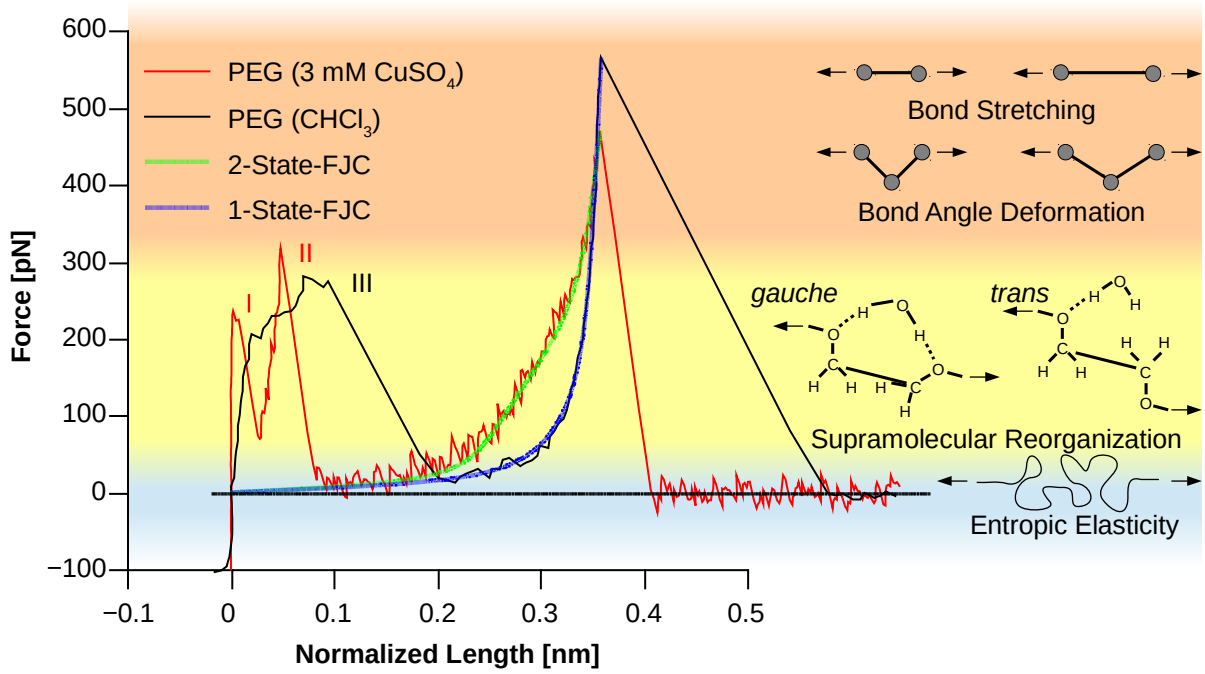

Figure 13: Representative force-distance plots (tip-sample-separation representation) of PEG in aqueous solvent (continuous red line) and chloroform (continuous black line). Additionally the FJC model fit (blue, dashed line, equation 37) and the 2-state-FJC extension by Oesterhelt et al. [93] (green, dashed line, equation 80) are shown (L_{trans} = 0.36 nm, L_{gauche} = 0.28 nm, ΔG = 3 k_B T, l_K = 0.7 nm, T = 298 K, and free fit parameters: N_s and K_s). Signal I is due to direct interaction between tip and surface, signal II due to a simultaneously pulled polymer, and signal III due to unspecific interactions. The elastic (and reversible)[113] elongation of polymers is accompanied by transformation processes in up to three different regimes: Entropic elasticity, supramolecular reorganization, and bond angle deformation + bond stretching.

A well studied example for supramolecular rearrangement is PEG, the polymer also used in this work. In 1999, Oesterhelt et al. discovered a significant difference in the mid-force regime when pulling this polymer in PBS buffer and hexane.[93] In the protic solvent, PEG starts to resist the pulling process at much smaller normalized lengths than in hexane. This behavior is illustrated in figure 13 using our measurements in 3 mM $CuSO_4$ (red) and chloroform (black), respectively. The authors attributed this behavior to a gauche conformation (net length: L_{gauche} = 2.8 Å), stabilized by hydrogen bound water from the solvent such as sketched in figure 13. Increased external forces release the water, leading to a trans conformation with a net length of L_{trans} = 3.6 Å. Oesterhelt et al. were able to describe all three force ranges, using a single 2-state-FJC master equation (80). The energy of the intermediate state was estimated by ΔG = 3 ± 0.3 k_BT (see also chapter 2.4.3 for further details).[93]

To date several methods for SMFS have been established. Instead of an SFM cantilever, also glass microneedles, magnetic and especially optical tweezers are frequently used. Those techniques are summarized in table 1.[114] DNA was studied extensively using all four methods: Already the first single-molecule experiment was performed by Smith et al. using magnetic beads, moved on a glass slide.[110] Their results lead to the force-distance formulation of the worm-like chain (WLC) model in 1994 (chapter 2.4).[115] In 1999 Leger et al. published a famous publication using a glass microneedle setup[14] to unwind, overwind and stretch ds-DNA.[100] The ability to rotate single-polymers was prerequisite for unveiling of the force-torque phase diagram of DNA, nicely illustrated in the review paper by Bustamante et al.[116] As compared in table 1, magnetic beads offer a better resolution in the low-force regime than glass microneedles. Using paramagnetic beads, rotational experiments are possible as well, for example revealing a spontaneous overwinding when nicked DNA is stretched.[117] In recent years optical tweezers made large progress. Of huge interest is the combination of low-force experiments in the horizontal axis with vertical fluorescent observation.[118] This enabled Gross et al. to refute the B-S-form phase transition in nicked DNA. Their findings suggest, that the phase transition at 65 pN is probably due to an unzipping of DNA base pairs.[98] SFM based SMFS benefits from sophisticated devices and a broad range of commercially available cantilever probes. Therefore it is the most versatile method, offering a large force range, fast feedback systems and the compatibility with various media ranging from aqueous buffer solvents, “difficult” non-polar and volatile solvents, air and UHV.

Table 1: Overview of single-molecule force spectroscopy methods

SMFS Method	Force Range [pN]	Force Sensor
Magnetic Tweezers	0.01-100	modified paramagnetic beads that are moved and rotated by a permanent magnet, optical particle tracking, calibration possible using the thermal noise method [15]
Glass Microneedles	>0.1	modified optical fibers with diameters of 5-15 µm, tracking by CCD detection of laser light coupled through the fiber, calibration possible using the thermal noise method [14]
Optical Tweezers	0.01-200	modified objects (beads, algae[119], tools[120], etc.) with higher refractive index than the surrounding medium moved by a field gradient in the focus of laser light, tracking by back focal plane interferometry[16], calibration possible using the thermal noise method[121]

Scanning Force Microscopy	>10	modified cantilever probes, tracking by optical detection of lever deflection, various calibration procedures possible

2.2.1. Rupture Under Non-Equilibrium Conditions

Is force-induced rupture an equilibrium or non-equilibium process? Under equilibrium conditions, the broken bond has a nonzero rate of bond reformation. In the SMFS experiment, both interaction partners are pulled apart from each other due to the relaxing cantilever movement. However, the experimental timescale is orders of magnitude slower than motion on the level of single-molecules, leaving sufficient time for bond reformation. In the experiment, the most probable rupture force of an equilibrium process is independent of the loading rate, yielding a horizontal line in the dynamic force spectrum. But the same result is possible for non-equilibrium processes at high rupture lengths. Consequently there was some debate on this issue, which will be discussed in this chapter. It is especially relevant in the context of multivalent interactions, where the rebinding effect[122] plays a mayor role.

Between 2000 and 2004, Vancso et al. were the first to apply SMFS on host-guest systems.[123–125] Thereby ferrocene, adamantane, benzene, and other guests were covalently coupled to the SFM cantilever, using only small spacer chains of up to six CH_2 groups. As host, always a β-cyclodextrin SAM on Au(111) was used. Due to the lack of a polymeric spacer, a broad distribution of rupture forces from single-molecular and simultaneous rupture events were measured, characterized by periodic maxima. The observed force quanta were attributed to single-molecular interactions. Their most probable rupture forces did not change at varying loading rates, which was attributed to equilibrium bond rupture.[126,127] One year later, Anselmetti et al. used the polymeric spacer approach in SMFS to probe the host-guest interactions between resorc[4]arene and ammonium/triethylammonium guests.[30] Here, rupture forces were dependent on the loading rate. The KBE model was applicable and revealed a ratio of rupture lengths that correlated to the van der Waals radii of both guests: calculated 0.3 and 0.6 nm, measured 0.22 ± 0.04 and 0.38 ± 0.06 nm. The important difference in both experimental setups was the polymeric tether. Friddle et al. analyzed both configurations by means of analytical and numerical calculations (figure 14). They described the effective potential energy diagram as a convolution of three parts: cantilever, tether, and single-molecule. In the tetherless situation (a), equilibrium and non-equilibrium rupture are possible,

depending on the loading rate. At larger loading rates, typical rupture forces are larger, yielding also larger deflections x_p of the cantilever. At larger x_p, the dissociation rates are favored, the re-association rates are disfavored. As a result, the average timescale of bond reformation decreases and ultimately falls below the experimental timescale (non-equilibrium conditions). In contrast, rupture in the tethered setup (b) exhibits a semiharmonic potential, which yields rupture under non-equilibrium conditions for all loading rates.[64,127] The latter represents the experiments, performed in this thesis.

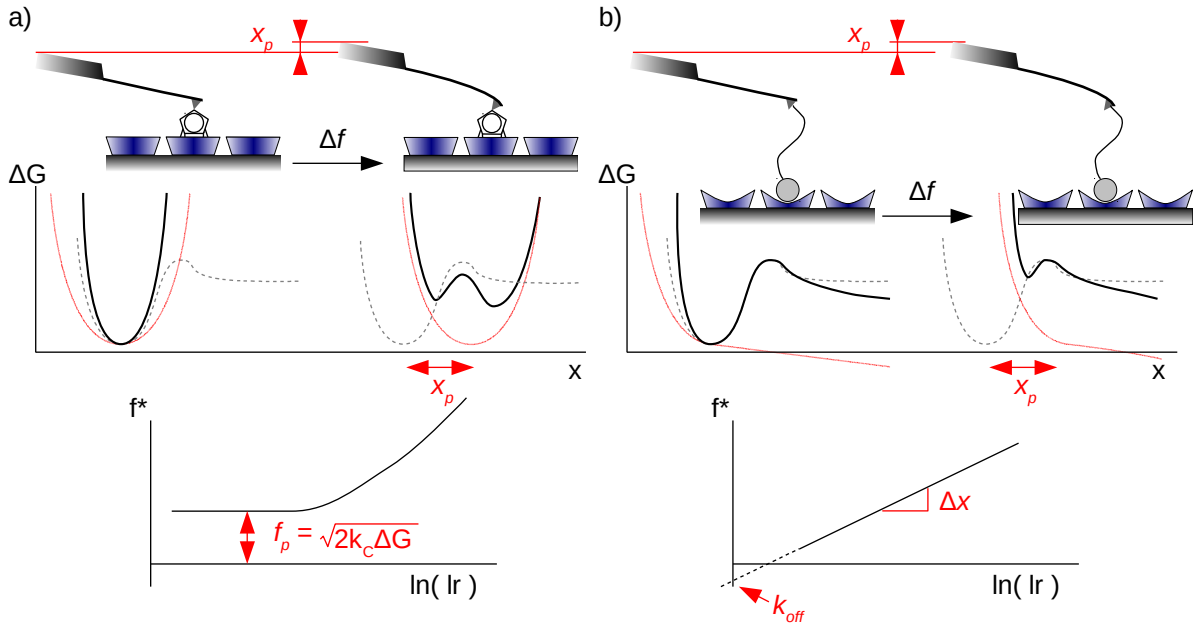

Figure 14: Schematic drawings, energy diagrams and dynamic force spectra of directly bound and tether mediated interactions. a) Overlap between the cantilever (dashed red) and sample (dashed gray) potentials yield the black overall energy diagrams. Below a certain lift of the cantilever x_p (corresponding to force $f_p = k_c\, x_p$), the bond does not break. Beyond the threshold force f_p, the overall potential allows quasi-equilibrium behavior. In the dynamic force spectrum, a constant rupture force is measured that depends of the square root of sample free energy difference ΔG and cantilever spring constant k_c.[127] At high loading rates, the system enters the non-equilibrium regime.[126] b) In tether-mediated experiments, cantilever and polymer exhibit an asymmetric potential (red), yielding the black energy diagram of irreversible bond rupture. The dynamic force spectrum shows the log-linear relationship described by the KBE model.[128]

The transition between the equilibrium and non-equilibrium regime in figure 14a could also be measured experimentally in a quite sophisticated system of mechanically interlocked calix[4]arenes, such as sketched in figure 15. After the concerted rupture of 16 hydrogen bonds between a pair of capsules (**a** → **b**), mechanically interlocked loops in the backbone still kept both interaction partners

nearby. Under slow pulling conditions (low force), the authors observed signatures of 2-state-fluctuations in the force-distance diagrams, characteristic for equilibrium conditions. This corresponds to the energy diagram sketched in figure 15, where states **a** and **b** are of similar depth, thus yielding similar thermal off- and on-rate constants k_{off} and k_{on}. At fast pulling speeds (larger forces), those signatures disappeared indicating a transition into the non-equilibrium regime.[129] In terms of ΔG, the tilt $-f\,x$ has a larger influence on state **b** than **a**. Consequently, k_{off} is increased, k_{on} decreased.

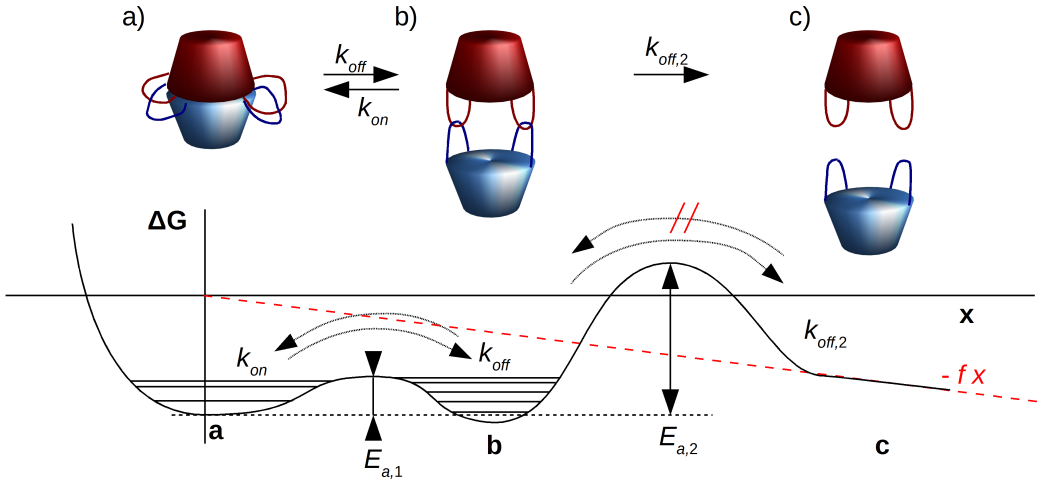

Figure 15: SMFS experiment on a pair of calix[4]arene capsules.[129] Top: Interlocked loops allow separation beyond the typical reach of hydrogen bonds, but keep both interaction partners in proximity to each other. Bottom: Under the influence of an external force, the energy diagram (ΔG) along pulling coordinate x is tilted by $-f\,x$. Due to the mechanical interlocks, states **a** and **b** are in equilibrium with each other. In contrast, the broken state **c** is characterized by irreversible rupture of the mechanical interlocks.

2.2.2. Application of the Balanced Interplay

The balanced interplay between mechanical stability and malleability and its corresponding motifs (shear and zipper) are important issues throughout this thesis. In 2008, a fascinating application using a SFM and ds-DNA was presented: the single-molecular cut-and-paste technique. [130] As sketched in figure 16, 30 base pair ds-DNA can withstand up to 60 pN in shear direction (step III), but only 20 pN in zipper configuration (step I).[131] The handle sequence consists of 20 base pairs, giving an intermediate shear force of 50 pN (steps I and III). Ultimately, this technique was used to arrange 500 fluorophores with a precision better than 10 nm.[132]

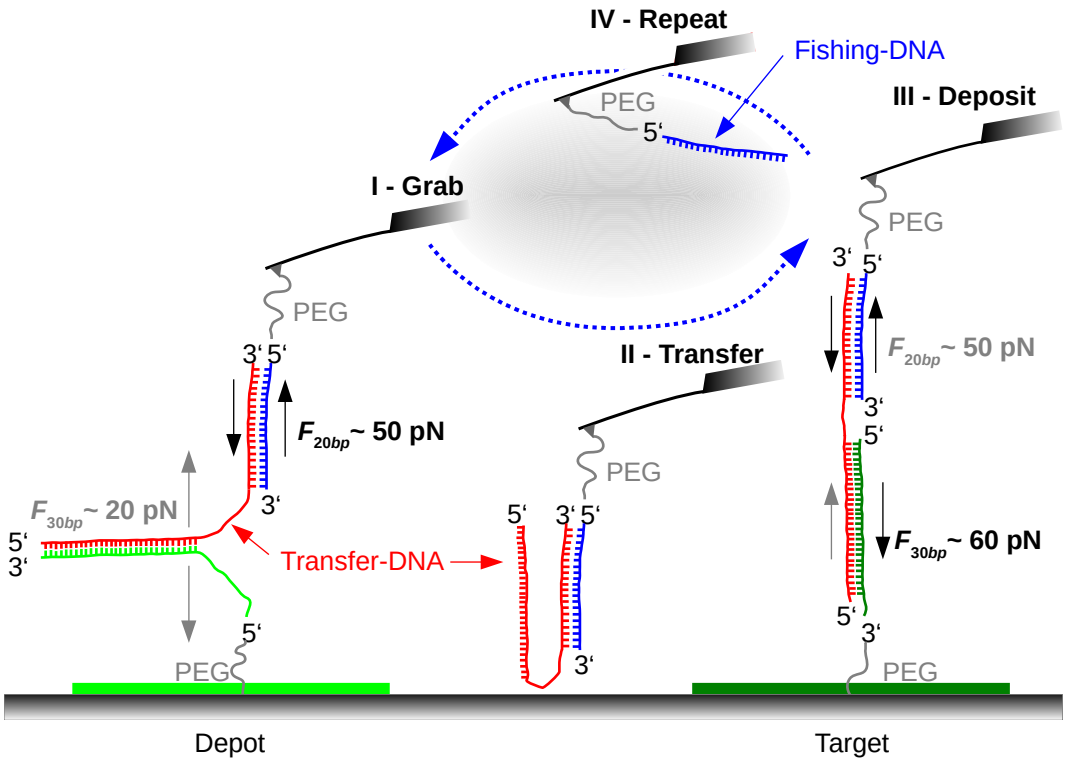

Figure 16: Forces applied to single-molecules are directed. The single-molecule cut-and-paste technique makes use of different force resistances of ds-DNA in shear- and zipper geometry in order to move transfer DNA from a depot to a target region on the sample. The 30 base-pairs anchor sequence at depot (light green) and target (dark green) is 3‘ – 5‘ reversed and dimerizes with the transfer DNA (red) in reversed orientations. The 20 bp sequence of the transfer DNA can be grabbed by its complementary sequence at the SFM cantilever (blue) in shear orientation. I) The 20 bp sequence at the SFM cantilever grabs transfer DNA from the depot region by melting the 30 bp sequence (red-light green) due to force. II) The SFM cantilever moves the transfer DNA to a target region some micrometers away. III) Here, the 20 bp sequence (red-blue) is molten due to the different geometry. The transfer DNA (red) remains at the target. IV) The 20 bp sequence of fishing DNA (blue) is remaining at the SFM cantilever enabling up to 900 transport cycles[133], each one requiring a time of approximately 3 s[134].

2.3. SFM Cantilever Calibration

Key element of quantitative single-molecule force spectroscopy is a reproducible calibration procedure with low standard deviation that should be interlaboratory comparable.[90,135] Usually the KBE or standard model is applied to data from a SMFS experiment. It yields two parameters: the rupture length Δx and the thermal off-rate constant k_{off}(0 pN) (chapter 2.5). A systematic error in the spring constant is inverse proportional to the error in the rupture length Δx. The thermal off rate k_{off}(0 pN) is not influenced but systematic errors, but profits from lower statistical errors due to its large inherent uncertainty.

All calibration methods we are aware of assume a linear force-distance response, valid for low degrees of cantilever bending. For example, the Olympus Biolever used in this work offers two rectangular shaped probes with lengths of 100 and 60 µm, as well as nominal spring constants of 6 and 30 pN/nm. This means, typical non-covalent interaction forces in the range of up to 500 pN can be probed with 83 and 17 nm deflection, each, which is less than 1‰ vertical bending. Then equation (15)[91] holds true, where k_c is the spring constant, F the force, and Z_c the vertical cantilever deflection. In terms of material properties, k_c is a function of elastic modulus E, cantilever width b, length L and thickness t_c.

$$k_c = \frac{F}{Z_c} = \frac{E\,b\,t_c^3}{4L^3} \tag{15}$$

Commercial probes are usually sold with a spring constant, calculated from nominal cantilever dimensions and elastic modulus. Predominantly variations in thickness lead to large systematic and statistic errors from these given values of up to 125%[135]. Thus the nominal spring constant is only an approximate value and a more precise calibration necessary. In table 2, common calibration procedures are summarized. They are grouped into methods that make use of static deflection due to some reference cantilever or molecule, and methods that use the dynamic oscillation or damping behavior.

Table 2: Frequently used methods for calibration of SFM cantilever probes

Method	Interlaboratory Reference	*in-situ* Calibration	Ease of Implementation	Reported Uncertainties
		Static Methods		
Reference Cantilever[136]	pre-calibrated cantilever	not possible	medium	5 - 10%[136]
Reference Molecules[137]	characterized molecules	possible	difficult	not yet analyzed
		Dynamic Methods		
Sader Hydrodynamic[138]	viscous damping	possible	easy / difficult	6%[135] (dimensions from SEM)
Cleveland Added Mass[139]	mass of a sphere	not possible	difficult	25%[140]
Thermal Noise[141]	thermal energy k_BT	possible	easy	15% [135]
Laser Doppler Vibrometry[142]	thermal energy k_BT	not yet reported	medium (but separate device needed)	1-5%[142,143]

Currently, the standard method in SMFS is the thermal noise method due to its ease of implementation and compatibility to *in-situ* calibration. However all methods have their advantages and disadvantages that make them useful in different application scenarios. In the following, we are will give an overview on both, static and dynamic modes, with a special focus on the “standard method”.

2.3.1. Static Methods

The reference cantilever method is probably most straightforward. As sketched in figure 17, the test probe with unknown spring constant k_{test} is calibrated by performing force-distance curves on a reference probe with known (similar) spring constant k_{ref}. In the contact region, a slope is measured: the Inverted optical lever sensitivity, InvOLS or S_C. S_C is then compared with the corresponding value from a hard surface S_H. Equation (16) yields the unknown spring constant k_{test}, which is also affected by the reference cantilever length L_{ref}, the relative position ΔL and tilt angle α.[136,144]

$$k_{test} = k_{ref}\left(\frac{S_c}{S_H} - 1\right)\cos^2\alpha\left(\frac{L_{ref}}{L_{ref} - \Delta L}\right)^3 \qquad (16)$$

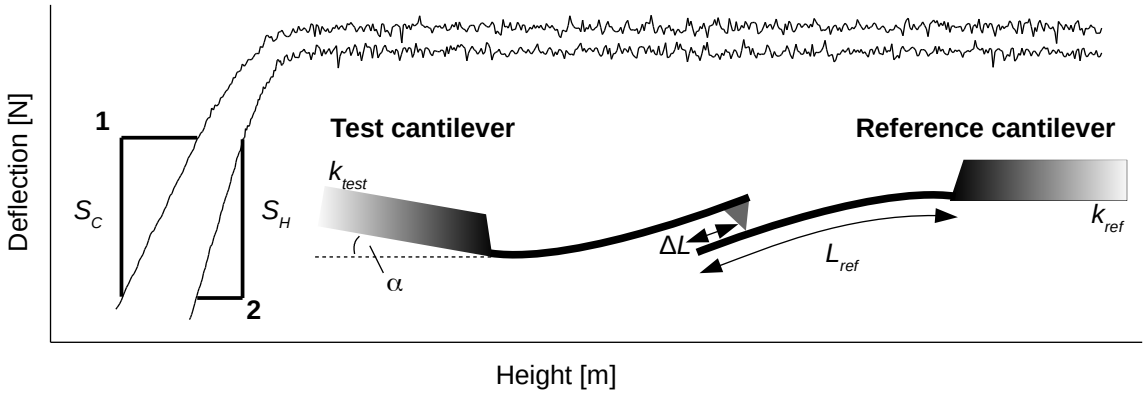

Figure 17: In the reference cantilever method[136], the test cantilever is pressed onto a reference probe with well defined spring constant k_{ref} giving force-distance curve **1** and onto a hard sample surface giving **2**. The corresponding inverse optical lever sensitivities (InvOLS) are S_C and S_H. Probe dimensions and deflections are not to scale.

Using the Euler-Bernoulli beam theory for ideally shaped reference cantilevers, a multi-point calibration can be performed to yield uncertainties between 5 and 10%[136] or even up to 2% for stiff probes[145] Prerequisite is a proper calibrated reference cantilever. Commercially available probes are usually calibrated using the laser Doppler vibrometry method as described below, owing uncertainties of 5%.[142] Since 2006, the Physical Measurement Laboratory of the National Institute of Standards and Technology (NIST) runs the project “Small Force Metrology” to achieve SI traceability for small force measurements and instrumentation. In 2008 Stan et al. presented a prototype sample of reference cantilevers with less than 2% relative standard deviation according to an extremely sophisticated electrostatic force balance (uncertainty better than ±0.6%[146]).[147]

The reference cantilever method is an external calibration procedure, meaning online recalibration during a measurement is difficult to perform. Additionally modified cantilevers may be damaged while being pressed on the reference cantilever. As all other slope-dependent techniques, the static method is also sensitive to friction or slip, twisting or buckling and tip-to-surface adhesion.[136]

An alternative approach for interlaboratory standardization are well studied natural systems, measured *in-situ* as internal standard. The idea originates from precise contour length measurements using proteins of well characterized folded structure by Dietz and Rief in 2004.[137] The molecule of interest is covalently linked to the well characterized protein. In the experiment both are pulled in a row, yielding force-distance spectra with both, the known unfolding sequence and signals of the

unknown molecule (internal standard).[148] Pratt et al. are currently working on a standardized protocol for NIST, using the characteristic melting transition of ds-DNA at 65 pN[98].[149]

The reference molecule approach is independent of any uncertainties in probe calibration and therefore promising for life-science samples. Its drawbacks are elaborate sample preparation (with some recent advances)[43] and specific solvent conditions (buffer, pH, temperature). For example, the metal ions used in this work would influence the rupture behavior of internal standards, thereby reducing its feasibility.

2.3.2. Dynamic Methods

In 1998 John Elie Sader introduced a beautiful dynamic method that makes use of the dissipative and inertial effects in (incompressible) fluids or air.[150] No physical contact with any surface is needed, which is useful to avoid wear of cantilever tips. Both experimental parameters, resonance frequency ω_R and quality factor Q, are accessible by measuring the thermal oscillation of the cantilever such as detailed below. Additionally, the physical dimensions of the cantilever are needed. The quality factor Q is a measure of energy dissipation due to damping and defined by equation (17). At resonance frequency ω_R, E_{stored} is the energy at highest oscillation amplitude A (equation 18), E_{diss} the energy dissipation per oscillation cycle.[138]

$$Q \equiv 2\pi \left. \frac{E_{stored}}{E_{diss}} \right|_{\omega=\omega_R} \tag{17}$$

$$E_{stored} = \frac{1}{2} k_c A^2 \tag{18}$$

E_{diss} is depending on the physical cantilever dimensions and its oscillation behavior (calculated by finite element methods). Sader derived equation (19) for rectangular cantilevers, where the length greatly exceeds the width (length/width ratios of 3.3 - 13.7 for ideally rectangular and 3.9 - 10 for slightly non-rectangular probes).[151] Here, the spring constant k_c is only depending on the cantilever plain view parameters length L, width b, the quality factor Q_R at the resonance frequency ω_R and the imaginary components of the hydrodynamic function $\Gamma_i(\omega)$[150] (see figure 18a for rectangular cantilever dimensions). $\Gamma_i(\omega)$ only depends on the Reynolds number $Re = \rho\omega_R b^2/(4\mu)$, where ρ and μ are the fluid density and viscosity, respectively.

$$k_c = 0.1906\, \rho_R b^2 L\, Q_R \Gamma_i(\omega_R) \omega_r^2 \tag{19}$$

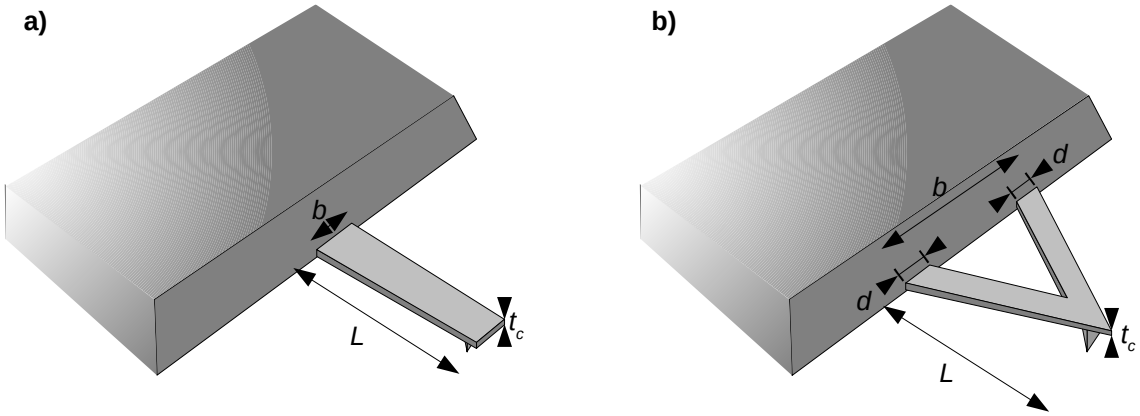

Figure 18: Schematic after [152] illustrating the dimensions of a) rectangular and b) V-shaped cantilevers.

In 2005 Sader extended his method to V-shaped MLCT/MSCT probes from Bruker, thereby emphasizing the general applicability to probes of arbitrary geometry.[152] Corresponding probe dimensions are sketched in figure 18b, *d* is the width of each cantilever arm.

C-Type: $$k_c = 3.57\,\rho d^2 L\,\mathrm{Re}^{-0.728+0.00915\ln \mathrm{Re}}\,\omega_R^2 Q \qquad (20)$$

D-Type: $$k_c = 2.97\,\rho d^2 L\,\mathrm{Re}^{-0.700+0.0215\ln \mathrm{Re}}\,\omega_R^2 Q \qquad (21)$$

In 2011, an “Interlaboratory round robin on cantilever calibration for AFM force spectroscopy” was published by nine research groups using equations (20) and (21).[135] Here, cantilever dimensions had been determined by scanning electron microscopy (SEM). Then the spring constant k_c was determined by various groups on various devices in air, yielding a variation of only ± 6%. When calibrated in fluids, the much smaller quality factor is expected to increase those variation.

Recently Sader et al. analyzed a wide selection of probes with more complex geometry, providing easy to use approximations.[138] Also torsional spring constants may be calibrated.[153] A drawback of this method is, that an SEM analysis of every cantilever probe is usually not applicable. The physical cantilever dimensions given by the manufacturer are not sufficiently accurate (for example ± 16 µm in length and ± 1 µm in width for the Olympus Biolever). A compromise is optical microscopy with a reported resolution of up to 2 µm.[154]

The Cleveland added mass method is another purely dynamic calibration method. The resonance frequency of a cantilever ω_R is shifted, when an extra mass *M* is added.[139]

$$\omega_R = \sqrt{\frac{k_c}{m}} \tag{22}$$

$$\omega_R' = \sqrt{\frac{k_c}{m+M}} \tag{23}$$

Here, m is the unknown mass of the cantilever. Substituting equation (22) into equation (23), the unknown spring constant k_c can be determined.

$$k_c = \frac{M}{1/\omega_R'^2 - 1/\omega_R^2} \tag{24}$$

This method can be improved by adding various extra masses M to the cantilever and performing a linear fit to the measured resonance frequencies $\omega_R'^2$. According to equation (25), directly derived from equation (23), the slope equals the spring constant k_c.

$$M = \frac{k_c}{\omega_R'^2} - m \tag{25}$$

The added masses M are usually determined by optical characterization of gold or tungsten spheres.[91] When capillary forces are used instead of glue, particles may be removed or even moved to different positions at the cantilever by active oscillation (such as in intermittent contact mode). The latter is quite convenient, because the effective mass is related to the distance ΔL from the cantilever end and the overall cantilever length L (equation 26), enabling a multi-point calibration with only one sphere.[155]

$$M_{effective} = M_{sphere}\left(\frac{L - \Delta L}{L}\right) \tag{26}$$

In 2004 Green et al. reported calibration of torsional spring constants using the Cleveland method.[153] The major source of error in the Cleveland method is the optical characterization of sphere radii and their position at the cantilever, yielding an uncertainty of up to 25%[140]. Additionally this method is time-consuming.

The thermal noise method make use of the equipartition theorem, which states that each mode of the cantilever on average contains the energy of $\frac{1}{2}k_BT$.[135] In 1993 Hutter and Bechhoefer first described a calibration method combining this theorem and a simple harmonic oscillator model with spring constant k_c (equation 27).[156]

$$\frac{1}{2}k_c\langle z_c^2\rangle=\frac{1}{2}k_BT \tag{27}$$

Here k_B is the Boltzmann constant and T the absolute temperature. As shown in figure 19b, the mean square displacement $\langle z_c^2\rangle$ of the cantilever is usually calculated from the area below a power spectral analysis in order to exclude noise sources and drift. The area is commonly fitted by a simple harmonic potential with additional damping (SHO) model[157] (equation 28). Usually the first resonance peak is fitted, yielding the resonance frequency ω_R, the quality factor Q, the amplitude noise at resonance A and the amplitude background noise A_{white}.[141] To gain A in units of $z_c/\sqrt{(Hz)}$, the optical laser deflection (the CCD photo diode signal) is converted into a height signal using the InvOLS on a hard substrate (Figure 19a).

$$S_{SHO}(\omega)=A_{\text{white}}^2+\frac{A^2\omega_R^4}{Q^2(\omega^2-\omega_R^2)^2+\omega^2\omega_R^2} \tag{28}$$

$$\langle z_c^2\rangle=\frac{\pi A^2\omega_R}{2Q} \tag{29}$$

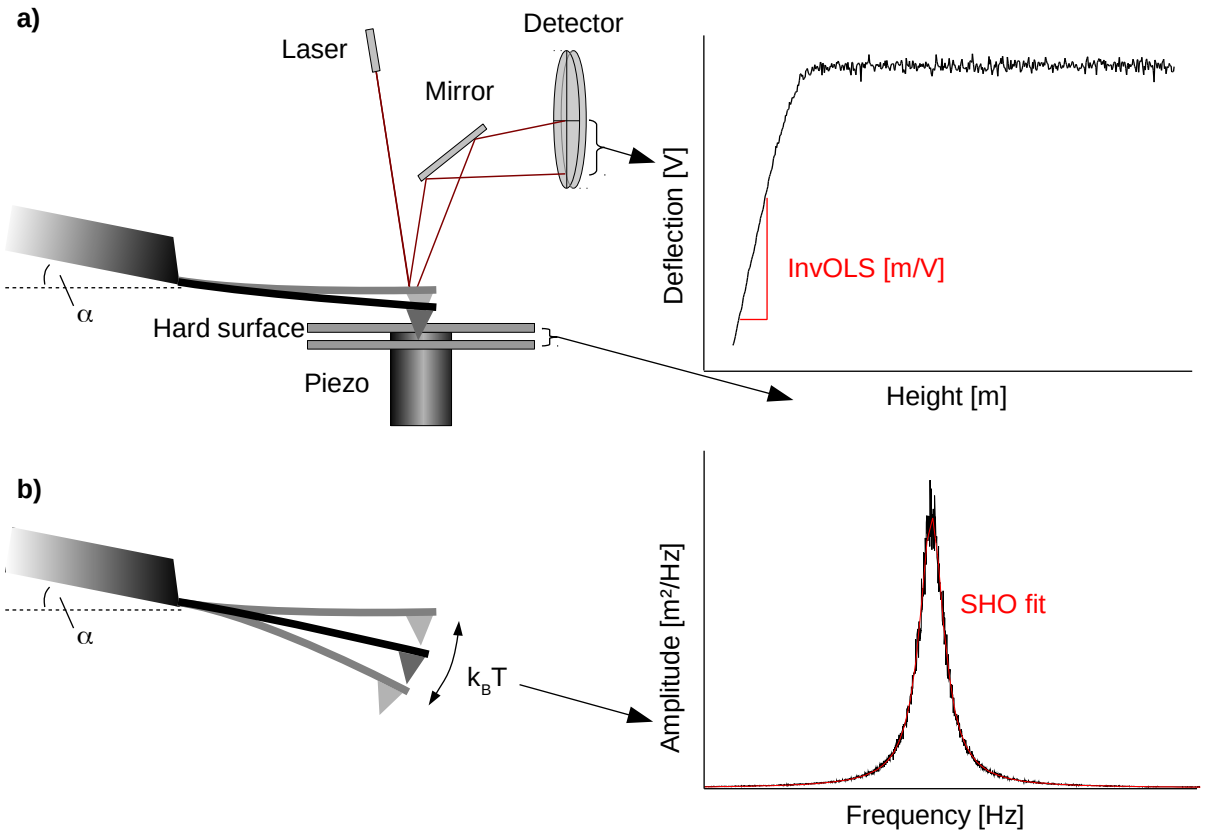

Figure 19: The thermal noise method is a 2-step calibration procedure. a) First the InvOLS is calculated from the repulsive part of a force-distance curve, measured by pressing the cantilever onto

a hard surface. Thereby the detector signal in arbitrary units is converted into a deflection value in meters due to the calibrated z-piezo. b) Second the thermal power spectral density is measured after lifting the cantilever somewhat above the surface. A simple harmonic oscillator SHO fit is utilized to calculate the mean square deflection, needed in equation (29).

A liquid environment changes the thermal oscillation behavior by reducing ω_R and increasing Q.[158] Already a fluid with medium viscosity such as 4 M phosphate buffer will be carried along with the cantilever, leading to a frequency dependent effective mass and damping coefficient. In 2009 Pirzer and Hugel introduced a modified SHO model that, when fitted from at least 1/3 of the resonance frequency to the minimum between the first and second maximum, is able to decrease the damping error from approximately 30% to 10% (equations 30 and 31).[141] In fluids also the InvOLS measurement may be a problem. Wetted molecules on the surfaces are not hard, but show a compressible response. Therefore it is useful to perform force-distance curves at several sample spots and use the lowest InvOLS, presumably measured at the hardest sample spot.

$$S_{SHO}(\omega) = A_{\text{white}}^2 + \frac{A^2 \omega_R^4}{4Q^2(\omega - \omega_R)^2 + \omega_R^2} \tag{30}$$

$$\langle z_c^2 \rangle = \frac{A^2 \omega_R}{2Q}\left[\frac{\pi}{2} + \tan^{-1}(2Q)\right] \tag{31}$$

The thermal noise and direct Sader methods are the most frequently used calibration methods.[159] Both are non-destructive, fast and probe material independent. Another advantage is the online calibration in a SFM device and during measurements. Force spectroscopy experiments are usually performed over larger periods of time, usually several hours. Due to thermal drift of the laser spot position on the cantilever the InvOLS may change and mechanical stress of usually several thousands of bending cycles may even alter the cantilever spring constant. In the “Interlaboratory round robin on cantilever calibration for AFM force spectroscopy” mentioned above, also the thermal noise method was studied. The main source of error was the InvOLS measurement, yielding from ± 3 to ± 11% random error and ± 15% variation between instruments.[135]

Laser Doppler Vibrometry (LDV) is the most recent technique among those discussed here. It also uses the equipartition theorem, but avoids its largest source of error: the InvOLS measurement. Using the Doppler shift of laser light reflected on the cantilever, velocity and displacement of the SFM cantilever are measured directly

and applied to equation (27). This means, also contact between the tip and some surface is avoided.[142] The idea to use interferometric techniques in SFM setups is not new and was even applied in some early force microscopes.[160] Due to recent advances in digital decoding of the Doppler signal it may be embedded again into future devices. To date, the LDV calibration method is used for *ex-situ* calibration, especially by probe manufacturers that sell pre-calibrated cantilevers. Its uncertainty was estimated to be 5%[142] or near 1%, "when carefully performed".[143] It may as well be used to calibrate torsional spring constants with an uncertainty of approximately 5%.)[143]

In the SMFS experiment, molecules are probed under static conditions. As first mentioned by Butt and Jaschke in 1995,[161] spring constants determined by the equipartition theorem need to be corrected for two systematic errors:

- First a cantilever is not an ideal harmonic oscillator, but vibrates in several modes with the sum of all modes giving the total mean square deflection. Taking only the *i*-th mode into consideration, one gains the dynamic spring constant of the corresponding flexural mode $k_{dynamic,i}$ (acting in intermittent contact measurements).[143] k_{static} can be obtained from the *i*-th resonance signal using the associated flexural mode correction factor (MCF) β_i (equation 32, α denotes the tilt angle between surface and cantilever).

$$k_{static} = \frac{k_B T}{\langle z_c^2 \rangle} \cos^2(\alpha) = \beta_i \frac{k_B T}{\langle z_{c,i}^2 \rangle} \cos^2(\alpha) = \beta_i k_{dynamic,i} \qquad (32)$$

For example, the first three modes of rectangular cantilevers are corrected by $\beta_1 = 0.971$, $\beta_2 = 0.025$ and $\beta_3 = 0.003$.[161] Alternatively, if all three modes are analyzed in the power spectral density measurement, one receives 99.9% of the displacement and no correction factor is needed.[145]

- Second and even more significant, the optical lever detection measures the slope rather than the deflection height of the cantilever. The slope-height behavior at dynamic noise and static load are proportional to each other, but not identical:[91,154] The normalized deflection due to a static end-loading is given by equation (33), where $u = 0$ is at the base and $u = 1$ is at the tip. The normalized shape of a freely vibrating cantilever at its fundamental resonance frequency is given by equation (34), where $\kappa = 1.8751$.[154] As illustrated in figure 20, this slight difference has significant effect on the slope. The laser correction factor (LCF) X corrects for these effects.

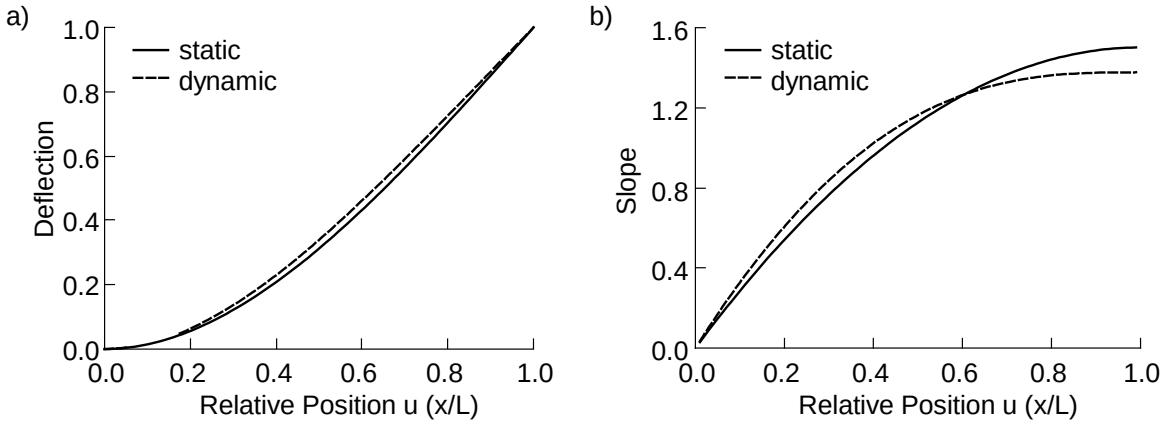

Figure 20: Normalized shapes (a) and corresponding slopes (b) of cantilevers, bent due to end loading (static) or thermal energy (dynamic) as given in equations (33) and (34).[154] A laser deflection system detects the slope rather than deflection. According to the relative position on the cantilever and laser spot size, a laser correction factor (LCF) is necessary. The commonly used "Butt and Jaschke factor" of $\beta^*_1 = 0.817$ [161] is valid for small spot sizes at the end of the cantilever ($u \approx 1.0$).

$$z_{static}(u) = \frac{3u^2 - u^3}{2} \tag{33}$$

$$z_{dynamic}(u) = 0.5000\left(\cosh\kappa u - \cos\kappa u\right) - 0.3670\left(\sinh\kappa u - \sin\kappa u\right) \tag{34}$$

$$X = \frac{InvOLS_{free}}{InvOLS_{end}} \tag{35}$$

Overall correction factors for rectangular cantilevers including the MCF and LCF above are calculated by $\beta^* = \beta_i X^{-2}$ (note the asterisk). Values for rectangular cantilever probes are: $\beta^*_1 = 0.817$, $\beta^*_2 = 0.251$ and $\beta^*_3 = 0.086$. Oscillation modes in V-shaped cantilevers are different: $\beta_1 = 0.965$, $\beta_2 = 0.037$, and $\beta_3 = 0.004$, yielding $\beta^*_1 = 0.764$, $\beta^*_2 = 0.297$ and $\beta^*_3 = 0.103$.[162] Schäffer et al. pointed out, that the standard LCF of 1.09 is only valid when focusing the laser spot at the end of the cantilever.[154,163] This is the reason, why the correction factors used in this thesis were different from the values above.

2.3.3. Summary on Cantilever Calibration

To date different static and dynamic methods have been developed to calibrate SFM cantilevers in an interlaboratory comparable way. An overview is given in figure 21. The static methods require knowledge on the Inverted optical lever sensitivity (InvOLS), gained by pressing the cantilever on a hard surface (and on a reference cantilever). In the dynamic methods, the thermal noise power spectrum is fitted to gain the average deflection $\langle z_c^2 \rangle$, resonance frequency ω_R and quality factor Q of the

first oscillation mode. Those are used in combination with an added mass *M* (Cleveland), solvent properties and cantilever dimensions (Sader) or the InvOLS from a static measurement (thermal noise). The average deflection of all oscillation modes is calculated using a mode correction factor (MCF). The InvOLS is corrected for different bending behaviors in the static and dynamic modes using a laser correction factor (LCF). Additionally, the vertical cantilever deflection is corrected by the mounting tilt angle α.

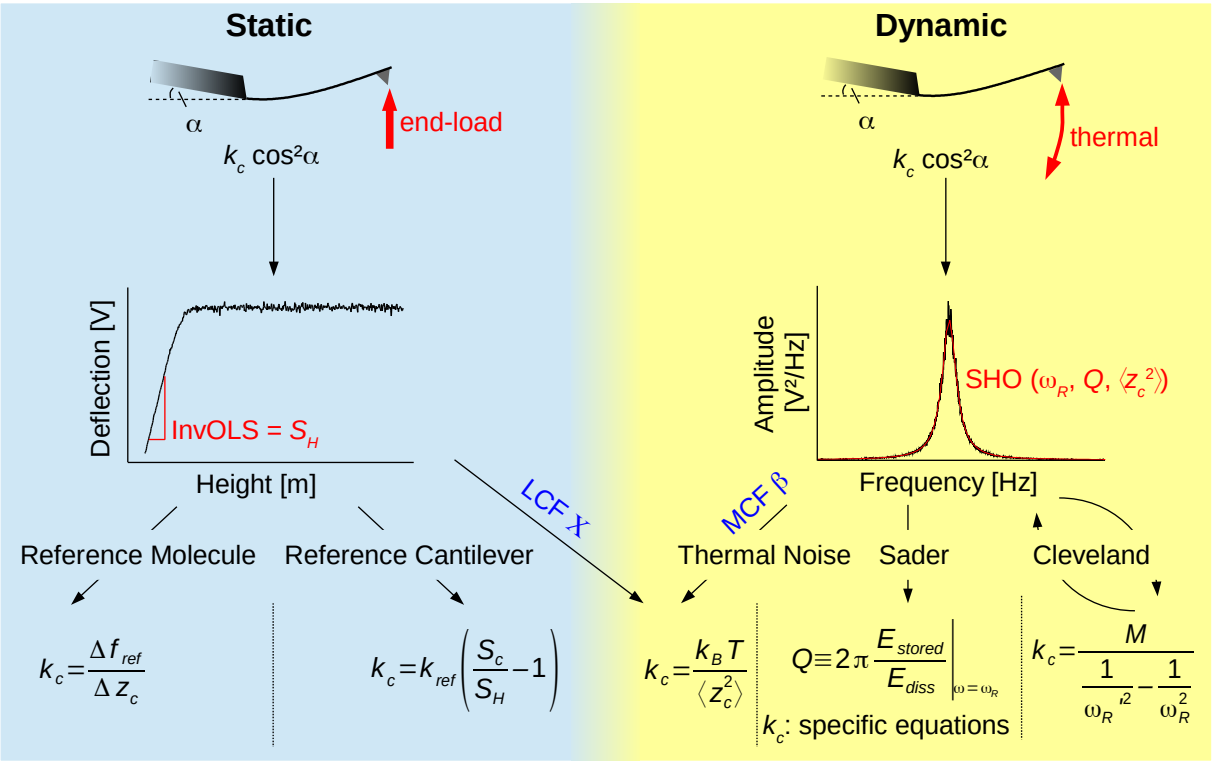

Figure 21: Overview of static (reference molecule or cantilever) and dynamic (thermal noise/LDV, Sader, Cleaveland added mass) calibration procedures.

The measurements on the pyridine coordination compounds presented in this thesis were performed on a ForceRobot 200 system.[164] This instrument was optimized for automated force spectroscopy, equipped with closed fluid cells and not compatible with any camera setup. The calibration procedure was automatized using the thermal noise method *in-situ* with MCF and LCF.

2.4. Polymeric Tethers under Force

Polymeric tethers are often utilized in SMFS experiments as tools to separate specific from unspecific interactions. In order to apply the KBE model, the loading rate at the moment of bond rupture is required. It is commonly calculated from the slope at the peak maximum in the force-*tss* representation, the pulling speed, and spring constant of the SFM cantilever. There are different established fit models, which are well suited for certain types of polymers and regimes of applied forces (entropic, intermediate, enthalpic). Also their practicability is an issue. For example, some models require the inverse data to be fitted. But in *tss*(*f*) plots, the dispersion of experimental data, the force, is displayed on the dependent coordinate of the fit function. Especially in the low-force regime with higher thermal noise this may yield inconsistent results.[165]

With the advent of SMFS, the force-extension behavior of polymeric tethers could be probed directly, with high precision, and over a broad range of forces (chapter 2.2). Soon various fit models had been developed, which were predominantly based upon the freely-jointed chain (FJC) model, proposed by Kuhn[166], or the worm-like chain model (WLC), also named Kratky Porod chain model after its inventors.[167,168] Both models are of conceptual nature and neither consider interactions between distant segments of the chain, nor they avoid occupation of the same point in space by two segments of a single chain (excluded volume effects). Nevertheless they are surprisingly good in describing the force-extension behavior of popular polymers within certain force ranges, each (table 3). The most prominent deviations occur at very large forces of several hundred piconewtons, as both models do not allow extension beyond their contour length L_c. There are various phenomenological extensions that include an additional segment elasticity K_s to fit the linear high-force regime observed in experiments. K_s corresponds to elastic stretching of bonds in the direction of force. Thus separations beyond the contour length may be fitted, such as illustrated in figure 22. Both, the extensible FJC model and the Odijk WLC representation, are force-*tss* inverted, whereas the extensible WLC model is a functional equation *f*(*f(tss)*,*tss*). Thus the Hooke-spring modified version of the WLC is an attractive alternative as it avoids complicated fitting procedures and enables a direct comparison of K_s^{III} with the spring constant from Hooke‘s law.[169]

Table 3: Popular chain models in their force-*tss* or *tss*-force representation.[165]

Model	Force-*tss* or *tss*-Force Relation	
FJC[110]	$tss(f)=L_c\left[\coth\left(\frac{f\,l_k}{k_BT}\right)-\frac{k_BT}{f\,l_k}\right]=L_c\,Lg\left(\frac{f\,l_k}{k_BT}\right)$	(36)
Extensible FJC[170]	$tss(f)=L_c\left[\coth\left(\frac{f\,l_k}{k_BT}\right)-\frac{k_BT}{f\,l_k}\right]\left(1+\frac{f}{K_s}\right)$	(37)
WLC[115,171]	$f(tss)=\frac{k_BT}{l_p}\left[\frac{1}{4}\left(1-\frac{tss}{L_c}\right)^{-2}+\frac{tss}{L_c}-\frac{1}{4}\right]$	(38)
Odijk WLC[172]	$tss(f)=L_c\left[1-\frac{1}{2}\left(\frac{k_BT}{f\,l_p}\right)^{1/2}+\frac{f}{K_s^I}\right]$	(39)
Extensible WLC[173]	$f(tss)=\frac{k_BT}{l_p}\left[\frac{1}{4}\left(1-\frac{tss}{L_c}+\frac{f(tss)}{K_s^{II}}\right)^{-2}+\frac{tss}{L_c}-\frac{f(tss)}{K_s^{II}}-\frac{1}{4}\right]$	(40)
Hooke-spring WLC[169]	$f(tss)=\frac{k_BT}{l_p}\left[\frac{1}{4}\left(1-\frac{tss}{L_c}\right)^{-2}+\frac{tss}{L_c}-\frac{1}{4}\right]+K_s^{III}\cdot tss$	(41)

f: force, *tss*: tip-sample-separation, l_k: Kuhn length, l_p: persistence length, k_B: Boltzmann constant, *T*: absolute temperature, K_s–K_s^{III}: elastic parameters, *Lg*(*x*): Langevin function of *x*, all equations are *tss* representations and do not require the cantilever spring constant k_s

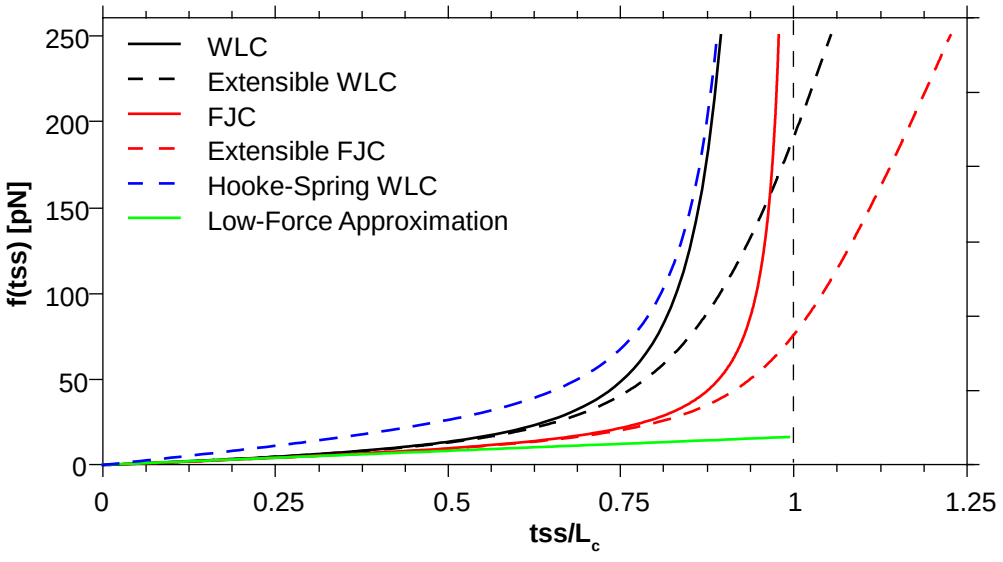

Figure 22: Exemplary force-*tss* plots of chain models from table 3 and the low-force approximation (equation 42), normalized by contour length L_c. The low-force approximation describes the restoring force solely due to a reduced number of possible overall chain configurations in the limit of low extensions $tss \ll L_c$. The FJC and WLC models additionally consider that forces are transferred along the chain. Stretching is confined due the orientation of Kuhn segments or bending of persistent chains (chapters 2.4.1 and 2.4.2). Extensible models allow stretching of segments along the pulling direction,

thus enabling $tss/L_c > 1$. In contrast, the hooke-spring WLC simply adds extensibility by a linear slope term K_s. The Odijk model differs only slightly from the extensible WLC model and is not plotted for clarity. Plot parameters for PEG, the polymer used in this thesis, are: $l_k = 2\,l_p = 0.76$ nm and $K_s^{II} = 1561$ pN or $K_s = 240$ nN/nm.[174] Segment elasticities are unphysically high for clarity.

Of all elasticity models in table 3 above, only the FJC model is an exact solution of the underlying polymer model. The WLC model is a combined approximation of two analytically solvable regions: For small forces ($f \ll k_BT/l_p$), where *tss* approaches the unstretched DNA coil size, it approaches the linear region of the low-force approximation.

$$f(tss) = \frac{3}{2}\frac{k_BT}{l_p}\frac{tss}{L_c} = 3\frac{k_BT}{l_k}\frac{tss}{L_c} \tag{42}$$

At large forces $f \gg k_BT/l_p$, the high-force WLC regime is dominating.

$$f(tss) = \frac{k_BT}{4\,l_p}\left(1 - \frac{tss}{L_c}\right)^{-2} \tag{43}$$

The interpolation formula equation (38) is asymptotically exact in the small- and large-force regions, but shows a systematic error of approximately 10% in the intermediate regime when compared to simulated worm-like chains.[171] Bouchiat et al. minimized the relative error in this regime to 0.01% by addition of a seventh order polynomial.[175]

According to the type of polymer, the system may enter the FJC high-force regime at $f \gg k_BTl_p/b^2$ instead of the WLC high-force regime (bond length b is: ~0.15 nm for C−C in synthetic polymer chains, ~0.34 nm for base pair stacking in ds-DNA, or ~7 nm such as the diameter of the globular protein in actin). Here, the orientation effect due to the external force (FJC model) exceeds the orientation effect of the chain persistence (WLC model) and one enters a discrete chain regime.[111] Equation (44) is the high-force approximation of the FJC for $b = l_k$.

$$f(tss) = \frac{k_BT}{b}\left(1 - \frac{tss}{L_c}\right)^{-1} \tag{44}$$

Summarizing both models, FJC and WLC, are suitable for different types of polymers and force regimes with errors around the corresponding transition forces:

- Rigid tethers of high persistence length such as ds-DNA (l_p ~ 45 nm)[173] exhibit a high-force transition around 1600 pN (k_BTl_p/b^2). This force is much larger, than relevant mechanical stabilities in SMFS experiments. Consequently, they

are well described by the interpolated WLC model equation (38) over the whole range of forces.

- Flexible tethers such as PEG in non-aqueous solvents have much lower persistence lengths (l_p ~ 0.35 nm)[93], yielding a transition force around 64 pN ($k_B T l_p / b^2$).The interpolated WLC model is precise for forces well below, the FJC model equation (36) for forces well above that transition.
- For chains such as polystyrene in isopropanol, where l_p (0.20 ± 0.02 nm)[176]and b (~0.15 nm) are small and similar, also the transition force is low (around 37 pN). Here, the interpolated WLC model is dominated by its low-force regime equation (42). However, the low-force WLC and FJC regimes are similar. Thus the FJC model may be applied to the whole range of forces; well below and well above the transition force with some errors near the transition force.
- PEG in water has a distinct behavior due to hydrogen bound water, which bridges neighboring ether groups from the chain. Here, a 2-state FJC model is more appropriate, which considers a bridged (gauche) and non-bridged (trans) conformation. This will be discussed in chapter 2.4.3 below.

Besides the theoretical considerations above, both models may also fit other regimes not precisely, but still reasonably well in relation to the experimental noise. Therefore the direct $f(tss)$ models, WLC and Hooke-spring WLC, are popular also outside the regimes listed above; especially, when only the loading rate is of interest and not the actual properties of the tether.

In the following, the force-induced extensions of freely-jointed and worm-like chains will be derived, yielding equations (36) and (38) from table 3 and the low-force approximation equation (42).

2.4.1. Freely-Jointed Chain Model

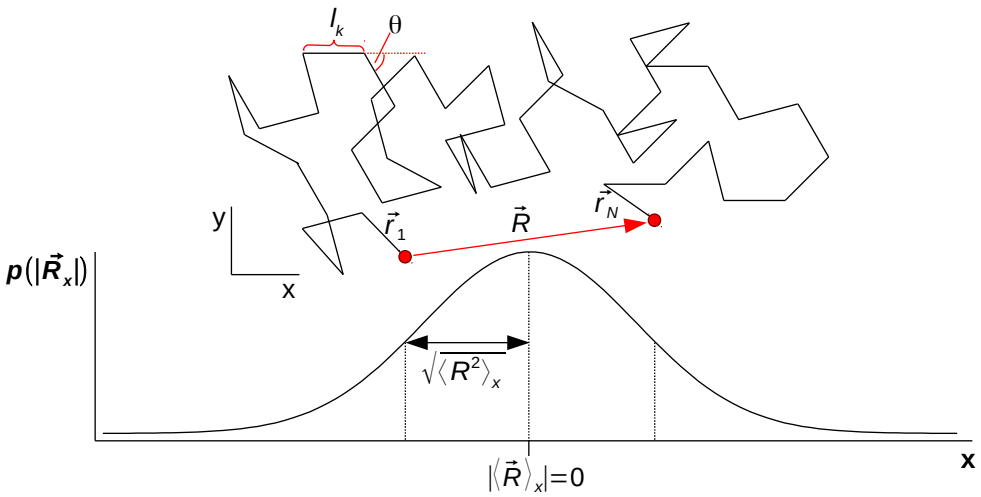

Figure 23: Schematic drawing of a FJC in the x-y-plane. It consists out of N independent chain segments $\vec{r}_i$ with Kuhn length l_k. The chain is not self-avoiding and allowed to cross itself (no excluded volume effects). The end-to-end vector projection to any arbitrary Cartesian coordinate (here *x*) follows a Gaussian probability distribution, centered at zero. Its variance is a measure of entropic restoring force for small extension.[177]

In the FJC model, a polymer is treated as a chain of *N* independent segments $\vec{r}_i$ of Kuhn length l_k (figure 23), consequently $L_c = N\,l_k$. The angle between any two segments θ_{ij} is arbitrary, thus the mean end-to-end vector of a long chain approaches the zero vector.

$$\langle\vec{R}\rangle = \sum_i \langle\vec{r}_i\rangle = \vec{0} \tag{45}$$

There is no preferred orientation in space, thus the behavior is identical in all Cartesian coordinates *x*, *y*, and *z*. For the sake of simplicity, we will focus on one direction and expand our results to three dimensions later.

$$\langle\vec{R}\rangle_x = \sum_i \langle\vec{r}_i\rangle_x = \vec{0} \tag{46}$$

The variance is the second momentum of the distribution, here in *x*-direction.

$$\sigma_x^2 = \langle\vec{R}^2\rangle_x - \langle\vec{R}\rangle_x^2 = \langle\vec{R}^2\rangle_x \tag{47}$$

For a high number of segments *N*, the mixed scalar products of all vectors $\vec{r}_{i<j}$ cancel each other out, leaving only $\vec{r}_i^{\,2}$.

$$\langle\vec{R}^2\rangle_x = \left\langle\left(\sum_i \vec{r}_i\right)^2\right\rangle_x = \sum_i \langle\vec{r}_i^{\,2}\rangle_x + 2\sum_{i<j}\langle\vec{r}_i\vec{r}_j\rangle_x = \sum_i \langle\vec{r}_i^{\,2}\rangle_x = \sum_i \left(l_k^2\right)_x \tag{48}$$

Due to the random orientation, the variance in *x*-direction is 1/3 of the variance in 3D

$$l_k^2=\left(l_k^2\right)_x+\left(l_k^2\right)_y+\left(l_k^2\right)_z=3\left(l_k^2\right)_x \text{ and} \tag{49}$$

$$\sigma_x^2=N\left(l_k^2\right)_x=\frac{N l_k^2}{3}. \tag{50}$$

Thus if one end of the FJC is fixed, the other one fluctuates in space around its origin with a standard deviation proportional to $N^{1/2}$ and l_k. In 3D this reads

$$\sqrt{\langle\vec{R}^2\rangle}=l_k\sqrt{N}. \tag{51}$$

Thus the Kuhn length is a measure of chain stiffness. The same relation holds true for the radius of gyration R_g, which will not be derived here.

$$R_g=\frac{l_k\sqrt{N}}{\sqrt{(6)}} \tag{52}$$

In the SMFS experiment, a chain is pulled in one direction of space. Due to the isotropic behavior of a FJC, we are free to assume a pulling in *x* direction. What is the entropic restoring force of the chain? According to the central limit theorem, the probability distribution of the end-to-end vector in *x* for a high number of segments *N* equals a Gaussian distribution.

$$p(\vec{R})_x=\frac{1}{\sigma_x\sqrt{2\pi}}\exp\left[-\frac{\vec{R}_x^2}{2\sigma_x^2}\right]=\frac{\sqrt{3}}{l_k\sqrt{2\pi N}}\exp\left[-\frac{3\vec{R}_x^2}{2N l_k^2}\right] \tag{53}$$

All micro-states are equally likely, thus the probability distribution is directly proportional to the partition function. The entropy associated with each end-to-end distance $\vec{R}_x$ in *x*-direction is:

$$S(\vec{R})_x=k_B\ln p(\vec{R})_x+C=\frac{3k_B\vec{R}_x^2}{2N l_k^2}+\widetilde{C} \tag{54}$$

Thus an increase of the end-to-end distance in an SMFS experiment decreases the entropy $S(\vec{R})_x$ and increases the free energy $F(\vec{R})_x$ of a FJC.

$$F(\vec{R})_x=U(\vec{R})_x-\frac{3}{2}k_B T\frac{\vec{R}_x^2}{N l_k^2}+\hat{C} \tag{55}$$

A freely-jointed polymer chain does not change its internal energy *U* upon stretching, thus $dU(\vec{R})/d\vec{R}_x=0$. The stretching process is purely entropic. We assume that the

(small) force applied by the experiment in *x*-direction $\vec{f}_{SMFS,x}$ equals the restoring force $\vec{f}_x$.

$$\vec{f}(\vec{R})_{SMFS} = -\vec{f}(\vec{R})_x = -\frac{dF(\vec{R})_x}{d\vec{R}_x} = 3k_B T \frac{\vec{R}_x}{N l_k^2} = 3k_B T \frac{\vec{R}_x}{L_C l_k} \tag{56}$$

We get equation (42) for low extensions of a Gaussian chain, where $\vec{R}_x = tss$.

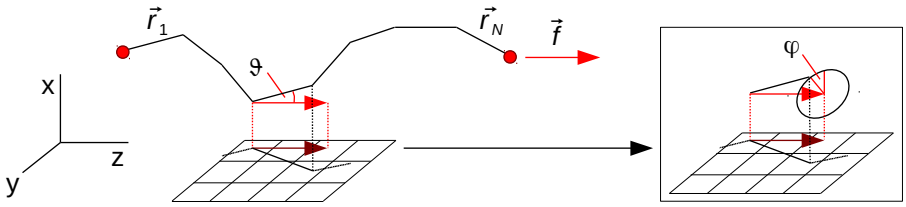

Figure 24: A force vector $\vec{f}$ applied to the ends of a freely-jointed chain (here in *z*-direction) is transferred through all segments of a chain. The energy ε_i of each chain vector $\vec{r}_i$ is influenced by $\vec{f}$ as a function of polar angle ϑ and azimuth angle φ.[177]

For larger forces and extensions, the mean end-to-end vector $\vec{R}$ is increased and does not satisfy equation (45) anymore. Instead the mean end-to-end vector is increased as the force $\vec{f}$ performs work upon increasing $d\vec{R}$. The force is transferred through the whole chain to each segment $d\vec{r}_i$.

$$\delta w = \vec{f}\, d\vec{R} = \sum_i^N \vec{f}\, d\vec{r}_i \tag{57}$$

Consequently in an extended FJC, the energy stored by every *i*-th segment of Kuhn length l_k may be written as

$$\varepsilon_i = -\vec{f}\,\vec{r}_i = -f\, l_k \cos\vartheta_i\,, \tag{58}$$

where ϑ_i is the polar angle between segment $\vec{r}_i$ and force $\vec{f}$ such as sketched in figure 24. The overall energy stored in a chain depends on the orientation of all *i* segments.

$$E = \sum_i \varepsilon_i = -f\, l_k \sum_i^N \cos\vartheta_i \tag{59}$$

To calculate thermodynamic properties, we are now interested in the partition function. Still all segments are uncorrelated and may be treated separately. The partition function of a single chain segment is

$$z_{segment,i} = \iint\limits_{sphere} \exp\left(-\frac{f\,l_k \cos\vartheta_i}{k_B T}\right) \sin\vartheta_i \, d\vartheta_i \, d\phi_i \,. \tag{60}$$

The segments are not correlated, thus the partition function of a chain is:

$$Z_{chain} = \prod_{i=1}^{N} z_{segment,i} = z_{segment,i}^{N} = \left[\iint\limits_{sphere} \exp\left(-\frac{f\,l_k \cos\vartheta}{k_B T}\right) \sin\vartheta \, d\vartheta \, d\phi\right]^N . \tag{61}$$

φ and ϑ are separated. First we yield

$$Z_{chain} = \left[2\pi \int \exp\left(\frac{f\,l_k \cos\vartheta}{k_B T}\right) d\cos\vartheta\right]^N \tag{62}$$

and finally

$$Z_{chain} = \left[\frac{4\pi k_B T}{f\,l_k} \sinh\left(\frac{f\,l_k}{k_B T}\right)\right]^N , \tag{63}$$

where sinh(x) is the hyperbolic sinus function

$$\sinh(x) = \frac{e^x - e^{-x}}{2} \,. \tag{64}$$

We use partition function equation (63) to get the free energy $F(f)$ as function of the applied force.

$$F(f) = U(f) - T\,S(f) = U(f) - N k_B T \ln\left[\frac{4\pi k_B T}{f\,l_k} \sinh\left(\frac{f\,l_k}{k_B T}\right)\right] \tag{65}$$

According to

$$R = -\frac{\partial F}{\partial f} \,, \tag{66}$$

we receive the corresponding end-to-end distance R (still the internal energy U is constant over this purely entropic stretching process, thus $\partial U / \partial f = 0$).

$$
\begin{aligned}
R(f) &= N k_B T \left[\frac{\frac{-4\pi k_B T}{f^2 l_k} \sinh\left(\frac{f l_k}{k_B T}\right) + \frac{4\pi}{f} \cosh\left(\frac{f l_k}{k_B T}\right)}{\frac{4\pi k_B T}{f l_k} \sinh\left(\frac{f l_k}{k_B T}\right)} \right] \\
R(f) &= N k_B T \left[\frac{-1}{f} + \frac{l_k}{k_B T} \coth\left(\frac{f l_k}{k_B T}\right) \right] \\
R(f) &= N l_k \left[\coth\left(\frac{f l_k}{k_B T}\right) - \frac{k_B T}{f l_k} \right]
\end{aligned}
\tag{67}
$$

Finally we have derived the force−*tss* relation of the FJC model (equation 36) with $N\,l_k = L_C$ and $R = tss$.

2.4.2. Worm-Like Chain Model

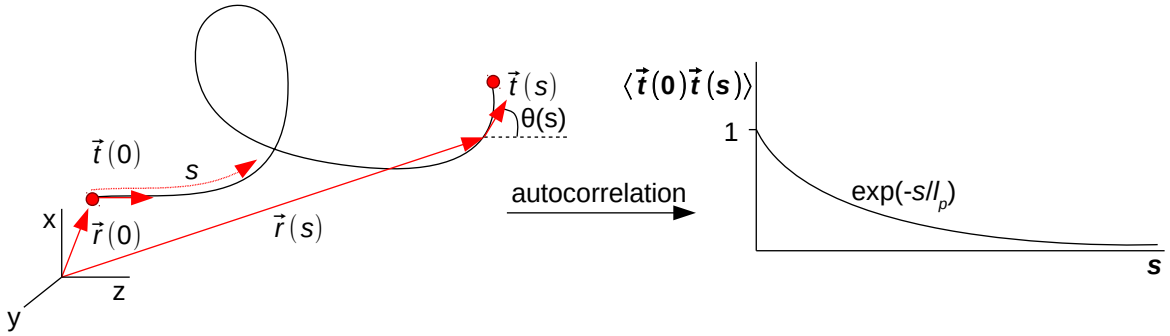

Figure 25: A worm-like chain is characterized as continuous chain with persistence against bending. For a mathematical description, the WLC is usually parameterized by *s* along its contour. The autocorrelation of tangent vectors $\vec{t}(0)$ and $\vec{t}(s)$ in 3D, or the average projection of each vector $\vec{t}(s)$ onto the initial chain orientation $\vec{t}(0)$, decays exponentially by the inverse persistence length l_p.

In contrast to the FJC model with discrete chain segments, the WLC model describes a tether as continuous chain. Here, the characteristic property is not the Kuhn length, but a certain persistence against bending. The autocorrelation between a pair of tangent vectors at internal chain coordinates *s* and *s*‘ decays exponentially. Its decay rate l_p is defined as persistence length.[177]

$$
\langle \vec{t}(s)\vec{t}(s') \rangle = \langle \cos\theta(s-s') \rangle = \exp\left(-\frac{|s-s'|}{l_p}\right) \tag{68}
$$

For $\Delta s \ll l_p$ the chain does not exhibit any flexibility, while two tangent vectors with separation $\Delta s \gg l_p$ fluctuate almost independent from each other. In other words, the persistence length roughly indicates after which distance the initial orientation of a

chain is lost. The mean end-to-end distance $\vec{R}$ of a chain with contour length L_c may be described using position vectors $\vec{r}(s)$ along the chain.

$$\vec{R}=\int_0^{L_c} d\vec{r}(s)=\vec{r}(L_c)-\vec{r}(0) \tag{69}$$

Equation (69) may be rewritten in terms of the tangent vectors $\vec{t}(s)$.

$$\vec{R}=\int_0^{L_c}\left(\frac{\partial\vec{r}(s)}{\partial s}\right)ds=\int_0^{L_c}\vec{t}(s)ds \tag{70}$$

Using equation (68), we are able to calculate the mean square end-to-end distance $\langle\vec{R}^2\rangle$.

$$\begin{aligned}
\langle\vec{R}^2\rangle &= \int_0^{L_c}\int\langle\vec{t}(s)t(s')\rangle ds'ds=\int_0^{L_c}\int\exp\left(-\frac{|s-s'|}{l_p}\right)ds'ds \\
\langle\vec{R}^2\rangle &= 2\int_0^{L_c}\int_0^{s}\exp\left(-\frac{s-s'}{l_p}\right)ds'ds=2\int_0^{L_c}\left[l_p-l_p\exp\left(\frac{-s}{l_p}\right)\right]ds \\
\langle\vec{R}^2\rangle &= 2l_p^2\left[\frac{L_c}{l_p}-1+\exp\left(\frac{-L_c}{l_p}\right)\right]
\end{aligned} \tag{71}$$

For $L_c \gg l_p$ this relationship simplifies to

$$\langle\vec{R}^2\rangle=2l_pL_c\,. \tag{72}$$

Upon comparison with equation (50, $\langle\vec{R}^2\rangle=l_kL_c$) we find the important relationship: $l_k = 2\,l_p$, valid for long polymers. The Kuhn length is larger, because the free orientation of FJC segments also allows inverted directions of consecutive segments.

The thermal distortion of a WLC is attributed to its bending energy E_{bend}, a measure of quadratic local curvature $\partial t(s)/\partial s$ and bending modulus κ. In other words, at a given thermal energy a high bending modulus yields a low chain deformation and vice versa.

$$E_{bend}=\frac{\kappa}{2}\int_0^{L_c}\left(\frac{\partial t(s)}{\partial s}\right)^2 ds \tag{73}$$

Bending modulus and persistence length are directly proportional to each other by $l_p = \kappa/k_BT$. In the limit $T \rightarrow 0$ K, a WLC approaches a rigid rod and gets floppy for higher temperatures. The density of states in the absence of external forces is:

$$z_{chain} = \exp\left[-\frac{E_{bend}}{k_B T}\right] = \exp\left[-\frac{l_p}{2}\int_0^{L_c}\left(\frac{\partial t(s)}{\partial s}\right)^2 ds\right] \quad (74)$$

Under the influences of external forces, the density of states in a single chain extends from equation (74) to

$$z_{chain} = \exp\left[-\frac{E_{bend}+E_{force}}{k_B T}\right] = \exp\int_0^{L_c}\left[-\frac{l_p}{2}\left(\frac{\partial \vec{t}(s)}{\partial s}\right)^2 - \frac{\vec{f}\,\vec{t}(s)}{k_B T}\right] ds\,. \quad (75)$$

The partition function is calculated by path integration along vector $\vec{t}(s)$.

$$Z = \int D\vec{t}(s) z_{chain} \quad (76)$$

There is no analytical solution of equation (76). Thus Marko et al.[171] suggested the approximate equation (38) that approximates the numerically calculated force-extension behavior.

2.4.3. Stretching of PEG

Throughout this thesis, we utilized PEG as spacer molecules. In aqueous solvents, this polymer shows a linear regime between 50 and 300 pN in its stretching behavior. In aprotic solvents such as hexadecane, chloroform or toluene, this regime is absent (figure 26).[93] MD simulations in the low-force regime suggest, that the conformation is predominantly gauche, stabilized by bridging water molecules. As larger forces are applied in the intermediate regime, those are successively broken into single-bonded water. In the high-force regime, the trans conformation is dominating.[178] To describe the overall force-extension behavior with a single master equation, Oesterhelt et al. suggested a phenomenological extension of the extensible FJC model. In their 2-state model, the contour length is a function of the applied force and allowed to equilibrate between the two states with different monomer lengths: L_{gauche} and L_{trans}, separated by an energy of ΔG:

$$L_C = N_{gauche} L_{gauche} + N_{tans} L_{trans} \quad (77)$$

with

$$\frac{N_{gauche}}{N_{trans}} = \exp\left[\frac{\Delta G}{k_B T}\right]. \quad (78)$$

Including the theory of force activated bond rupture (see also chapter 2.5)

$$\Delta G(f) = (G_{gauche} - G_{trans}) - f(L_{gauche} - L_{trans}) \quad (79)$$

and the extensible FJC model equation (37), the extensible 2-state FJC model was derived:

$$tss(f) = N_S \left(\frac{L_{gauche}}{e^{\Delta G / k_B T} + 1} + \frac{L_{trans}}{e^{-\Delta G / k_B T} + 1} \right) \left(\coth\left(\frac{f\, l_k}{k_B T} \right) - \frac{k_B T}{f\, l_k} \right) + N_s \frac{f}{K_s} . \qquad (80)$$

The authors applied equation (80) to SMFS data of PEG stretching in PBS buffered aqueous solution. With additional data from FJC fits on the force-extension experiments in hexadecane, L_{trans} = 0.36 nm, l_k = 0.7 nm, and K_S = 150 nN/nm, they received ΔG = 3.0 ± 0.3 k_BT and L_{gauche} = 0.28 ± 0.01 nm.

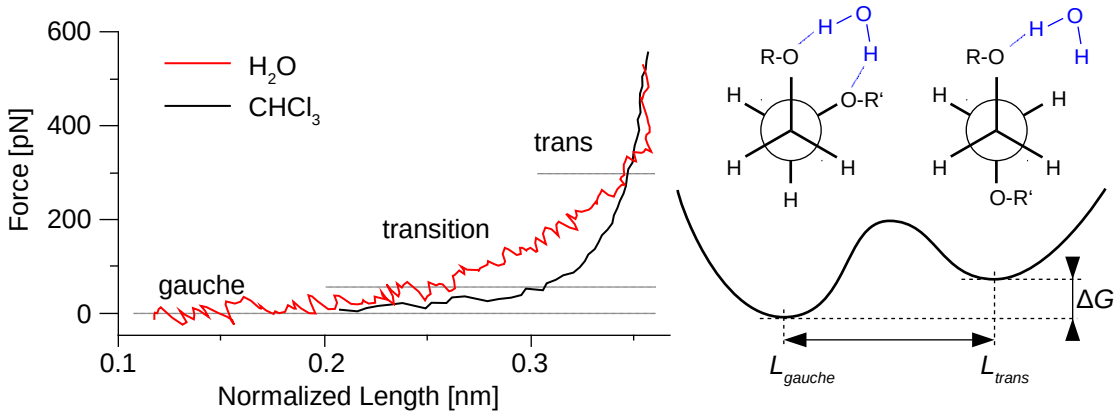

Figure 26: The force-extension behavior of PEG up to a very large rupture force around 500 pN is characterized by three distinct regions due to the PEG chain conformation: predominantly gauche (f < 50 pN), a transition regime, and predominantly trans (f > 300 pN). The gauche conformation is energetically favored by ΔG ~ 3 k_BT due to bridging water molecules as shown by Newman projections on the right. The trans conformation gets favored at higher forces due to its larger monomer length (L_{gauche} = 0.28 nm, L_{trans} = 0.36 nm). In aprotic solvents such as chloroform, the transition state is missing and the force-extension behavior approaches the FJC model.[93,178]

Kienberger et al. used the extensible WLC model to fit their experimental SMFS data of PEG in PBS buffer and calculated a reasonable persistence length of l_p = 0.38 nm[174], which was expected to be half the FJC Kuhn length of l_k = 0.7 nm[93]. In contrast, the stretch modulus of K_S^{II} = 1.6 nN was unreasonable low and yielded a relative contour length of tss/L_C = 1.3 at 250 pN (see also figure 22, where those values are used). Such a large contour length increase cannot be explained by elastic bond stretching. Considering the conformational transition of PEG discussed above, this modulus was actually result of a fit to the intermediate regime (Kienberger et al. measured up to a force of only 130 pN). A corresponding fit to the high-force regime above 300 pN yields a stretch modulus of 25 nN (fitted to a plot of equation 80). Still in the low- and intermediate force regimes, the extensible WLC

model is a suitable tool to determine the loading rate of a rupture process without the need of data inversion to *tss*(*f*). Also in this thesis, relevant rupture forces were far below 300 pN. Thus we also used the WLC model as reliable model to calculate the loading rate of force-extension cycles.

2.5. Kramers-Bell-Evans Model

Using calibrated probes, SMFS experiments are a direct measure of rupture forces and tip-sample-separation. Is there any additional information to extract by application of proper models? Much theoretical work has been carried out on bond rupture under external forces. One of the most practicable method has evolved to the “standard model”[64,179] and is named in various combinations after Evan Evans, Ken Ritchie, Hendrik A. Kramers, George I. Bell, and Serafim N. Zhurkov. Throughout this thesis, the term Kramers-Bell-Evans (KBE)[180] will be used. In order to apply the KBE model, force-distance measurements have to be performed at various pulling speeds. This methodology is called dynamic force spectroscopy (DFS).

Most models for SMFS refer back to the initial publication by Kramers in 1940, where he described thermally activated barrier crossing of particles due to Brownian motion dynamics.[181] He characterized the pre-exponential factor of the Arrhenius-Equation by the fluctuation-dissipation. In the extended Arrhenius-equation (81), ω_0 is the squared angular frequency inside the metastable minimum, E_a the activation energy, ω_b denotes the squared angular frequency at the transition state, and γ is a measure for molecular damping (figure 27).[22] Kramers overall prefactor yields a frequency scale for molecular bond escape, also denoted “attempt rate”, which is typically on the order of $1/t_D \approx 10^{12}$ s^{-1}.[128]

$$k_{off} = \frac{\omega_0 \omega_b}{2\pi\gamma} \exp\left(\frac{-E_a}{k_B T}\right) = \left(\frac{1}{t_D}\right) \exp\left(\frac{-E_a}{k_B T}\right) \tag{81}$$

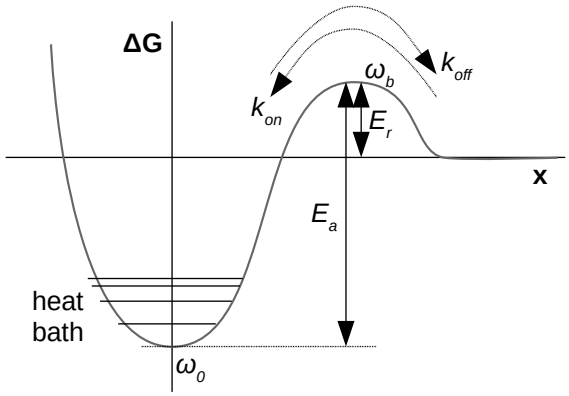

Figure 27: Schematic of thermally activated barrier crossing for a dissociation reaction (AB) → (A + B) according to Kramers[181] as summarized by Hänggi[22]. The thermal off-rate constant k_{off} is a function of activation energy barrier E_a, heat bath temperature T, and shape of the potential energy diagram (ω_0 and ω_b). If the thermal recombination rate constant k_{on} is influenced by solvent recombination, also the

association reaction has a transition state with E_r above the energetic level of full dissociation (large separation x).

The description of force activated bond rupture dates back to 1953, when Zhurkov described time dependent fracture processes of a broad range of materials at constant forces.[19] The observed behaviors differed from the rupture at critical forces, usually observed for macroscopic objects, and was attributed to growth of cavities and cracks in the material. He observed an exponential dependence between the applied stress σ and average material lifetime τ and suggested equation (82). He already measured the pre-exponential factor τ_0 to be close to 10^{-12} s, yet with an unknown structure-sensitive coefficient γ (not to be confused with the damping factor above).[20]

$$\tau = \tau_0 \exp\left(\frac{U_0 - \gamma\sigma}{k_B T}\right) \tag{82}$$

In his important work from 1978, Bell applied the theory of Zhurkov to cell dissociation.[21] The critical force, sufficient to detach two cells from each other, was assumed to be equally distributed among all bonds yielding f_c. He proposed, that the structure-sensitive coefficient γ of Zhurkov is a measure of the distance between bound state and transition state Δx (rupture length, figure 28), yielding equation (83). Here, $k_{off}(f_c)$ is the dissociation rate constant at critical force f_c, and $k_{off}(0)$ the thermal dissociation rate constant at an average external force of 0 pN. He estimated critical forces of single-molecular antigen-antibody dissociation (120 pN) and covalent interactions (3 nN), which were close to the values measured decades later.

$$k_{off}(f_c) = k_{off}(0)\exp\left(\frac{f_c \Delta x}{k_B T}\right) = \left(\frac{1}{t_D}\right)\exp\left(\frac{-E_a + f_c \Delta x}{k_B T}\right) \tag{83}$$

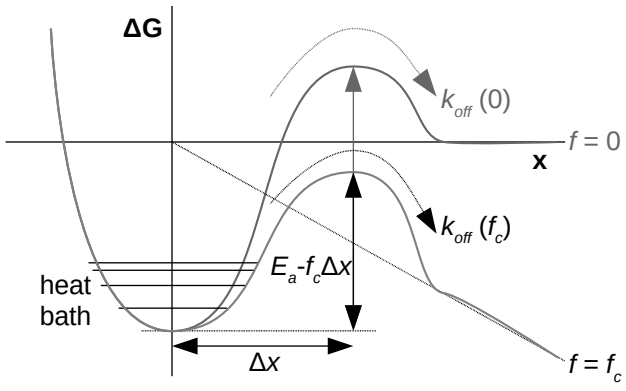

Figure 28: Schematic of thermally activated barrier crossing for a dissociation reaction (AB) → (A + B) at a critical force f_c according to Bell[21], Evans[182], and Ritchie[23]. An external force f in x-direction tilts the

potential energy diagram by $f\,\Delta x$. This effect is linearly proportional to the distance from the bound state. Here, the rupture length Δx does not change with force (limit for sharp transition states or small forces).

The development of new experimental methods for single-molecule experiments motivated Evans to combine the models by Kramers and Bell and apply them to detachment experiments of red blood cells.[182] Later Evans and Ritchie established an even broader theory of thermally activated barrier crossing under the influence of external forces and discussed various influences such as shape of the potential energy surface (PES) and regimes of various pulling speeds.[23,81,126,128,183] Making several assumptions that will be discussed in the following chapter 2.5.1, they received an analytical solution of force activated barrier crossing (equation 84) that predicted a logarithmic behavior of the most probable rupture force f^* as a function of the corresponding loading rate lr, which is the rate of force increase with time. A fit of equation (84) to experimental data yields the thermal dissociation rate constant extrapolated to zero forces $k_{off}(0)$ and the rupture length Δx.

$$f^*(lr) = \frac{k_B T}{\Delta x} \ln\left(\frac{\Delta x}{k_B T}\frac{lr}{k_{off}(0)}\right) \tag{84}$$

2.5.1. Derivation of the KBE Model

In a SMFS experiments, usually polymeric linkers are utilized to separate specific from non-specific interactions. As discussed in chapter 2.2.1, tether mediated rupture occurs under non-equilibrium conditions and back reactions (rebinding) can be neglected. The entropic elasticity of the flexible linker pulls the molecule apart and bonds will never be re-formed.[64] Thus the KBE theory starts with a simple first order dissociation reaction, characterized by a thermal off-rate constant at zero force $k_{off}(0)$: A-B → A + B. The corresponding thermal dissociation rate r_d is the concentration derivative over time t:

$$r_d = \frac{d\,[\text{A-B}]}{dt} = -k_{off}(0)[\text{A-B}] \tag{85}$$

$$\frac{d\,[\text{A-B}]}{[\text{A-B}]} = -k_{off}(0)\,dt \tag{86}$$

Here squared brackets denote for the corresponding concentrations. Consequently the concentration of intact interactions [A-B] after a given period of time T is:

$$[\text{A-B}] = \exp\left(-\int_0^T k_{off}(0)\,dt\right) \tag{87}$$

There is an enormous gap in time scale between thermal rates in solution (10^{12} s^{-1} or shorter) and the force ramp on a laboratory time scale (10^{4} s^{-1} or longer).[81] Additionally it is assumed that the escape process takes no time.[184] Then statistical oscillations may be averaged by using the rate theory of Kramers[181] (equation 81).

$$[\text{A-B}] = \exp\left(-\int_0^T t_D^{-1} \exp\left[-\frac{E_a}{k_B T}\right] dt\right) \tag{88}$$

Here, t_D is the diffusive relaxation constant and E_a the activation energy barrier. Now, a time dependent external force $f(t)$ is introduced using Bells formalism (equation 83), where Δx is the rupture length.

$$[\text{A-B}] = \exp\left(-\int_0^T t_D^{-1} \exp\left[-\frac{E_a - f(t)\Delta x}{k_B T}\right] dt\right) \tag{89}$$

If the force is a reversible continuous function of time, the time-domain may be transferred into a force domain. The force derivative with respect to time is called “loading rate” $df/dt = lr$. Then the concentration of A-B while ramping from zero force up to a certain force F is:

$$[\text{A-B}] = \exp\left(-\int_0^F t_D^{-1} \exp\left[-\frac{E_a - f\,\Delta x}{k_B T}\right] \frac{df}{lr}\right) \tag{90}$$

This equation may be rewritten with respect to the concentration of broken compounds [A] = [B] and the initial concentration $[\text{A-B}]_0$.

$$[\text{A}] = [\text{A-B}]_0 - [\text{A-B}] = [\text{A-B}]_0 - \exp\left(-\int_0^F t_D^{-1} \exp\left[-\frac{E_a - f\,\Delta x}{k_B T}\right] \frac{df}{lr}\right) \tag{91}$$

Up to this step, the KBE theory is still of broad validity. At this step changes in diffusive relaxation time t_D and the initial activation energy barrier E_a due to the applied force are neglected.[23] We receive equation (92), including the phenomenological and measurable pre-exponential factor $k_{off}(0)$ as defined in equation (81).

$$[\text{A}] = [\text{A-B}]_0 - \exp\left(-k_{off}(0)\int_0^F \exp\left[\frac{f\,\Delta x}{k_B T}\right] \frac{df}{lr}\right) \tag{92}$$

Assuming statistically independent rupture events, the concentrations in equation (91) also reflect the number of detected events in a SMFS experiment, where $[A\text{-}B]_0$ is the maximum number of single-molecule rupture events N, and [A] the number of detected rupture events N_r when pulling up to force F.

$$N_r = N - \exp\left(-k_{off}(0)\int_0^F \exp\left[-\frac{f\,\Delta x}{k_B T}\right]\frac{df}{lr}\right) \tag{93}$$

(In the literature, equation (93) is also written in a normalized form, divided by N. Then $N_r/N = S(f)$ is called "survival probability".)[185] The probability to detect bond ruptures during the ramp up to a certain force $p(F)$ (rupture force probability distribution, RFPD) is the derivation of equation (93) with respect to F.

$$p(F, lr) = \frac{d\,N_r(F)}{d\,F} = k_{off}(0)\exp\left(\frac{F\,\Delta x}{k_B T}\right)\frac{1}{lr}\exp\left(-k_{off}(0)\int_0^F \exp\left[\frac{f\,\Delta x}{k_B T}\right]\frac{df}{lr}\right) \tag{94}$$

In other words, equation (93) corresponds to the cumulative frequency distribution, equation (94) to the rupture force histogram of a SMFS experiment. As sketched in figure 29, $p(F, lr)$ is characterized by a bimodal shape. First, the probability of bond rupture increases due to an increased off-rate at higher forces. Then, its value decreases as only a low population in the initial state has remained up to this point of force (respectively time).

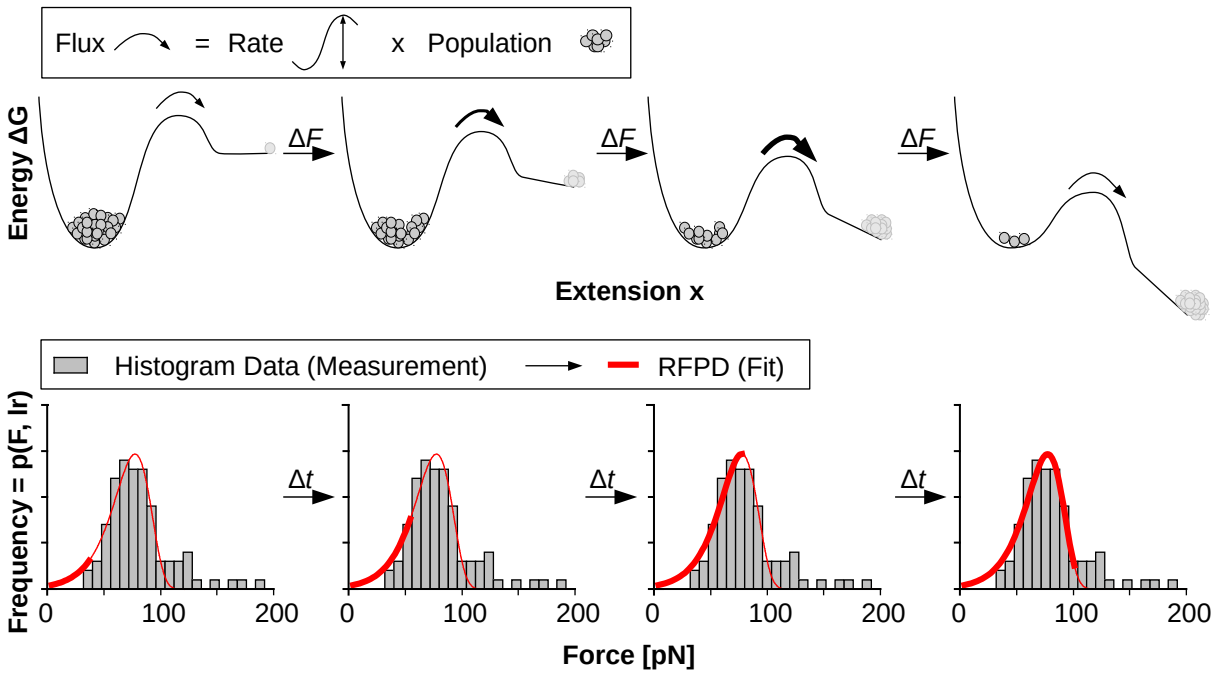

Figure 29: The average characteristics of a population (top) equals the behavior of a repeated single-molecule experiment (bottom). Thus the flux across the potential energy barrier (top) is equal to the

probability of bond rupture (bottom). In the experiment, the force is increased monotonically with time (from left to right). In the beginning, low forces yield a low probability of rupture. As the force increases over time, flux and $p(F, lr)$ increase. At high forces, flux and $p(F, lr)$ drop due to the process history. The rupture force probability distribution (RFPD) is equivalent to the histogram of rupture forces (gray bars). Sketch after Garai et al.[186], data from bi-pyridine **2c** in pure H_2O at 5000 nm/s with a fit (red line) according to equation (96) (Δx = 0.25 ± 0.01 nm, $k_{off}(0)$ = 14.4 ± 3.1 s^{-1}).

To solve the integral expression in equation (94) analytically, now two significant assumptions are made:

a. The rupture length Δx is independent of the applied force (sharp transition state or low force approximation).

b. The loading-rate lr is constant (linear force-ramp).

Then equations (93) and (94) yield:

$$N_r = N - \exp\left(\frac{k_{off}(0)\,k_B T}{lr\,\Delta x}\left[1 - \exp\left(\frac{F\,\Delta x}{k_B T}\right)\right]\right) \tag{95}$$

$$p(F, lr) = \frac{k_{off}(0)}{lr}\exp\left(\frac{F\,\Delta x}{k_B T}\right)\exp\left(\frac{k_{off}(0)\,k_B T}{lr\,\Delta x}\left[1 - \exp\left(\frac{F\,\Delta x}{k_B T}\right)\right]\right) \tag{96}$$

Husson and Pincet analyzed the error due to assumption (a) by comparison of the standard model with a full microscopy theory using Kramers rate equation.[187] The resulting RFPD showed only slight deviations. For example, when applied to the rupture process of P-Selectin and corresponding ligands on neutrophils[188], the relative error in Δx was less than 7%.[187] Friedsam et al. analyzed the effect of assumption (b) by fitting force histograms, calculated using MD simulations. They estimated a relative error of 3% in Δx and of 25% in $k_{off}(0)$.[189]

As illustrated in figure 29, equation (96) may be used to fit rupture force histogram data directly (direct fit method). However in a SMFS experiment, rupture force distributions may be broadened due to noise fluctuations of the cantilever.[190] Also simultaneous bond rupture,[191,192] more complex potential energy profiles,[186] or overlap with competitive interactions of similar probability[67] influence the measured rupture force histograms. Consequently fit parameters Δx and $k_{off}(0)$ are highly dependent on various effects and careful interpretation is needed.[187] This is the reason why another variant of the KBE model is more popular, which uses only one value per RFPD: the most probable rupture force (f^*). Solving:

$$\frac{d\,p(F)}{d\,F} \equiv 0 \tag{97}$$

we receive

$$f^*(lr) = \frac{k_B T}{\Delta x} \ln\left(\frac{\Delta x}{k_B T} \frac{lr}{k_{off}(0)} \right) = \frac{k_B T}{\Delta x} \ln(c\,lr) + \frac{k_B T}{\Delta x} \ln\left(\frac{\Delta x}{c\,k_B T\,k_{off}(0)} \right). \tag{98}$$

(Note that the notation to the right requires dimensionless values in both logarithmic terms and thus include an implicit transformation constant of c = 1 s/pN. For the sake of clarity, we will use the notation *ln*(*lr* [pN/s]) throughout this thesis.)

A typical application of equation (98) to experimental data illustrated in figure 30. Rupture force histograms are measured over a broad range of loading rates (*lr*) and analyzed as described in the caption. The loading rate parameter may be changed by pulling at various velocities (usually spanning the experimentally accessible range). Optional to a linear regression, equation (98) may also be utilized directly for damped least-squares optimization. Then one has to take care of convergence at local minima instead of the global optimum. Usually there is a maximum number of force-distance curves per experiment until experimental issues, such as wear of tip modification, require exchange the SFM cantilever. Within one experiment one has to consider a balance between more force-distance measurements per pulling velocity, or less individual force-distance curves at a higher amount of pulling velocities. This issue was discussed by Björnham et al., who suggested to aim at not less than 100 specific rupture force signals per velocity histogram.[190] In this thesis, we applied up to seven velocities per experiment (100, 300, 500, 1000, 3000, 5000, and 10000 nm/s).

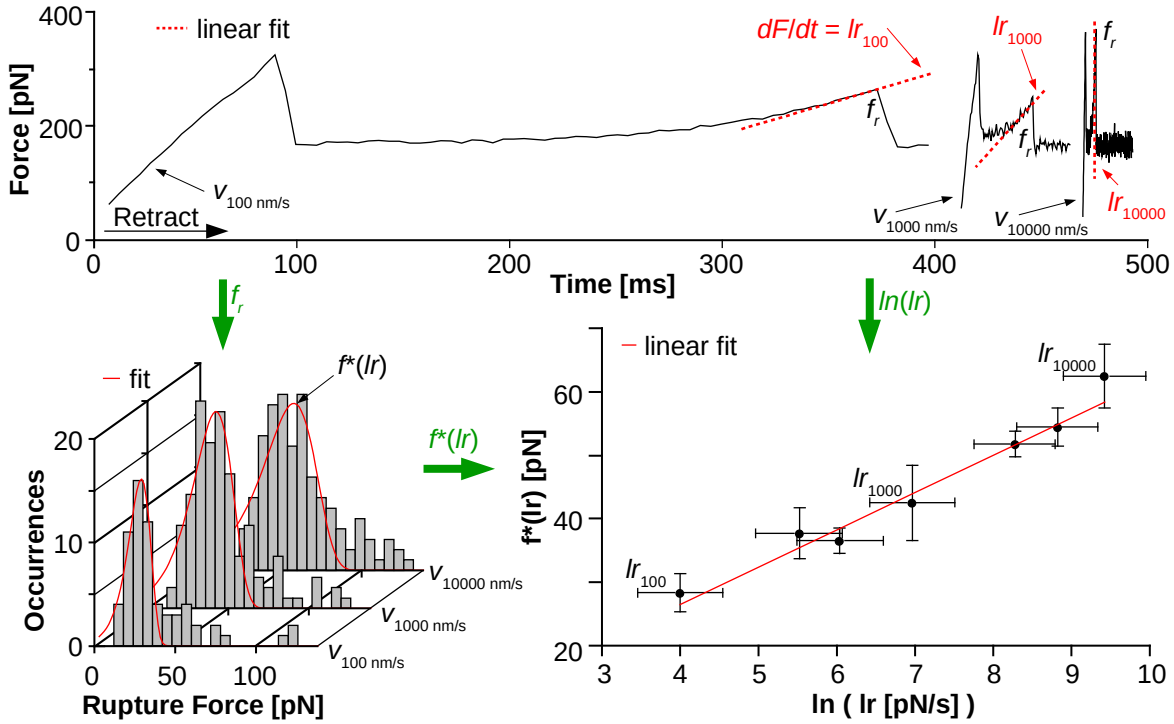

Figure 30: Scheme of data analysis according to the KBE model. Top) Force-distance measurements are performed over a broad range of pulling velocities (here 100 - 10000 nm/s). Saw-tooth signals are characteristic for the polymeric spacer approach. Peak heights are the rupture forces (f_r), a fit to some polymer model (chapter 2.4) yields the corresponding slope *df*/*dt* or loading rates *lr* at the moment of bond rupture. Bottom left) Rupture forces are binned into histograms, for each pulling velocity separately. The fit maximum is the most probable rupture force *f**(*lr*). Bottom right) Finally, the average *lr* and *f**(*lr*) values are added into a dynamic force spectrum. A linear fit yields Δx from the slope and $k_{off}(0)$ from the *x*-crossing at *f**(*lr*) = 0.

The most probable rupture force method is more robust than direct histogram fitting using equation (96), because it is less influenced by thermal broadening and enables separation of multiple peaks in rupture force histograms. Also implementation is easy. However, according to the MD study of Friedsam et al. mentioned above, this procedure introduces higher variations of 15% in Δx and a factor of two in $k_{off}(0)$.[189] So the researcher has to decide according to his specific system and device.

2.5.2. Issues of the KBE Model and Method

The KBE model makes two serious simplifications by assuming (a) a static rupture length Δx and (b) a constant loading rate *lr*. In a real experiment at a constant pulling speed, the loading rate changes due to the elastic properties of the polymer. However as discussed in chapter 2.4, the force-extension behavior of many tethers enters a linear high-force regime well above a transition force of $f_{tr} \gg k_B T l_p / b^2$, where l_p is the persistence and *b* the typical bond length. Here, forces are indeed ramped

with a constant loading rate. Its magnitude depends on segment elasticity of the corresponding polymer K_s and the cantilever spring constant k_c. For soft cantilever probes ($K_s > k_c$), the loading rate approaches $lr = k_c\, v$. Especially in earlier works, only the spring constant was utilized to determine the dynamic force spectrum.[113,193] Today it is generally not considered a good method anymore.[185] Instead it is common to perform either a linear fit to force-distance sawtooth signals, using the latest data points in advance of the bond rupture peak,[30,194] or a polymer fit to the force-distance signals (such as the WLC or FJC model).[195,196] Both methods yield the "apparent loading rate", which also applies to loading rates below the transition force f_{tr}.[185]

Assumption (a) of a static rupture length Δx is valid for sharp transition states such as in the zig-zag potential representing the Bell or standard model (figure 31). It fails to describe the shift of Δx due to applied forces in more realistic potentials such as the cusp-like (discussed by Hummer et al.[197]), or the linear-cubic (discussed by Dudko et al.[198]).

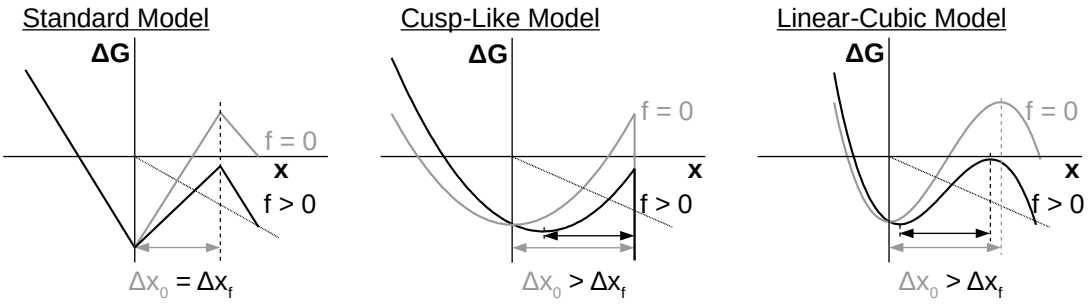

Figure 31: Analytically solved potential energy profiles, used in the KBE model. The constant rupture length assumption in the "standard model" can be represented by a zig-zag potential.[199] The cusp-like model is characterized by $\Delta G(x) = E_a\,(x/\Delta x)^2$ for $(x < \Delta x)$ and $\Delta G(x) = -\infty$ for $(x \geq \Delta x)$, the linear-cubic model by $\Delta G(x) = (3/2)\, E_a\, x/\Delta x - 2\, E_a\, (x/\Delta x)^3$.[200]

Finally careful interpretation of KBE model results should take into consideration that forces induced by a mechanical probe have a direction. As illustrated in figure 32, the underlying path of bond dissociation may be different between the thermally relevant and force-induced process. In other words, $k_{off}(0)$ may not reflect the thermal off-rate constant of process **I**, but of the mechanically catalyzed process **II** with higher thermal activation energy barrier. A prominent example is the mechanically induced ring opening of cyclobutadien (figure 33). This pericyclic reaction can yield different diastereomeric products. Due to symmetry of the participating LUMO- and HOMO-orbitals, light-induced ring opening occurs in a disrotatory pathway, thermally induced ring opening in a conrotatory reaction. However an external force is able to pull the

ligands apart in a specific direction, either con- or disrotatory.[12] A deeper theoretical discussion was published two years later by Marx et al., who calculated the 2-dimensional potential energy landscape using the relevant con- and disrotatory coordinates. The result is a more elaborate picture than the one shown in figure 32, because their model does not just tilt the energy profile, but recalculates the energy surface explicitly as a function of the applied forces. They concluded that external forces lead to various deformations of the landscape, allowing thermal escape to new reaction products.[201]

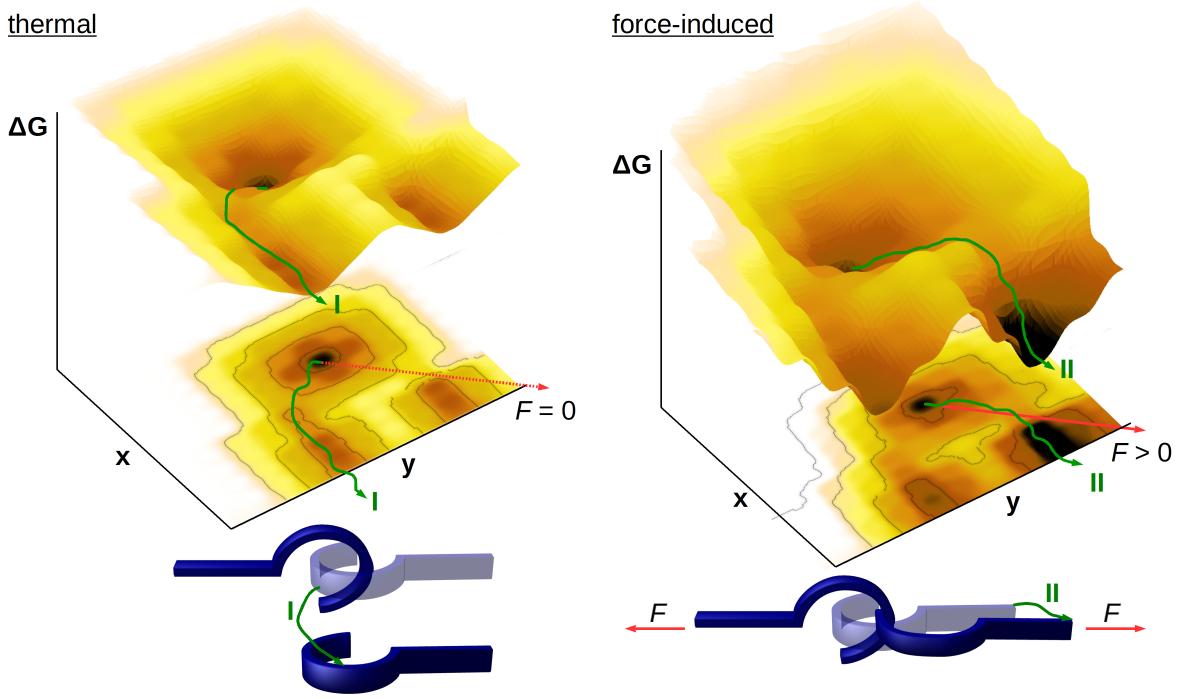

Figure 32: Model, where the thermally activated process (left) is different from the force induced process (right), adapted from[202]. The dominant thermal pathway **I** passes the lower saddle point in slightly negative *y*-direction. For example, the two hooks may be de-threaded to the front. A directed external force tilts the potential energy surface. As a consequence the saddle point energy in direction of *F* is lowered and pathway **II** becomes the dominant process. For example, the hook may deform due to the *F*, allowing deformation and de-threading to the right.

Other illustrative examples are force-directed unfolding processes of proteins. The trimeric titin-telethonin complex and the green fluorescent protein (GFP) exhibit very different mechanical stabilities, depending on the direction of applied forces. Titin unfolds either around 200 or 700 pN,[103] the GFP varies between 100 and 500 pN.[103]

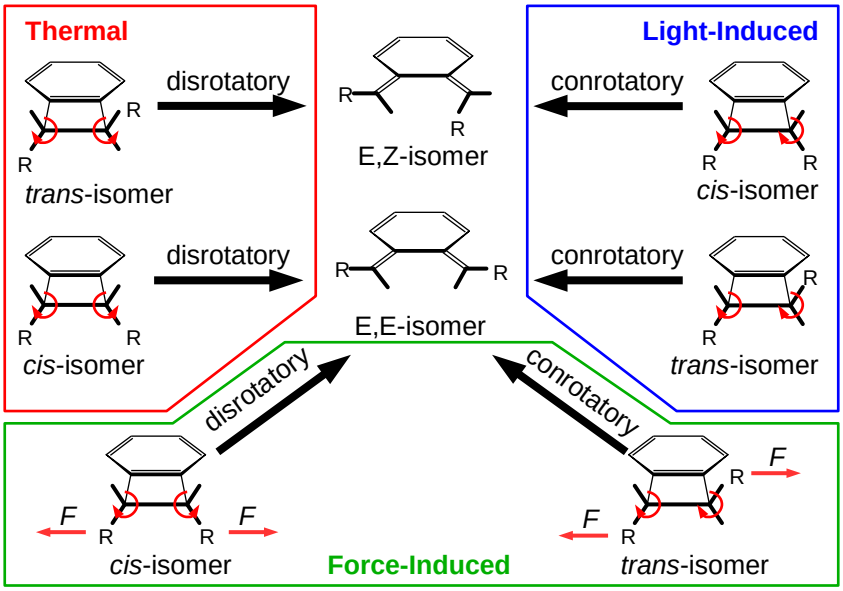

Figure 33: There are two different ring opening mechanisms of cyclobutadiene: disrotatory and conrotatory. The thermal or light-induced ring opening only occurs under preservation of orbital symmetry. According to the Woodward-Hoffmann rules,[203] the HOMO only allows for a disrotatory process. When the LUMO has been occupied by photoactivation, only the corresponding products of conrotatory ring opening are found. In 2007 Hickenboth et al. published a letter on the force-directed ring opening. Here, PEG chains were added to the molecule at position R, which mediated forces from an external ultrasonic source to the cyclobutadien group. Independent of the isomeric reactant state, only the E,E-isomer had been found as reaction product.[12]

2.5.3. Complex Dynamic Force Spectra

As discussed so far, the KBE theory only considers a single transition state along the direction of force. However real systems are frequently characterized by various interactions and a rough potential energy surface with several local minima and transition states. The probability of finding the system in a certain of N local minima (the population p_i) is given by the Boltzmann distribution of states.

$$p_i = \frac{\exp\left(-\frac{E_i}{k_B T}\right)}{Z} \tag{99}$$

with partition function

$$Z = \sum_i^N e^{-\frac{E_i}{k_B T}} . \tag{100}$$

The overall stability of the interaction is characterized by a hierarchy of back and forth rate constants between all intermediate states: $k_{i\rightarrow i\text{-}1}$ and $k_{i\leftarrow i\text{-}1}$. The rupture process may occur over several pathways, each with its own activation energy barrier. The overall thermal off-rate constant k_{off} also depends on the population of

their corresponding local minima p_i and the Arrhenius prefactor A_i (characterized by the shape of the reaction pathway).

$$k_{off} = \sum_{i}^{N} p_i A_i \exp\left(\frac{-E_{a,i}}{k_B T}\right) \tag{101}$$

Due to the exponential relationships, usually only one of the N summands in equation (101) dominates the thermal off-rate constant k_{off}. In the experiment this dominant mechanism (or pathway of rupture) is measured, all other rates and the actual surface profile are kinetically invisible.

External forces influence the population of states $p_i(f)$ and the activation energy barriers ($E_{a,i}$ - $f\,\Delta x$),[81] yielding

$$k_{off}(f) = \sum_{i}^{N} p_i(f) A_i \exp\left(-\frac{E_{a,i} - f\,\Delta x}{k_B T}\right). \tag{102}$$

Consequently an external force may change the dominant mechanism such as shown in figure 32. Other examples are two-state two-path catch-bond mechanisms,[204] and one-path two-barrier energy diagrams such as sketched in figure 34. In the latter model, bond rupture requires transition of two barriers in a row. As long as the population of the intermediate state between $E_{a,1}$ and $E_{a,2}$ is low, only the transition from the ground state with a rupture length of Δx_2 is dominant. At larger forces the system enters a transition regime, where both barriers are of similar activation energy barrier $E_{a,1} \approx E_{a,2}$. As the force is further increased, the first barrier gets dominant. Still, the system is not broken at the intermediate state. But as soon as the system enters the intermediate state, the probability of thermal rupture by passing $E_{a,2}$ is much higher than of rebinding over the larger inner activation energy barrier $E_{a,1}$. Here in a SMFS experiment, Δx_2 is kinetically invisible and the KBE model yields a rupture length of Δx_1.[128]

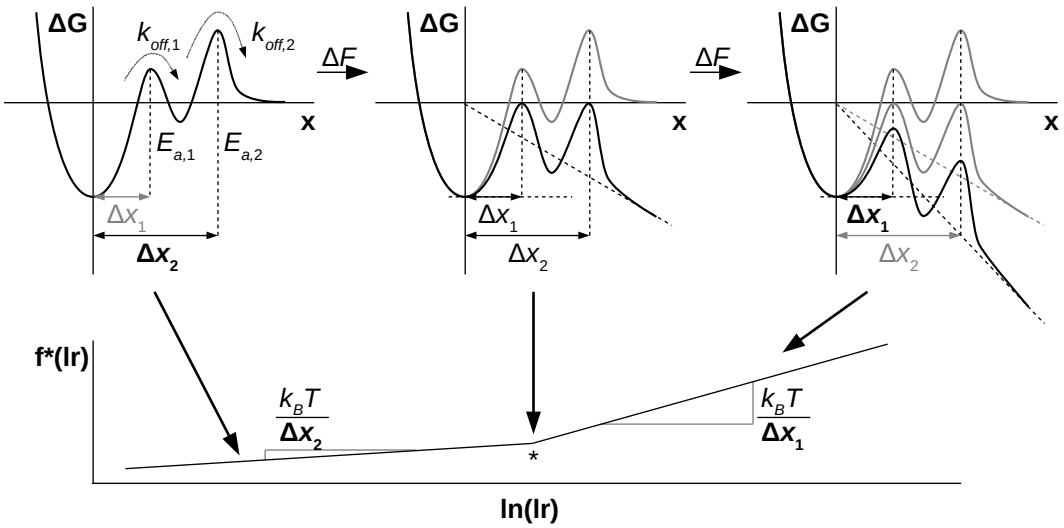

Figure 34: In a SMFS experiment, the most probable rupture force *f** is a measure of the dominant transition state with highest activation energy barrier. Transition states with higher rupture length ($\Delta x_2 > \Delta x_1$) are more sensitive to applied external forces. Thus, a shorter transition state with lower barrier can get dominant beyond certain *f** respectively loading rates *lr* (center). The corresponding dynamic force spectrum is characterized by a kink (marked by *), separating regions of different slope ($k_BT/\Delta x$).[128]

For example, the dissociation of biotin-(strept)avidin interactions is characterized by at least two transition states: one with a very short rupture length ($\Delta x \leq 0.1$ nm), and one with a larger one ($\Delta x \geq 0.4$ nm).[27,193] As sketched in figure 35, the shorter one is attributed to the initial H-bond breakage, the second one due to interactions with a tryptophan group of the (strept)avidin pocket (nonpolar[205] or steric[27]). Yuan et al. exchanged this tryptophan in streptavidin by a phenylalanine and indeed discovered a much higher thermal off-rate for the second barrier, while the first transition state was only slightly changed.[206]

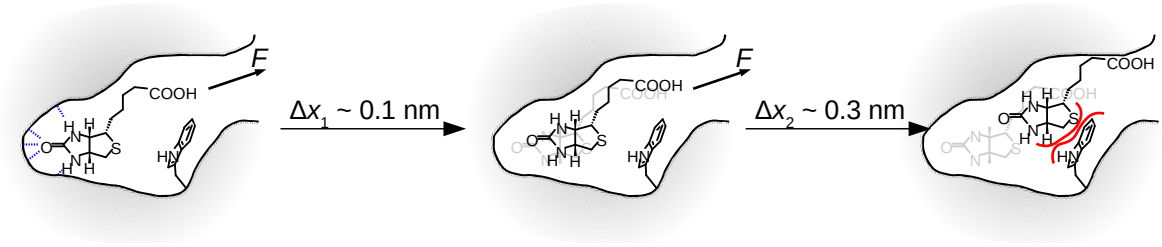

Figure 35: Schematic of biotin de-threading from a binding pocket of (strept)avidin. left) In its bound state, five hydrogen bonds to amino acids of the protein yield one of the strongest non-covalent interactions one in nature. The thermal off-rate constant between wild-type biotin and streptavidin is 6.8 10^{-5} s^{-1} (with additional interactions at the terminal COOH-group.[207] center) When the molecule is pulled out of the binding pocket by approximately 0.1 nm, all five initial hydrogen bounds are broken. right) After additional 0.3 nm of movement, the biotin interacts with a tryptophan group. This interaction is origin of the larger rupture length.[27]

MD simulations of the biotin-avidin interaction by Izrailev et al. in 1997 gave insight into the mechanism, but calculated rupture forces were much higher than those of the corresponding experiments.[205] This issue was addressed by Heymann and Grubmüller in 1999. They emphasized that above a certain pulling speed of approximately 1 m/s, Stokes' friction gets relevant (equation 103), where γ is the friction coefficient and v_{cant} the pulling speed of a cantilever spring with harmonic potential.[208]

$$F_{friction} = \gamma v_{cant} \tag{103}$$

The corresponding master equation (104) describes all three pulling regimes:

- a drift regime for fast pulling speeds, relevant in MD simulations (> 1 m/s)
- an activated regime for slow pulling speeds, relevant in SMFS experiments
- a diffusion regime for intermediate pulling speeds

$$F_{unbind}(v_{cant}) = F_{friction}(v_{cant}) + F_{act}(v_{cant}) \tag{104}$$

$F_{friction}(v_{cant})$ corresponds to equation (103) and $F_{act}(v_{cant})$ to equation (84). Although the drift regime is not accessible by experimental setups and the activated regime takes too much computational time to be calculated in MD simulations, equation (104) made it possible to compare experiment and theory just with one free parameter: the friction coefficient γ.

Dynamic force spectra measured at different temperatures vary in their slope $k_BT/\Delta x$, and in their y-crossing due to different thermal off-rate constants k_{off} (equation 81). Assuming a temperature independent rupture length Δx, the Zou et al. suggested the conversion formula (105).[194] Here, lr_1 is the loading rate at T_1, lr_2 the corresponding rate at a different temperature T_2. Thermal off-rate constants k_{off1} and k_{off2} may be experimentally measured at two different temperatures or extrapolated according to equation (81). Using this equation, data measured at different temperatures can be translated to a single master curve in the dynamic force spectrum. Equation (106) is the corresponding representation on a logarithmic scale.

$$lr_1 = \frac{k_B T_1 k_{off1}}{\Delta x} \exp\left(\frac{T_2}{T_1} \ln\left[\frac{lr_2 \Delta x}{k_B T_2}\right]\right) \tag{105}$$

$$\ln(lr_1) = \frac{T_2}{T_1} \ln(lr_2) + \frac{T_2}{T_1} \ln\left(\frac{\Delta x}{k_B T_2 k_{off2}}\right) + \ln\left(\frac{k_B T_1 k_{off1}}{\Delta x}\right) \tag{106}$$

This means, spectra measured at higher temperatures are shifted to lower loading rates and vice versa. Zou et al. applied equation (106) to extend the experimentally accessible range of loading rates using measurements at 301 and 330 K and transfer the latter results into the master curve at 301 K.[194]

2.5.4. The DHS Model

According to the KBE model, f^* scales logarithmically with the loading rate $f^* \sim ln(lr)$. In 2003, Hummer and Szabo developed a more sophisticated model by applying Kramers rate theory to a simple cusp-like potential energy diagram (figure 31, center). Their model includes the thermal off-rate constant k_{off}, rupture length Δx, and additionally the activation energy barrier E_a. In contrast to the KBE model, it scales at intermediate pulling speeds by $f^* \sim ln(lr)^{1/2}$.[197] Also in 2003, Dudko et al. applied Kramers rate theory to linear-cubic potentials (figure 31, right) and received a third scaling law of $f^* \sim ln(lr)^{3/2}$.[198] The different scaling was puzzling. Thus all three authors joined forces and combined their models in an analytical master equation (107), where $\nu = 1/2$ represents a cusp-like and $\nu = 2/3$ a linear-cubic potential. For $\nu = 1$ one gets the phenomenological KBE model equation (83). This model is valid in the high-barrier limit (small and intermediate forces, well below the critical force f_c) and is called Dudko-Hummer-Szabo (DHS) model.[200]

$$k_{off}(F) = k_{off}(0)\left(1-\frac{\nu F \Delta x}{E_a}\right)^{1/\nu-1}\exp\left(\frac{E_a}{k_B T}\left[1-\left(1-\frac{\nu F \Delta x}{E_a}\right)^{1/\nu}\right]\right) \qquad (107)$$

Analogue to the KBE model, the survival probability of a bond under (linear) force-ramp conditions was calculated, leading to the RFPD equation (108).

$$p(F, lr) = \frac{k_{off}(F)}{lr}\exp\left(\frac{k_{off}(0) k_B T}{lr\,\Delta x}\right)\exp\left(\frac{-k_{off}(F) k_B T}{lr\,\Delta x}\left[1-\frac{F\,\Delta x\,\nu}{E_a}\right]^{1-1/\nu}\right) \qquad (108)$$

The mean rupture force $\langle F\rangle = \int F\,p(F, lr)\,dF$ and variance $\sigma_F^2 = \langle F^2\rangle - \langle F\rangle^2$ are then

$$\langle F\rangle = \frac{E_a}{\nu\,\Delta x}\left(1-\left[\frac{k_B T}{E_a}\ln\left(\frac{k_B T\, k_{off}(0)}{\Delta x\, lr}\exp\left[\frac{E_a}{k_B T}+\gamma\right]\right)\right]^{\nu}\right), \text{ and} \qquad (109)$$

$$\sigma_F^2 = \frac{(k_B T\,\pi)^2}{6\,\Delta x^2}\left(\frac{k_B T}{E_a}\ln\left[\frac{k_B T\, k_{off}(0)}{\Delta x\, lr}\exp\left(\frac{E_a}{k_B T}+\gamma_2\right)\right]\right)^{2\nu-2}. \qquad (110)$$

Here $\gamma \approx 0.577$ is the Euler-Mascheroni constant and $\gamma_2 \approx 1.064$ an additional parameter. When γ is set to zero, equation (109) yields the most probable rupture force instead of its mean value and may be used as fit function for dynamic force spectra. For $\nu = 1$, E_a cancels out and with $\gamma = 0$ one receives the KBE expression equation (84). As illustrated in figure 36, the cusp-like and linear-cubic potentials yield a bow-shaped spectrum. Thus the DHS model is an alternative approach to discuss non-linear results from SMFS experiments.[200] Other possible source of bow-shaped spectra are complex potential energy diagrams with varying dominant energy barriers and simultaneous bond rupture events.

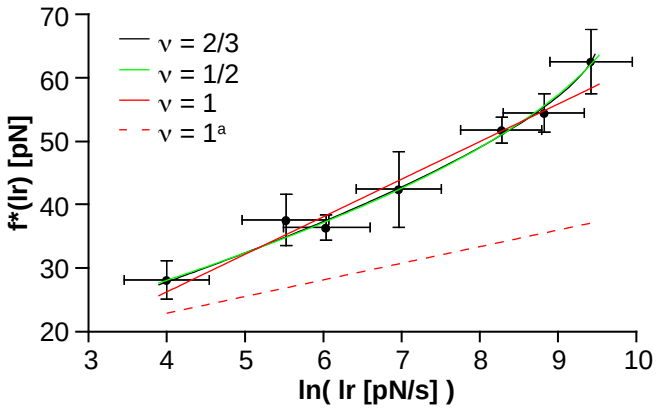

Figure 36: The DHS model equation (109) applied to a measurement with pronounced bow-shape in the dynamic force spectrum, using the linear-cubic potential ($\nu = 2/3$), cusp-like potential ($\nu = 1/2$) and the KBE model ($\nu = 1$). Concerning experimental error bars, all three models are reasonable. However their corresponding fit parameters vary strongly. For illustration, the dashed line is a KBE model plot using fit parameters of the linear-cubic model. Fit parameters are: $\nu = 2/3$, $\Delta x = 1.2 \pm 0.3$ nm, $k_{off}(0) = 0.009 \pm 0.015$ s^{-1}, $E_a = 13.0 \pm 1.6\ k_BT$, $\nu = 1/2$, $\Delta x = 1.6 \pm 0.6$ nm, $k_{off}(0) = 0.003 \pm 0.009$ s^{-1}, $E_a = 14.9 \pm 2.5\ k_BT$, $\nu = 1$, $\Delta x = 0.70 \pm 0.08$ nm, $k_{off}(0) = 0.10 \pm 0.08$ s^{-1}

Although the DHS model attracted lots of attention, the KBE model is still used much more frequently. First, equations (108) and (109) are not as easy to handle as equations (96) and (84). Second, the 3-parameter fit to a dynamic force spectrum often yields large uncertainties for the activation energy barrier. This is the reason, why Dudko et al. rather suggest a global fit to rupture force histogram distributions.[200] But as discussed for the KBE model (chapter 2.5.1) above, direct fit methods are very sensitive to various effects in the experiment. Successful application of the DHS model was reported for systems with prominent bow-shape in the DFS such as nanopore unzipping of DNA hairpins[209] or systems with non-linear behavior in the high-force regime such as the thiol/disulfide exchange between DTT and *I27*.[210]

“Measure what is measurable,
and make measurable what is not so.”

Attributed to Galileo Galilei (1564 − 1642)

3. Materials and Methods

Mono- **3**, bi- (**4a** - **c**), and trivalent **5** model systems were synthesized and coupled to heterobifunctional PEG **6** (Rapp Polymere GmbH, Tübingen, M = 9040 g/mol, PDI = 1.04) via EDAC mediated esterification by Christian Eidamshaus, Maurice Taszarek, and Hans-Ulrich Reißig as published in detail elsewhere (fig. 37).[67,83] All solvents and salts were used as received without further purification. Millipore water with a typical resistivity of 18 MΩ cm^{-1} was freshly prepared by a Milli-Q ultra-purifier (EMD Millipore, Billerica, Massachusetts, USA) and degassed by ultrasonication for 30 minutes.

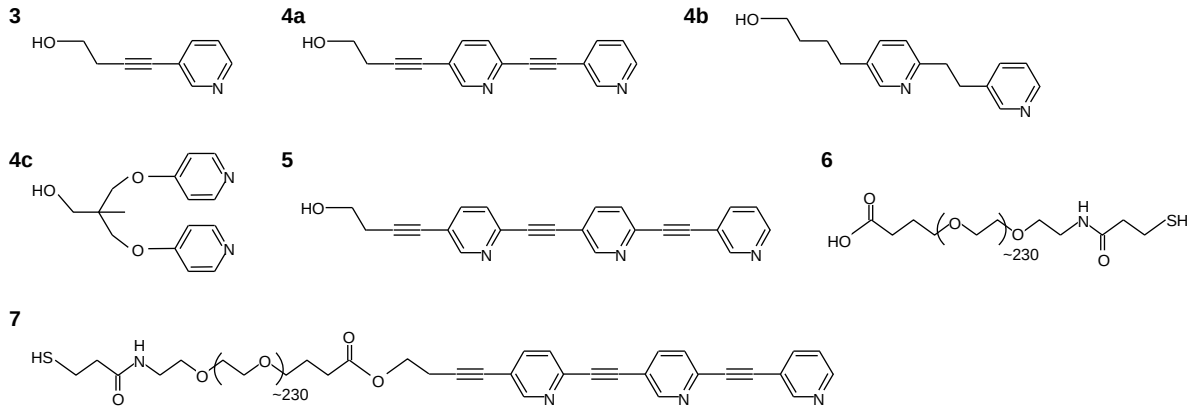

Figure 37: Chemical structures of monovalent **3**, bivalent **4a** - **c**, and trivalent **5** pyridines and the PEG polymer **6** used in this thesis. After a final esterification reaction, the corresponding tethered molecules **1** and **2a** - **c** (figure 6) as well as the corresponding trivalent conjugate **7** were received.

Template-stripped gold supports[211] (JPK Instruments, Berlin, Germany) had been prepared by evaporating gold onto mica and gluing the composite upside down to a solid support. Immediately before use, they were cleaved as sketched in figure 38, yielding a clean surface of amorphous gold with a roughness amplitude of ± 0.4 nm and up to 40 nm deep holes (see also chapter 4.1.1).

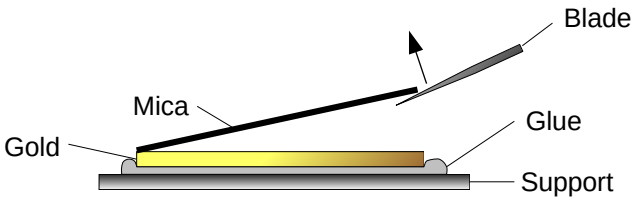

Figure 38: Clean gold surfaces for SMFS were prepared by cleaving the mica on top of evaporated gold by means of a razor blade or adhesive tape.

3.1. Cantilever probe calibration

At the beginning of each measurement, SFM cantilever probes were calibrated *in-situ* according to the thermal noise method[156] taking LCF[154] and MCF[161] into consideration (chapter 2.3.3). External calibration procedures using a reference cantilever or added sphere with known properties were not applied, because the subsequent modification with polymers of high molar mass would have changed the cantilever spring constants. The thermal noise and direct Sader methods (chapter 2.3.2) are both *in-situ* methods and frequently used.[135] However, all relevant reference experiments mentioned in this thesis utilized the first one, due to a better instrumental implementation.

3.2. Modification of cantilever probes and surfaces

Gold-coated Si_3Ni_4 cantilevers (Biolever, Olympus Corporation, Tokyo, Japan) of both spring constants were used (table 4) and cleaned by the UV-ozone method using a low-pressure mercury discharge tube (Penray, UVP, Upland, CA) in an enclosed air volume for 30 min. During this procedure, oxygen from the air is absorbing the emission band at 184.9 nm, leading to the generation of ozone. Additionally the emission band at 253.7 nm is absorbed by most hydrocarbons. In this way possible organic contaminants are oxidized to volatile species and removed from the cantilever surfaces.[212] For example, SAMs of butanethiol on gold are fully oxidized after 30 minutes of exposure time, as analyzed by secondary ion mass spectrometry.[213]

Table 4: Typical properties of Olympus Biolever probes used in this thesis

	A-lever	B-lever
Length × width	60 × 30 µm	100 × 30 µm
Thickness (incl. Au coating)	180 nm	180 nm
Resonant frequency	37 kHz	13 kHz
Spring constant	30 pN/nm	6 pN/nm
Tip height, radius	7 µm, 30 nm	7 µm, 30 nm
Laser correction factor (LCF)	1.06	1.08
Overall correction factor β^*	0.864	0.832

Freshly cleaned cantilever probes and cleaved gold surfaces were modified using thiol − gold coating, which is reliable and frequently used.[91] In detail, a 1 mM aqueous solution of the heterobifunctional PEG polymer was applied for 12 − 24 h at room temperature. The samples were kept in an enclosed vessel with a water

reservoir to avoid evaporation. Afterwards they are thoroughly rinsed with water and equipped to the fluid cell.

3.3. Scanning Force Microscopy

Scanning force microscopy (SFM) images were recorded either on a NanoWizard II (JPK Instruments AG, Berlin, Germany) or Multimode IV (Veeco Instruments Inc., Santa Barbara, California, USA) equipped with a 10 µm E-scanner in intermittent contact mode. Olympus edged silicon cantilevers with a typical resonance frequency of 70 (OMCL-AC240TS) or 300 kHz (OMCL-AC160TS) and nominal spring constants of 1.8 and 42 N/m were used, respectively.

3.4. Single-Molecule Force Spectroscopy

The majority of SMFS experiments were performed on a ForceRobot 200 system[164] (nAmbition GmbH, Dresden, Germany). Some comparative studies were performed on ForceRobot 300 (JPK Instruments AG, Berlin, Germany) and NanoWizard II (JPK Instruments AG, Berlin, Germany) instruments. Probes and surfaces were thoroughly rinsed with water before equipping the fluid cell. Measurements were performed in 3 mM (30 mM for **2c**) aqueous solutions of $CuSO_4$, $Zn(NO_3)_2$, or $FeSO_4$. Reference experiments were performed in deionized H_2O.

DFS requires force-distance measurements under various loading rates. In order to achieve an equal distribution of data points in the DFS, a logarithmic distribution of pulling velocities was chosen: 100, 300, 500, 1000, 3000, 5000, and 10000 nm/s (with 300 and 3000 nm/s left out in some measurements). All velocities were measured several times on one position of the surface. Then the cantilever was moved to the next position, finally screening a two-dimensional grid. Consequently potential inhomogeneities of the surface modification (such as non-modified areas and edges of gold with possible attraction to the sample molecules) were averaged out. Additionally, measurements were repeated using different cantilevers and surfaces, yielding several thousand force-distance curves of raw data.

For batch data analysis, raw data was first transferred into the force-*tss* representation and then processed using Hooke, an open software platform for force spectroscopy.[214] Thereby possible peaks were detected using a simplified version of the convolution algorithm described by Kasas et al.[215] Those peaks were also used to separate different segments of polymer stretching, as illustrated in figure 39. The WLC model equation (38) was applied to each segment in order to calculate the

slope at the *tss* of rupture. For each force-distance curve, only the last peak, its slope in the force-time representation (loading rate), its initial value and the corresponding errors were saved for further analysis. Possible preceding signals were influenced by the subsequent events and thus excluded. (Note that the 2-state FJC model (equation 80) is a more appropriate model for PEG, but requires the inverse data to be fitted. Especially in the low-force regime this may yield inconsistent results.[165] Indeed, the fits to our data were more reliable using the WLC model.)

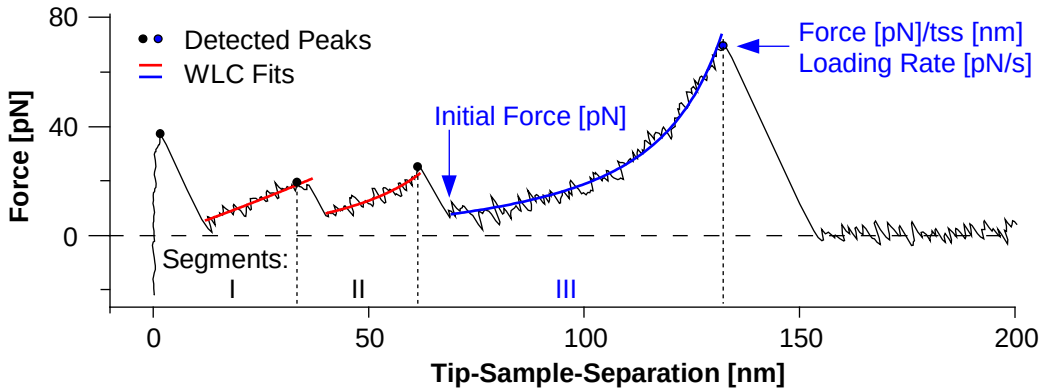

Figure 39: Representative example of an automatically processed force-distance plot. Detected peaks are marked with black circles. WLC model fits (equation 38) were applied to segments I, II, and III, respectively. We used data from the last peak (blue) for further processing.

Further analysis was performed using the data analysis software QTIPlot. First, only interactions with a sawtooth-like shape were selected using the fit errors in contour and persistence length. They were large for non-WLC shapes such as in segment I (figure 39). Second, the KBE model used in this thesis describes bond rupture using a force ramp starting from 0 pN (equation 91). Due to the thermal noise oscillation of the SFM cantilever and preload of the tether, the initial force (figure 39) is usually above zero. Nonetheless using of a minimal threshold force f_{min} of sixfold thermal noise oscillation improved reproducibility between repeated experiments. Only signals with an initial force below f_{min} were taken for further analysis. In figure 40 some force-*tss* diagrams are shown, peaks marked with a * were kept, peaks marked with an x discarded.

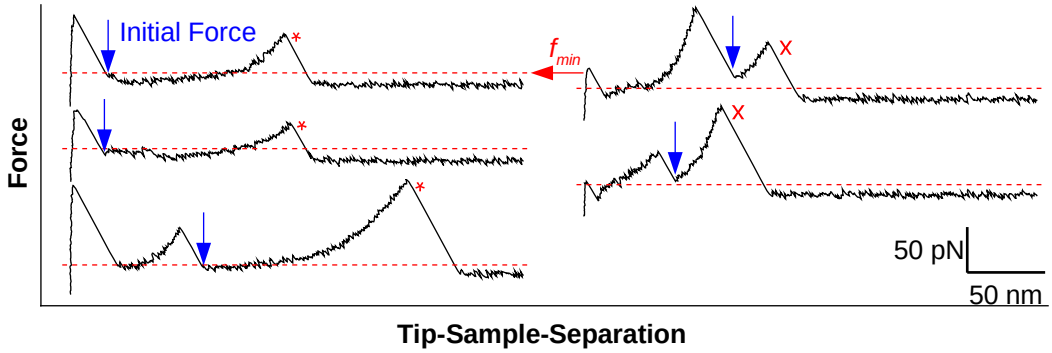

Figure 40: Force vs. *tss* diagrams for a cantilever modified by polymer **1** on a similarly modified gold surface in 3 mM $CuSO_4$, pulled at 1 µm/s. Dashed lines represent six times the thermal noise standard deviation, yielding f_{min}. Only continuous peaks with lower initial force (marked with *) were taken into consideration for the KBE model analysis. In contrast, the last peaks of both plots on the right side (marked with x) had been influenced by the preceding rupture events and were discarded.

At this step, all selected peak maxima were summarized into force-*tss* density plots as shown in figure 41. Typically rupture events accumulated along certain force-extension profiles, which are represented by the known PEG contour length (continuous red line) with repeats at twice (blue) and thrice (green) the tip-sample-separation. Due to the different contour length, all three segments differed in their slope (or loading rate) at a certain force and were separated for further analysis.

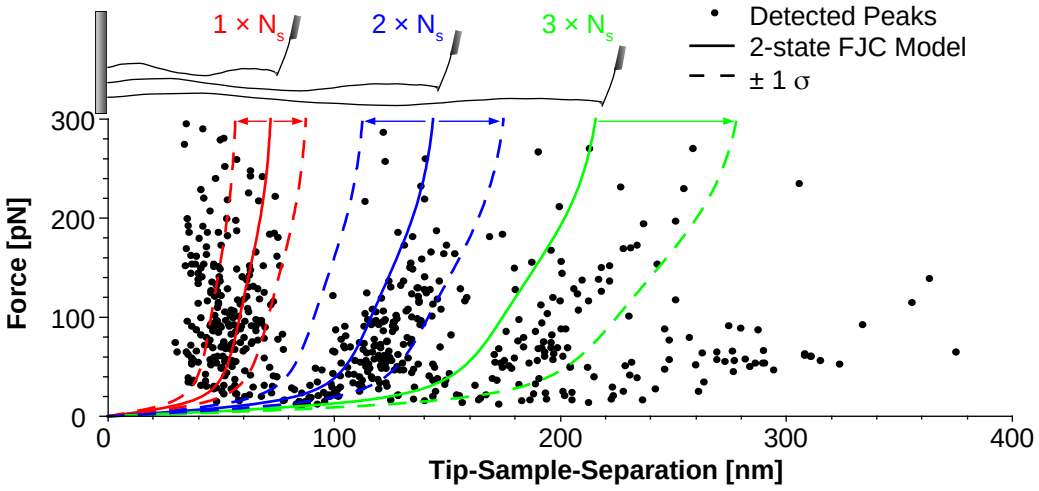

Figure 41: Force-*tss* density plot of rupture events (peak positions) from the experiment also used in figure 40, considering only last-peak events of WLC shape with an initial force below f_{min}. The expected 2-state FJC behavior of PEG (equation 80) with 1, 2, and 3 times the expected contour length (number of segments per chain: N_s = 205) are sketched in red, blue and green continuous lines, respectively. Standard deviations of a Schulz-Zimm distribution with a PDI of 1.05 are indicated with dashed lines: ± 44 N_s (single), ± 88 N_s (twice), and + 132 N_s (thrice). The standard deviation of - 132 N_s is omitted for clarity.

All rupture events per segment were binned into force histograms. Usually they exhibited two, seldom three distinct distributions, (figure 42 a) which were fitted by a sum of two or three distributions of equation (113). We received the corresponding most probable rupture forces f^*_1 *and* f^*_2. Rupture force errors were estimated using the larger value of two options: histogram bin width or fit error in f^*. The corresponding loading rates (*lr*) were calculated from equation (112) with mean parameters for persistence (l_p), contour length (L_c), as well as the corresponding spring constant k. Equation (112) is a different representation of the WLC model, describing the slope (or loading rate) as a function of force.[216] As illustrated in figure 42 b), the experimental behavior was described reasonably well. Errors were estimated using equation (112) with $2 \times l_p$ (dashed lines).

$$p(F) = C \exp\left[\frac{F - f^*}{\omega} - \exp\left(\frac{F - f^*}{\omega}\right)\right] \tag{111}$$

$$lr(F) = v \times slope = v\left[\frac{1}{k} + \frac{2L_c l_p (k_B T)^{-1}\left(1 + (k_B T)^{-1} F l_p\right)}{3 + 5(k_B T)^{-1} F l_p + 8\left((k_B T)^{-1} F l_p\right)^{5/2}}\right] \tag{112}$$

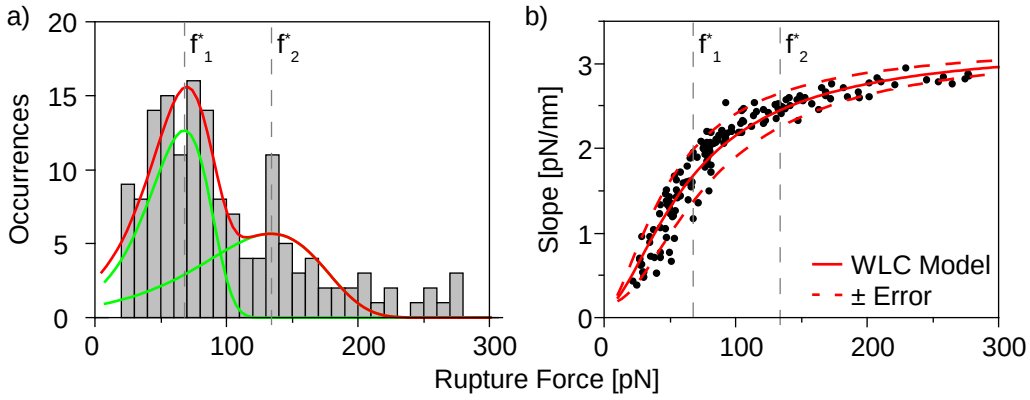

Figure 42: a) Exemplary rupture force histogram, fitted by a sum of two probability distributions (equation 111), yielding the most probable rupture forces f^*_1 and f^*_2. b) Slope of all rupture events in a) with a plot of equation (112) using mean values of L_c and l_p from direct fits to force-*tss* data as shown in figure 39. Dashed red lines mark the estimated range of uncertainty. Upper line: $lr(2 \times l_p)$, lower line: $lr(l_p)$ - [$lr(2 \times l_p)$ - $lr(l_p)$]. The product of slope at the most probable rupture forces f^*_1 and f^*_2, and pulling velocity v is the loading rate (*lr*).

In the KBE model, the rupture process is determined approximately by a constant loading rate over the whole range of forces (chapter 2.5.1), only changing due to the different pulling speeds v. Therefore each most probable rupture force f^* was now attributed to a single loading rate *lr*. Figure 42 b) clearly demonstrates, that this was not the case in a real experiment. Which loading rate is the most appropriate? We

used the “apparent loading rate” method, which uses the extrapolated slopes at f^* (equation 112). This method is known to reduce inconsistency due to different cantilever spring constants and polymers with different contour lengths,[185] both a relevant in our experimental setup. In figure 43 dynamic force spectra of two measurements are plotted. Although the cantilever spring constants varied by a factor of six, both results are the same within the error limits.

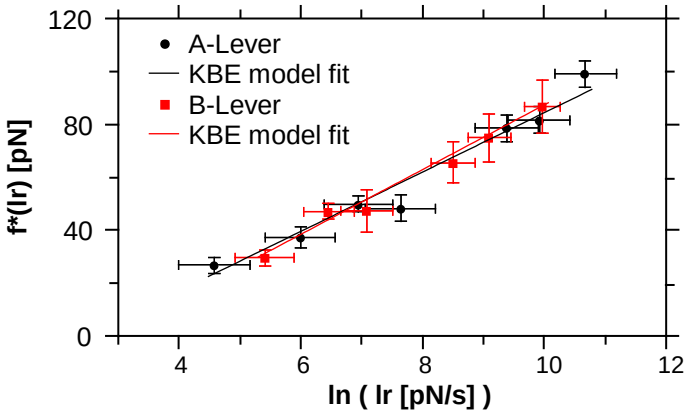

Figure 43: Dynamic force spectra of A- and B-type levers on modified gold surfaces (both modified by mono-polymer **1**) in 3 mM aqueous $CuSO_4$ solution are similar within the range of errors. Continuous lines show KBE model fits, yielding the following results: $\Delta x_A = 3.7 \pm 0.2$ nm, $k_{off,A} = 1.1 \pm 0.3$ s^{-1} ($k_A = 30.7$ pN/nm), and $\Delta x_B = 3.4 \pm 0.4$ nm, $k_{off,B} = 1.4 \pm 0.5$ s^{-1} ($k_B = 4.8$ pN/nm), rupture length Δx, thermal off-rate constant k_{off}, spring constant k_c.

Finally dynamic force spectra of the first and second maximums f^*_1 and f^*_2 were fitted separately according to the KBE model (equation 84) yielding rupture length Δx and thermal off-rate constant k_{off}. Alternatively, we also tested the more sophisticated DHS model to our results (chapter 2.5.4). However the third parameter of that model, the activation energy barrier E_a, is a measure of the curvature and slope in the dynamic force spectra. Such a bow-shape was not present in our data, yielding huge DHS fit errors. For the analysis of simultaneous rupture events, we also fitted the rupture force histograms directly (direct fit method). The corresponding code for Wolfram Mathematica is given in the appendix chapter 6.3.

3.5. Theoretical Calculations

Elaborate theoretical DFT calculations were performed by Arthur Galstyan and Ernst-Walter Knapp using the constraint geometries simulate external forces (COGEF) model, first suggested by Beyer in 2000.[25] In this method, the individual calculations do not include any forces. Instead they are indirectly represented by their effect: separation of interaction partners. As sketched in figure 44, the two end atoms (red

points) serve as fix points. In the experiment, the molecule is connected to the PEG polymer at those positions. The vector connecting both fix points represents the reaction coordinate with magnitude r and equilibrium point $r_{eq} \equiv 0$. Elongation of r was performed in a stepwise manner, including a geometrical relaxation with respect to all remaining degrees of freedom, each. Also the potential energy $V_f(r)$ that is influenced by the constraint was calculated. The KBE parameter rupture length Δx is the distance, where a bond breaks during the calculation.

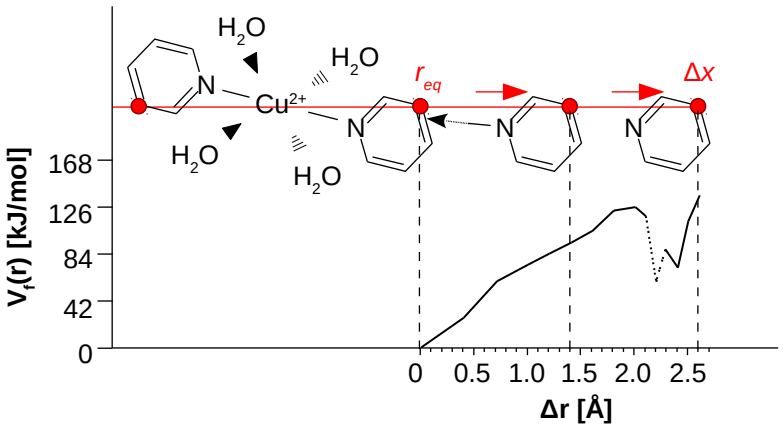

Figure 44: Principles of the COGEF method demonstrated exemplary for the octahedral para-complex $[Cu(H_2O)_4py_2]^{2+}$, calculated with a dielectric continuum representing the water environment. The complex is fixed at two force-points (red dots), that represent the experimental connections, and "stretched" in a stepwise manner by Δr. At each step, a full geometry optimization is done. The last stable configuration yields the rupture length Δx, also gained from the KBE analysis of experiments.

The water environment was represented by an implicit solvation model, using the Poisson-Boltzmann finite element method[217,218] implemented in Jaguar[219,220]. A dielectric constant of 80.0 and probe radius of 1.4 Å were used. The B3LYP[221–224] functional was used in combination with a 6-31G basis set (except for Zn^{2+} and Cu^{2+}, which were calculated with a LACVP[225] effective core potential). The van der Waals radii were 1.0 (H), 1.6 (C), 1.5 (N, O), 1.381 (Zn), and 1.748 Å (Cu). To describe the process more realistic in terms of energy, the calculations should include explicit water molecules from the second solvation shell. However this was computationally too expensive. In this thesis, we were mainly interested in the rupture lengths.

Single point energies were calculated with a larger basis set (6-311++G**) and effective core potential (LACV3P), using the M06-D3[226,227] functional. Those calculations were performed in vacuum and used for the solvent models. The covalent part of the electronic energy is nearly invariant from the electrostatic environment, whose energy was calculated separately. Solvation energies were

calculated using the program “Solvate” included in the MEAD program suite. Thereby, the Poisson equation was solved numerically by a finite difference method.[228,229] For details and parameters see [67,230].

“Single Molecules are 100% pure,
but Single Molecules are 99% trash.”

Hermann E. Gaub (* 1954) on the detection of specific interactions, Berliner Physikalisches Kolloquium on 09.02.2012

4. Results and Discussion

In the following we will present the results of single-molecule force spectroscopy (SMFS) experiments on our mono- (**1**), bi- (**2a** − **2c**), and trivalent (**7**) pyridine model systems, analyze their malleabilities by means of the Kramers-Bell-Evans (KBE) model and discuss the corresponding rupture mechanisms according to the constraint geometries simulate external forces (COGEF) theory. Thereby we will address the yet unknown cell in overview table 5: Are there rupture mechanisms in systems of low valency that exhibit a high malleability?

Table 5: Overview on possible rupture mechanisms of high malleability or mechanical stability in systems of low and high valency as discussed in the introduction chapter 1.

	Monovalent	Bivalent	Multivalent
Malleable (large rupture length Δx)	long-ranged interaction (R[4]a + $NH(Me)_3^+$)	?	zipper-type rupture (PAS-B, etc.)
Mechanical stable (large rupture forces f^*)	short-ranged interaction (R[4]a + NH_4^+)	simultaneous rupture (C_{60} + Zn-Porphyrin)	shear-type rupture (Ubiquitin, etc.)

This chapter is partitioned into three sections. In the chapter 4.1, we will address the issue of measuring reproducible (specific) interactions. Therefore the modification of gold coated SFM cantilever probes and gold surfaces, minimization of simultaneous bond rupture events and the utilized double-tether approach will be discussed. In chapter 4.2, we will present our experimental results on pyridines **1**, **2a** - **2c** and **7**. All systems showed specific interactions in water, but different ones in aqueous solutions of Zn^{2+} and Cu^{2+}. In particular, the mechanical stability of both interactions $\mathbf{1}_2$−Zn^{2+} and $\mathbf{2a}_2$−Zn^{2+} was similar, indicating a monovalent interaction both systems. Thus we continued with a stronger complexing agent, yielding the specific interactions $\mathbf{1}_2$−Cu^{2+}, $\mathbf{2a}_2$−Cu^{2+}, $\mathbf{2b}_2$−Cu^{2+}, and $\mathbf{2c}_2$−Cu^{2+}. The equivalent trivalent system **7**−Cu^{2+} did not form. We will discuss possible additional conformations arising as a second peak in the measured rupture force histograms as well as tilted pulling angles. In chapter 4.3, we will combine our experimental results and the COGEF simulations of our cooperation partners to propose models of the rupture mechanisms: In $\mathbf{2b}_2$−Cu^{2+} simultaneous bond rupture yielded high mechanical stability. In $\mathbf{2a}_2$−Cu^{2+} and $\mathbf{2c}_2$−Cu^{2+} water mediated intermediate states and stepwise

rupture processes resulted in high malleability. With the latter ones, we had found two examples for bivalent systems with large rupture length, filling the gap in table 5.

4.1. Specific Interactions

In bulk experiments, data is measured for an ensemble of molecules simultaneously. In contrast single-molecule experiments determine physical states of one molecule at a time. Typically, such experiments are repeated to receive a distribution of data, similar to the bulk experiment. The advantage is, that data from a single molecule is pure. On the other hand they are very sensitive to contaminations or artifacts. A single impurity, repeatedly measured, is sufficient to disturb the distribution of data. Therefore it is paramount importance to distinguish and select the specific interactions of interest, for example by their force-extension behavior in SMFS.

In this thesis, we used PEG spacer molecules to attach our pyridines to the SFM cantilever and surface. First, the modification process will be characterized with the help of SFM imaging on atomically flat Au(111) and force spectroscopy (chapter 4.1.1). Then we will address the issue of simultaneous bond rupture. During sample preparation, an unknown number of polymers is attached to the SFM tip. As a result, data from an SMFS experiment is a mixture of single-molecular and simultaneous bond rupture events. Thus we will discuss several methods for the separation of both event types during the measurement and data analysis (chapter 4.1.2). Finally we will present the double tether approach: The contour length distribution of the PEG polymer is known. Specific rupture lengths are expected at twice the contour length, which will be confirmed by reproducibility of the measured data. We will also address an issue that occurred in our system, which yielded contour lengths of three and four times the contour length (chapter 4.1.3).

4.1.1. Modification of Gold Substrates and Cantilever Probes

Commercially available cantilever probes for SFM are micro fabricated structures of (n-type) silicon or silicon nitride. The corresponding probe tips are usually made of the same material and allow chemical modification by silanes after a pre-oxidization step.[231] Alternatively, gold-thiol coatings are widely used due to the easy to handle process and highly reproducible results.[91] Silicon nitride cantilevers with a 30 to 100 nm thick coating of evaporated or sputtered gold are offered by probe manufacturers, such as the Olympus Biolevers used throughout this thesis. Sample surfaces for the ForceRobot 200 system[164] were available as template-stripped gold.[211] They had been prepared by evaporation of gold onto mica at elevated temperatures. The substrate was then glued upside down to a support. Immediately before sample preparation, we removed the mica from the gold using a razor blade.

We received amorphous or polycrystalline surfaces with a height amplitude of ± 0.4 nm and maximally 40 nm deep holes (figure 45). SFM images of the corresponding mica surface did show some remaining gold, but not as much as the missing material from the holes. Thus they had been formed during surface preparation and not in the peeling process.

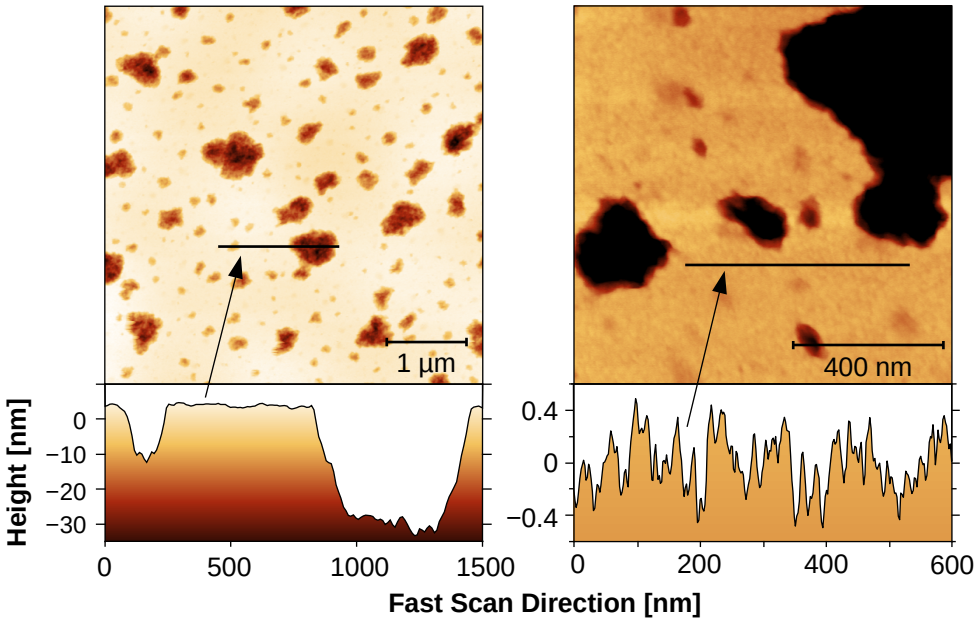

Figure 45: SFM images in intermittent contact mode of freshly cleaved gold surface show holes of up to 40 nm depth and flat areas with a height amplitude of ± 0.4 nm as illustrated in the cross-sections.

In this thesis we used the heterobifunctional PEG polymer **6** to modify gold coated cantilever probes and template stripped gold surfaces. A similar protocol was capable of forming self-assembled monolayers of cysteamine dihydrochloride on template stripped Au(111)[232] and thus at least a random attachment onto the SFM cantilevers and our surfaces was reasonable. SFM images of modified ForceRobot 200 surfaces were blurred, thus we applied the same coating procedure to Au(111) surfaces immediately after 15 minutes of UV-ozone cleaning. In figure 46, SFM images before and after modification with PEG polymer **1** are shown. Application of **1** had a significant effect and increased the roughness amplitude of flat terraces to ± 0.2 nm. Thus our protocol was suitable to modify Au(111) and was reasonable to expect a modification of the ForceRobot 200 surfaces as well. Interestingly, the increase in height of only 0.2 nm was much lower than the radius of gyration in solution, extrapolated from Devanand et al. (R_g = 4.6 ± 1.4 nm).[233] Either the polymers were lying flat on the surface with a radius of up to 0.2 nm or they had formed a dense layer with protrusions of up to 0.2 nm. There were some granular

objects at the edges of Au(111) terraces of 1.5 to 3 nm height in non-modified samples, but not more than 1.5 nm height in the modified sample (marked by green line-arrows in figure 46). This decrease may indicate an up to 1.5 nm thick layer with up to 3 nm high granular objects as yardsticks inside.

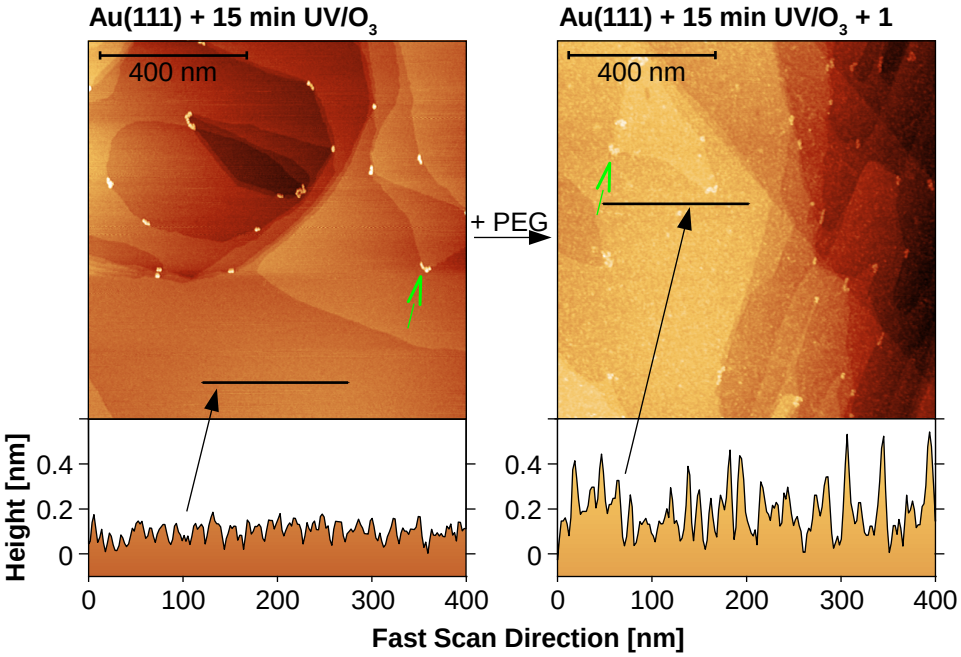

Figure 46: SFM images in intermittent contact mode of an Au(111) surface after the UV/O_3 cleaning procedure (left) and modification with PEG conjugate **1** (right). Thereby the height amplitude increased from ± 0.1 nm to ± 0.2 nm as shown in the exemplary cross-sections. Step heights in the non-modified sample matched the reported value of 0.236 nm reported for Au(111).[234] Green arrows mark two of several granular objects, also observed on gold surfaces as received from the manufacturer. In the literature they had also been reported on flame annealed surfaces[235] and were not removable by aqueous or organic solvents. Probably they are of non-crystallized gold.

The modification of SFM cantilever probes was detectable in the SMFS experiments. In figure 47, representative force − *tss* diagrams with a modified cantilever probe on template-stripped gold (black) and modified gold (red and blue) are shown. Thick continuous lines are plots according to the 2-state FJC model[93] (equation 80) with repeat units $N_{s,black}$ = 205 and $N_{s,red}$ = 410 as expected by the average molar weight of **6**. Using non-modified cantilever probes and non-modified surfaces, only tip-surface peaks of very large forces (up to the nanonewton range) at a *tss* of 0 nm were measured (**I**). Using modified cantilever probes on non-modified surfaces, additional sawtooth-like signals with a *tss* below $N_{s,black}$ appeared (**II**). On non-modified surfaces we measured tip-surface peaks of large forces (up to the nanonewton range) at a *tss* around 0 nm (**I**) in every curve and some sawtooth-like signals with a *tss* below (**II**).

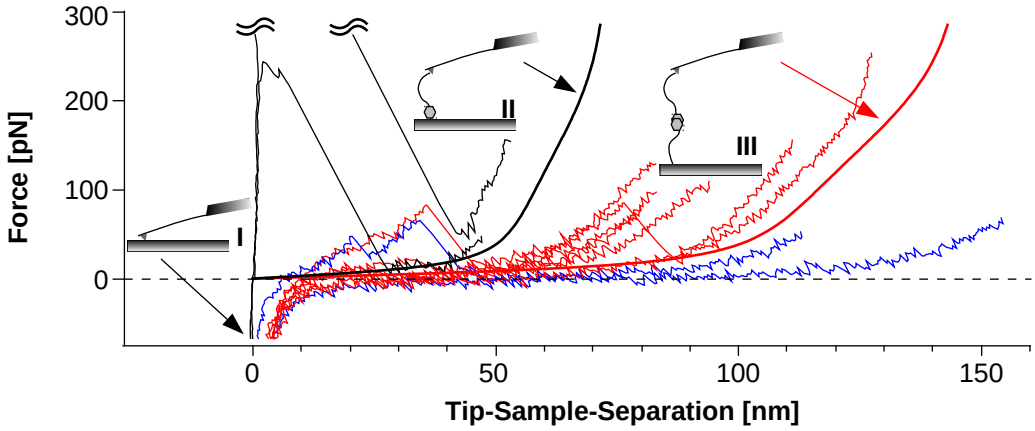

Figure 47: Force vs. tip-sample-separation (*tss*) diagrams for a cantilever modified by **1** on freshly template-stripped gold before (black) and after (red, blue) modification with **1** in H_2O. For clarity, all measurements are truncated beyond their rupture force (maximum value). Continuous lines show 2-state FJC model plots according to equation 80 using $N_{s(black)}$ = 205, $N_{s(red)}$ = 410 and parameters from Oesterhelt et al.[93] Schematic pictures indicate tip-surface adhesion (**I**), stretching of a single tether (**II**), and of two polymers in a double-tether configuration (**III**).

The force-extension measurements in figure 47 are shifted to lower *tss* compared to the 2-state FJC model plots. This was attributed to molecules that are attached to the sides of the cantilever. Molecules at the tip apex are expected along the continuous lines (with some variation due to polydispersity), but those are prone to get worn off during the first force-distance measurements. As a result, force-*tss* plots start with some offset in *tss*. This effect was probably increased due to the up to 40 nm deep holes in the gold substrate.

Using modified cantilever probes on modified surfaces, the frequency of occurrence and the force of adhesion peaks (**I**) was strongly reduced, indicating passivation of the gold surface. Now, rupture events at *tss* in between (**II**) and (**III**) were frequently observed as expected for surface modification with **6**. Rupture events colored in blue were detected beyond (**III**), indicating polymers that are longer than expected. Possible origins of such signals will be discussed in chapter 4.2.1.

4.1.2. Simultaneous Bond Rupture

The KBE model requires single-molecular rupture events, or at least knowledge about the number of broken interactions. However due to the finite size of the tip, there is always a certain probability that two or more bonds are pulled simultaneously. The rupture force histograms measured throughout this thesis frequently varied from the theoretical KBE probability distribution. For example, all three rupture force histograms shown in figure 48 occurred in the same

measurement at different pulling speeds. The left histogram was symmetric and well fitted by the KBE model distribution equation 96. If two of such bonds broke simultaneously (or during the relaxation of the SFM cantilever), a second peak occurred such as observed in the right histogram with bimodal fit. A troublesome example is shown in the center. Here both distributions overlapped and the fit was shifted to a higher most probable rupture force *f**. Thus it was important to minimize the detection of simultaneous bond rupture events and to separate the remaining signals from simultaneous bond rupture by further data processing.

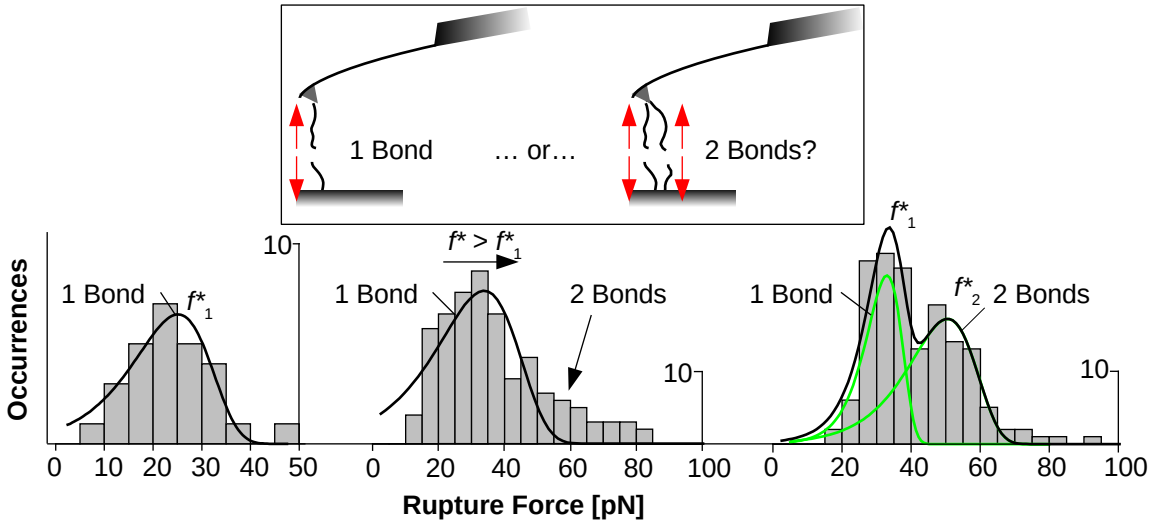

Figure 48: A pure single-molecular rupture process that follows the KBE model, shows a distribution with lower slope below and slightly higher slope above *f** (fronting, shown on the left side). Such a behavior is well represented by the probability distribution of rupture forces according to equation 96. A mixture of rupture events from 1 and 2 bonds may yield a tailing (shown in the center) or a bimodal rupture force histogram (shown on the right side). Examples are (from left to right) **2c**$_2$–Cu^{2+} at 1, 10, and 3 µm/s.

The most efficient method of separating single-molecular interactions from simultaneous bond rupture events is the introduction of spacer molecules (tethers) with well known force-extension profile into the tethered backbone as internal standard. For example, Horejs et al. applied the *I27* domain of the muscle protein titin[94] to identify single-molecular rupture events in the unfolding of a surface layer protein. As shown in figure 49 the protein of interest was flanked by five *I27* domains in a row, each with an unfolding force of approximately 200 pN. The surface layer protein had a mechanical stability of up to 100 pN and broke in advance, resulting in force-distance curves including signals of the unknown protein (sketched in red) and the well known sequence of five *I27* unfolding events (sketched in black).[148] Pratt et al. from NIST suggest using the characteristic melting transition of ds-DNA at 65 pN

(when one end is dangling). [98].[149] This approach is sketched on the right side of figure 49. Here, the protein of interest is covalently linked to ds-DNA. The measured force-distance curve includes the melting transition plateau (sketched in black) and the protein refolding signal (sketched in red) instead of the detachment peak. In both approaches, one receives rupture force histograms of single-molecular events that perfectly match the probability distribution as expected by the KBE model.[236,237]

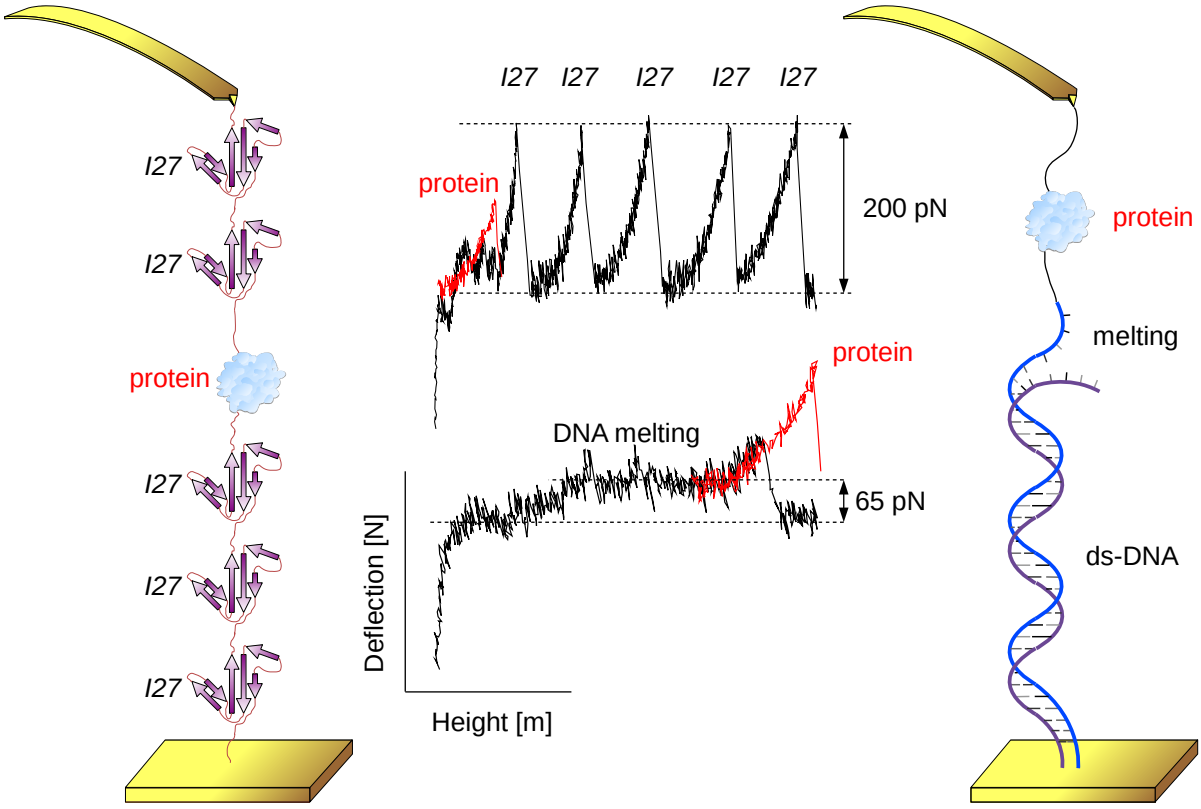

Figure 49: The reference molecule method exploits well studied processes such as refolding of the domain *I27* from the muscle protein titin[94] (left) or the melting of ds-DNA, which is fixed at three ends[98] (right). The molecule of interest, for example a protein, is bound in a row. The resulting force-distance diagrams include the well known fingerprint signals (black) and additionally the unknown protein signal (red sawtooth). (The plotted fd curves of *I27* and ds-DNA have been measured by our ForceRobot 200 system as test samples)

The drawback of protein unfolding or ds-DNA melting is the strong dependence on solvent conditions such as added salts or pH value. Our experiments with metal ions would have changed the fingerprint signatures. Additionally, the internal standard needs to be an innocent spectator, which was questionable with respect to the pyridine moieties used throughout this thesis. Especially the aromatic π-system of pyridine may interact with hydrophobic protein sequences or the nucleobases of ds-DNA. Thus we utilized poly-ethylene glycol (PEG) as tether, which is hydrophilic, also exhibits well characterized mechanical properties (chapter 2.4.3) and is frequently

used in SMFS.[165] In aqueous solvents, the surrounding network of hydrogen bound water molecules leads to a characteristic stretching behavior.[178] As sketched in figure 50 a, the slope in the intermediate regime between 50 and 300 pN is larger if two PEG tethers are pulled simultaneously. If the molecule of interest exhibits sufficiently large rupture forces, this property facilitates the detection of single-molecular rupture events.[238]

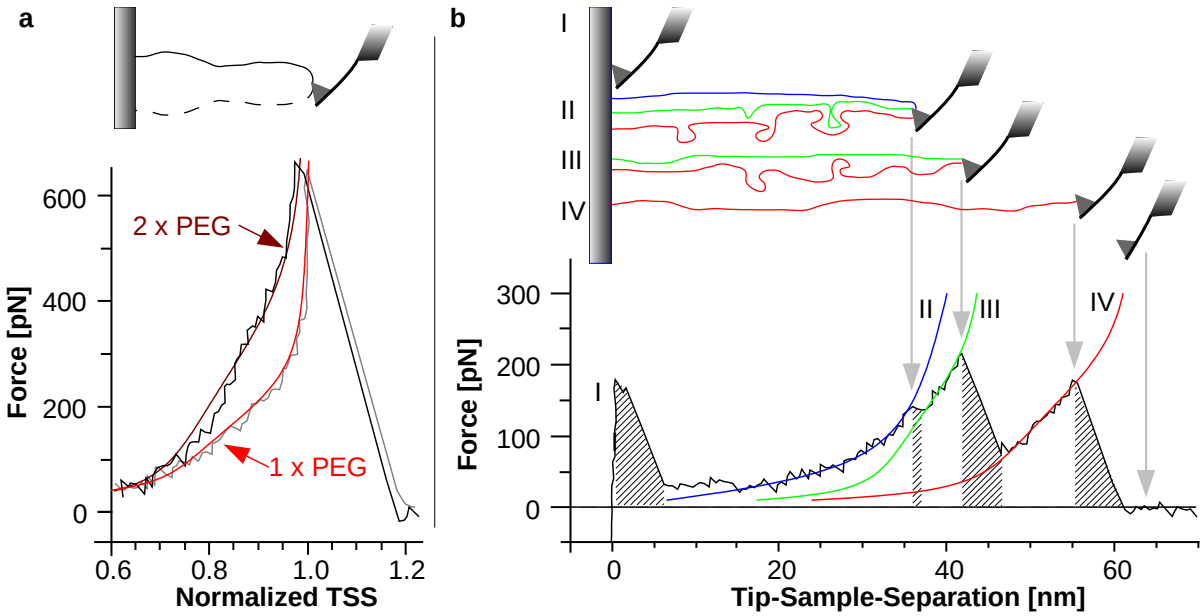

Figure 50: Force-*tss* diagrams of PEG a) The stretching behavior of two simultaneously pulled PEG tethers shows a different slope in the intermediate regime between 50 and 300 pN when compared to the single-tether experiment. 2-state FJC model fits using parameters from[93] yield n_2 = 1.92 ± 0.05 and n_1 = 1.02 ± 0.02. Thereby *f* in equation 80 was exchanged by *f*/*n*, yielding the number *n* of simultaneously pulled tethers. b) Stepwise bond rupture can be detected by separate peaks in the force-distance diagram (I – tip-sample-interaction, II – first rupture event, III – second rupture event, IV – last rupture event). Dashed areas are blind for possible simultaneous bond rupture. Continuous lines show 2-state FJC model fits yielding: N_{sII} = 144.7 ± 1.8, N_{sIII} = 124.1 ± 1.7, N_{sIV} = 171.1 ± 4.3, n_{II} = 3.5 ± 0.1, n_{III} = 1.0 ± 0.6, n_{IV} = 0.9 ± 0.1 (*N* represents the number of monomers in the PEG chain).

Additionally PEG and tethers in general allow separation of simultaneous rupture events using the stretching length, corrected for cantilever bending (tip-sample-separation, *tss*). This technique was introduced by Hinterdorfer et al. in 1996 and is now state-of-the-art in SMFS.[65,239] The rupture of one bond leads to a rapid relaxation of the SFM cantilever. As sketched in figure 50 b, this process leads to separable peaks in the force-*tss* diagram. Only the last peak is not influenced by other, simultaneously pulled polymers and selected for further analysis (last-peak method).[27] Some simultaneous rupture events remain hidden, when two tethers

break almost instantaneously (within the dashed ares of figure 50 b). Thus we still received the mixed rupture force histograms such as shown in figure 48 above. Consequently we aimed to improve separation of simultaneous rupture events on this level of data analysis as well.

According to the KBE model (equation 96), a non-symmetric distribution is expected. It exhibits a moderate increase at low forces, but a sharp drop beyond *f** (fronting). This shape is independent of a possible non-linear loading rate behavior[185] or polydispersity of the polymer[189]. A common method to analyze *p*(*f*) distributions are Gaussian fits, because they directly deliver *f** and its standard error as fit parameter. However when applied to a set of ideal distributions with fronting, Gaussian fits yield too low *f** and overestimate the thermal off-rates.[190] Within the scope of this thesis we introduced a new fit equation, which is a simplified representation of equation 96. Equation 113 directly yields *f** as fit parameter such as the Gaussian fit model, but represents the theoretical distribution more accurate. ω is a measure of peak with and *C* a scaling factor.

$$p(F) = C \exp\left[\frac{F - f^*}{\omega} - \exp\left(\frac{F - f^*}{\omega}\right)\right] \tag{113}$$

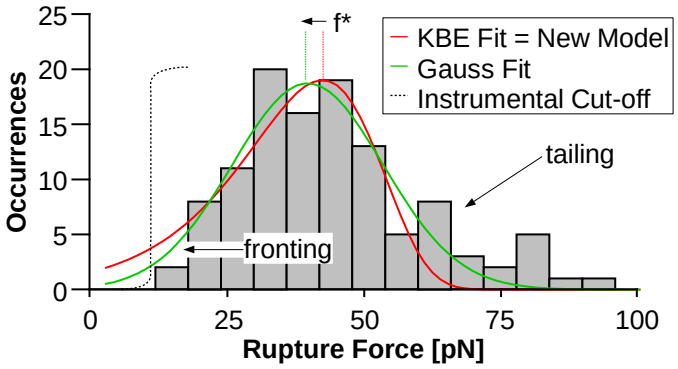

Figure 51: The new fit model equation 113 (red) is a simplified form of the KBE distribution (equation 96), thus both red fits overlap. The Gaussian fit delivers an *f** that is slightly lower.

Noteworthy, in the literature there are various other sources of the tailing effect discussed such as multiple energy barriers,[193] an asymmetric shape of the energy barrier,[198] fluctuations of the rupture length Δ*x*,[179] or simply artifacts from data processing.[240] However the rupture force histograms of our pyridine coordination compounds frequently showed distinct separate peaks, which cannot be explained by the alternative models mentioned above. Distinct separate peaks may originate from simultaneous rupture events and other types of interactions, which will be

discussed in detail below. In both cases, the multi-peak fit using equation 113 in order to receive the most probable rupture force *f** is reasonable.

In repeated experiments on the same type of molecule, a combination of the last-peak method and multi-peak fit gave reproducible results. The slope in the intermediate stretching regime of PEG was not generally applicable, because the average rupture forces of our pyridines were too low.

4.1.3. The Double Tether Approach

Polymeric tethers are not only useful for the detection of single-molecular rupture events. They also help to separate possible side interactions such as between the pyridine moieties and gold surface due to defects in the coating of SFM cantilever probes and surfaces. The methodology is called double-tether approach. As sketched in figure 52a, interaction partners (gray circles) are attached to the ends of heterobifunctional polymers with a known number of repeat units (N_s) or contour length, respectively. During the retract in a force-distance cycle, rupture events are expected around tip-sample-separations of two repeat units of the polymer (red segment in figure 52b). Possible unspecific interactions with non-modified parts of surface or cantilever tip occur in the single-tether region (gray segment in figure 52b).

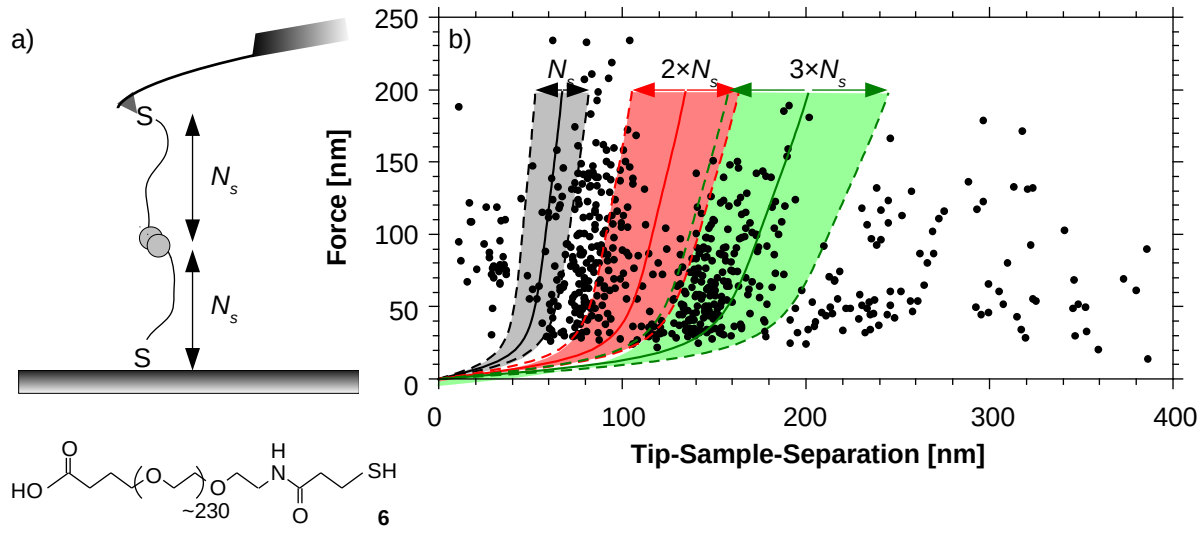

Figure 52: The double tether approach makes use of two polymeric spacers with known number of segments N_s. a) Sample molecules (gray circles) were coupled to the SFM cantilever and surface using a tether of N_s segments, each. b) Rupture of PEG polymer **6** were expected to follow the 2-state FJC model (equation 80) for $2 \times N_s$ (red) in the force-*tss* diagram, where $N_s = 230$. Filled regions represent the standard deviation of **6** (PDI = 1.05). Here, the accumulation was shifted to lower tss, but still measured right to the gray region. Additionally, lots of rupture events were detected at $3 \times N_s$ (green).

The force−*tss* diagram in figure 52b was recorded using the PEG polymer **6**, just as received from the supplier. Its thiol group was used to modify gold coated cantilever probes and surfaces. The SMFS experiment was performed in 3 mM aqueous $FeSO_4$ to measure the coordination of COOH to Fe^{2+}.[241,242] As expected, the first accumulation of rupture events occurred to the right of the single-tether region (gray). It was slightly below the double-tether region (red), probably due to a worn SFM tip and the rough gold surface. Surprisingly, a second cluster was detected in the green section, representing three polymers of N_s in a row and even some rupture events with at *tss* beyond $3\times N_s$. Only rupture events with sawtooth-like signals had been analyzed, which are characteristic for polymeric tethers. This indicates that, either the raw materials contained polymers of twice the length, or some side reaction had occurred during the process of sample preparation. Unprotected thiol groups are prone oxidative dimerization when exposed to air. Dimerized thiols still bind to gold surfaces,[243] but have twice the length when attaching with their other end-group to the gold surface. This type of interaction is well possible for pyridines,[244,245] but puzzling for carboxylic acids such as in polymer **6**, for which such an interaction was only reported at high electric potentials or oxidized surfaces of noble metals.[246] It is also possible, that the elongated polymers are byproducts of the synthesis. Purification of soluble polymers is frequently done by dialysis, only separating low molecular weight byproducts. When one elongated polymer in SMFS is sufficient to yield lots of rupture events beyond $2\times N_s$. Attempts to gain further information on the elongated polymers using MALDI-TOF failed.

In any case, the presence of a tether with twice the contour length enables unspecific interactions with defects in the coating of surface or cantilever that are supposed to be excluded by the double tether approach. Thus we generally performed a full analysis of all segments by DFS to detect such interactions by their different mechanical stabilities in the dynamic force spectra. In figure 53, the corresponding rupture events (a), four exemplary rupture force histograms (b) and dynamic force spectra (c) are shown exemplary for one experiment with **1** in 3 mM $CuSO_4$.

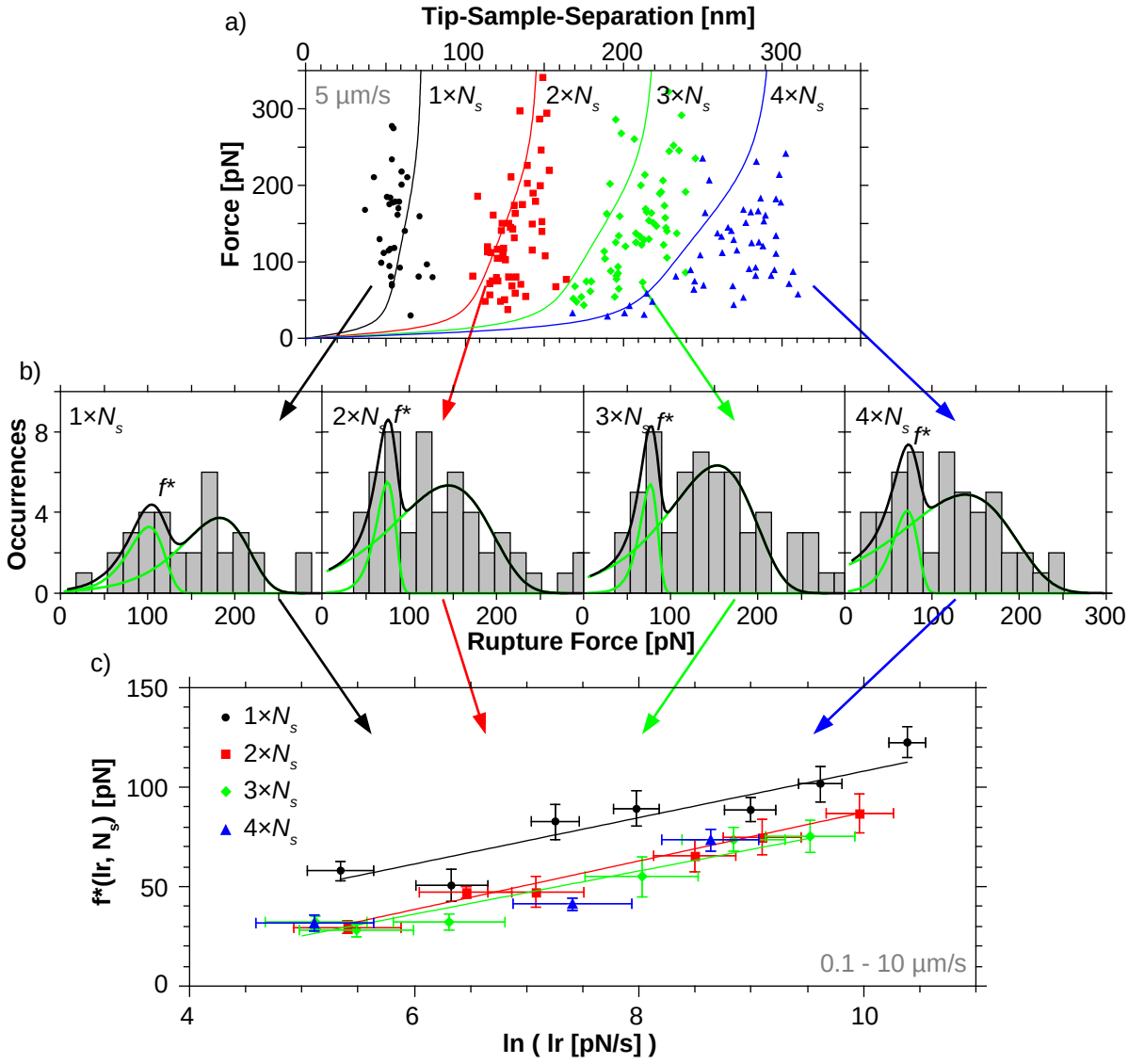

Figure 53: The double tether approach shown in figure 52 applied to **1** in 3 mM $CuSO_4$. a) The rupture points at a pulling speed of 5 µm/s accumulated as expected by the 2-state FJC model (equation 80, continuous lines) with 1−4 times the number of repeat units N_s in a single PEG tether. b) The corresponding histograms of rupture forces were fitted by bimodal probability distributions (equation 113) for 1-4×N_s. c) Dynamic force spectra including most probable rupture forces *f** gathered at 7 different pulling velocities (0.1, 0.3 0.5, 1.0, 3.0, 5.0, and 10.0 µm/s) for 1, 2, 3, and 4 N_s. Some data points are missing due to insufficient rupture events for histogram analysis. Linear regression parameters are ($y = Ax + B$): A_1 = 11.6 ± 1.5 pN, B_1 = -8.5 ± 11.5 pN, A_2 = 12.2 ± 1.6 pN, B_2 = -34.8 ± 10.3 pN, A_3 = 10.8 ± 1.3 pN, B_3 = -28.9 ± 8.1 pN, for segments 1, 2, and 3 respectively.

As shown in a), rupture events of $\mathbf{1}_2$−Cu^{2+} at 5 µm/s accumulated around 1-4×N_s, such as observed for the unmodified polymer **6**. In contrast to figure 52b, the second segment (2×N_s) marked in red followed the expected 2-state FJC model much better and we could also analyze the rupture events at 4×N_s marked in blue. All four segments at 5 µm/s were binned into histograms (b), yielding similar fits of bimodal

probability distributions. The corresponding dynamic force spectra (c) using data at all 7 pulling speeds were similar for 2 and 3×N_s. In contrast the dynamic force spectrum (DFS) of 1×N_s was significantly different and not reproducible in additional experiments. This means, that besides the polymers of twice the length, the double tether approach was useful to separate unspecific rupture events in the first segment from the reproducible interactions in all other segments. The other segments may still have contained some unspecific interactions as well, but with lower ratio to the specific signals. This also means that the polymer of twice the expected contour length had a terminal pyridine. According to the dimerized sulfur model, we suggest the following model of all four segments:

- 1×N_s: Au ⋯ Py−PEG−S−Au (unspecific)
- 2×N_s: Au−S−PEG−Py ⋯ Cu^{2+} ⋯ Py−PEG−S−Au
- 3×N_s: Au−S−PEG−Py ⋯ Cu^{2+} ⋯ Py−PEG−SS−PEG−Py−Au
- 4×N_s: Au−Py−PEG−SS−PEG−Py ⋯ Cu^{2+} ⋯ Py−PEG−SS−PEG−Py−Au

4.2. Single-Molecule Force Spectroscopy

In the previous chapter, we have identified single-molecular interactions. Now we will discuss the results of blank measurements on pyridines **1**, and **2a** - **2c** in deionized water. Surprisingly all four systems $\mathbf{1}_2$−H_2O, $\mathbf{2a}_2$−H_2O, $\mathbf{2b}_2$−H_2O, and $\mathbf{2c}_2$−H_2O showed specific interactions. We will propose the model of an antiparallel stacking interaction including the aqueous solvent (chapter 4.2.1). Afterwards we will present results of SMFS in aqueous solutions of $Zn(NO_3)_2$ and $CuSO_4$. The mechanical stability of both interactions $\mathbf{1}_2$−Zn^{2+} and $\mathbf{2a}_2$−Zn^{2+} was different than in pure water. However the mono- and bivalent system showed identical behavior indicating a monovalent binding for $\mathbf{2a}_2$−Zn^{2+}. With the stronger complexing metal ion, we received specific interactions $\mathbf{1}_2$−Cu^{2+}, $\mathbf{2a}_2$−Cu^{2+}, $\mathbf{2b}_2$−Cu^{2+}, and $\mathbf{2c}_2$−Cu^{2+} that were different from the blank measurements and different from each other. The equivalent trivalent system $\mathbf{7}_2$−Cu^{2+} did not form, but $\mathbf{7}_2$−H_2O instead (chapter 4.2.2). Most of the recorded rupture force histograms showed a pronounced second peak. This may be due to simultaneous bond rupture events or an additional conformation of the metal complex (chapter 4.2.3). Finally we discuss possible consequences of tilted pulling. Measured and applied force coincide in a symmetric interaction such as $\mathbf{2c}_2$−Cu^{2+}, but not in $\mathbf{1}_2$−Cu^{2+}, $\mathbf{2a}_2$−Cu^{2+}, $\mathbf{2b}_2$−Cu^{2+}. As a consequence, the effective rupture lengths Δx may be larger in those systems. We will show, that the trend between all four systems still does not change (chapter 4.2.4).

4.2.1. Metal Free Pyridine Interactions

As reference experiments, we studied the interactions of all pyridines in pure water without additional metal ions. Although neutral charged pyridine, as well as 2-, 3-, and 4-methylpyridine are fully miscible with water,[247] the molecules analyzed in this study showed reproducible rupture forces, thus specific interactions. In figure 54, dynamic force spectra of mono-pyridine **1** are shown. The smaller (black) and larger f^* (red) peaks in the rupture force histograms were analyzed separately, yielding $\Delta x_1 = 0.75 \pm 0.07$ nm, $k_{off1} = 0.20 \pm 0.10$ s^{-1} and $\Delta x_2 = 0.44 \pm 0.02$ nm, $k_{off2} = 0.15 \pm 0.05$ s^{-1}. As discussed in the previous chapter, the interaction with larger f^* may also be due to simultaneous rupture events as long as $f^*_2 \leq 2 \times f^*_1$ for similar loading rates. Also the similar thermal off-rate constants indicate a simultaneous bond rupture, as they are characterized by the loading rate at $f^*_2 = f^*_1 = 0$ pN. Thus in the following, only the interactions with lowest rupture forces will be discussed.

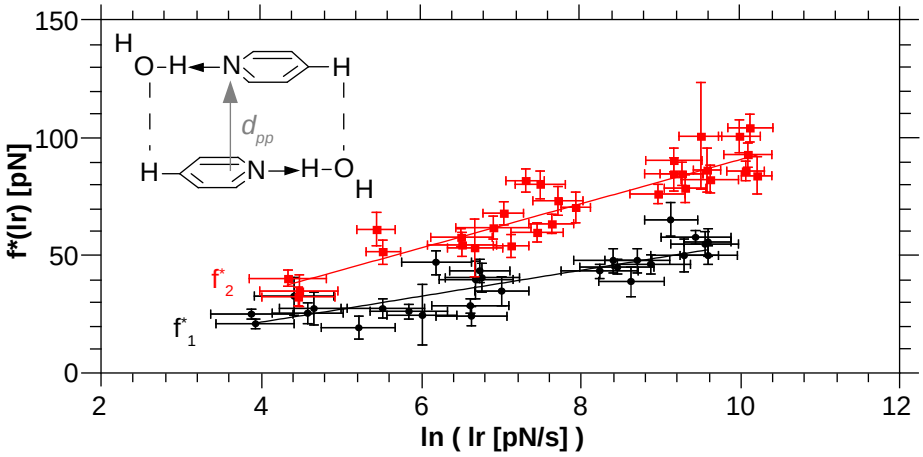

Figure 54: Dynamic force spectra of monovalent pyridine **1** (modified SFM tip and surface) in pure Milli-Q H_2O. Rupture force histograms were fitted by a bimodal distribution, yielding most probable rupture forces f^*_1 and f^*_2. The chemical structure of a possible anti-parallel aligned stacking interaction with a stacking distance of d_{pp} = 0.33 nm is shown, as suggested by *ab-inito* calculations.[248]

Which type of interaction could explain such a malleable metal free interaction? Pyridines are able to interact in-plane by their lone pair σ orbital or in perpendicular orientation by their π-orbital.[249] Pyridine and 4-methylpyridine could be crystallized as trihydrates, where the nitrogen forms a σ-type hydrogen bond to one water molecule and the rings are stacked in anti-parallel sheets with an offset.[250,251] DFT calculations indicate that the nitrogen atom is an approximately 30 % stronger acceptor of protons than the oxygen atom in water (H_2O−H_2O: 19.93 kJ/mol, pyridine−H_2O: 26.21 kJ/mol).[252] Thus it is reasonable to assume a σ-type hydrogen bond to water as well in our experiments. According to *ab-initio* studies, their stacking interaction is 60 % stronger than the similar interaction of non-coordinated pyridines (with σ-water: 28.72 kJ/mol, without water: 17.08 kJ/mol). The optimal geometry is slipped with additional binding energy through the coordinated water, such as shown in figure 54.[248] Their the average vertical distance is 0.33 nm, indicating a flat potential energy surface that may yield the calculated rupture length of 0.79 nm after a stepwise rupture of both hydrogen bonds.[253] Thus we suggest such a type of interaction detected in pure water with **1**.

All reference experiments on pyridines performed throughout this thesis are summarized in table 6. Interestingly, the behavior of pyridine nanorod **2a** was identical to the monovalent system **1**. As sketched in figure 55, a simultaneous anti-parallel stacking of both pyridine moieties in **2a** is sterically possible. However some steric or entropic constraints may disfavor this type of interaction, for example due to the planar arrangement of both pyridines. This assumption is supported by the

measurements on metal complexes discussed below. The stronger metal center Cu^{2+} was able to form a bivalent complex with **2a**, but not Zn^{2+}. $\mathbf{2b}_2$ and $\mathbf{2c}_2$ showed shorter rupture lengths, but similar or higher thermal off-rate constants. A stacking of both pyridine moieties would have decreased the rate constants. Thus a different monovalent type of interaction was probed, each. In contrast to **1** and **2a**, their pyridine rings are not substituted by an alkine, but by saturated groups. Therefore the different rupture lengths are not surprising. In addition as sketched in figure 55, complex $\mathbf{2c}_2$ is not able to stabilize by additional water coordination due to substitution in para-position to the nitrogen. The yielding complex is thermally less stable such as expected for a pure stacking interaction.

Table 6: Rupture lengths and thermal off-rate constants of reference experiments in pure water without additional metal ions.

	Δx_1 [nm]	k_{off1} [s^{-1}]
$\mathbf{1}_2$–H_2O	0.75 ± 0.07	0.20 ± 0.10
$\mathbf{2a}_2$–H_2O	0.79 ± 0.12	0.26 ± 0.31
$\mathbf{2b}_2$–H_2O	0.38 ± 0.03	0.33 ± 0.13
$\mathbf{2c}_2$–H_2O	0.47 ± 0.02	0.61 ± 0.12

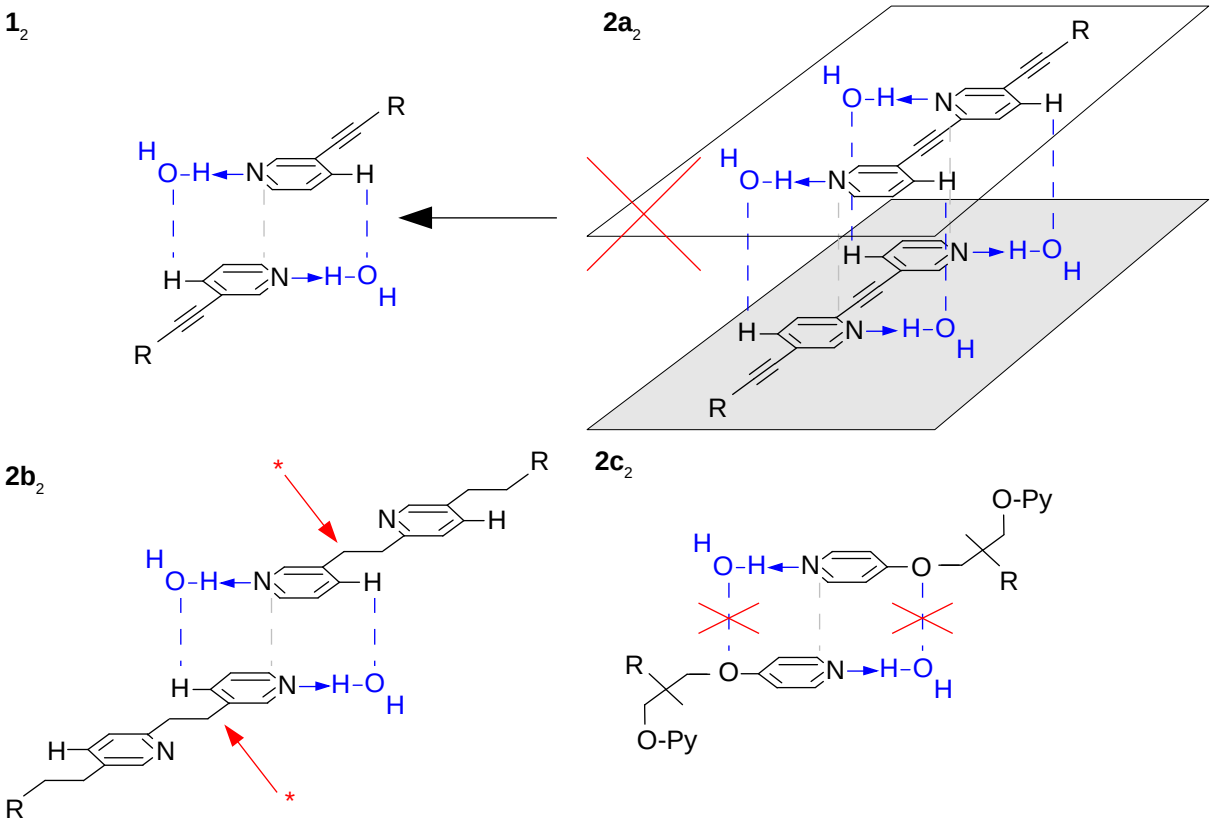

Figure 55: The water-mediated stacking interaction, proposed for the monovalent interaction $\mathbf{1}_2$ is sterically possible for the bivalent system $\mathbf{2a}_2$ as well. However the monovalent type of interaction was

measured. The proposed monovalent interaction **2b**$_2$ had a different rupture length due to the missing alkine substituents (marked by *). In system **2c**$_2$, the stabilizing hydrogen bonds are not possible, increasing its thermal off-rate constant. KBE fit parameters Δx and k_{off} are collected in table 6.

This metal free interaction turned out to be a competitive interaction in measurements with metal ions Zn^{2+} and Cu^{2+} discussed below. Careful analysis was necessary to separate those signals from the data. Figure 56a shows the rupture force histogram of **1** in 3 mM aqueous $CuSO_4$ solution at 10000 nm/s pulling speed. It was possible to fit the data by a trimodal distribution (red). Additionally the force distribution using results from the blank interaction were included (black line). Obviously the first peak was not due to the intended coordination interaction with Cu^{2+} (py−Cu^{2+}−py), but the stacking (py−π−py). In figure 56b, data from the same experiment at 1000 nm/s is shown. In contrast to figure 56a, a trimodal fit did not converge. Assuming the same ratio between py−Cu^{2+}−py and py−π−py, only a small bulge adds to the overall plot (marked by *), not influencing the most probable rupture force. In general, the ratio of stacking interactions was varying, sometimes being absent, sometimes even appearing in a 1:1 ratio with the metal complex (figure 56c). The complexes of **2c** were only measurable by increasing the concentration of $CuSO_4$ to 30 mM, thereby shifting this ratio in favor of the metal complex.

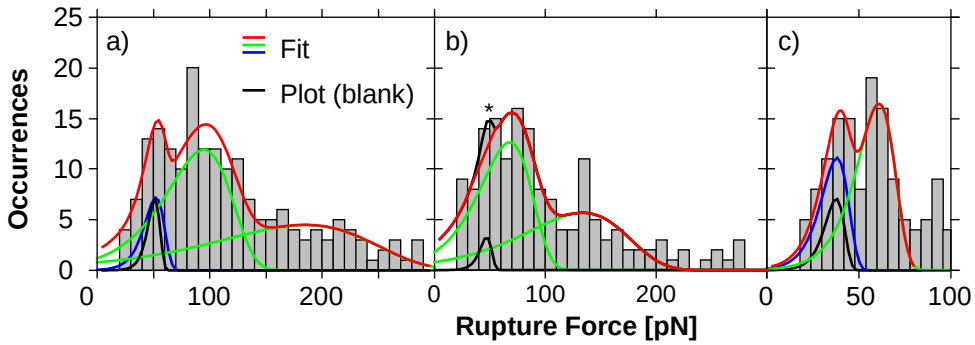

Figure 56: Examples of rupture force histograms containing events from the metal free (blank) interaction. Black lines show expected probability distributions according to equation 96 using Δx = 0.79 nm and k_{off} = 0.2 s^{-1}. a) **1** in 3 mM $CuSO_4$, measured at 10000 nm/s showed a trimodal distribution. The location of the first peak was expected from the metal free interaction. b) **1** in 3 mM $CuSO_4$, measured at 1000 nm/s with the expected metal free signal according to the ratio in a. c) **1** in 3 mM $Zn(NO_3)_2$, measured at 1000 nm/s. The first peak was similar to the metal free interaction, the second due to the metal complex. Here, the height of the black plot was reduced for clarity.

4.2.2. Pyridine Complexes with Zn^{2+} and Cu^{2+}

Having characterized the interactions in pure water, we were able to differentiate between the antiparallel stacking and metal complex interactions: If the analyzed

dynamic force spectra (or fit parameters Δx and k_{off}(0 pN)) were significantly different from those discussed in the previous chapter, a different type of interaction had been probed. For example in figure 57, a measurement on monovalent pyridine **1** in 3 mM $CuSO_4$ is shown. Afterwards the fluid cell was rinsed with pure water and filled with 10 mM Na_2EDTA to remove remaining Cu^{2+}. The repeated experiment using the same SFM cantilever probe on the same surface is shown in red. Without added metal ions, significantly lower rupture forces were measured (green arrows). For comparison, the blue continuous line in b) shows the averaged result of $\mathbf{1}_2$−H_2O (see also figure 54). Indeed, the measurement on **1** in 3 mM $CuSO_4$ did not probe the antiparallel stacking interaction, but in EDTA this behavior was recovered. This example was a rare case, where the cantilever had not been worn off over the course of one measurement with typically several thousand force-distance measurements, thus such a reference experiment with two consecutive experiments was not applicable in general.

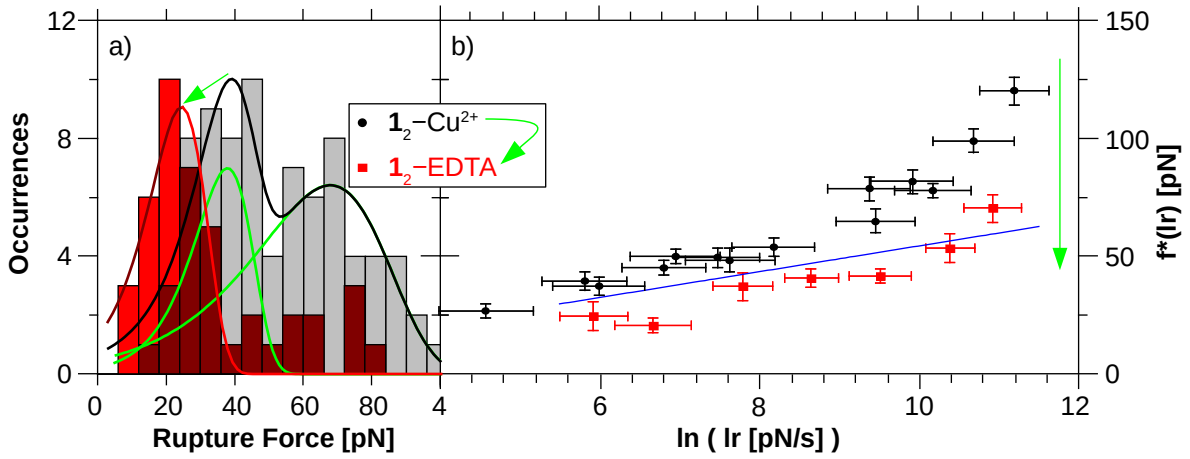

Figure 57: In this reference experiment, two dynamic force spectra were recorded in 3 mM $CuSO_4$ (gray histogram bars and black circles) and afterwards a third one in 10 mM Na_2EDTA to remove the Cu^{2+} (red histogram bars and squares). a) Exemplary rupture force histograms corresponding to a loading rate of exp(6). b) Dynamic force spectra, the continuous blue line shows the fit $\mathbf{1}_2$−H_2O.

First, we measured pyridines **1** and **2a** in 3 mM $FeSO_4$, but did not receive reproducible results due to the high oxidizability of Fe^{2+}. Pyridine complexes of Fe^{3+} are thermally less stable than those with Fe^{2+},[254] probably changing also the measured mechanical stability over the course of the measurements (typically more than 24 hours). Thus we took advantage of the variability in our model systems and switched to Zn^{2+}, another essential trace element in biological systems. In 3 mM $Zn(NO_3)_2$ solvents, we gained reproducible results that were different from those measured in pure water. In figure 58, both dynamic force spectra are shown in a

joined diagram. KBE fits yielded $\Delta x(\mathbf{1}_2{-}Zn^{2+}) = 0.35 \pm 0.02$ nm, $k_{off}(\mathbf{1}_2{-}Zn^{2+}) = 1.8 \pm 0.3\ s^{-1}$, $\Delta x(\mathbf{2a}_2{-}Zn^{2+}) = 0.30 \pm 0.01$ nm, and $k_{off}(\mathbf{2a}_2{-}Zn^{2+}) = 2.4 \pm 0.3\ s^{-1}$. Although rupture lengths were slightly different according to the standard deviations, both spectra made clear that the overall differences of the measured data were rather small. This indicated that the interactions of **1** and **2a** were similar, which could be explained by **2a** exhibiting the same type of interactions as **1**. For example, only the terminal pyridine units in both complexing ligands may have coordinated to Zn^{2+}, forming a monovalent interaction.

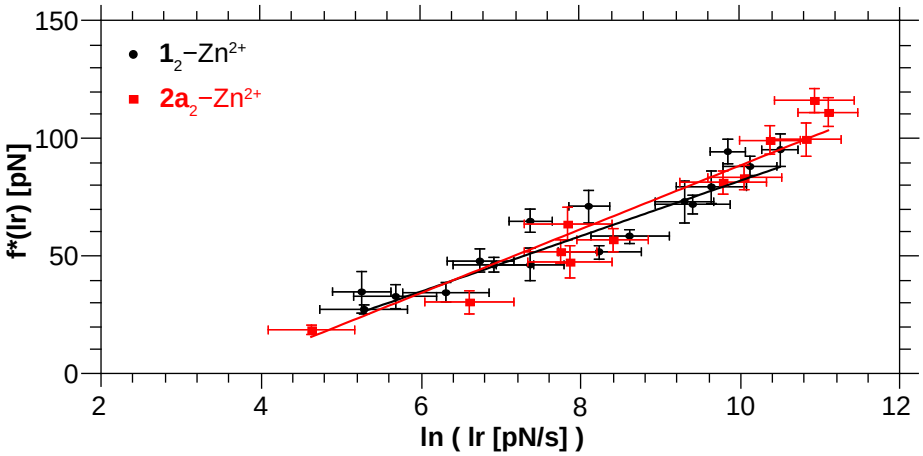

Figure 58: Dynamic force spectra for monovalent pyridine **1** (black circles) and bivalent nanorod **2a** (red squares) in 3 mM $Zn(NO_3)_2$. Continuous lines are the corresponding KBE model fits.

Our goal was to characterize rupture processes of bivalent systems. According to the Irving-Williams-Series, Cu^{2+} is forming complexes of higher thermal stability than Zn^{2+}[60–62] and was a promising candidate for bivalent coordination of **2a**. In figure 59, the corresponding dynamic force spectra for **1** and **2a** in 3 mM $CuSO_4$ are shown. Again the range of mechanical stabilities was similar in the measured range of loading rates. However, $\mathbf{2a}_2{-}Cu^{2+}$ showed a lower slope due to slightly larger forces in the slow-pulling and slightly lower forces in the fast-pulling regime. Consequently, the KBE model parameters were significantly different with: $\Delta x(\mathbf{1}_2{-}Cu^{2+}) = 0.33 \pm 0.01$ nm, $k_{off}(\mathbf{1}_2{-}Cu^{2+}) = 1.7 \pm 0.2\ s^{-1}$, and $\Delta x(\mathbf{2a}_2{-}Cu^{2+}) = 0.51 \pm 0.03$ nm, $k_{off}(\mathbf{2a}_2{-}Cu^{2+}) = 0.14 \pm 0.06\ s^{-1}$.

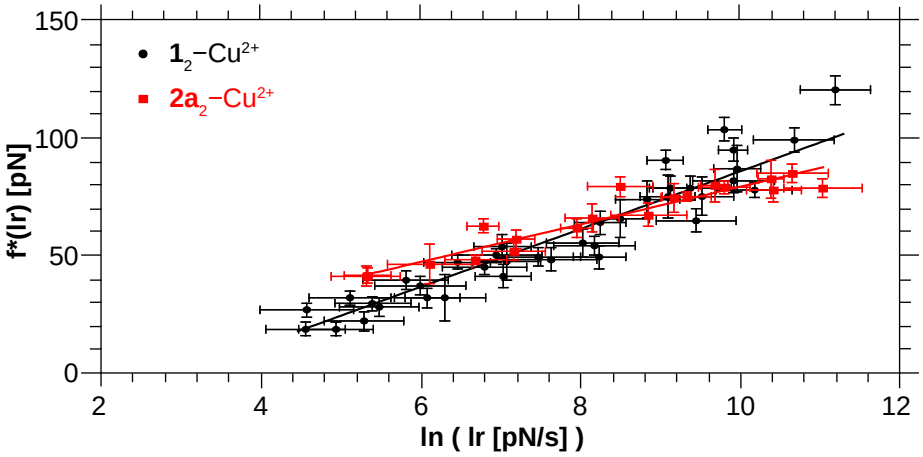

Figure 59: Dynamic force spectra of monovalent pyridine **1** (black circles) and bivalent nanorod **2a** (red squares) in 3 mM $CuSO_4$. Continuous lines are the corresponding KBE model fits.

This means, Cu^{2+} formed interactions with different malleability and thermal stability. We suggest, that the additional coordination energy was sufficient to outperform effects, that prevented bivalent complex formation with Zn^{2+}. For example, the rotation around the rigid triple-bond connection in **2a** is further restricted upon bivalent coordination, creating entropic cost.

Having found a metal ion with the ability of forming bivalent interactions, we also studied the pyridines **2b** and **2c** in aqueous solutions of $CuSO_4$. For **2c** in 3 mM $CuSO_4$ we received the DFS as measured in pure water, at 30 mM $CuSO_4$ **2c** showed a different behavior. The mechanical stabilities of both bivalent pyridines were much more different from $\mathbf{1}_2$−Cu^{2+} than those of $\mathbf{2a}_2$−Cu^{2+} shown above. As visualized in figure 60, $\mathbf{2b}_2$−Cu^{2+} showed higher f^* than $\mathbf{1}_2$−Cu^{2+} over the whole range of probed loading rates. There was no crossing of both linear fits due to a similar slope, yielding a similar rupture length Δx, but a lower thermal off-rate constant. $\mathbf{2c}_2$−Cu^{2+} showed surprisingly small f^* that were below the monovalent stabilities at loading rates of exp(5) and above. KBE model fit parameters were: $\Delta x(\mathbf{2b}_2\text{−}Cu^{2+}) = 0.30 \pm 0.01$ nm, $k_{off}(\mathbf{2b}_2\text{−}Cu^{2+}) = 0.36 \pm 0.07$ s^{-1}, $\Delta x(\mathbf{2c}_2\text{−}Cu^{2+}) = 1.12 \pm 0.07$ nm, and $k_{off}(\mathbf{2c}_2\text{−}Cu^{2+}) = 0.09 \pm 0.04$ s^{-1}.

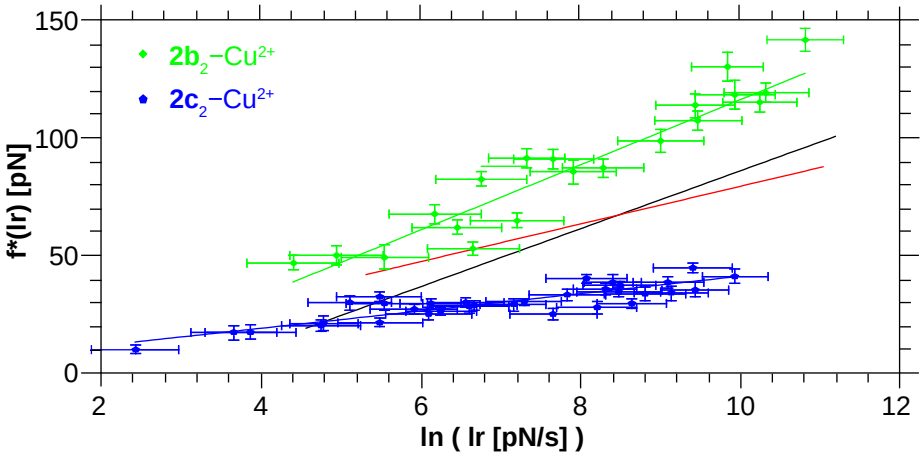

Figure 60: Dynamic force spectra of bivalent pyridines **2b** (green diamonds) in 3 mM and **2c** (blue octagons) in 30 mM $CuSO_4$ with corresponding KBE fits as continuous lines. For comparison, KBE fit lines for $\mathbf{2a}_2$−Cu^{2+} and $\mathbf{1}_2$−Cu^{2+} are added from figure 59. The plot of $\mathbf{2c}_2$−Cu^{2+} was shifted to lower loading rates due to the nonlinear stretching behavior of PEG in this force regime, yielding lower slopes in the force-*tss* plots (*lr* = slope × pulling speed).

Finally we measured dynamic force spectra of the trivalent pyridine **7** in 3 mM $CuSO_4$ and pure water. As shown in figure 61, $\mathbf{7}_2$−Cu^{2+} and $\mathbf{7}_2$−H_2O had the same mechanical stabilities. Probably the stacking interaction was favored over complex formation. This was corroborated by the extremely low solubility of the tri-pyridine without PEG spacer in most organic solvents except pyridine. KBE model fit parameters were: $\Delta x(\mathbf{7}_2\text{−}H_2O) = 0.26 \pm 0.02$ nm, $k_{off}(\mathbf{7}_2\text{−}H_2O) = 2.5 \pm 0.7\ s^{-1}$, $\Delta x(\mathbf{7}_2\text{−}Cu^{2+}) = 0.24 \pm 0.04$ nm, and $k_{off}(\mathbf{2c}_2\text{−}Cu^{2+}) = 1.1 \pm 1.0\ s^{-1}$.

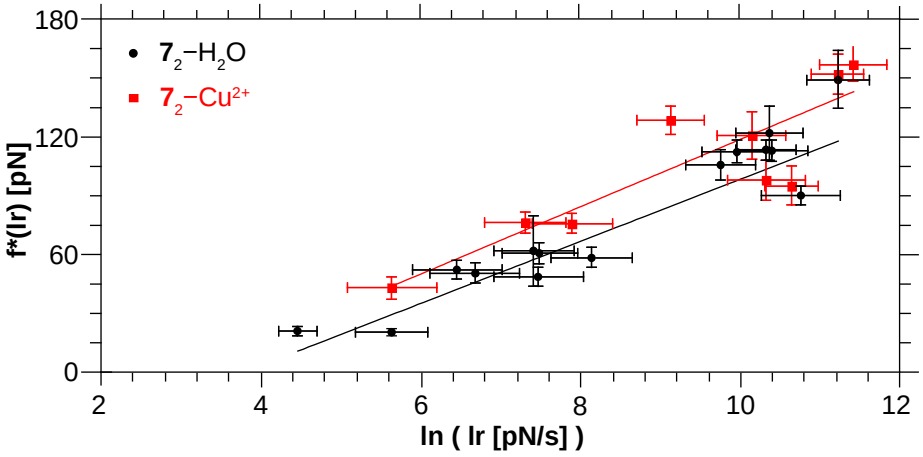

Figure 61: Dynamic force spectra of the trivalent pyridine **7** in pure water (black circles) and 3 mM $CuSO_4$ (red squares). Continuous lines show the corresponding KBE model fits.

In summary all three bivalent systems formed specific interactions with Cu^{2+} that were different from those in pure water and different among themselves. Their rupture force histograms frequently showed a distinct second maximum. As

mentioned in chapter 4.1.2 above, they may be due to simultaneous bond rupture events or a different type of interaction, for example cis- and trans-conformations. The latter would be of interest. In the following chapter we will apply a direct fit method to analyze the second maximum in detail.

4.2.3. Additional Conformations

A single force-distance cycle represents the initial bond and conformation that had been formed during the preceding contact between SFM cantilever tip and surface. Usually the most probably type of interaction dominates the rupture force histograms and thus the dynamic force spectra. However it is well possible, that two conformations exhibit similar probabilities of formation. For example both ligands, pyridine and water, only have a weak trans-effect. Thus the octahedral complex $[Cu(py)_2(H_2O)_4]^{2+}$ may form in cis- or trans-configuration. The corresponding rupture processes should have different malleabilities, if the cis-complex is able to undergo force-induced reconfiguration of its coordination sphere to the trans-configuration before bond breakage occurs.

The alternative origin of the second maximum is simultaneous bond rupture. Having identified the single-molecular rupture events, the distribution of the second maximum is expected within a certain range of forces. Thus we addressed the question of possible additional conformations by assuming simultaneous bond rupture. If the known models are not able to describe the full distribution properly, additional conformations may be discussed.

According to the Williams formalism, it is oversimplified to assume twice the force for simultaneous bond rupture compared to the single-molecular events. $F_{bi}(lr) = 2\ F_{single}(lr)$ overestimates F_{bi}. Both tethers may be stretched unevenly, yielding a different loading rate, each ($F_{bi}(lr_1,lr_2) = F_{single}(lr_1) + F_{single}(lr_2)$).[27,255,256] In the following we will use the adaptation of Akhremitchev et al.[192,257] They introduced an additional parameter δL_c, describing the contour length difference between two simultaneously pulled polymers with L_{c1} and L_{c2}:

$$\delta L_c = \frac{L_{c2} - L_{c1}}{L_{c1}} \tag{114}$$

The measured force of two simultaneously pulled polymers F_{bi} is the sum of both single-molecule forces F_1 and F_2. The *tss* of both tethers is identical, thus

$$tss_1(F_{1,}L_{c1}) = tss_2(F_{bi} - F_{1,}L_{c2}) = tss_2(F_{bi} - F_{1,}L_{c1}(1+\delta L_c)) \ . \tag{115}$$

Assuming some stretching model for polymers (for example FJC or WLC), equation 115 is able to predict the distribution of the measured force F_{bi} between both tethers (F_1 and F_2). The authors gave an analytical solution for the FJC model far above the thermal Kuhn force ($F_K = k_BT/l_k$). For PEG at room temperature F_K = 6 pN, which is well above the typical forces measured here. Considering $F_2 = F_{bi} - F_1$ and a FJC, F_1 is

$$F_1 = \frac{F_{\mathrm{bi}}}{2} + \frac{\sqrt{4F_k F_{\mathrm{bi}} \delta L_c + (F_{\mathrm{bi}} \delta L_c - F_k(2+\delta L_c))^2} - F_k(2+\delta L_c)}{2\delta L_c}. \qquad (116)$$

F_1 and F_2 may now utilized in equation 96 of the KBE model to predict the RFPD of both single-molecule events: $p(F_1)$,and $p(F_2)$. The corresponding distribution of simultaneously and parallel pulled tethers is

$$P(F_{bi}) = (1+2\delta L_c^{max}) s(F_{bi}/2) \frac{p(F_2) - p(F_1)}{F_1 - F_2}. \qquad (117)$$

Here, δL_c^{max} is the highest contour length difference, not detectable by additional peaks in the force-distance diagram. In the experiment, δL_c^{max} is due to the blind windows (dashed areas in figure 50). $\delta L_c^{max} = 0$ represents two polymers of identical contour length, where $F_{bi}(lr) = 2\,F_{single}(lr)$. In figure 62, equation 117 was used to exemplary fit all seven rupture force histograms of one $\mathbf{1}_2$-Cu^{2+} experiment simultaneously.

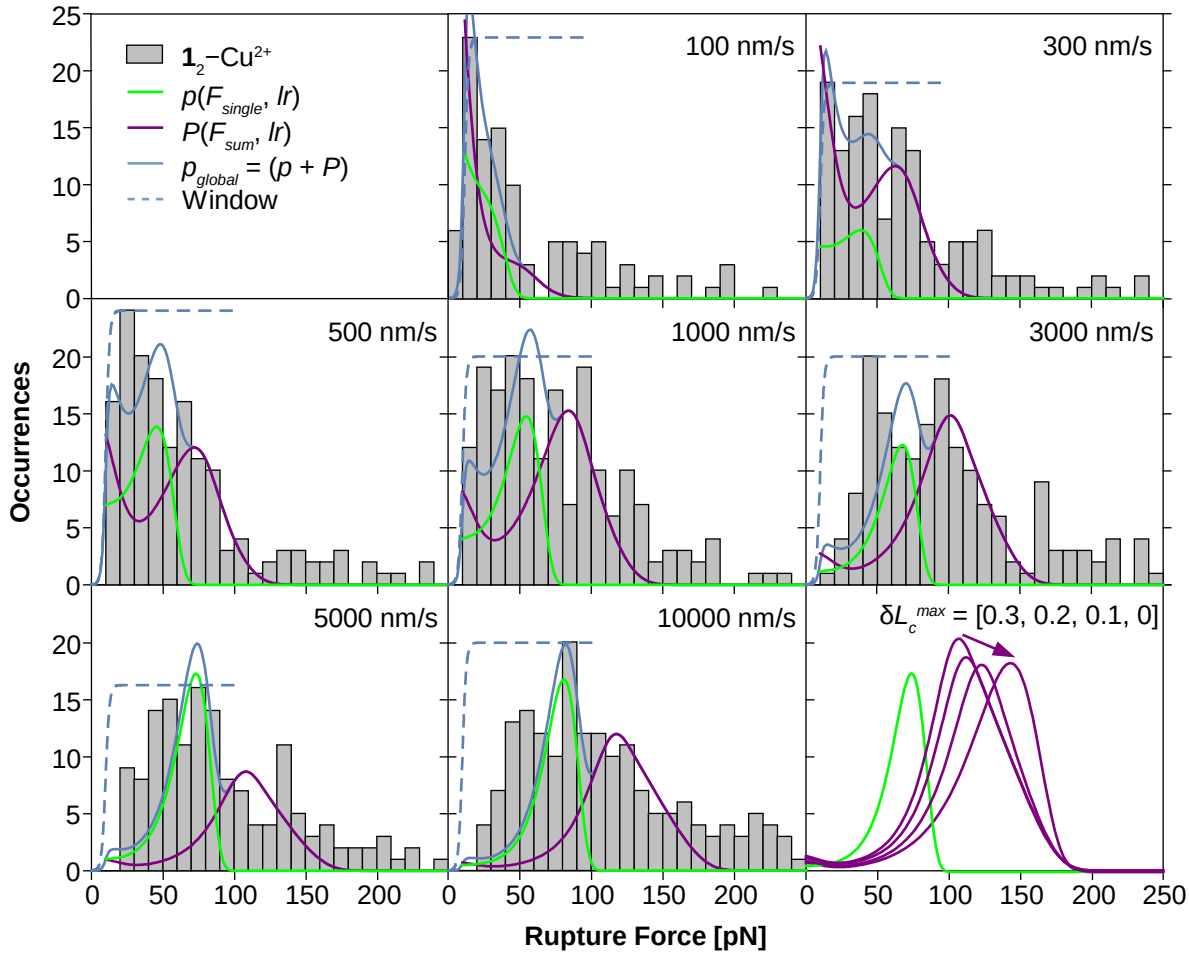

Figure 62: The direct fit method assuming a mixture of single-molecular rupture events (green) and simultaneous rupture of 2 bonds (purple) and the Williams formalism[27,255,256] was applied to rupture force histogram data from $\mathbf{1}_2$−Cu^{2+}. A window function (dashed line) takes into account that the thermal noise oscillation of the cantilever hides rupture forces below 10 pN. The contour length difference parameter δL_c^{max} influences the distribution of simultaneous bond rupture as shown in the lower right. Fit parameters are: $\Delta x = 0.41 \pm 0.03$ nm, $k_{off}(0) = 0.74 \pm 0.14$ s^{-1}, and $\delta L_c^{max} = 0.20 \pm 0.06$ (the 65% confidence errors were calculated by bootstrapping)[192,257]. The corresponding code for Wolfam Mathematica is given in the appendix chapter 6.3.

The model of simultaneous bond rupture described the high force tailing quite reasonable. At 1000 nm/s and above, it lacked in describing rupture events at lower forces. This was due to additional metal-free interactions, discussed in chapter 4.2.1 above. Noteworthy, at 500 nm/s and below the shape of $p(F_{single}, lr)$ and $p(F_{bi}, lr)$ differed much from the generic shape as shown in the lower right of the diagram. This was due to the underlying FJC model instead of the constant loading rate assumption made in the KBE model. At low pulling speeds the system has more time to break in the low extension regime before the tether begins to apply a relevant restoring force to the bond. The result is a high probability around the most probable

rupture force *f** and at low forces close to zero. Luckily the most probable rupture forces *f** did not change significantly for 500 nm/s and above, yielding the same behavior for f^*_{single} when the standard model was used.

Also in the other experiments, the second peak in the rupture force histograms matched the expected behavior of simultaneous bond rupture. Thus we received a mixture of single-molecular and simultaneous rupture events instead of an additional conformation. In the following discussions we will focus on the first maxima, representing f^*_{single}.

4.2.4. Tilted Pulling

Our model systems had been designed such, that their main difference was the pyridine connecting backbone. But also the angles between the coordination bonds (py−Cu^{2+}−py) and the applied forces were different. Only the force vector component in parallel to the rupture trajectory is transferred into the bond. In other words, there may be a difference between the amount of force measured by cantilever and the amount of force applied to the interaction. Thus we will now discuss, whether the different results for the first maxima in **2a**, **2b** and **2c** were due to different rupture mechanisms or an artifact of the tilted pulling.

On larger scales, tilted pulling is possible due to askew pulling of the spacer polymers. For example, the rupture force of 30 bp ds-DNA was measured to be strongly dependent on the pulling angle α, set by the SFM cantilever (figure 63). The highest rupture force was measured at vertical pulling, where $F_{measured}$ and $F_{applied}$ coincided. Tilted pulling reduced the measured force as a function of cos(α), just as expected from vector decomposition (eq. 118).[258]

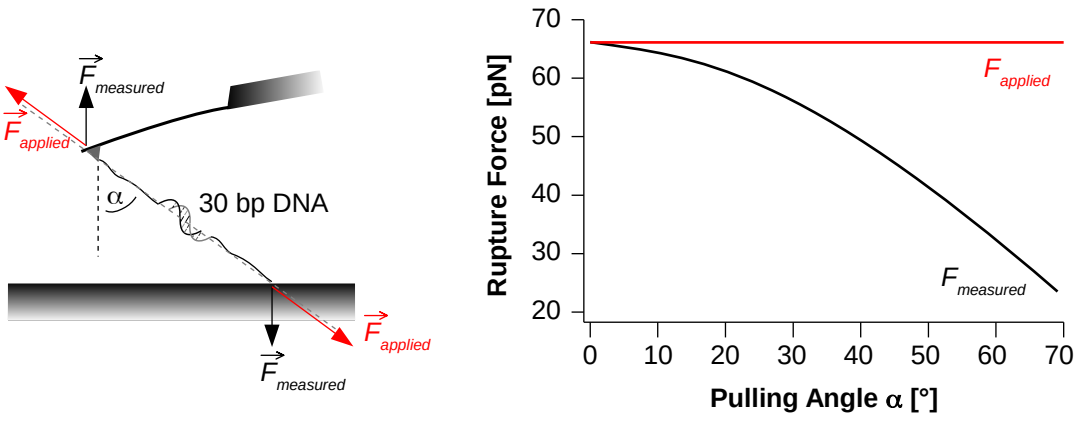

Figure 63: In the experiment, two ss-DNA strands of 30 base pairs (bp) are covalently attached to the SFM cantilever and surface. When both are brought in contact with each other, they dimerized to 30 bp

ds-DNA. When pulled at different angles from 0 to 70°, a the measured rupture force decreased in a cosine manner compared to the applied rupture force as sketched on the right.[258]

$$|\vec{F}_{measured}| = |\vec{F}_{applied}| \cos\alpha \tag{118}$$

In our setup, the situation sketched on the left side of figure 63 can be neglected due to the small radius of gyration of PEG in the relaxed (initial) state (R_g = 3.5 nm for a PEG with 20000 g/mol).[259] In a standard SMFS setup using this polymer, pulling is expected to be orthogonal to the sample surface.[260] However also the structure of interacting units themselves can lead to a vector decomposition. In figure 64, the systems analyzed in this thesis are sketched. The direction of measured force is given by the red points, where the flexible PEG tether is attached to the rigid molecules of interest. The tether reacts to the external force by reorientation, a fully rigid molecule and coordination bond not. Interaction **2c** is not sketched, because both coordination bonds and the connection between both attachment points are parallel to each other (α_{2c} = 0°). In contrast to equation 118, here the measure force is larger than the applied one yielding

$$|\vec{F}_{applied}| = |\vec{F}_{measured}| \cos\alpha \ . \tag{119}$$

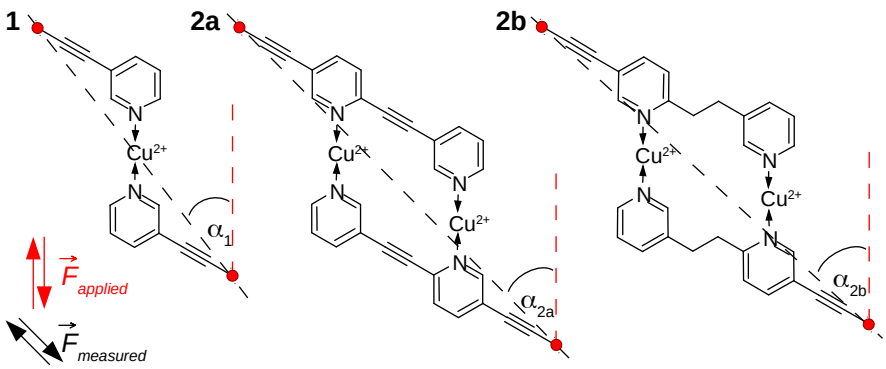

Figure 64: Estimated upper limits for tilt angles α_{max} between the direction of $F_{measured}$ (straight line between red points) and a possible orientation of $F_{applied}$ in a fully rigid system, using standard bond angles and equal bond lengths. Only the coordination bonds to the metal center are longer by a factor of 1.3 as estimated from single-crystal X-ray data between pyridine and Cu^{2+} (0.20 nm vs. 0.15 nm for a C-C interaction).[261] Possible backbone deformation or bond stretching in direction of $F_{applied}$ decrease, but not increase the tilt angles.

In table 7, corrected rupture lengths Δx_{corr} according to those tilt angles are summarized. The thermal off-rate constants had been calculated from the *lr*-axis crossing at f^* = 0 pN, thus they are not influenced. Still all three bivalent samples were different from each other and show the same sequence of Δx_{corr}.

Table 7: KBE model fit parameters, tilt angles, and corrected rupture lengths according to figure 64.

	Δx [nm]	Δx_{corr} [nm]	k_{off} [s^{-1}]	α_{max} [°]
1$_2$−Cu^{2+}	0.33 ± 0.01	0.43 ± 0.01	1.7 ± 0.2	40
2a$_2$−Cu^{2+}	0.51 ± 0.03	0.74 ± 0.04	0.14 ± 0.06	46
2b$_2$−Cu^{2+}	0.30 ± 0.01	0.51 ± 0.02	0.36 ± 0.07	54
2c$_2$−Cu^{2+}	1.12 ± 0.07	1.12 ± 0.07	0.09 ± 0.04	0

In the real systems, not all bonds are rigid and pulling angles may be lower than those suggested in table 7 due to a reorientation such as sketched in figure 65. For example, the pyridine - Cu^{2+} bond is a mixture of a directed σ-type interaction (due to the lone pair of electrons at the nitrogen atom) and a not directed electrostatic interaction (due to the permanent dipole moment in pyridine and increased electron density at the nitrogen atom), giving it some flexibility. Additionally our COGEF simulations shown in the following chapter suggest water-mediated intermediate states, which are even more flexible.

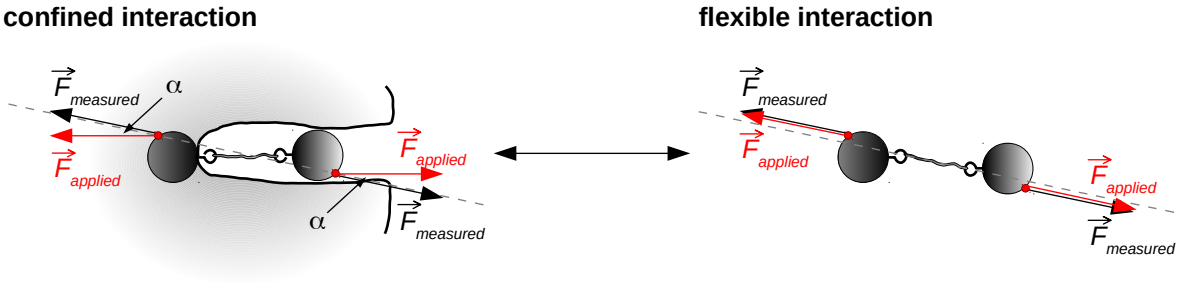

Figure 65: Confinement (or a rigid chemical structure) leads to vector decomposition of applied and measured forces (equation 119). Without confinement there are no opposing orthogonal forces and both interaction partners rearrange their positions, until applied and measured forces are parallel to each other (α = 0°). Then: $F_{measured} = F_{applied}$. Interactions in SMFS are usually semi-confined.

Thus the real pulling angles are expected to lie somewhere between the maxima shown in table 7 and α = 0° as expected for fully flexible systems. But no matter which angles are assumed; all three bivalent systems still show different rupture lengths and the same sequence (**2c**$_2$−Cu^{2+} > **2a**$_2$−Cu^{2+} > **2b**$_2$−Cu^{2+}). Thus tilted pulling alone cannot explain the observed differences. As the amount of tilt is unknown and probably even changes during bond rupture with intermediate state, we will use non-corrected rupture lengths in the following discussion on the rupture mechanisms.

4.3. Rupture Mechanisms

All bivalent coordination compounds with Cu^{2+} exhibited different dynamic force spectra for different backbone structures. However they differed only slightly in their thermal off-rate constants. $k_{off,bi}$ was approximately 10 times smaller than in the monovalent reference interaction $\mathbf{1}_2$−Cu^{2+} ($k_{off,bi}$ = 0.1 $k_{off,mono}$). As derived in chapter 2.1.2, effective concentration C_{eff} and thermal off-rate constant $k_{off,bi}$ correlate inversely with each other,[49] which increases the stability at strong rebinding effects (equation 120). K_{mono} is the equilibrium constant of the monovalent interaction, where a second pyridine is coordinating to a Cu^{2+} metal center with already one pyridine ligand. Considering K_{mono} = 72 l/mol from experiments in 0.5 mol/l KNO_3 solution at 25°C,[262] C_{eff} is approximately 3 mmol/l, a typical value also found in other bivalent supramolecular interactions without additional allosteric effects.[73,82]

$$k_{off,bi} = 2\frac{k_{off,mono}}{K_{mono} C_{eff}} \tag{120}$$

Comparing all three bivalent systems with each other, we were surprised to measure similar thermal off-rate constants. Especially in $\mathbf{2a}_2$−Cu^{2+}, the rigid backbone structure was supposed to increase C_{eff}. Instead $\mathbf{2a}_2$−Cu^{2+}, $\mathbf{2b}_2$−Cu^{2+}, and $\mathbf{2c}_2$−Cu^{2+} differed much in their rupture length parameter Δx. This means, the different backbone structures had a paramount influence on the malleability, but not on the effective concentration. Interestingly, the sequence of malleability did not correlate with backbone flexibilities: **2c** > **2a** > **2b** (malleability) vs. **2c** > **2b** > **2a** (backbone flexibility). Also interesting, even when we assume the non-tilted case (fully flexible bond) the monovalent interaction $\mathbf{1}_2$-Cu^{2+} had a rupture length around 0.3 nm. This value was much larger than the average bond length in a coordination bond between Cu^{2+} and pyridine (0.2 nm)[261]. It was not plausible, that both partners maintain their initial bonds up to an overall distance of 0.5 nm (0.2 nm initial distance + 0.3 nm Δx). Thus it was promising to study the rupture mechanisms in detail. First, we applied DFT simulations in the COGEF methodology to our systems $\mathbf{1}_2$−Zn^{2+}, $\mathbf{1}_2$−Cu^{2+}, $\mathbf{2a}_2$−Zn^{2+}, and $\mathbf{2a}_2$−Cu^{2+}. The discovered mechanisms were then transferred to the experimental results of systems $\mathbf{2b}_2$−Cu^{2+} and $\mathbf{2c}_2$−Cu^{2+}, finally leading to a combined model. We also studied the influence of the metal center to complex malleability exemplary for $\mathbf{1}_2$−Zn^{2+} and $\mathbf{2a}_2$−Zn^{2+}.

4.3.1. Rupture Mechanisms for Monovalent Pyridine 1

In figure 66, the calculated potential energy diagram for the dimeric trans-complex between **1** and Zn^{2+} is shown. The four remaining coordination sites of the octahedral complex were coordinated to explicit water, bulk water was considered by an implicit solvation model. All data points corresponded to geometry optimized complexes at fixed stretching lengths Δ*r*. Test computations using different initial geometries as starting point for geometry optimization showed no differences in computed energies. Beyond a stretching length of 0.09 nm, the initial metal-bound (MB) complex (a) fell apart with subsequent formation of a hydrogen bond to ligand water (hydrogen-bound HB complex, b). In the SMFS experiment, the remaining coordination site at the Zn^{2+} would be substituted by bulk water from the environment immediately. As discussed in the materials and methods section, this was not included into the computations. The discontinuity at a stretching length of 0.2 nm was due to a rearrangement of the bridging water from axial to para-configuration (c). The highest stretching length, still yielding a stable interaction, was 0.35 nm (d).

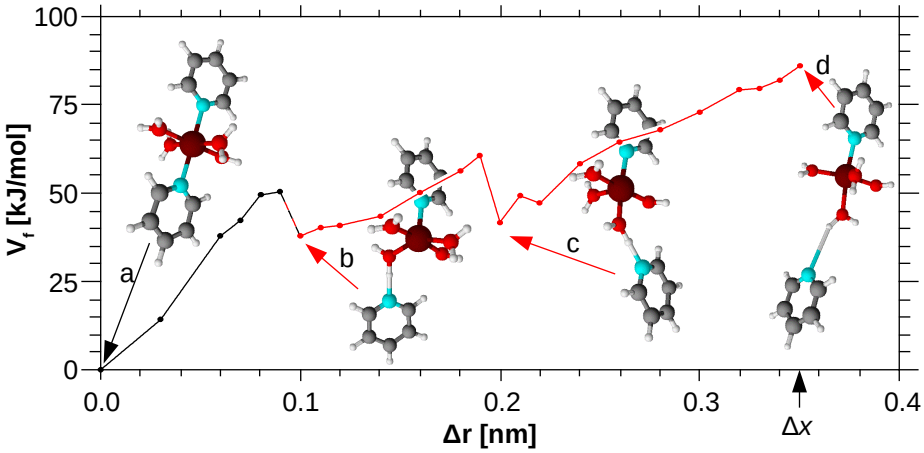

Figure 66: Potential energy diagram for $\mathbf{1}_2$–Zn^{2+} as a function of stretching length Δ*r*, calculated by the COGEF method. Black points indicate metal-bound MB states, red points hydrogen-bound HB compounds. Geometry optimized structures are shown for a) the initial complex, b) the shortest hydrogen-bound complex, c) the complex with rearranged geometry, and d) the complex with highest stretching length.

Which transition state was measured in the corresponding SMFS experiment as rupture length Δ*x*? If multiple transition states are present, the Δ*x* is the global maximum in V_f. Due to applied external forces, this dominant transition state may change. As described in chapter 2.5.3, this leads to separate linear regimes in the dynamic force spectrum,[128] such as observed for the interaction between (strept)avidin and biotin.[27] Throughout this thesis, we never detected such

signatures. A coarse estimation assuming an applied force of 100 pN yields to a PES deformation of only 6 kJ/mol per 0.1 nm stretching length. Considering figure 66 it was reasonable that point (d) remained the dominant transition state over the whole range or probed forces (or loading rates) in $\mathbf{1}_2$−Zn^{2+} and thus was equal to the measured rupture length Δx. Thus the theoretical stretching length Δr_{max} = 0.35 nm matches the experimental rupture length Δx = 0.35 ± 0.2 nm.

Is a HB type of interaction reasonable? *Ab-initio* calculations indicate that hydrogen bonds to pyridine are well possible and even energetically favored above hydrogen bonds between water molecules.[252] In experiments, pyridine and 4-methylpyridine are able to crystallize in structures with N-coordinated water.[250,251] In addition to the pyridine ligand, also the cationic metal center strongly polarizes coordinated water, increasing its ability to donate hydrogen bonds. Thus in the moment of bond rupture between the metal center and pyridine ligand, there are polarized protons in close proximity to the just unbound σ-electron pair of the pyridine nitrogen. The timescale of molecular motion is in the picosecond range and orders of magnitude smaller than the experimental pulling speed, even in the moment of “quick” cantilever relaxation.[208] Hence such a reorganization is well possible. A certain fraction of interactions may also break without HB intermediate state and result in high-force noise. Indeed in our experiments at fast pulling speeds we sometimes observed such signals, but their frequency was too low for a quantitative evaluation.

In figure 67, the calculated potential energy diagram for the dimeric trans-complex $\mathbf{1}_2$−Cu^{2+} is shown. Here, the MB complex was stable over a longer range of deformation Δr than in $\mathbf{1}_2$−Zn^{2+}. The subsequent HB intermediate broke at a shorter rupture length of Δr_{max} = 0.26 nm and at a higher potential energy (V_f = 136 kJ/mol compared to 86 kJ/mol). This was explained by the different number of valence electrons in both metal centers. Cu^{2+} with an electronic configuration of $[Ar]3d^9$ stabilizes through the Jahn-Teller effect. Due to the filled 3d-shell in Zn^{2+} ($[Ar]3d^{10}$), the electron charge distribution is spherically more symmetric and can more easily adopt to external constraints. For example, the pyridine coordinated water ligand in figure 67 (c) did not reach a full trans configuration such as in figure 66 (d). This was in contrast to the experiment, where rupture lengths and thermal off-rate constants for Cu^{2+} and Zn^{2+} were identical. This indicates, that also $\mathbf{1}_2$−Cu^{2+} exhibited stable trans-complexes beyond a stretching length of Δr_{max} = 0.26 nm. Maybe a fifth water ligand, not implemented into the calculations, stabilized the interaction. Besides this

limitations, also here a HB intermediate was well reasonable and will be suggested in the following.

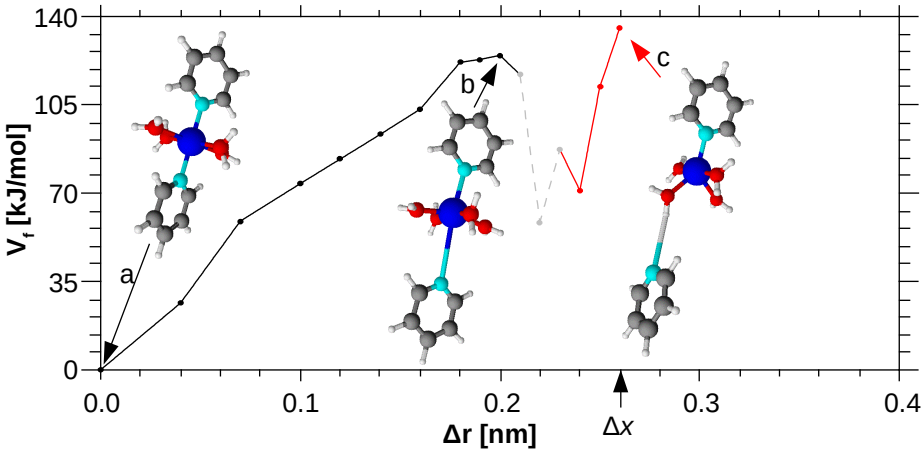

Figure 67: Potential energy diagram for **1**$_2$−Cu^{2+} as a function of stretching length Δ*r*, calculated by the COGEF method. Black points indicate MB states, red points HB compounds. gray points (dashed line) indicate a transition state between detachment from the Cu^{2+} and subsequent coordination to ligand water. Three representative geometry optimized structures a, b, and c are shown. The last stable configuration c is not in full trans configuration such as calculated for **1**$_2$−Zn^{2+}.

4.3.2. Rupture Mechanisms for Bivalent Pyridine 2a

The calculated rupture process of the bivalent **2a**$_2$−Zn^{2+} had the same rupture length as the monovalent complex **1**$_2$−Zn^{2+} (figure 68). Mono- and bivalent compounds changed to the HB state at approximately the same stretching around 0.1 nm with a mixed compound at 0.11 nm (b). The last stable HB_2 structure at Δr_{max} = 0.35 nm (c) was followed by a simultaneous rupture of both connections. Also in the experiment, both compounds **1**$_2$−Zn^{2+} and **2a**$_2$−Zn^{2+} had similar rupture lengths, but also similar thermal off-rate constants. The latter indicates that the bivalent ligand **2a** rather formed a monovalent interaction with its terminal pyridine and not the aimed bivalent complex with larger potential energy (V_f = 116 kJ/mol compared to 86 kJ/mol), or lower k_{off}.

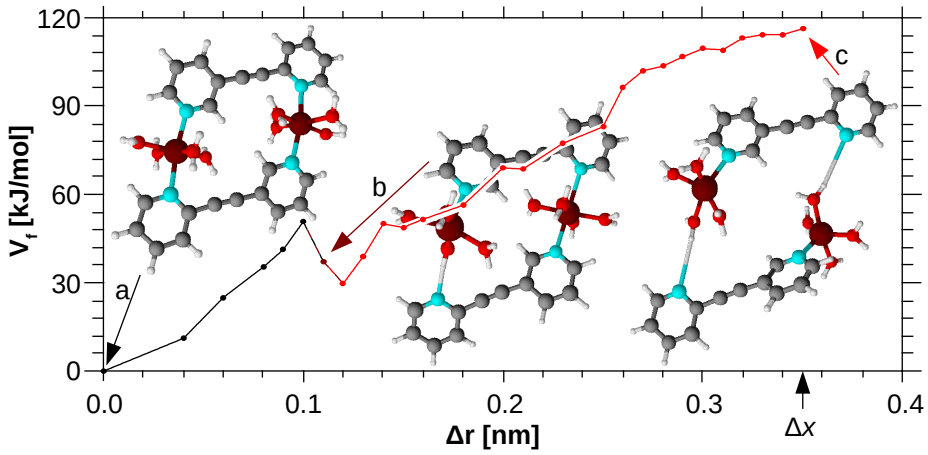

Figure 68: Potential energy diagram for **2a**$_2$−Zn^{2+} as a function of stretching length Δ*r*, calculated by the COGEF method. Black points indicate MB states, red points HB compounds. At the dark red point b, one of the connections was transferred to the HB state, while the second was still MB (HB−MB). Three representative geometry optimized structures a, b, and c are shown.

In contrast to **2a**$_2$−Zn^{2+}, the experimental thermal off-rate constant of **2a**$_2$−Cu^{2+} was one order of magnitude lower than for the corresponding monovalent interaction, indicating a bivalent interaction. Thus it was promising to calculate this rupture mechanism as well. In the COGEF simulations (figure 69) a maximum stretching length of $\Delta r_{max} = 0.38$ nm was calculated. The HB_2 intermediate did not break simultaneously at Δr_{max} such as in **2a**$_2$−Zn^{2+}. Instead the system reduced sterical constraints and gained stabilization energy at rupture of the first interaction, yielding a HB_1 complex (c). In contrast to **1**$_2$−Cu^{2+} HB_1 showed a full trans-configuration between the pyridine and the pyridine-bound water ligand. Together, both effects led to a higher overall stretching length up to the full rupture at (c). Noteworthy, the quantum chemical computations only allowed three water ligands per Cu^{2+} due to steric effects. Furthermore, Δr_{max} was not the point of largest V_f. However at a rupture length of 0.27 nm, the quantum mechanical software arrived a convergence problem. This problem could be solved by truncation of one ligand into a 1-methylpyridine (c, marked by *). The energies of the truncated complex (light gray) were normalized to the original compound, but the large oscillations of $V_f(\Delta r)$ beyond 0.27 nm indicated, that the energy still may be erroneous. Thus in the following we will attribute the rupture length Δx to Δr_{max} resting upon the previous calculations, where Δr_{max} exhibited the largest V_f.

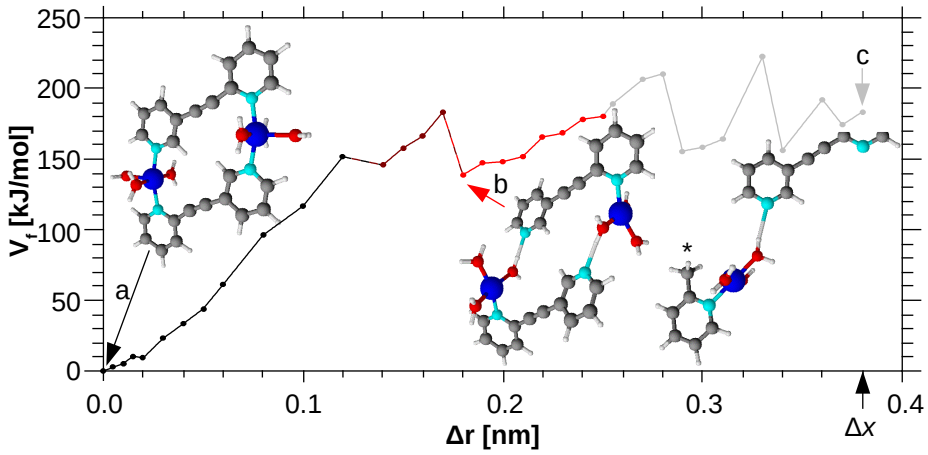

Figure 69: Potential energy diagram for **2a**$_2$−Cu^{2+} as a function of stretching length Δ*r*, calculated by the COGEF method. Black points indicate MB_2 states, red points HB_2 compounds. At the dark red points an intermediate compound b (MB−HB) had formed. At a rupture length of 0.27 nm the rupture of one of the HB states took place, yielding a HB_1 complex (light gray). Due to a convergence problem, here one ligand had to be truncated into 1-methylpyridine (c, marked by *).

The measured rupture length for **2a**$_2$−Cu^{2+} (Δ*x* = 0.51 ± 0.03 nm) was larger than the calculated Δr_{max}. We also considered a sliding mechanism, where the terminal pyridines formed a monovalent intermediate state as sketched in figure 70. However the estimated overall rupture length of 0.86 nm differed more from the experimental value than the stepwise rupture mechanism suggested above. Thus in the following we will suggest the stepwise process instead of the sliding mechanism.

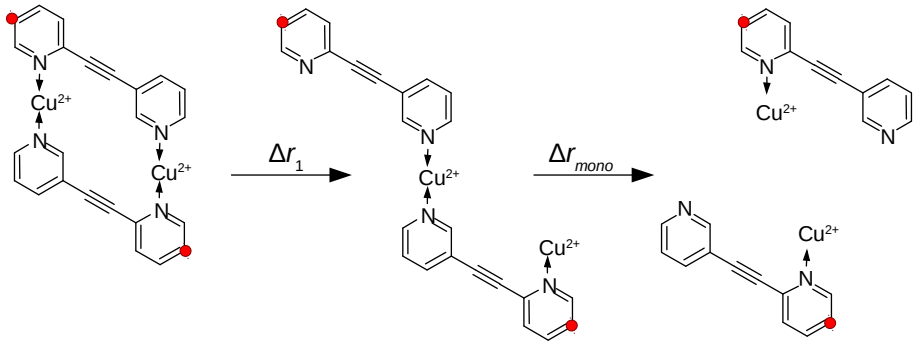

Figure 70: An alternative sliding mechanism for **2a**$_2$−Cu^{2+} could start with an initial displacement of Δr_1 = 0.60 nm. With additional Δr_{mono} = 0.26 nm, calculated for **1**$_2$−Cu^{2+}, the overall rupture length is Δr_{max} = 0.86 nm.

4.3.3. Rupture Mechanism for Bivalent Pyridine 2b

The bivalent coordination compound with medium backbone flexibility, **2b**$_2$−Cu^{2+}, showed the highest mechanical stability of all analyzed compounds. Its rupture length Δ*x* was similar to the monovalent interaction **1**$_2$−Cu^{2+} with significantly lower thermal off-rate constant k_{off} (table 8). In comparison to the nanorod complex

2a$_2$−Cu^{2+}, the rupture length was much lower, but thermal off-rate constant similar. Due to time limitations, our cooperation partners could not perform COGEF simulations for systems **2b**$_2$−Cu^{2+} and **2c**$_2$−Cu^{2+}. Thus we will discuss a possible mechanism for **2b**$_2$−Cu^{2+}, using the conceptual potential energy landscape for simultaneous and stepwise bond rupture, adapted from Suzuki and Dudko.[202]

Table 8: Overview on theoretical (COGEF) rupture lengths and experimental (KBE) results

	Δx [nm] COGEF	Δx [nm] KBE	k_{off} [s^{-1}] KBE
1$_2$−Zn^{2+}	0.35	0.35 ± 0.02	1.8 ± 0.3
1$_2$−Cu^{2+}	0.26	0.33 ± 0.01	1.7 ± 0.2
2a$_2$−Zn^{2+}	0.35	0.30 ± 0.01	2.4 ± 0.3
2a$_2$−Cu^{2+}	0.38	0.51 ± 0.03	0.14 ±0.06
2b$_2$−Cu^{2+}	---	0.30 ± 0.01	0.36 ± 0.07
2c$_2$−Cu^{2+}	---	1.12 ± 0.07	0.09 ± 0.04

In figure 71, the trajectories for simultaneous (red line) and stepwise (green line) bond rupture are sketched as function of stretching length Δr and tilt angle α. Both originate at the double hydrogen bound intermediate HB_2. For clarity, the previous transformations from the initial metal bound MB_2-state is omitted. The red path corresponds to a simultaneous bond rupture along transition state TS_1, yielding a stretching length of Δr_{sim}. In contrast the green trajectory shows a behavior, corresponding to the stepwise rupture mechanism such as calculated for complex **2a**$_2$−Cu^{2+}. Here, an HB_1 intermediate allowed the system to release strain by tilting both partners with respect to angle α. Due to this tilt, the stretching length Δr_{step} was larger than Δr_{sim}, yielding the calculated Δx_{bi} = 0.38 nm compared to Δx_{mono} = 0.26 nm for **1**$_2$−Cu^{2+}. In the experiment, **2b**$_2$−Cu^{2+} exhibited a much shorter rupture length than **2a**$_2$−Cu^{2+}, which indicated a simultaneous rupture process (red trajectory).

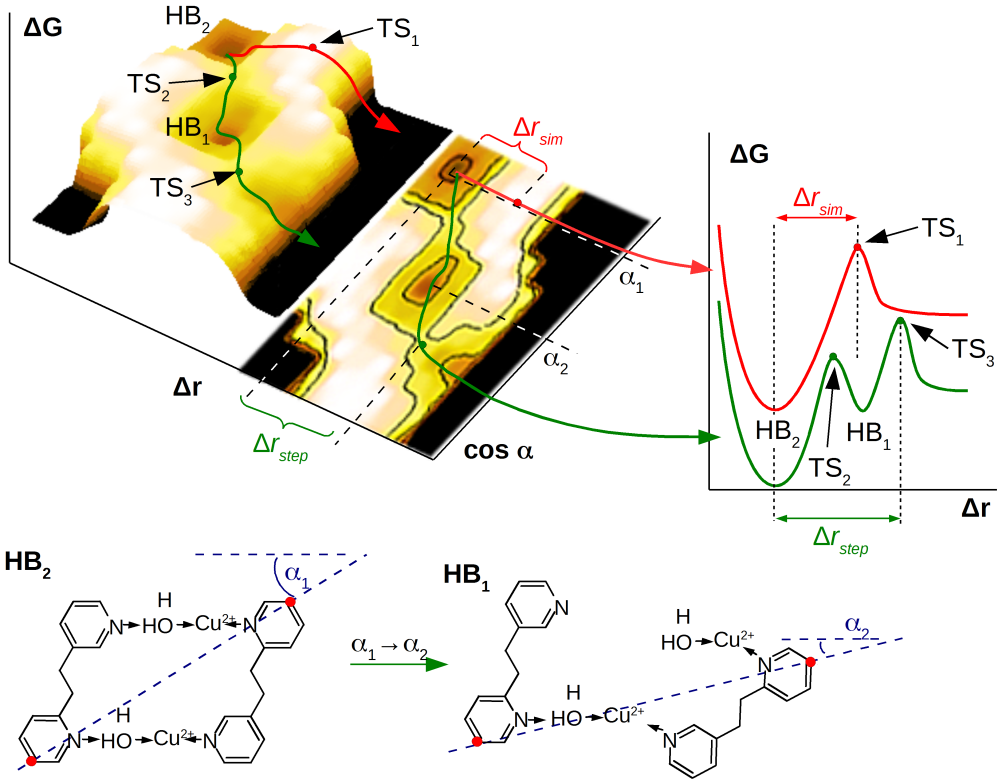

Figure 71: Possible potential energy diagram of HB_2 bond rupture in a simultaneous (red) and stepwise (green) manner. Top: 3-dimensional representation as a function of stretching length Δ*r* and tilt angle α with additional two-dimensional projection. Black areas correspond to broken interactions. Right: Projection of both trajectories onto the stretching coordinate Δ*r* as used in the KBE model (with offset in Δ*G* for clarity). Down: Schematic drawing of HB_2 and HB_1 configurations at maximum constraints (full 60° bond angles between C−N and N−Cu^{2+}). In the HB_1 form, a tilt of both interaction partners is followed by an increase in Δ*r* such as calculated in the COGEF simulations for **2a**$_2$−Cu^{2+}.

The dominant rupture mechanism is determined by saddle points of the potential energy surface, here: TS_1 in the simultaneous and TS_2 or TS_3 in the stepwise rupture process. From the COGEF simulations of **2a**$_2$−Cu^{2+} we have learned, that due to steric reasons the initial MB_2 complex was not able to host eight water ligands in the first coordination sphere such as shown in figure 69 (a). However it was well possible, that in the open HB_1 intermediate state (figure 69 c) a water molecule from the surrounding solvent filled the coordination sphere up (although not implemented into the calculations). In other words, after rupture of one bond, the remaining Cu^{2+} bond probably was coordinated in an octahedral configuration such as the monovalent complex **1**$_2$−Cu^{2+}. Then, the gain in energy would have stabilized the HB_1 intermediate and TS_3 transition state. As a result, the stepwise rupture along TS_3 (green trajectory) instead along TS_1 (red trajectory) was dominant. In contrast the backbone of **2b**$_2$−Cu^{2+} was more flexible, leaving enough space for the full octahedral

coordination already in the HB_2 intermediate. Consequently the gain in energy at HB_1 and TS_3 was not possible. Now, if TS_1 exhibited a lower energy than TS_3, the simultaneous bond rupture was dominant. Such a mechanism was calculated for **2a**$_2$−Zn^{2+} with fully coordinated Zn^{2+} ions in the MB_2 and HB_2 state (figure 68) and will be suggested in the following for **2b**$_2$−Cu^{2+} as well.

Another explanation for the short rupture length of **2b**$_2$−Cu^{2+} could be a stepwise rupture mechanism (green trajectory), but with a dominant transition state TS_2. This is the case, when the saddle point energy of TS_2 is above that of TS_3 and TS_1, also at applied external forces. Under these conditions, the KBE model yields Δx_{TS2} instead of Δx_{step} or Δx_{sim} (see also chapter 2.5.3). In other words, rupture of the second bond is inevitable in succession to the first bond rupture and does not influence the measured dynamic force spectrum. However in this situation, also the thermal off-rate constant $k_{off,TS2}$ calculated by the KBE model only corresponds to the first rupture step. The first rupture step is equivalent to rupture of the monovalent interaction **1**$_2$−Cu^{2+}. This was observed for **2a**$_2$−Zn^{2+}, but not for **2b**$_2$−Cu^{2+} with $k_{off,\mathbf{2b}\text{-Cu}} = 0.2\ k_{off,\mathbf{1}-Cu}$.

4.3.4. Rupture Mechanism for Bivalent Pyridine 2c

DFS on **2c**$_2$−Cu^{2+} delivered a remarkably high rupture length of $\Delta x_{\mathbf{2c}\text{-}Cu} = 1.12 \pm 0.07$ nm. **2c** was more flexible than **2a** and **2b**, but the backbone could not release enough constraint to explain this malleability. However **2c** was flexible enough to allow formation of a cis-complex to the metal center. As sketched in figure 72, such an initial conformation could have broken stepwise with a rupture length of $\Delta x = 0.94$ nm. Here, the first and second structures were geometry optimized using CHARMM force fields. The rupture length $\Delta r_{mono} = 0.33$ nm was taken from the experimental results of **1**$_2$−Cu^{2+}. A cis-isomer did not benefit from additional stabilization energy by the Jahn-Teller effect. This may be the reason, why a higher concentration of $CuSO_4$ was necessary in order to drive the equilibration to **2c**$_2$−Cu^{2+}(cis) in favor of the competing stacked or unbound interactions.

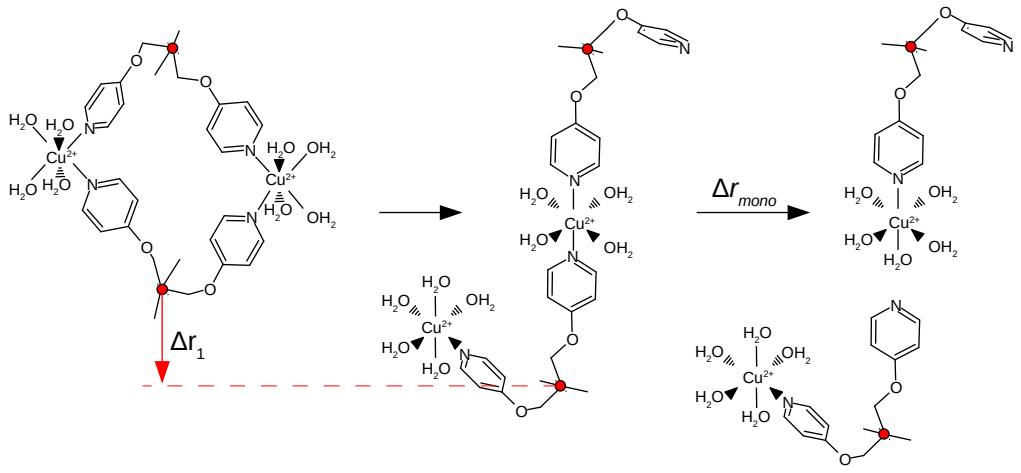

Figure 72: Estimated rupture mechanism for **2c**$_2$−Cu^{2+} using geometric considerations and a possible initial complex in cis-configuration as shown in [83]. After rupture of one interaction and a force-induced reorganization into a trans-complex, Δr_1 = 0.61 nm of strain are released. In sum with additional Δr_{mono} = 0.33 nm as measured for complex **1**$_2$−Cu^{2+}, a rupture length of Δx = 0.94 nm is possible. Structures were optimized using the molecular mechanics tool in ChemSketch (based on CHARMM force fields, v 14.01, ACD/Labs, Toronto, Canada).

4.3.5. A Combined Model for the Stability-Malleability Relationship

Considering our results with Cu^{2+}, we have characterized a set of rupture processes with different malleabilities Δx and − in comparison with the monovalent interaction − also different thermal stability k_{off}. Using **1**$_2$−Cu^{2+}, **2a**$_2$−Cu^{2+}, **2b**$_2$−Cu^{2+}, and **2c**$_2$−Cu^{2+}, we are now able to mimic all facets of the stability-malleability relationship mentioned in the introduction. Figure 73 illustrates their stability-malleability relationship exemplary for an average loading rate of 5000 pN/s with additional examples from the literature.

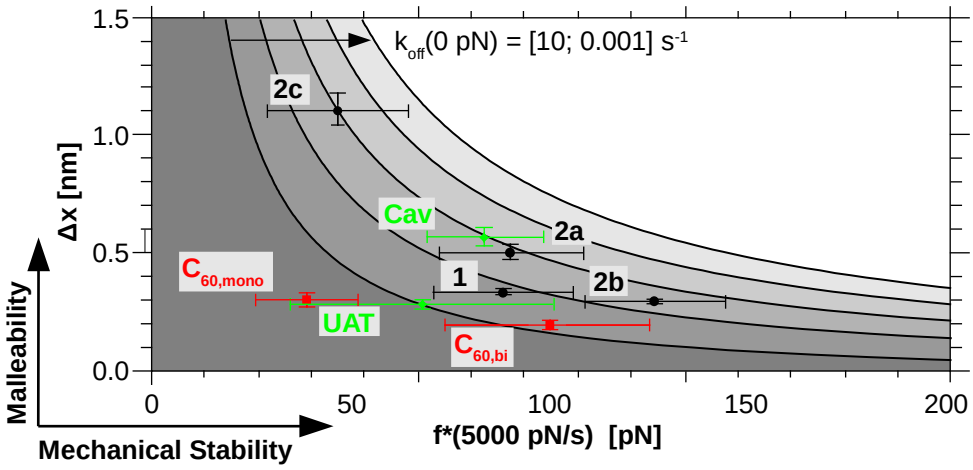

Figure 73: Plot of *f** (mechanical stabilities) at a loading rate of 5000 pN/s against the corresponding rupture lengths Δ*x* (malleabilities) for **1**$_2$−Cu^{2+}, **2a**$_2$−Cu^{2+}, **2b**$_2$−Cu^{2+}, and **2c**$_2$−Cu^{2+} and examples from the literature, discussed in the introduction (figure 5).[4,32,55]

- **Higher Mechanical Stability (shear-motif):** The trend between **1**$_2$−Cu^{2+} and **2b**$_2$−Cu^{2+} shows, that a simultaneous rupture mechanism between both interactions in a bivalent complex yields a higher mechanical stability at similar malleability. This is similar to the interaction between **C_{60}** and a pair of porphyrin tweezers.[4]
- **Higher Malleability (zipper-motif):** Higher thermal stability (k_{off}) does not necessarily lead to a higher mechanical stability. The trend between **1**$_2$−Cu^{2+} and **2a**$_2$−Cu^{2+} shows, that a stepwise bond rupture mechanism increases the malleability at similar mechanical stability (if the second rupture step is rate determining). This trend was known from polyvalent systems. In supramolecular systems, we observed such a by comparison of two different studies. The tetravalent hydrogen bond system **UAT**[32] is less malleable than the host-guest system of four hydrogen bonds with an additional guest molecule **Cav**[55].
- **Higher Malleability + Lower Mechanical Stability (zipper-motif):** Geometrical reconfiguration of the coordination sphere in addition to the zipper-motif is the proposed mechanism behind the trend between **1**$_2$−Cu^{2+} and **2c**$_2$−Cu^{2+}. Here, the mechanical stability is even lower than in the monovalent system. To our knowledge, such a behavior was not yet published in the literature.

“May the Force be with you!”

Han Solo to Luke Skywalker, Star Wars: Episode IV A New Hope (1977)

5. Conclusions and Perspectives

In this thesis we addressed the question, whether bivalent systems also show the balanced interplay between malleability and mechanical stability such as known for systems of higher valency. We successfully designed a set of bivalent model systems with various backbone flexibilities. Specifically we studied complexes of pyridine with the metal ions Zn^{2+} and Cu^{2+}. Only the latter showed specific bivalent interactions, bivalent Zn^{2+} complexes were not detected. This observation was attributed to the thermal stability as ranked in the Irving-Williams series,[60–62] where Cu^{2+} is forming the most stable complexes of all first row transition metals with oxidation state (II). Comparing our bivalent complexes of Cu^{2+}, their thermal stabilities (average bond lifetimes) were surprisingly similar and did not depend on the backbone structures. This indicated only a low change in effective concentration (low rebinding effect). In contrast their mechanical stabilities (most probable rupture forces) differed a lot, but not as expected by the backbone flexibility (flexibility: **2c** > **2b** > **2a**). Instead the rupture mechanism was crucial. Combining DFT simulations and our experimental results analyzed by the KBE model, we suggested the mechanisms summarized in figure 74. Rupture always occurred through a hydrogen bound intermediate complex with water in the first coordination sphere. Stepwise bond rupture (**2a** and **2c**) and an initial cis-conformation (**2c**) increased the rupture length and decreased the mechanical stability. For the first time we could show, that the mechanical stability of a bivalent interaction (**2c**) can even drop below the stability of its monovalent counterpart (**1**). This behavior was similar to rupture processes in systems of higher valency such as pairs of β-sheets in proteins, where shear and zipper motifs determine the mechanical stability.[42,43] According to our results, even in the smallest multivalent systems those motifs play a role: simultaneous (shear-like) or stepwise (zipper-like) bond rupture.

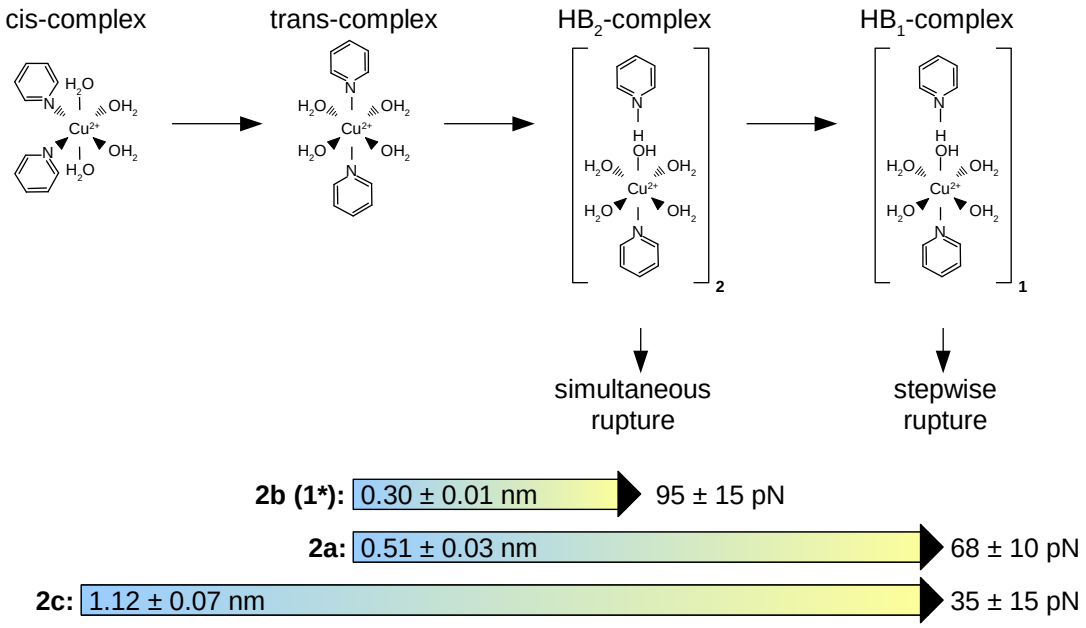

Figure 74: The bivalent model systems **2a**, **2b**, and **2c** broke through a different number of intermediate states, yielding a broad range of rupture lengths. Less intermediate states allowed for shorter rupture lengths and higher most probable rupture forces (mechanical stabilities, here forces are shown for a loading rate of 5000 pN/s). Chemical structures are truncated to show the metal-complex part, similar in all three systems. *Monovalent complex **1** had a similar rupture length of 0.33 ± 0.01 nm, but a mechanical stability of only 65 ± 10 pN due to its lower thermal off-rate constant.

In the literature, there is an increasing awareness of possible discrepancies between the mechanical and thermal stability of interactions.[90] A key issue is the underlying rupture mechanism. Through the research presented in this thesis we discovered the important influence of water mediated intermediate states on the rupture mechanism for the first time.[67] Another recent example from the literature are catch-bonds. Here, a constant external force even increases the thermal stability instead of decreasing the average bond lifetimes. Such behavior was attributed to a two-state two-path potential energy diagram, where the rupture mechanism changes to a second path at larger external forces.[204] In order to access the full spectrum of biologically relevant samples *in-vitro*[263] and even *in-vivo*[264], techniques for single-molecule force spectroscopy are continuously improved. Interlaboratory collaborations aim to improve the process of probe calibration[263] and promising new instrumentation may reduce systematic calibration errors, which are still one of the largest issues.[136,146]

In future work, the water mediated mechanisms could be analyzed in more detail. For example, it is not clear whether polarized metal-bound water ligands are needed to form the hydrogen bound intermediates observed in our bivalent systems. Alternatively the water molecules may be introduced from the surrounding aqueous

solvent. A promising system are terpyridine complexes, where all octahedral coordination sites are fully coordinated by the pyridine instead of water. In a recent study, dimeric terpyridine complexes with Os^{2+} and Os^{3+} showed a very low malleability around 0.1 nm,[265] indicating a missing hydrogen bound intermediate state. Full or partial coordination of the metal ion could also be achieved with tweezers complexes.[266] In addition to investigations of interactions in aqueous solvents, the rupture mechanisms of pyridine complexes in polar non-aqueous solvents could provide a deeper understanding of the rupture mechanisms in pyridine-metal complexes. Since salts of Cu^{2+} are sparsely soluble in organic solvents, a possible experimental strategy may involve pyridine structures with inherent metal ions.[267]

The established toolkit can now be applied to study the balanced interplay between malleability and mechanical stability with respect to several factors that influence multivalency, for example backbone flexibility, distance of interaction partners, steric match/mismatch, or allosteric effects. It is compatible to biologically relevant aqueous solvents and probably extensible to higher valency. In this thesis our “tools”, the pyridine coordination compounds with Cu^{2+}, were connected by different backbone structures to yield $\mathbf{2a}_2$−Cu^{2+}, $\mathbf{2b}_2$−Cu^{2+} and $\mathbf{2c}_2$−Cu^{2+}. The interactions exhibited very different mechanical stabilities and malleabilities. We have shown, that bivalency can lead either to an increase or a decrease of mechanical stability, strongly depending on the actual rupture mechanism.[83] In future work, it would be of great interest to design bivalent systems of similar malleability, but different backbone flexibility. Then the influence of backbone structure and effective concentration (rebinding effect) on the mechanical stability could be compared directly. For this purpose, two different strategies could be followed. First, bivalent systems similar to **2b** would allow a full coordination with four water ligands per Cu^{2+} (not with three as in **2a**). They should be less flexible than **2c** to avoid the initial cis-complexes. Allosteric effects may be studied by comparison of conjugated and non-conjugated backbone structures. In the latter, both pyridine π-systems are sterically connected, but electronically decoupled. Second, a different backbone approach could be based on the “molecular rulers” method, which has been illustrated in the example of PNA-DNA conjugates.[268] In these systems, the interaction partners are characterized by well defined distances with tunable backbone flexibility. It would be fascinating to study, whether those systems exhibit predictable correlations between backbone flexibility

and mechanical stability. In this thesis we also analyzed the extensibility of our toolkit to higher valencies using the trivalent analogue of nanorod **2a** (conjugate **7**), which formed stacking interactions instead of $\mathbf{7}_2$−Cu^{2+} due to its linear structure yielding a geometric preorientation. It is well possible, that backbone structures with higher flexibility such as **2b** or the PNA-DNA conjugates can be extended to higher valency. The ultimate goal is a comprehensive model on the structure-malleability relationship of multivalent systems.

“There is only one good, knowledge, and one evil, ignorance.”

Socrates

6. Appendix

6.1. Abbreviations

β_2AR	human β_2-adrenergic receptor
bp	base pairs (in DNA)
Ca-TBS	calcium supplemented TRIS-buffered saline (25 mM TRIS, 72 mM NaCl, 1 mM $CaCl_2$, pH 7.2 at 25 °C)
COGEF	constrained geometries simulate external forces
DFS	dynamic force spectrum
DFT	density functional theory
DMSO	dimethyl sulfoxide
DNA	deoxyribonucleic acid (ds: double-stranded, ss: single-stranded)
EtOAc	ethyl acetate
FJC	freely-jointed chain
HB	hydrogen-bound
InvOLS	inverted optical lever sensitivity
KBE	Kramers-Bell-Evans (model)
MB	metal-bound
MD	molecular dynamics
*f**	most probable rupture force ($f^*(lr)$)
NTA	nitrilotriacetic acid
PBS	phosphate buffered saline (137 mM NaCl, 10 mM phosphate buffer, 2.7 mM KCl, pH 7.4 at 25 °C)
PDI	polydispersity index
PEG	poly-ethylene glycol
PES	potential energy surface
PNA	peptide nucleic acid
PSGL-1	p-selectin glycoprotein ligand-1
RFPD	rupture force probability distribution
SAM	self-assembled monolayer
SFM	scanning force microscope/microscopy
SHO	simple harmonic oscillator
SMFS	single-molecule force spectroscopy
S_N2	bimolecular nucleophilic substitution
TRIS	tris(hydroxymethyl)-aminomethane
tss	tip-sample-separation
UAT	urea-aminotriazine
UPy	2-ureido-4[1H]-pyrimidinone
VWF	von-Willebrand Factor
WLC	worm-like chain

6.2. Mechanical Stabilities of Supramolecular and Biomolecular Systems

In this chapter, SMFS data from various supramolecular and biomolecular systems is tabulated. Most probable rupture forces at a loading rate of 5000 pN/s are estimated using the KBE model and average values for t_{off}(0 N) and Δx.

Table 9: Illustrative supramolecular examples for average lifetimes (at 0 N), most probable rupture forces (*f, at a loading rate of 5000 pN/s) and rupture lengths on the level of single-molecules.**

Interaction	Solvent	t_{off}(0 N) [s]	*f** [pN]	Δx [nm]
Resorc[4]arene + NH_4^+ [30]	Ethanol	1.01 ± 0.83	104	0.22 ± 0.04
Resorc[4]arene + $NH(Me)_3^+$ [30]	Ethanol	53.5 ± 21.4	109	0.38 ± 0.06
Pd^{2+}-complex + Pyridine[266]	DMSO	1.4 ± 0.8	110 (2 bonds in a row)	0.19 ± 0.02
Pd^{2+}-complex + 4-(piperidin-1-yl)pyridine[266]	DMSO	0.050 ± 0.008	39 (2 bonds in a row)	0.17 ± 0.02
C_{60} + Zn-Porphyrin [4]	Water	0.023 ± 0.003	29	0.31 ± 0.03
C_{60} + Zn-Porphyrin (pincer complex) [4]	Water	0.15 ± 0.03	74	0.20 ± 0.02
C_{60} + C_{60} [192]	PBS	0.36 ± 0.18	72	0.27 ± 0.02
Heterodimeric capsule (4 H-bonds + p-Xylene guest) [55]	p-Xylene	7.14 ± 7.14	62	0.56 ± 0.08
UAT + UAT (4 H-bonds of donor-acceptor-donor-acceptor type)[32]	Hexadecane	0.10 ± 0.08	50	0.29 ± 0.02
UPy + UPy (4 H-bonds of donor-donor-acceptor-acceptor type)[32]	Hexadecane	3.9 ± 0.9	140	0.20 ± 0.02
β-cyclodextrin + adamantane (monovalent)[49]	PBS	$5\ 10^{-4}$ (estimated)	not measurable	not measurable
β-cyclodextrin + adamantane (bivalent)[49]	PBS	5 (0.3 – 100)	125	0.24 ± 0.09

β-cyclodextrin + adamantane (trivalent)[49]	PBS	250 (20 - 30000)	170	0.27 ± 0.10
Os^{2+} + Terpyridine [265]	PBS	0.07 ± 0.01	105	0.07 ± 0.01
Os^{3+} + Terpyridine [265]	PBS	0.22 ± 0.26	145	0.09 ± 0.03

Table 10: Illustrative examples for average lifetimes (at 0 N), most probable rupture forces (*f, at a loading rate of 5000 pN/s) and rupture lengths on the level of single-molecules.**

Interaction	Solvent	t_{off}(0 N) [s]	*f** [pN]	Δ*x* [nm]
Streptavidin + Biotin (1^{st}/2^{nd} transition state) [27]	PBS	0.23 ± 0.13 / 14.3 ± 18.4	158 91	0.08 ± 0.004 0.40 ± 0.08
Avidin + Biotin (1^{st}/2^{nd} transition state) [27]	PBS	0.077 ± 0.066 / 2.86 ± 2.86	96 98	0.09 ± 0.01 0.29 ± 0.05
Digoxigenin + Antibody (1^{st}/2^{nd} transition state) [269]	PBS	0.22 66.7	53 41	0.35 1.15
Recombinant Antibody Fragment + Protein [26]	PBS	256 ± 375	58	0.88 ± 0.12
P-Selectin + PSGL-1 [33]	PBS	5.0	198	0.14
I27 domain unfolding (proximal Ig domain in human muscle) [270]	PBS	$6.7\ 10^3$	184	0.33
Dockerin + Cohesin (cellulosome-adhesion complex) [34]	Ca-TBS	$1.4\ 10^6$	606	0.13

6.3. Wolfram Mathematica Code for the Direct Fit Method

In the direct fit method, rupture force histograms from different pulling velocities are fitted simultaneously by rupture force probability distributions such as equation (96) from the KBE model (see figure 62). This is different from the standard procedure, where rupture force histograms are first fitted separately. Then their most probable rupture forces are analyzed simultaneously in a dynamic force spectrum using equation (98) (see figure 30). In chapter 4.2.3, the direct fit method is applied to discuss the origin of a second peak in rupture force histograms. Here, the probability distribution consideres simultaneous bond rupture according to the Williams formalism[27,255,256] as extended by Akhremitchev et al.[192,257] In the following the corresponding code for Wolfram Mathematica is given, that may be adapted easily to other models as well.

```
(*Disable some warnings*)
Off[NIntegrate::"inumr"]
Off[General::stop]
Off[General::unfl]

(*Data import and histogram binning*)
ClearAll[input, data, ones, hist, bin]
(*Import of histogram files. Enter file paths here.*)
DataPath = "D:\My_Home_Folder\Data_Folder\\"
(*enter the number of files here*)
amount = 7;
(*Enter filenames here*)
dat[1] = Import[DataPath <> "100-sII-fmin.txt", "Table"];
dat[2] = Import[DataPath <> "300-sII-fmin.txt", "Table"];
dat[3] = Import[DataPath <> "500-sII-fmin.txt", "Table"];
dat[4] = Import[DataPath <> "1k-sII-fmin.txt", "Table"];
dat[5] = Import[DataPath <> "3k-sII-fmin.txt", "Table"];
dat[6] = Import[DataPath <> "5k-sII-fmin.txt", "Table"];
dat[7] = Import[DataPath <> "10k-sII-fmin.txt", "Table"];
(*Procedure that summarizes the data into histogram bins. Bootstrapping can
be turned on by setting the third value to 1 and will be used to estimate
standard deviations.*)
bin[width_, max_, bootstrap_] := {
  ClearAll[input, ones, hist, data, bsdat];
  Array[ones, amount];
  Do[{ClearAll[temp, temp2, temp3, temp4];
    len = Length[dat[i]];
```

```
    Array[bsdat, len];
    If[bootstrap == 1,
     bsdat[i] = Table[dat[i][[RandomInteger[{1, len}]]], {len}],
     bsdat[i] = dat[i]];
    temp2 = BinCounts[bsdat[i][[All, 1]], {0, max, width}];
    Len = Length[temp2];
    Nges = Sum[temp2[[j]], {j, Len}];
    temp3 = Sum[temp2[[j]], {j, Len}];
    temp = Table[j*width + width/2, {j, 0, Len - 1}];
    temp4 = Table[j*width, {j, 0, Len - 1}];(*for histogram printing*)
    ones = Table[i, {Len}];
    input[i] =
     Join[Transpose[{N[temp]}], Transpose[{ones}],
      Transpose[{N[temp2/Nges/width]}], 2];
    hist[i] = Join[Transpose[{temp4}], Transpose[{temp2/Nges/width}], 2]
    (*for histogram printing*)}, {i, 1, amount}];
(*Merge all histogram data into one table. The additional z-component is
necessary to fit all data instanteneously.*)
  data = input[1];
  Do[data = Join[data, input[i]], {i, 2, amount}]}
(*Example: Create a set of histograms with bin width of 10 pN, up to a
force of 300 pN, without bootstrapping.*)
bin[12, 300, 0]
(*Plot the histograms*)
Do[Print[ListPlot[hist[i], Filling -> Axis, InterpolationOrder -> 0,
   Joined -> True, PlotRange -> Full, AxesOrigin -> {0, 0}]], {i, 1,
amount}]

(*Definition of global parameters, here using values for the FJC in water.
Units: pN, nm, s.*)
therm = 4.11; (*kB*T at 298 K*)
lk = 0.7; (*Kuhn length of PEG*)
Fk = therm/lk; (*Kuhn force*)
Lg = 0.28; (*Monomer length of PEG in gauche conformation*)
Lt = 0.36; (*Monomer length of PEG in trans conformation*)
Ks = 150000; (*Segment elasticity*)
dG0 = 3*therm; (*Free energy difference between the gauche and trans
conformation*)
Ns = 410; (*Number of monomers in the PEG chain*)
fmin = 10; (*Detection limit, minimal force*)
k = 3.5; (*Cantilever spring constant*)
Clear[set] (*Pulling speeds of the data sets imported above.*)
```

```
Array[set, amount];
set[1] = {v -> 100};
set[2] = {v -> 300};
set[3] = {v -> 500};
set[4] = {v -> 1000};
set[5] = {v -> 3000};
set[6] = {v -> 5000};
set[7] = {v -> 10000};

(*The fit model including simultaneous bond rupture and a contour length
difference dLc between simultaneously pulled PEG tethers.*)
ClearAll[dG, l, pF, sig, F1, F2, toff, s, g, f, model]
dG[F_] := dG0 - F (Lg – Lt)
l[F_] := Ns (Lg/(Exp[dG[F]/therm] + 1) + Lt/(Exp[-dG[F]/therm] +
1))*(Coth[F*lk/therm] - therm/(F*lk)) + Ns*F/Ks
(*Calculation of the loading rate pF.*)
pF[F_, v_] = ((v*k)^-1 + D[l[F], F]/v)^-1;
(*Sigmoidal cut-off function to include the instrumental resolution
limit.*)
sl = 3/4;
sig[F_] := 1/2*(1 + Tanh[sl*(F – fmin)/2])
(*The forces, acting on the separate bonds can be estimated analytically
using the high-force FJC approximation.*)
F1[F_, dLc_] := F/2 + (Sqrt[4*Fk*F*dLc + (F*dLc - Fk*(2 + dLc))^2] - Fk*(2
+ dLc))/(2 dLc)
F2[F_, dLc_] := F - F1[F, dLc]
(*The force dependent average bond lifetime is.*)
toff[F_, dx_, toff0_] := toff0*Exp[-F*dx/therm]
(*Option 1: Numerical calculation of the survival probability (exact, but
computationally expensive).*)
s[F_?NumericQ, dx_?NumericQ, toff0_?NumericQ, v_?NumericQ] := Exp[-
NIntegrate[1/(pF[f, v]*toff[f, dx, toff0]), {f, 0, F}]]
(*Option 2: Approximate calculation of the survival probability
(computationally much less expensive and still very precise).*)
s[F_, dx_, toff0_, v_] = Exp[-Integrate[1/(pF[F, v]*toff[f, dx, toff0]),
{f, 0, F}]];
(*Its corresponding probability density functions are g(F) for the first
and f(F) for the second maximum, each. A is the ratio between single and
double rupture, B is a scaling factor as we fit absolute the numbers of
rupture that are not normalized.*)
g[F_, toff0_, dx_, A_, B_, v_] := B*A/(pF[F, v]*toff[F, dx, toff0])*s[F,
dx, toff0, v];
```

```
f[F_, toff0_, dx_, A_, dLc_, B_, v_] := B*(1 - A)*(1 + 2*dLc)* s[(F/2), dx,
toff0, v]*(s[F2[F, dLc], dx, toff0, v] - s[F1[F, dLc], dx, toff0, v])/
(F1[F, dLc] - F2[F, dLc]);
(*Finally we define the model function to run the fit above, simultaneously
for the whole set of z rupture force distributions. Specifically only for
the corresponding data set z = a, the fit function is non zero.*)
model[F_, z_, toff0_, dx_, A_, dLc_, B_, v_] := If[z == a, sig[F]*(g[F,
toff0, dx, A, B, v] + f[F, toff0, dx, A, dLc, B, v]) , 0]

(*Do repetitive fits over a range of bin widths and save data to a table.*)
start = 5; (*Smallest bin width is 5 pN*)
end = 20; (*Largest bin width is 20 pN*)
steps = 15; (*Run 15 steps: 5, 6, 7, ..., 20*)
binsize = (end – start)/steps;
Clear[fit]
(*Initial parameters*)
fit[0] = {toff0 -> 0.6, dx -> 0.33, dLc -> 0.5, A1 -> 0.4, A2 -> 0.3, A3 ->
0.4, A4 -> 0.4, A5 -> 0.3, A6 -> 0.5, A7 -> 0.4, B1 -> 0.6, B2 -> 0.5, B3
-> 0.5, B4 -> 0.5, B5 -> 0.52, B6 -> 0.52, B7 -> 0.51};
(*Do the acutal fit. The fit of each bin width uses results of the previous
run. Parameters A, B, and dLc are fixed to a range of 0-1. Parameters dx
and toff0 are larger than 0.*)
Do[
 step = start + (i – 1)*binsize;
 bin[step, 250, 0];
 fit[i] =
  FindFit[data, {Sum[
     model[F, z, toff0, dx, ToExpression["A" <> ToString[i]], dLc,
ToExpression["B" <> ToString[i]], v] /. {a -> i} /. set[i], {i, 1,
amount}], {0 <= A1 <= 1, 0 <= A2 <= 1, 0 <= A3 <= 1, 0 <= A4 <= 1, 0 <= A5
<= 1, 0 <= A6 <= 1, 0 <= A7 <= 1, 0 <= B1 <= 1, 0 <= B2 <= 1, 0 <= B3 <= 1,
0 <= B4 <= 1, 0 <= B5 <= 1, 0 <= B6 <= 1, 0 <= B7 <= 1, 0 < dx, 0 < toff0,
0 < dLc < 1}}, {{toff0, toff0 /. fit[i - 1]}, {dx, dx /. fit[i - 1]}, {dLc,
dLc /. fit[i - 1]}, {A1, A1 /. fit[i - 1]}, {A2, A2 /. fit[i - 1]}, {A3, A3
/. fit[i - 1]}, {A4, A4 /. fit[i - 1]}, {A5, A5 /. fit[i - 1]}, {A6, A6 /.
fit[i - 1]}, {A7, A7 /. fit[i - 1]}, {B1, B1 /. fit[i - 1]}, {B2, B2 /.
fit[i - 1]}, {B3, B3 /. fit[i - 1]}, {B4, B4 /. fit[i - 1]}, {B5, B5 /.
fit[i - 1]}, {B6, B6 /. fit[i - 1]}, {B7, B7 /. fit[i - 1]}}, {F, z},
MaxIterations -> 200];
 Print["result -> ", i, ", width -> ", step, ", " , fit[i][[2]], ", ",
fit[i][[1]], ", ", fit[i][[3]]];, {i, 1, steps + 1}]
```

```
(*Save results into a txt file*)
Save[DataPath <> "Results.txt", fit]

(*Plot the fit result 1*)
result = 1;
step = start + (result – 1)*binsize;
bin[step, 250, 0];
Print["result -> ", i, ", width -> ", step, ", " , fit[result][[2]], ", ",
fit[result][[1]], ", ", fit[result][[3]]];
ClearAll[plt, gplt, fplt, coff, his]
Array[plt, amount]; (*overall fit function*)
Array[gplt, amount]; (*distribution of the first maximum*)
Array[fplt, amount]; (*distribution of the second maximum*)
Array[coff, amount]; (*cut-off function*)
Array[his, amount]; (*histogram data*)
Do[plt[i] = Plot[model[F, a, toff0, dx, ToExpression["A" <> ToString[i]],
dLc, ToExpression["B" <> ToString[i]], v] /. set[i] /. fit[result], {F, 0,
250}, PerformanceGoal -> "Speed", PlotRange -> All], {i, 1, amount}]
Do[gplt[i] = Plot[g[F, toff0, dx, ToExpression["A" <> ToString[i]],
ToExpression["B" <> ToString[i]], v] /. set[i] /. fit[result], {F, fmin,
250}, PerformanceGoal -> "Speed", PlotRange -> All, PlotStyle -> Green],
{i, 1, amount}]
Do[fplt[i] = Plot[f[F, toff0, dx, ToExpression["A" <> ToString[i]], dLc,
ToExpression["B" <> ToString[i]], v] /. set[i] /. fit[result], {F, fmin,
250}, PerformanceGoal -> "Speed", PlotRange -> All, PlotStyle -> Purple],
{i, 1, amount}]
Do[coff[i] = Plot[Max[hist[i][[All, 2]]]*sig[F, fmin] /. set[i], {F, 0,
100}, PlotStyle -> {Dashed, Thick}, PlotRange -> Full], {i, 1, amount}]
Do[his[i] = ListPlot[hist[i], Filling -> Axis, InterpolationOrder -> 0,
Joined -> True, PlotRange -> All], {i, 1, amount}]
Do[Print[Show[{plt[i], his[i], fplt[i], gplt[i], coff[i]}]], {i, 1,
amount}]

(*Bootstrapping: Bootstrap estimates are created using sampling with
replacement on the input data and fitted to gain bootstrap estimates of fit
parameters. This process is repeated "steps=1000" times at a binsize of 10
to gain an estimate of the shape of the distribution of fit parameters.*)
binsize = 10;
steps = 1000;
Clear[fit, histbs]
(*Start parameters*)
fit[0] = {toff0 -> 0.6, dx -> 0.33, dLc -> 0.5, A1 -> 0.4, A2 -> 0.3, A3 ->
```

```
0.4, A4 -> 0.4, A5 -> 0.3, A6 -> 0.5, A7 -> 0.4, B1 -> 0.6, B2 -> 0.5, B3
-> 0.5, B4 -> 0.5, B5 -> 0.52, B6 -> 0.52, B7 -> 0.51};
Do[
 bin[binsize, 250, 1];
 fit[i] =
  FindFit[data, {Sum[
     model[F, z, toff0, dx, ToExpression["A" <> ToString[i]], dLc,
ToExpression["B" <> ToString[i]], v] /. {a -> i} /. set[i], {i, 1,
amount}], {0 <= A1 <= 1, 0 <= A2 <= 1, 0 <= A3 <= 1, 0 <= A4 <= 1, 0 <= A5
<= 1, 0 <= A6 <= 1, 0 <= A7 <= 1, 0 <= B1 <= 1, 0 <= B2 <= 1, 0 <= B3 <= 1,
0 <= B4 <= 1, 0 <= B5 <= 1, 0 <= B6 <= 1, 0 <= B7 <= 1, 0 < dx, 0 < toff0,
0 < dLc < 1}}, {{toff0, toff0 /. fit[0]}, {dx, dx /. fit[0]}, {dLc, dLc /.
fit[0]}, {A1, A1 /. fit[0]}, {A2, A2 /. fit[0]}, {A3, A3 /. fit[0]}, {A4,
A4 /. fit[0]}, {A5, A5 /. fit[0]}, {A6, A6 /. fit[0]}, {A7, A7 /. fit[0]},
{B1, B1 /. fit[0]}, {B2, B2 /. fit[0]}, {B3, B3 /. fit[0]}, {B4, B4 /.
fit[0]}, {B5, B5 /. fit[0]}, {B6, B6 /. fit[0]}, {B7, B7 /. fit[0]}}, {F,
z}, MaxIterations -> 100];
 Print["result -> ", i, ", width -> ", step, ", " , fit[i][[2]], ", ",
fit[i][[1]], ", ", fit[i][[3]]];
histbs[i] = hist;, {i, 1, steps}]
(*Save the bootstrap data*)
filename = "Bootstrap-data.dat";
Clear[export]
(*The first line in the data file will be the heading, for example when
imported into spreadsheet software.*)
export = {{toff0, dx, dLc, A1, A2, A3, A4, A5, A6, A7, B1, B2, B3, B4, B5,
B6, B7}};
Do[export = Append[export, fit[i][[All, 2]]], {i, 1, steps}];
Export[DataPath <> filename, export];
```

“If I have seen further, it is by standing on the shoulders of giants.”

Isaac Newton (1642 - 1726) in a letter to Robert Hooke in 1676

7. References

(1) Fantner, G. E.; Hassenkam, T.; Kindt, J. H.; Weaver, J. C.; Birkedal, H.; Pechenik, L.; Cutroni, J. A.; Cidade, G. A. G.; Stucky, G. D.; Morse, D. E.; Hansma, P. K. Sacrificial bonds and hidden length dissipate energy as mineralized fibrils separate during bone fracture. *Nat. Mater.* **2005**, *4* (8), 612–616. DOI: 10.1038/nmat1428.

(2) Zhou, M.; Pesika, N.; Zeng, H.; Tian, Y.; Israelachvili, J. Recent advances in gecko adhesion and friction mechanisms and development of gecko-inspired dry adhesive surfaces. *Friction* **2013**, *1* (2), 114–129. DOI: 10.1007/s40544-013-0011-5.

(3) Huber, G.; Gorb, S. N.; Spolenak, R.; Arzt, E. Resolving the nanoscale adhesion of individual gecko spatulae by atomic force microscopy. *Biol. Lett.* **2005**, *1* (1), 2–4. DOI: 10.1098/rsbl.2004.0254.

(4) Zhang, Y.; Yu, Y.; Jiang, Z.; Xu, H.; Wang, Z.; Zhang, X.; Oda, M.; Ishizuka, T.; Jiang, D.; Chi, L.; Fuchs, H. Single-molecule study on intermolecular interaction between C60 and porphyrin derivatives: toward understanding the strength of the multivalency. *Langmuir* **2009**, *25* (12), 6627–6632. DOI: 10.1021/la901360c.

(5) Marshall, B. T.; Long, M.; Piper, J. W.; Yago, T.; McEver, R. P.; Zhu, C. Direct observation of catch bonds involving cell-adhesion molecules. *Nature* **2003**, *423* (6936), 190–193. DOI: 10.1038/nature01605.

(6) Sarangapani, K. K.; Yago, T.; Klopocki, A. G.; Lawrence, M. B.; Fieger, C. B.; Rosen, S. D.; McEver, R. P.; Zhu, C. Low force decelerates L-selectin dissociation from P-selectin glycoprotein ligand-1 and endoglycan. *J. Biol. Chem.* **2004**, *279* (3), 2291–2298. DOI: 10.1074/jbc.M310396200.

(7) Woelke, A. L.; Kuehne, C.; Meyer, T.; Galstyan, G.; Dernedde, J.; Knapp, E.-W. Understanding selectin counter-receptor binding from electrostatic energy computations and experimental binding studies. *J. Phys. Chem. B* **2013**, *117* (51), 16443–16454. DOI: 10.1021/jp4099123.

(8) Zhang, X.; Halvorsen, K.; Zhang, C.-Z.; Wong, W. P.; Springer, T. A. Mechanoenzymatic cleavage of the ultralarge vascular protein von Willebrand factor. *Science* **2009**, *324* (5932), 1330–1334. DOI: 10.1126/science.1170905.

(9) Rief, M. Reversible Unfolding of Individual Titin Immunoglobulin Domains by AFM. *Science* **1997**, *276* (5315), 1109–1112. DOI: 10.1126/science.276.5315.1109.

(10) Li, H.; Linke, W. A.; Oberhauser, A. F.; Carrion-Vazquez, M.; Kerkvliet, J. G.; Lu, H.; Marszalek, P. E.; Fernandez, J. M. Reverse engineering of the giant muscle protein titin. *Nature* **2002**, *418* (6901), 998–1002. DOI: 10.1038/nature00938.

(11) Lv, S.; Dudek, D. M.; Cao, Y.; Balamurali, M. M.; Gosline, J.; Li, H. Designed biomaterials to mimic the mechanical properties of muscles. *Nature* **2010**, *465* (7294), 69–73. DOI: 10.1038/nature09024.

(12) Hickenboth, C. R.; Moore, J. S.; White, S. R.; Sottos, N. R.; Baudry, J.; Wilson, S. R. Biasing reaction pathways with mechanical force. *Nature* **2007**, *446* (7134), 423–427. DOI: 10.1038/nature05681.

(13) Groote, R.; Jakobs, Robert T. M.; Sijbesma, R. P. Mechanocatalysis: forcing latent catalysts into action. *Polym. Chem.* **2013**, *4* (18), 4846. DOI: 10.1039/c3py00071k.

(14) Léger, J.-F.; Robert, J.; Bourdieu, L.; Chatenay, D.; Marko, J. F. RecA binding to a single double-stranded DNA molecule: A possible role of DNA conformational fluctuations. *Proc. Natl. Acad. Sci. USA* **1998**, *95* (21), 12295–12299. DOI: 10.1073/pnas.95.21.12295.

(15) Strick, T.; Allemand, J.-F.; Bensimon, D.; Bensimon, A.; Croquette, V. The Elasticity of a Single Supercoiled DNA Molecule. *Science* **1996**, *271* (5257), 1835–1837. DOI: 10.1126/science.271.5257.1835.

(16) Gittes, F.; Schmidt, C. F. Interference model for back-focal-plane displacement detection in optical tweezers. *Opt. Lett.* **1998**, *23* (1), 7. DOI: 10.1364/OL.23.000007.

(17) Moy, V. T.; Florin, E.; Gaub, H. E. Intermolecular forces and energies between ligands and receptors. *Science* **1994**, *266* (5183), 257–259. DOI: 10.1126/science.7939660.

(18) Lee, G. U.; Kidwell, D. A.; Colton, R. J. Sensing Discrete Streptavidin-Biotin Interactions with Atomic Force Microscopy. *Langmuir* **1994**, *10* (2), 354–357. DOI: 10.1021/la00014a003.

(19) Zhurkov, S. N.; Narzullaev, B. N. Vremennaya i temperaturnaya zavisimost prochnosti tverdykh tel. *Zh. Tekh. Fiz.* **1953**, *23* (10), 1677–1689.

(20) Regel, V. R.; Leksovsky, A. M. A study of fatigue within the framework of the kinetic concept of fracture. *Int. J. Fract.* **1967**, *3* (2). DOI: 10.1007/BF00182688.

(21) Bell, G. Models for the specific adhesion of cells to cells. *Science* **1978**, *200* (4342), 618–627. DOI: 10.1126/science.347575.

(22) Hänggi, P.; Talkner, P.; Borkovec, M. Reaction-rate theory: Fifty years after Kramers. *Rev. Mod. Phys.* **1990**, *62* (2), 251–341. DOI: 10.1103/RevModPhys.62.251.

(23) Evans, E.; Ritchie, K. Dynamic strength of molecular adhesion bonds. *Biophys. J.* **1997**, *72* (4), 1541–1555. DOI: 10.1016/S0006-3495(97)78802-7.

(24) Fernandez, J. M.; Li, H. Force-clamp spectroscopy monitors the folding trajectory of a single protein. *Science* **2004**, *303* (5664), 1674–1678. DOI: 10.1126/science.1092497.

(25) Beyer, M. K. The mechanical strength of a covalent bond calculated by density functional theory. *J. Chem. Phys.* **2000**, *112* (17), 7307. DOI: 10.1063/1.481330.

(26) Morfill, J.; Blank, K.; Zahnd, C.; Luginbühl, B.; Kühner, F.; Gottschalk, K.-E.; Plückthun, A.; Gaub, H. E. Affinity-matured recombinant antibody fragments analyzed by single-molecule force spectroscopy. *Biophys. J.* **2007**, *93* (10), 3583–3590. DOI: 10.1529/biophysj.107.112532.

(27) Teulon, J.-M.; Delcuze, Y.; Odorico, M.; Chen, S.-w. W.; Parot, P.; Pellequer, J.-L. Single and multiple bonds in (strept)avidin-biotin interactions. *J. Mol. Recognit.* **2011**, *24* (3), 490–502. DOI: 10.1002/jmr.1109.

(28) Zocher, M.; Zhang, C.; Rasmussen, Søren G F; Kobilka, B. K.; Müller, D. J. Cholesterol increases kinetic, energetic, and mechanical stability of the human β2-adrenergic receptor. *Proc. Natl. Acad. Sci. USA* **2012**, *109* (50), 72. DOI: 10.1073/pnas.1210373109.

(29) Kawamura, S.; Colozo, A. T.; Ge, L.; Müller, D. J.; Park, P. S.-H. Structural, energetic, and mechanical perturbations in rhodopsin mutant that causes congenital stationary night blindness. *J. Biol. Chem.* **2012**, *287* (26), 21826–21835. DOI: 10.1074/jbc.M112.340182.

(30) Eckel, R.; Ros, R.; Decker, B.; Mattay, J.; Anselmetti, D. Supramolecular chemistry at the single-molecule level. *Angew. Chem. Int. Ed.* **2005**, *44* (3), 484–488. DOI: 10.1002/anie.200461382.

(31) Talotta, C.; Gaeta, C.; Neri, P. Endo-complexation of alkylammonium ions by calix[4]arene cavity: facilitating cation-π interactions through the weakly coordinating anion approach. *J. Org. Chem.* **2014**, *79* (20), 9842–9846. DOI: 10.1021/jo5016689.

(32) Embrechts, A.; Velders, A. H.; Schönherr, H.; Vancso, G. J. Self-complementary recognition of supramolecular urea-aminotriazines in solution and on surfaces. *Langmuir* **2011**, *27* (23), 14272–14278. DOI: 10.1021/la203433z.

(33) Hanley, W.; McCarty, O.; Jadhav, S.; Tseng, Y.; Wirtz, D.; Konstantopoulos, K. Single molecule characterization of P-selectin/ligand binding. *J. Biol. Chem.* **2003**, *278* (12), 10556–10561. DOI: 10.1074/jbc.M213233200.

(34) Schoeler, C.; Malinowska, K. H.; Bernardi, R. C.; Milles, L. F.; Jobst, M. A.; Durner, E.; Ott, W.; Fried, D. B.; Bayer, E. A.; Schulten, K.; Gaub, H. E.; Nash, M. A. Ultrastable cellulosome-adhesion complex tightens under load. *Nat. Commun.* **2014**, *5*, 5635. DOI: 10.1038/ncomms6635.

(35) Krykbaev, R. A.; Tsantili, P.; Jeffrey, P. D.; Margolies, M. N. Modifying specificity of antidigoxin antibodies using insertional mutagenesis. *Protein Sci.* **2002**, *11* (12), 2899–2908. DOI: 10.1110/ps.0223402.

(36) Kiessling, L. L.; Gestwicki, J. E.; Strong, L. E. Synthetic multivalent ligands as probes of signal transduction. *Angew. Chem. Int. Ed.* **2006**, *45* (15), 2348–2368. DOI: 10.1002/anie.200502794.

(37) Badjić, J. D.; Nelson, A.; Cantrill, S. J.; Turnbull, W. B.; Stoddart, J. F. Multivalency and cooperativity in supramolecular chemistry. *Acc. Chem. Res.* **2005**, *38* (9), 723–732. DOI: 10.1021/ar040223k.

(38) Fasting, C.; Schalley, C. A.; Weber, M.; Seitz, O.; Hecht, S.; Koksch, B.; Dernedde, J.; Graf, C.; Knapp, E.-W.; Haag, R. Multivalency as a chemical organization and action principle. *Angew. Chem. Int. Ed.* **2012**, *51* (42), 10472–10498. DOI: 10.1002/anie.201201114.

(39) Mammen, M.; Choi, S.-K.; Whitesides, G. M. Polyvalent Interactions in Biological Systems: Implications for Design and Use of Multivalent Ligands and Inhibitors. *Angew. Chem. Int. Ed.* **1998**, *37* (20), 2754–2794. DOI: 10.1002/(SICI)1521-3773(19981102)37:20<2754:AID-ANIE2754>3.0.CO;2-3.

(40) Brockwell, D. J.; Beddard, G. S.; Paci, E.; West, D. K.; Olmsted, P. D.; Smith, D. A.; Radford, S. E. Mechanically unfolding the small, topologically simple protein L. *Biophys. J.* **2005**, *89* (1), 506–519. DOI: 10.1529/biophysj.105.061465.

(41) Li, M. S. Secondary structure, mechanical stability, and location of transition state of proteins. *Biophys. J.* **2007**, *93* (8), 2644–2654. DOI: 10.1529/biophysj.107.106138.

(42) Hoffmann, T.; Tych, K. M.; Hughes, M. L.; Brockwell, D. J.; Dougan, L. Towards design principles for determining the mechanical stability of proteins. *Phys. Chem. Chem. Phys.* **2013**, *15* (38), 15767–15780. DOI: 10.1039/c3cp52142g.

(43) Hoffmann, T.; Tych, K. M.; Crosskey, T.; Schiffrin, B.; Brockwell, D. J.; Dougan, L. Rapid and Robust Polyprotein Production Facilitates Single Molecule Mechanical Characterization of β-Barrel Assembly Machinery Polypeptide Transport Associated Domains. *ACS Nano* **2015**, *9* (9), 8811–8821**.** DOI: 10.1021/acsnano.5b01962.

(44) Sikora, M.; Sulkowska, J. I.; Witkowski, B. S.; Cieplak, M. BSDB: the biomolecule stretching database. *Nucleic Acids Res.* **2011**, *39* (Database issue), 50. DOI: 10.1093/nar/gkq851.

(45) Sikora, M.; Cieplak, M. Cystine Plug and Other Novel Mechanisms of Large Mechanical Stability in Dimeric Proteins. *Phys. Rev. Lett.* **2012**, *109* (20). DOI: 10.1103/PhysRevLett.109.208101.

(46) Mulder, A.; Huskens, J.; Reinhoudt, D. N. Multivalency in supramolecular chemistry and nanofabrication. *Org. Biomol. Chem.* **2004**, *2* (23), 3409–3424. DOI: 10.1039/b413971b.

(47) Diestler, D. J.; Knapp, E.-W. Statistical Mechanics of the Stability of Multivalent Ligand−Receptor Complexes. *J. Phys. Chem. C* **2010**, *114* (12), 5287–5304. DOI: 10.1021/jp904258c.

(48) Hosono, N.; Kushner, A. M.; Chung, J.; Palmans, A. R. A.; Guan, Z.; Meijer, E. W. Forced unfolding of single-chain polymeric nanoparticles. *J. Am. Chem. Soc.* **2015**, *137* (21), 6880–6888. DOI: 10.1021/jacs.5b02967.

(49) Gomez-Casado, A.; Dam, H. H.; Yilmaz, M. D.; Florea, D.; Jonkheijm, P.; Huskens, J. Probing Multivalent Interactions in a Synthetic Host–Guest Complex by Dynamic Force Spectroscopy. *J. Am. Chem. Soc.* **2011**, *133* (28), 10849–10857. DOI: 10.1021/ja2016125.

(50) Beijer, F. H.; Sijbesma, R. P.; Kooijman, H.; Spek, A. L.; Meijer, E. W. Strong Dimerization of Ureidopyrimidones via Quadruple Hydrogen Bonding. *J. Am. Chem. Soc.* **1998**, *120* (27), 6761–6769. DOI: 10.1021/ja974112a.

(51) Embrechts, A.; Schönherr, H.; Vancso, G. J. Rupture force of single supramolecular bonds in associative polymers by AFM at fixed loading rates. *J. Phys. Chem. B* **2008**, *112* (25), 7359–7362. DOI: 10.1021/jp803260n.

(52) Embrechts, A.; Schönherr, H.; Vancso, G. J. Forced unbinding of individual urea-aminotriazine supramolecular polymers by atomic force microscopy: a closer look at the potential energy landscape and binding lengths at fixed loading rates. *J. Phys. Chem. B* **2012**, *116* (1), 565–570. DOI: 10.1021/jp2089752.

(53) Beijer, F. H.; Kooijman, H.; Spek, A. L.; Sijbesma, R. P.; Meijer, E. W. Self-Complementarity Achieved through Quadruple Hydrogen Bonding. *Angew. Chem. Int. Ed.* **1998**, *37* (1-2), 75–78. DOI: 10.1002/(SICI)1521-3773(19980202)37:1/2<75:AID-ANIE75>3.0.CO;2-R.

(54) Blight, B. A.; Hunter, C. A.; Leigh, D. A.; McNab, H.; Thomson, Patrick I T. An AAAA–DDDD quadruple hydrogen-bond array. *Nat. Chem.* **2011**, *3* (3), 244–248. DOI: 10.1038/NCHEM.987.

(55) Schröder, T.; Geisler, T.; Walhorn, V.; Schnatwinkel, B.; Anselmetti, D.; Mattay, J. Single-molecule force spectroscopy of supramolecular heterodimeric capsules. *Phys. Chem. Chem. Phys.* **2010**, *12* (36), 10981–10987. DOI: 10.1039/c0cp00227e.

(56) Luzar, A.; Chandler, D. Structure and hydrogen bond dynamics of water–dimethyl sulfoxide mixtures by computer simulations. *J. Chem. Phys.* **1993**, *98* (10), 8160. DOI: 10.1063/1.464521.

(57) Hogben, H. J.; Sprafke, J. K.; Hoffmann, M.; Pawlicki, M.; Anderson, H. L. Stepwise effective molarities in porphyrin oligomer complexes: preorganization results in exceptionally strong chelate cooperativity. *J. Am. Chem. Soc.* **2011**, *133* (51), 20962–20969. DOI: 10.1021/ja209254r.

(58) Liese, S.; Netz, R. R. Influence of length and flexibility of spacers on the binding affinity of divalent ligands. *Beilstein J. Org. Chem.* **2015**, *11*, 804–816. DOI: 10.3762/bjoc.11.90.

(59) O'Hagan, D. Pyrrole, pyrrolidine pyridine, piperidine, azepine and tropane alkaloids. *Nat. Prod. Rep.* **1997**, *14* (6), 637. DOI: 10.1039/np9971400637.

(60) Kapinos, L. E.; Sigel, H. Acid–base and metal ion binding properties of pyridine-type ligands in aqueous solution. *Inorg. Chim. Acta* **2002**, *337*, 131–142. DOI: 10.1016/S0020-1693(02)00993-3.

(61) Irving, H.; Williams, R. J. P. Order of Stability of Metal Complexes. *Nature* **1948**, *162* (4123), 746–747. DOI: 10.1038/162746a0.

(62) Bjerrum, J.; Stålhandske, C.; Husebye, S.; Mikalsen, Ø.; Leander, K.; Swahn, C.-G. Metal Ammine Formation in Solution. XVI. Stability Constants of Some Metal(II)-Pyridine System. *Acta Chem. Scand.* **1973**, *27*, 970–976. DOI: 10.3891/acta.chem.scand.27-0970.

(63) Schmitt, L.; Ludwig, M.; Gaub, H. E.; Tampé, R. A Metal-Chelating Microscopy Tip as a New Toolbox for Single-Molecule Experiments by Atomic Force Microscopy. *Biophys. J.* **2000**, *78* (6), 3275–3285. DOI: 10.1016/S0006-3495(00)76863-9.

(64) Noy, A. Force spectroscopy 101: how to design, perform, and analyze an AFM-based single molecule force spectroscopy experiment. *Curr. Opin. Chem. Biol.* **2011**, *15* (5), 710–718. DOI: 10.1016/j.cbpa.2011.07.020.

(65) Hinterdorfer, P.; Baumgartner, W.; Gruber, H. J.; Schilcher, K.; Schindler, H. Detection and localization of individual antibody-antigen recognition events by atomic force microscopy. *Proc. Natl. Acad. Sci. USA* **1996**, *93* (8), 3477–3481. DOI: 10.1073/pnas.93.8.3477.

(66) Sharma, R. P.; Saini, A.; Singh, S.; Singh, A.; Venugopalan, P.; Starynowicz, P.; Jezierska, J. Spectra–structure relationship: Syntheses, characterization, single crystal X-ray structural studies and packing analyses of two novel copper(II) complexes: [Cu(pyridine)2(H2O)4](p-toluenesulfonate)2 and [Cu(β-picoline)2(H2O)4](p-toluenesulfonate)2. *J. Mol. Struct.* **2011**, *994* (1-3), 21–28. DOI: 10.1016/j.molstruc.2011.02.043.

(67) Gensler, M.; Eidamshaus, C.; Galstyan, A.; Knapp, E.-W.; Reissig, H.-U.; Rabe, J. P. Mechanical Rupture of Mono- and Bivalent Transition Metal Complexes in Experiment and Theory. *J. Phys. Chem. C* **2015**, *119* (8), 4333–4343. DOI: 10.1021/jp511104m.

(68) Vestweber, D.; Blanks, J. E. Mechanisms that regulate the function of the selectins and their ligands. *Physiol. Rev.* **1999**, *79* (1), 181–213.

(69) Hunter, C. A.; Anderson, H. L. What is Cooperativity? *Angew. Chem. Int. Ed.* **2009**, *48* (41), 7488–7499. DOI: 10.1002/anie.200902490.

(70) Schwarzenbach, G. Chelate complex formation as a basis for titration processes. *Anal. Chim. Acta* **1952**, *7*, 141–155. DOI: 10.1016/S0003-2670(01)83321-3.

(71) Zhang, B.; Breslow, R. Enthalpic domination of the chelate effect in cyclodextrin dimers. *J. Am. Chem. Soc.* **1993**, *115* (20), 9353–9354. DOI: 10.1021/ja00073a087.

(72) Chou, K.-C. Low-frequency resonance and cooperativity of hemoglobin. *Trends Biochem. Sci.* **1989**, *14* (6), 212. DOI: 10.1016/0968-0004(89)90026-1.

(73) Jiang, W.; Nowosinski, K.; Löw, N. L.; Dzyuba, E. V.; Klautzsch, F.; Schäfer, A.; Huuskonen, J.; Rissanen, K.; Schalley, C. A. Chelate Cooperativity and Spacer Length Effects on the Assembly Thermodynamics and Kinetics of Divalent Pseudorotaxanes. *J. Am. Chem. Soc.* **2012**, *134* (3), 1860–1868. DOI: 10.1021/ja2107096.

(74) Ercolani, G.; Piguet, C.; Borkovec, M.; Hamacek, J. Symmetry Numbers and Statistical Factors in Self-Assembly and Multivalency. *J. Phys. Chem. B* **2007**, *111* (42), 12195–12203. DOI: 10.1021/jp0740705.

(75) Jencks, W. P. On the attribution and additivity of binding energies. *Proc. Natl. Acad. Sci. USA* **1981**, *78* (7), 4046–4050. DOI: 10.1073/pnas.78.7.4046.

(76) Anderson, H. L. Conjugated Porphyrin Ladders. *Inorg. Chem.* **1994**, *33* (5), 972–981. DOI: 10.1021/ic00083a022.

(77) Taylor, P. N.; Anderson, H. L. Cooperative Self-Assembly of Double-Strand Conjugated Porphyrin Ladders. *J. Am. Chem. Soc.* **1999**, *121* (49), 11538–11545. DOI: 10.1021/ja992821d.

(78) Nowosinski, K.; von Krbek, Larissa K. S.; Traulsen, N. L.; Schalley, C. A. Thermodynamic Analysis of Allosteric and Chelate Cooperativity in Di- and Trivalent Ammonium/Crown-Ether Pseudorotaxanes. *Org. Lett.* **2015**, *17* (20), 5076–5079. DOI: 10.1021/acs.orglett.5b02592.

(79) Carter, P. J.; Winter, G.; Wilkinson, A. J.; Fersht, A. R. The use of double mutants to detect structural changes in the active site of the tyrosyl-tRNA synthetase (Bacillus stearothermophilus). *Cell* **1984**, *38* (3), 835–840. DOI: 10.1016/0092-8674(84)90278-2.

(80) Cockroft, S. L.; Hunter, C. A. Chemical double-mutant cycles: Dissecting non-covalent interactions. *Chem. Soc. Rev.* **2007**, *36* (2), 172–188. DOI: 10.1039/B603842P.

(81) Evans, E. Looking inside molecular bonds at biological interfaces with dynamic force spectroscopy. *Biophys. Chem.* **1999**, *82* (2-3), 83–97. DOI: 10.1016/S0301-4622(99)00108-8.

(82) Mulder, A.; Auletta, T.; Sartori, A.; Del Ciotto, S.; Casnati, A.; Ungaro, R.; Huskens, J.; Reinhoudt, D. N. Divalent binding of a bis(adamantyl)-functionalized calix4arene to beta-cyclodextrin-based hosts: an experimental and theoretical study on multivalent binding in solution and at self-assembled monolayers. *J. Am. Chem. Soc.* **2004**, *126* (21), 6627–6636. DOI: 10.1021/ja0317168.

(83) Gensler, M.; Eidamshaus, C.; Taszarek, M.; Reissig, H.-U.; Rabe, J. P. Mechanical stability of bivalent transition metal complexes analyzed by single-molecule force spectroscopy. *Beilstein J. Org. Chem.* **2015**, *11*, 817–827. DOI: 10.3762/bjoc.11.91.

(84) Fyfe, M. C. T.; Stoddart, J. F. Synthetic Supramolecular Chemistry. *Acc. Chem. Res.* **1997**, *30* (10), 393–401. DOI: 10.1021/ar950199y.

(85) Allen, A. E.; MacMillan, D. W. C. Synergistic catalysis: A powerful synthetic strategy for new reaction development. *Chem. Sci.* **2012**, *3* (3), 633. DOI: 10.1039/c2sc00907b.

(86) Qi, Z.; Bharate, P.; Lai, C.-H.; Ziem, B.; Böttcher, C.; Schulz, A.; Beckert, F.; Hatting, B.; Mülhaupt, R.; Seeberger, P. H.; Haag, R. Multivalency at Interfaces: Supramolecular Carbohydrate-Functionalized Graphene Derivatives for Bacterial Capture, Release, and Disinfection. *Nano Lett.* **2015**, *15* (9), 6051–6057. DOI: 10.1021/acs.nanolett.5b02256.

(87) Binnig, G.; Quate, C. F. Atomic Force Microscope. *Phys. Rev. Lett.* **1986**, *56* (9), 930–933. DOI: 10.1103/PhysRevLett.56.930.

(88) Poggi, M. A.; Gadsby, E. D.; Bottomley, L. A.; King, W. P.; Oroudjev, E.; Hansma, H. Scanning probe microscopy. *Anal. Chem.* **2004**, *76* (12), 3429–3443. DOI: 10.1021/ac0400818.

(89) Meyer, E.; Hug, H. J.; Bennewitz, R. *Scanning Probe Microscopy: The Lab on a Tip*; Advanced Texts in Physics; Springer: Berlin, Heidelberg, 2004.

(90) Dufrêne, Y. F.; Evans, E.; Engel, A.; Helenius, J.; Gaub, H. E.; Müller, D. J. Five challenges to bringing single-molecule force spectroscopy into living cells. *Nat. Methods* **2011**, *8* (2), 123–127. DOI: 10.1038/nmeth0211-123.

(91) Butt, H.-J.; Cappella, B.; Kappl, M. Force measurements with the atomic force microscope: Technique, interpretation and applications. *Surf. Sci. Rep.* **2005**, *59* (1-6), 1–152. DOI: 10.1016/j.surfrep.2005.08.003.

(92) Verbelen, C.; Gruber, H. J.; Dufrêne, Y. F. The NTA-His6 bond is strong enough for AFM single-molecular recognition studies. *J. Mol. Recognit.* **2007**, *20* (6), 490–494. DOI: 10.1002/jmr.833.

(93) Oesterhelt, F.; Rief, M.; Gaub, H. E. Single molecule force spectroscopy by AFM indicates helical structure of poly(ethylene-glycol) in water. *New J. Phys.* **1999**, *1*, 6. DOI: 10.1088/1367-2630/1/1/006.

(94) Linke, W. A.; Grützner, A. Pulling single molecules of titin by AFM--recent advances and physiological implications. *Pflugers Arch.* **2008**, *456* (1), 101–115. DOI: 10.1007/s00424-007-0389-x.

(95) Horinek, D.; Serr, A.; Geisler, M.; Pirzer, T.; Slotta, U.; Lud, S. Q.; Garrido, J. A.; Scheibel, T.; Hugel, T.; Netz, R. R. Peptide adsorption on a hydrophobic surface results from an interplay of solvation, surface, and intrapeptide forces. *Proc. Natl. Acad. Sci. USA* **2008**, *105* (8), 2842–2847. DOI: 10.1073/pnas.0707879105.

(96) Schwierz, N.; Horinek, D.; Liese, S.; Pirzer, T.; Balzer, B. N.; Hugel, T.; Netz, R. R. On the relationship between peptide adsorption resistance and surface contact angle: a combined experimental and simulation single-molecule study. *J. Am. Chem. Soc.* **2012**, *134* (48), 19628–19638. DOI: 10.1021/ja304462u.

(97) Kocun, M.; Janshoff, A. Pulling tethers from pore-spanning bilayers: towards simultaneous determination of local bending modulus and lateral tension of membranes. *Small* **2012**, *8* (6), 847–851. DOI: 10.1002/smll.201101557.

(98) Gross, P.; Laurens, N.; Oddershede, L. B.; Bockelmann, U.; Peterman, Erwin J. G.; Wuite, Gijs J. L. Quantifying how DNA stretches, melts and changes twist under tension. *Nat. Phys.* **2011**, *7* (9), 731–736. DOI: 10.1038/NPHYS2002.

(99) Herrero-Galán, E.; Fuentes-Perez, M. E.; Carrasco, C.; Valpuesta, J. M.; Carrascosa, J. L.; Moreno-Herrero, F.; Arias-Gonzalez, J. R. Mechanical identities of

RNA and DNA double helices unveiled at the single-molecule level. *J. Am. Chem. Soc.* **2013**, *135* (1), 122–131. DOI: 10.1021/ja3054755.

(100) Léger, J.-F.; Romano, G.; Sarkar, A.; Robert, J.; Bourdieu, L.; Chatenay, D.; Marko, J. F. Structural Transitions of a Twisted and Stretched DNA Molecule. *Phys. Rev. Lett.* **1999**, *83* (5), 1066–1069. DOI: 10.1103/PhysRevLett.83.1066.

(101) Kühner, F.; Morfill, J.; Neher, R. A.; Blank, K.; Gaub, H. E. Force-induced DNA slippage. *Biophys. J.* **2007**, *92* (7), 2491–2497. DOI: 10.1529/biophysj.106.095836.

(102) Wang, M.; Liechti, K. M.; White, J. M.; Winter, R. M. Nanoindentation of polymeric thin films with an interfacial force microscope. *J. Mech. Phys. Solids* **2004**, *52* (10), 2329–2354. DOI: 10.1016/j.jmps.2004.03.005.

(103) Bertz, M.; Wilmanns, M.; Rief, M. The titin-telethonin complex is a directed, superstable molecular bond in the muscle Z-disk. *Proc. Natl. Acad. Sci. USA* **2009**, *106* (32), 13307–133310. DOI: 10.1073/pnas.0902312106.

(104) Grandbois, M. How Strong Is a Covalent Bond? *Science* **1999**, *283* (5408), 1727–1730. DOI: 10.1126/science.283.5408.1727.

(105) Ribas-Arino, J.; Marx, D. Covalent mechanochemistry: theoretical concepts and computational tools with applications to molecular nanomechanics. *Chem. Rev.* **2012**, *112* (10), 5412–5487. DOI: 10.1021/cr200399q.

(106) Schmidt, S. W.; Kersch, A.; Beyer, M. K.; Clausen-Schaumann, H. Mechanically activated rupture of single covalent bonds: evidence of force induced bond hydrolysis. *Phys. Chem. Chem. Phys.* **2011**, *13* (13), 5994–5999. DOI: 10.1039/c0cp02827d.

(107) Aktah, D.; Frank, I. Breaking Bonds by Mechanical Stress: When Do Electrons Decide for the Other Side? *J. Am. Chem. Soc.* **2002**, *124* (13), 3402–3406. DOI: 10.1021/ja004010b.

(108) Beyer, M. K. Coupling of mechanical and chemical energy: proton affinity as a function of external force. *Angew. Chem. Int. Ed.* **2003**, *42* (40), 4913–4915. DOI: 10.1002/anie.200351748.

(109) Clausen-Schaumann, H.; Seitz, M.; Krautbauer, R.; Gaub, H. E. Force spectroscopy with single bio-molecules. *Curr. Opin. Chem. Biol.* **2000**, *4* (5), 524–530. DOI: 10.1016/S1367-5931(00)00126-5.

(110) Smith, S. B.; Finzi, L.; Bustamante, C. Direct mechanical measurements of the elasticity of single DNA molecules by using magnetic beads. *Science* **1992**, *258* (5085), 1122–1126. DOI: 10.1126/science.1439819.

(111) Livadaru, L.; Netz, R. R.; Kreuzer, H. J. Stretching Response of Discrete Semiflexible Polymers. *Macromol.* **2003**, *36* (10), 3732–3744. DOI: 10.1021/ma020751g.

(112) Hugel, T.; Rief, M.; Seitz, M.; Gaub, H. E.; Netz, R. R. Highly Stretched Single Polymers: Atomic-Force-Microscope Experiments Versus Ab-Initio Theory. *Phys. Rev. Lett.* **2005**, *94* (4). DOI: 10.1103/PhysRevLett.94.048301.

(113) Kienberger, F.; Kada, G.; Gruber, H. J.; Pastushenko, V. P.; Riener, C.; Trieb, M.; Knaus, H.-G.; Schindler, H.; Hinterdorfer, P. Recognition Force Spectroscopy Studies of the NTA-His6 Bond. *Single Mol.* **2000**, *1* (1), 59–65. DOI: 10.1002/(SICI)1438-5171(200004)1:1<59:AID-SIMO59>3.0.CO;2-V.

(114) Beyer, M. K.; Clausen-Schaumann, H. Mechanochemistry: the mechanical activation of covalent bonds. *Chem. Rev.* **2005**, *105* (8), 2921–2948. DOI: 10.1021/cr030697h.

(115) Bustamante, C.; Marko, J. F.; Siggia, E. D.; Smith, S. B. Entropic elasticity of lambda-phage DNA. *Science* **1994**, *265* (5178), 1599–1600. DOI: 10.1126/science.8079175.

(116) Bustamante, C.; Bryant, Z.; Smith, S. B. Ten years of tension: single-molecule DNA mechanics. *Nature* **2003**, *421* (6921), 423–427. DOI: 10.1038/nature01405.

(117) Gore, J.; Bryant, Z.; Nöllmann, M.; Le, M. U.; Cozzarelli, N. R.; Bustamante, C. DNA overwinds when stretched. *Nature* **2006**, *442* (7104), 836–839. DOI: 10.1038/nature04974.

(118) Walter, N. G.; Bustamante, C. Introduction to single molecule imaging and mechanics: seeing and touching molecules one at a time. *Chem. Rev.* **2014**, *114* (6), 3069–3071. DOI: 10.1021/cr500059w.

(119) Olof, S. N.; Grieve, J. A.; Phillips, D. B.; Rosenkranz, H.; Yallop, M. L.; Miles, M. J.; Patil, A. J.; Mann, S.; Carberry, D. M. Measuring nanoscale forces with living probes. *Nano Lett.* **2012**, *12* (11), 6018–6023. DOI: 10.1021/nl303585w.

(120) Phillips, D. B.; Gibson, G. M.; Bowman, R.; Padgett, M. J.; Hanna, S.; Carberry, D. M.; Miles, M. J.; Simpson, S. H. An optically actuated surface scanning probe. *Opt. Express* **2012**, *20* (28), 29679–29693. DOI: 10.1364/OE.20.029679.

(121) Berg-Sørensen, K.; Flyvbjerg, H. Power spectrum analysis for optical tweezers. *Rev. Sci. Instrum.* **2004**, *75* (3), 594. DOI: 10.1063/1.1645654.

(122) Weber, M.; Bujotzek, A.; Haag, R. Quantifying the rebinding effect in multivalent chemical ligand-receptor systems. *J. Chem. Phys.* **2012**, *137* (5), 54111. DOI: 10.1063/1.4739501.

(123) Schönherr, H.; Beulen, Marcel W. J.; Bügler, J.; Huskens, J.; van Veggel, Frank C. J. M.; Reinhoudt, D. N.; Vancso, G. J. Individual Supramolecular Host−Guest Interactions Studied by Dynamic Single Molecule Force Spectroscopy. *J. Am. Chem. Soc.* **2000**, *122* (20), 4963–4967. DOI: 10.1021/ja994040i.

(124) Zapotoczny, S.; Auletta, T.; Jong, M. R. de; Schönherr, H.; Huskens, J.; van Veggel, Frank C. J. M.; Reinhoudt, D. N.; Vancso, G. J. Chain Length and Concentration Dependence of β-Cyclodextrin−Ferrocene Host−Guest Complex Rupture Forces Probed by Dynamic Force Spectroscopy. *Langmuir* **2002**, *18* (18), 6988–6994. DOI: 10.1021/la0259095.

(125) Auletta, T.; Jong, M. R. de; Mulder, A.; van Veggel, Frank C. J. M.; Huskens, J.; Reinhoudt, D. N.; Zou, S.; Zapotoczny, S.; Schönherr, H.; Vancso, G. J.; Kuipers, L. β-Cyclodextrin Host−Guest Complexes Probed under Thermodynamic Equilibrium: Thermodynamics and AFM Force Spectroscopy. *J. Am. Chem. Soc.* **2004**, *126* (5), 1577–1584. DOI: 10.1021/ja0383569.

(126) Evans, E. Probing the relation between force--lifetime--and chemistry in single molecular bonds. *Annu. Rev. Biophys. Biomol. Struct.* **2001**, *30*, 105–128. DOI: 10.1146/annurev.biophys.30.1.105.

(127) Friddle, R. W.; Podsiadlo, P.; Artyukhin, A. B.; Noy, A. Near-Equilibrium Chemical Force Microscopy. *J. Phys. Chem. C* **2008**, *112* (13), 4986–4990. DOI: 10.1021/jp7095967.

(128) Evans, E. Introductory Lecture Energy landscapes of biomolecular adhesion and receptor anchoring at interfaces explored with dynamic force spectroscopy. *Farad. Discuss.* **1999**, *111*, 1–16. DOI: 10.1039/A809884K.

(129) Janke, M.; Rudzevich, Y.; Molokanova, O.; Metzroth, T.; Mey, I.; Diezemann, G.; Marszalek, P. E.; Gauss, J.; Böhmer, V.; Janshoff, A. Mechanically interlocked calix[4]arene dimers display reversible bond breakage under force. *Nat. Nanotechnol.* **2009**, *4* (4), 225–229. DOI: 10.1038/NNANO.2008.416.

(130) Puchner, E. M.; Kufer, S. K.; Strackharn, M.; Stahl, S. W.; Gaub, H. E. Nanoparticle self-assembly on a DNA-scaffold written by single-molecule cut-and-paste. *Nano Lett.* **2008**, *8* (11), 3692–3695. DOI: 10.1021/nl8018627.

(131) Rief, M.; Clausen-Schaumann, H.; Gaub, H. E. Sequence-dependent mechanics of single DNA molecules. *Nat. Struct. Biol.* **1999**, *6* (4), 346–349. DOI: 10.1038/7582.

(132) Strackharn, M.; Stahl, S. W.; Puchner, E. M.; Gaub, H. E. Functional assembly of aptamer binding sites by single-molecule cut-and-paste. *Nano Lett.* **2012**, *12* (5), 2425–2428. DOI: 10.1021/nl300422y.

(133) Strackharn, M.; Pippig, D. A.; Meyer, P.; Stahl, S. W.; Gaub, H. E. Nanoscale arrangement of proteins by single-molecule cut-and-paste. *J. Am. Chem. Soc.* **2012**, *134* (37), 15193–15196. DOI: 10.1021/ja305689r.

(134) Heucke, S. F.; Baumann, F.; Acuna, G. P.; Severin, P. M. D.; Stahl, S. W.; Strackharn, M.; Stein, I. H.; Altpeter, P.; Tinnefeld, P.; Gaub, H. E. Placing individual molecules in the center of nanoapertures. *Nano Lett.* **2014**, *14* (2), 391–395. DOI: 10.1021/nl401517a.

(135) te Riet, J.; Katan, A. J.; Rankl, C.; Stahl, S. W.; van Buul, Arend M; Phang, I. Y.; Gomez-Casado, A.; Schön, P.; Gerritsen, J. W.; Cambi, A.; Rowan, A. E.; Vancso, G. J.; Jonkheijm, P.; Huskens, J.; Oosterkamp, T. H.; Gaub, H. E.; Hinterdorfer, P.; Figdor, C. G.; Speller, S. Interlaboratory round robin on cantilever calibration for AFM force spectroscopy. *Ultramicroscopy* **2011**, *111* (12), 1659–1669. DOI: 10.1016/j.ultramic.2011.09.012.

(136) Slattery, A. D.; Blanch, A. J.; Quinton, J. S.; Gibson, C. T. Calibration of atomic force microscope cantilevers using standard and inverted static methods assisted by FIB-milled spatial markers. *Nanotechnol.* **2013**, *24* (1), 15710. DOI: 10.1088/0957-4484/24/1/015710.

(137) Dietz, H.; Rief, M. Exploring the energy landscape of GFP by single-molecule mechanical experiments. *Proc. Natl. Acad. Sci. USA* **2004**, *101* (46), 16192–16197. DOI: 10.1073/pnas.0404549101.

(138) Sader, J. E.; Sanelli, J. A.; Adamson, B. D.; Monty, J. P.; Wei, X.; Crawford, S. A.; Friend, J. R.; Marusic, I.; Mulvaney, P.; Bieske, E. J. Spring constant calibration of atomic force microscope cantilevers of arbitrary shape. *Rev. Sci. Instrum.* **2012**, *83* (10), 103705. DOI: 10.1063/1.4757398.

(139) Cleveland, J. P.; Manne, S.; Bocek, D.; Hansma, P. K. A nondestructive method for determining the spring constant of cantilevers for scanning force microscopy. *Rev. Sci. Instrum.* **1993**, *64* (2), 403. DOI: 10.1063/1.1144209.

(140) Clifford, C. A.; Seah, M. P. Improved methods and uncertainty analysis in the calibration of the spring constant of an atomic force microscope cantilever using static experimental methods. *Meas. Sci. Technol.* **2009**, *20* (12), 125501. DOI: 10.1088/0957-0233/20/12/125501.

(141) Pirzer, T.; Hugel, T. Atomic force microscopy spring constant determination in viscous liquids. *Rev. Sci. Instrum.* **2009**, *80* (3), 35110. DOI: 10.1063/1.3100258.

(142) Ohler, B. Cantilever spring constant calibration using laser Doppler vibrometry. *Rev. Sci. Instrum.* **2007**, *78* (6), 63701. DOI: 10.1063/1.2743272.

(143) Gates, R. S.; Osborn, W. A.; Pratt, J. R. Experimental determination of mode correction factors for thermal method spring constant calibration of AFM cantilevers using laser Doppler vibrometry. *Nanotechnol.* **2013**, *24* (25), 255706. DOI: 10.1088/0957-4484/24/25/255706.

(144) Gibson, C. T.; Watson, G. S.; Myhra, S. Determination of the spring constants of probes for force microscopy/spectroscopy. *Nanotechnol.* **1996**, *7* (3), 259–262. DOI: 10.1088/0957-4484/7/3/014.

(145) Gates, R. S.; Reitsma, M. G. Precise atomic force microscope cantilever spring constant calibration using a reference cantilever array. *Rev. Sci. Instrum.* **2007**, *78* (8), 86101. DOI: 10.1063/1.2764372.

(146) Gates, R. S.; Pratt, J. R. Accurate and precise calibration of AFM cantilever spring constants using laser Doppler vibrometry. *Nanotechnol.* **2012**, *23* (37), 375702. DOI: 10.1088/0957-4484/23/37/375702.

(147) Reitsma, Mark G., Gheorghe, Stan, DelRio, Frank, Pratt, Jon R., Cook, Robert F. Scanning Probe Microscopy Measurements and Standards. https://www.nist.gov/sites/default/files/documents/mml/mmsd/852_09_91b.pdf.

(148) Horejs, C.; Ristl, R.; Tscheliessnig, R.; Sleytr, U. B.; Pum, D. Single-molecule force spectroscopy reveals the individual mechanical unfolding pathways of a surface layer protein. *J. Biol. Chem.* **2011**, *286* (31), 27416–27424. DOI: 10.1074/jbc.M111.251322.

(149) *MEMS and nanotechnology: Proceedings of the 2010 Annual Conference on Experimental and Applied Mechanics;* Proulx, T., Ed., 2011.

(150) Sader, J. E. Frequency response of cantilever beams immersed in viscous fluids with applications to the atomic force microscope. *J. Appl. Phys.* **1998**, *84* (1), 64. DOI: 10.1063/1.368002.

(151) Sader, J. E.; Chon, James W. M.; Mulvaney, P. Calibration of rectangular atomic force microscope cantilevers. *Rev. Sci. Instrum.* **1999**, *70* (10), 3967. DOI: 10.1063/1.1150021.

(152) Sader, J. E.; Pacifico, J.; Green, C. P.; Mulvaney, P. General scaling law for stiffness measurement of small bodies with applications to the atomic force microscope. *J. Appl. Phys.* **2005**, *97* (12), 124903. DOI: 10.1063/1.1935133.

(153) Green, C. P.; Lioe, H.; Cleveland, J. P.; Proksch, R.; Mulvaney, P.; Sader, J. E. Normal and torsional spring constants of atomic force microscope cantilevers. *Rev. Sci. Instrum.* **2004**, *75* (6), 1988. DOI: 10.1063/1.1753100.

(154) Proksch, R.; Schäffer, T. E.; Cleveland, J. P.; Callahan, R. C.; Viani, M. B. Finite optical spot size and position corrections in thermal spring constant calibration. *Nanotechnol.* **2004**, *15* (9), 1344–1350. DOI: 10.1088/0957-4484/15/9/039.

(155) Sader, J. E.; Larson, I.; Mulvaney, P.; White, L. R. Method for the calibration of atomic force microscope cantilevers. *Rev. Sci. Instrum.* **1995**, *66* (7), 3789. DOI: 10.1063/1.1145439.

(156) Hutter, J. L.; Bechhoefer, J. Calibration of atomic-force microscope tips. *Rev. Sci. Instrum.* **1993**, *64* (7), 1868. DOI: 10.1063/1.1143970.

(157) Walters, D. A.; Cleveland, J. P.; Thomson, N. H.; Hansma, P. K.; Wendman, M. A.; Gurley, G.; Elings, V. Short cantilevers for atomic force microscopy. *Rev. Sci. Instrum.* **1996**, *67* (10), 3583. DOI: 10.1063/1.1147177.

(158) Oden, P. I.; Chen, G. Y.; Steele, R. A.; Warmack, R. J.; Thundat, T. Viscous drag measurements utilizing microfabricated cantilevers. *Appl. Phys. Lett.* **1996**, *68* (26), 3814. DOI: 10.1063/1.116626.

(159) Cook, S. M.; Lang, K. M.; Chynoweth, K. M.; Wigton, M.; Simmonds, R. W.; Schäffer, T. E. Practical implementation of dynamic methods for measuring atomic force microscope cantilever spring constants. *Nanotechnol.* **2006**, *17* (9), 2135–2145. DOI: 10.1088/0957-4484/17/9/010.

(160) Rugar, D.; Mamin, H. J.; Erlandsson, R.; Stern, J. E.; Terris, B. D. Force microscope using a fiber-optic displacement sensor. *Rev. Sci. Instrum.* **1988**, *59* (11), 2337. DOI: 10.1063/1.1139958.

(161) Butt, H.-J.; Jaschke, M. Calculation of thermal noise in atomic force microscopy. *Nanotechnol.* **1995**, *6* (1), 1–7. DOI: 10.1088/0957-4484/6/1/001.

(162) Stark, R. W.; Drobek, T.; Heckl, W. M. Thermomechanical noise of a free v-shaped cantilever for atomic-force microscopy. *Ultramicroscopy* **2001**, *86* (1-2), 207–215. DOI: 10.1016/S0304-3991(00)00077-2.

(163) Schäffer, T. E.; Fuchs, H. Optimized detection of normal vibration modes of atomic force microscope cantilevers with the optical beam deflection method. *J. Appl. Phys.* **2005**, *97* (8), 83524. DOI: 10.1063/1.1872202.

(164) Struckmeier, J.; Wahl, R.; Leuschner, M.; Nunes, J.; Janovjak, H.; Geisler, U.; Hofmann, G.; Jähnke, T.; Müller, D. J. Fully automated single-molecule force spectroscopy for screening applications. *Nanotechnol.* **2008**, *19* (38), 384020. DOI: 10.1088/0957-4484/19/38/384020.

(165) Giannotti, M. I.; Vancso, G. J. Interrogation of Single Synthetic Polymer Chains and Polysaccharides by AFM-Based Force Spectroscopy. *ChemPhysChem* **2007**, *8* (16), 2290–2307. DOI: 10.1002/cphc.200700175.

(166) Kuhn, W. Über die Gestalt fadenförmiger Moleküle in Lösungen. *Kolloid-Zeitschrift* **1934**, *68* (1), 2–15. DOI: 10.1007/BF01451681.

(167) Porod, G. Zusammenhang zwischen mittlerem Endpunktsabstand und Kettenlänge bei Fadenmolekülen. *Monatshefte für Chemie* **1949**, *80* (2), 251–255. DOI: 10.1007/BF00906469.

(168) Kratky, O.; Porod, G. Röntgenuntersuchung gelöster Fadenmoleküle. *Recl. Trav. Chim. Pays-Bas* **1949**, *68* (12), 1106–1122. DOI: 10.1002/recl.19490681203.

(169) Zhang, B.; Evans, J. S. Modeling AFM-Induced PEVK Extension and the Reversible Unfolding of Ig/FNIII Domains in Single and Multiple Titin Molecules. *Biophys. J.* **2001**, *80* (2), 597–605. DOI: 10.1016/S0006-3495(01)76040-7.

(170) Smith, S. B.; Cui, Y.; Bustamante, C. Overstretching B-DNA: the elastic response of individual double-stranded and single-stranded DNA molecules. *Science* **1996**, *271* (5250), 795–799.

(171) Marko, J. F.; Siggia, E. D. Stretching DNA. *Macromol.* **1995**, *28* (26), 8759–8770. DOI: 10.1021/ma00130a008.

(172) Odijk, T. Stiff Chains and Filaments under Tension. *Macromol.* **1995**, *28* (20), 7016–7018. DOI: 10.1021/ma00124a044.

(173) Wang, M. D.; Yin, H.; Landick, R.; Gelles, J.; Block, S. M. Stretching DNA with optical tweezers. *Biophys. J.* **1997**, *72* (3), 1335–1346. DOI: 10.1016/S0006-3495(97)78780-0.

(174) Kienberger, F.; Pastushenko, V. P.; Kada, G.; Gruber, H. J.; Riener, C.; Schindler, H.; Hinterdorfer, P. Static and Dynamical Properties of Single Poly(Ethylene Glycol) Molecules Investigated by Force Spectroscopy. *Single Mol.* **2000**, *1* (2), 123–128. DOI: 10.1002/1438-5171(200006)1:2<123:AID-SIMO123>3.0.CO;2-3.

(175) Bouchiat, C.; Wang, M. D.; Allemand, J.-F.; Strick, T.; Block, S. M.; Croquette, V. Estimating the persistence length of a worm-like chain molecule from force-extension measurements. *Biophys. J.* **1999**, *76* (1 Pt 1), 409–413.

(176) Zou, S.; Korczagin, I.; Hempenius, M. A.; Schönherr, H.; Vancso, G. J. Single molecule force spectroscopy of smart poly(ferrocenylsilane) macromolecules: Towards highly controlled redox-driven single chain motors. *Polymer* **2006**, *47* (7), 2483–2492. DOI: 10.1016/j.polymer.2005.12.091.

(177) Grosberg, A. Y.; Khokhlov, A. R. *Statistical physics of macromolecules*; American Inst. of Physics: New York, 1994.

(178) Heymann, B.; Grubmüller, H. Elastic properties of poly(ethylene-glycol) studied by molecular dynamics stretching simulations. *Chem. Phys. Lett.* **1999**, *307* (5-6), 425–432. DOI: 10.1016/S0009-2614(99)00531-X.

(179) Raible, M.; Evstigneev, M.; Bartels, F. W.; Eckel, R.; Nguyen-Duong, M.; Merkel, R.; Ros, R.; Anselmetti, D.; Reimann, P. Theoretical analysis of single-

molecule force spectroscopy experiments: heterogeneity of chemical bonds. *Biophys. J.* **2006**, *90* (11), 3851–3864. DOI: 10.1529/biophysj.105.077099.

(180) Walhorn, V.; Schäfer, C.; Schröder, T.; Mattay, J.; Anselmetti, D. Functional characterization of a supramolecular affinity switch at the single molecule level. *Nanoscale* **2011**, *3* (11), 4859–4865. DOI: 10.1039/c1nr10912j.

(181) Kramers, H. A. Brownian motion in a field of force and the diffusion model of chemical reactions. *Physica* **1940**, *7* (4), 284–304. DOI: 10.1016/S0031-8914(40)90098-2.

(182) Evans, E.; Berk, D.; Leung, A. Detachment of agglutinin-bonded red blood cells. I. Forces to rupture molecular-point attachments. *Biophys. J.* **1991**, *59* (4), 838–848. DOI: 10.1016/S0006-3495(91)82296-2.

(183) Evans, E.; Ritchie, K. Strength of a Weak Bond Connecting Flexible Polymer Chains. *Biophys. J.* **1999**, *76* (5), 2439–2447. DOI: 10.1016/S0006-3495(99)77399-6.

(184) Shillcock, J.; Seifert, U. Escape from a metastable well under a time-ramped force. *Phys. Rev. E* **1998**, *57* (6), 7301–7304. DOI: 10.1103/PhysRevE.57.7301.

(185) Ray, C.; Brown, J. R.; Akhremitchev, B. B. Correction of systematic errors in single-molecule force spectroscopy with polymeric tethers by atomic force microscopy. *J. Phys. Chem. B* **2007**, *111* (8), 1963–1974. DOI: 10.1021/jp065530h.

(186) Garai, A.; Zhang, Y.; Dudko, O. K. Conformational dynamics through an intermediate. *J. Chem. Phys.* **2014**, *140* (13), 135101. DOI: 10.1063/1.4869869.

(187) Husson, J.; Pincet, F. Analyzing single-bond experiments: Influence of the shape of the energy landscape and universal law between the width, depth, and force spectrum of the bond. *Phys. Rev. E* **2008**, *77* (2). DOI: 10.1103/PhysRevE.77.026108.

(188) Chen, S.; Springer, T. A. Selectin receptor-ligand bonds: Formation limited by shear rate and dissociation governed by the Bell model. *Proc. Natl. Acad. Sci. USA* **2001**, *98* (3), 950–955. DOI: 10.1073/pnas.98.3.950.

(189) Friedsam, C.; Wehle, A. K.; Kühner, F.; Gaub, H. E. Dynamic single-molecule force spectroscopy: bond rupture analysis with variable spacer length. *J. Phys.: Condens. Matter* **2003**, *15* (18), S1709–S1723. DOI: 10.1088/0953-8984/15/18/305.

(190) Björnham, O.; Schedin, S. Methods and estimations of uncertainties in single-molecule dynamic force spectroscopy. *Eur. Biophys. J.* **2009**, *38* (7), 911–922. DOI: 10.1007/s00249-009-0471-8.

(191) Hukkanen, E. J.; Wieland, J. A.; Gewirth, A.; Leckband, D. E.; Braatz, R. D. Multiple-bond kinetics from single-molecule pulling experiments: evidence for multiple NCAM bonds. *Biophys. J.* **2005**, *89* (5), 3434–3445. DOI: 10.1529/biophysj.105.061606.

(192) Gu, C.; Kirkpatrick, A.; Ray, C.; Guo, S.; Akhremitchev, B. B. Effects of Multiple-Bond Ruptures in Force Spectroscopy Measurements of Interactions between Fullerene C 60 Molecules in Water. *J. Phys. Chem. C* **2008**, *112* (13), 5085–5092. DOI: 10.1021/jp709593c.

(193) Merkel, R.; Nassoy, P.; Leung, A.; Ritchie, K.; Evans, E. Energy landscapes of receptor-ligand bonds explored with dynamic force spectroscopy. *Nature* **1999**, *397* (6714), 50–53. DOI: 10.1038/16219.

(194) Zou, S.; Schönherr, H.; Vancso, G. J. Force spectroscopy of quadruple H-bonded dimers by AFM: dynamic bond rupture and molecular time-temperature superposition. *J. Am. Chem. Soc.* **2005**, *127* (32), 11230–11231. DOI: 10.1021/ja0531475.

(195) Fuhrmann, A.; Anselmetti, D.; Ros, R.; Getfert, S.; Reimann, P. Refined procedure of evaluating experimental single-molecule force spectroscopy data. *Phys. Rev. E* **2008**, *77* (3). DOI: 10.1103/PhysRevE.77.031912.

(196) Ray, C.; Brown, J. R.; Kirkpatrick, A.; Akhremitchev, B. B. Pairwise interactions between linear alkanes in water measured by AFM force spectroscopy. *J. Am. Chem. Soc.* **2008**, *130* (30), 10008–10018. DOI: 10.1021/ja801568y.

(197) Hummer, G.; Szabo, A. Kinetics from Nonequilibrium Single-Molecule Pulling Experiments. *Biophys. J.* **2003**, *85* (1), 5–15. DOI: 10.1016/S0006-3495(03)74449-X.

(198) Dudko, O. K.; Filippov, A. E.; Klafter, J.; Urbakh, M. Beyond the conventional description of dynamic force spectroscopy of adhesion bonds. *Proc. Natl. Acad. Sci. USA* **2003**, *100* (20), 11378–11381. DOI: 10.1073/pnas.1534554100.

(199) Fuhrmann, A.; Ros, R. Single-molecule force spectroscopy: a method for quantitative analysis of ligand-receptor interactions. *Nanomedicine (London, England)* **2010**, *5* (4), 657–666. DOI: 10.2217/nnm.10.26.

(200) Dudko, O. K.; Hummer, G.; Szabo, A. Intrinsic Rates and Activation Free Energies from Single-Molecule Pulling Experiments. *Phys. Rev. Lett.* **2006**, *96* (10). DOI: 10.1103/PhysRevLett.96.108101.

(201) Ribas-Arino, J.; Shiga, M.; Marx, D. Unravelling the mechanism of force-induced ring-opening of benzocyclobutenes. *Chemistry* **2009**, *15* (48), 13331–13335. DOI: 10.1002/chem.200902573.

(202) Suzuki, Y.; Dudko, O. K. Biomolecules under mechanical stress: a simple mechanism of complex behavior. *J. Chem. Phys.* **2011**, *134* (6), 65102. DOI: 10.1063/1.3533366.

(203) Woodward, R. B.; Hoffmann, R. The Conservation of Orbital Symmetry. *Angew. Chem. Int. Ed.* **1969**, *8* (11), 781–853. DOI: 10.1002/anie.196907811.

(204) Harder, A.; Möller, A.-K.; Milz, F.; Neuhaus, P.; Walhorn, V.; Dierks, T.; Anselmetti, D. Catch Bond Interaction between Cell-Surface Sulfatase Sulf1 and Glycosaminoglycans. *Biophys. J.* **2015**, *108* (7), 1709–1717. DOI: 10.1016/j.bpj.2015.02.028.

(205) Izrailev, S.; Stepaniants, S.; Balsera, M.; Oono, Y.; Schulten, K. Molecular dynamics study of unbinding of the avidin-biotin complex. *Biophys. J.* **1997**, *72* (4), 1568–1581. DOI: 10.1016/S0006-3495(97)78804-0.

(206) Yuan, C.; Chen, A.; Kolb, P.; Moy, V. T. Energy Landscape of Streptavidin−Biotin Complexes Measured by Atomic Force Microscopy. *Biochemistry* **2000**, *39* (33), 10219–10223. DOI: 10.1021/bi992715o.

(207) Chivers, C. E.; Crozat, E.; Chu, C.; Moy, V. T.; Sherratt, D. J.; Howarth, M. A streptavidin variant with slower biotin dissociation and increased mechanostability. *Nat. Methods* **2010**, *7* (5), 391–393. DOI: 10.1038/nmeth.1450.

(208) Heymann, B.; Grubmüller, H. AN02/DNP-hapten unbinding forces studied by molecular dynamics atomic force microscopy simulations. *Chem. Phys. Lett.* **1999**, *303* (1-2), 1–9. DOI: 10.1016/S0009-2614(99)00183-9.

(209) Dudko, O. K.; Mathé, J.; Szabo, A.; Meller, A.; Hummer, G. Extracting kinetics from single-molecule force spectroscopy: nanopore unzipping of DNA hairpins. *Biophys. J.* **2007**, *92* (12), 4188–4195. DOI: 10.1529/biophysj.106.102855.

(210) Li, W.; Gräter, F. Atomistic evidence of how force dynamically regulates thiol/disulfide exchange. *J. Am. Chem. Soc.* **2010**, *132* (47), 16790–16795. DOI: 10.1021/ja104763q.

(211) Hegner, M.; Wagner, P.; Semenza, G. Ultralarge atomically flat template-stripped Au surfaces for scanning probe microscopy. *Surf. Sci.* **1993**, *291* (1-2), 39–46. DOI: 10.1016/0039-6028(93)91474-4.

(212) Vig, J. R. UV/ozone cleaning of surfaces. *J. Vac. Sci. Technol. A* **1985**, *3* (3), 1027. DOI: 10.1116/1.573115.

(213) Cooper, E.; Leggett, G. J. Static Secondary Ion Mass Spectrometry Studies of Self-Assembled Monolayers: Influence of Adsorbate Chain Length and Terminal Functional Group on Rates of Photooxidation of Alkanethiols on Gold. *Langmuir* **1998**, *14* (17), 4795–4801. DOI: 10.1021/la9802567.

(214) Sandal, M.; Benedetti, F.; Brucale, M.; Gomez-Casado, A.; Samorì, B. Hooke: an open software platform for force spectroscopy. *Bioinformatics* **2009**, *25* (11), 1428–1430. DOI: 10.1093/bioinformatics/btp180.

(215) Kasas, S.; Riederer, B. M.; Catsicas, S.; Cappella, B.; Dietler, G. Fuzzy logic algorithm to extract specific interaction forces from atomic force microscopy data. *Rev. Sci. Instrum.* **2000**, *71* (5), 2082. DOI: 10.1063/1.1150583.

(216) Dudko, O. K.; Hummer, G.; Szabo, A. Theory, analysis, and interpretation of single-molecule force spectroscopy experiments. *Proc. Natl. Acad. Sci. USA* **2008**, *105* (41), 15755–15760. DOI: 10.1073/pnas.0806085105.

(217) Tannor, D. J.; Marten, B.; Murphy, R. B.; Friesner, R. A.; Sitkoff, D.; Nicholls, A.; Honig, B.; Ringnalda, M. N.; Goddard, W. A. Accurate First Principles Calculation of Molecular Charge Distributions and Solvation Energies from Ab Initio Quantum Mechanics and Continuum Dielectric Theory. *J. Am. Chem. Soc.* **1994**, *116* (26), 11875–11882. DOI: 10.1021/ja00105a030.

(218) Marten, B.; Kim, K.; Cortis, C.; Friesner, R. A.; Murphy, R. B.; Ringnalda, M. N.; Sitkoff, D.; Honig, B. New Model for Calculation of Solvation Free Energies: Correction of Self-Consistent Reaction Field Continuum Dielectric Theory for Short-Range Hydrogen-Bonding Effects. *J. Phys. Chem.* **1996**, *100* (28), 11775–11788. DOI: 10.1021/jp953087x.

(219) Schrödinger, L. L. *Jaguar*; Schrödinger, LLC: New York, NY, 2010.

(220) Schrödinger, L. L. *Jaguar*; Schrödinger, LLC: New York, NY, 2012.

(221) Becke, A. D. Density-functional exchange-energy approximation with correct asymptotic behavior. *Phys. Rev. A*, 3098–3100.

(222) Lee, C.; Yang, W.; Parr, R. G. Development of the Colle-Salvetti correlation-energy formula into a functional of the electron density. *Phys. Rev. B*, 785–789.

(223) Slater, J. C.; Phillips, J. C. *Quantum Theory of Molecules and Solids Vol. 4: The Self-Consistent Field for Molecules and Solids* 27, 1974.

(224) Vosko, S. H.; Wilk, L.; Nusair, M. Accurate spin-dependent electron liquid correlation energies for local spin density calculations: A critical analysis. *Can. J. Phys.* **1980**, *58* (8), 1200–1211. DOI: 10.1139/p80-159.

(225) Hay, P. J.; Wadt, W. R. Ab initio effective core potentials for molecular calculations. Potentials for K to Au including the outermost core orbitals. *J. Chem. Phys.* **1985**, *82* (1), 299. DOI: 10.1063/1.448975.

(226) Grimme, S.; Antony, J.; Ehrlich, S.; Krieg, H. A consistent and accurate ab initio parametrization of density functional dispersion correction (DFT-D) for the 94 elements H-Pu. *J. Chem. Phys.* **2010**, *132* (15), 154104. DOI: 10.1063/1.3382344.

(227) Zhao, Y.; Truhlar, D. G. The M06 suite of density functionals for main group thermochemistry, thermochemical kinetics, noncovalent interactions, excited states, and transition elements: Two new functionals and systematic testing of four M06-class functionals and 12 other functionals. *Theor. Chem. Acc.* **2008**, *120* (1-3), 215–241. DOI: 10.1007/s00214-007-0310-x.

(228) Bashford, D. An object-oriented programming suite for electrostatic effects in biological molecules An experience report on the MEAD project **1997**, *1343*, 233–240. DOI: 10.1007/3-540-63827-X_66.

(229) Bashford, D.; Gerwert, K. Electrostatic calculations of the pKa values of ionizable groups in bacteriorhodopsin. *J. Mol. Biol.* **1992**, *224* (2), 473–486. DOI: 10.1016/0022-2836(92)91009-E.

(230) Galstyan, A.; Knapp, E.-W. Accurate redox potentials of mononuclear iron, manganese, and nickel model complexes. *J. Comput. Chem.* **2009**, *30* (2), 203–211. DOI: 10.1002/jcc.21029.

(231) Limanskii, A. P. Functionalization of amino-modified probes for atomic force microscopy. *Biophysics* **2006**, *51* (2), 186–195. DOI: 10.1134/S0006350906020059.

(232) Wagner, P.; Hegner, M.; Guentherodt, H.-J.; Semenza, G. Formation and in Situ Modification of Monolayers Chemisorbed on Ultraflat Template-Stripped Gold Surfaces. *Langmuir* **1995**, *11* (10), 3867–3875. DOI: 10.1021/la00010a043.

(233) Devanand, K.; Selser, J. C. Asymptotic behavior and long-range interactions in aqueous solutions of poly(ethylene oxide). *Macromol.* **1991**, *24* (22), 5943–5947. DOI: 10.1021/ma00022a008.

(234) McDermott, C. A.; McDermott, M. T.; Green, J.-B.; Porter, M. D. Structural Origins of the Surface Depressions at Alkanethiolate Monolayers on Au(111): A Scanning Tunneling and Atomic Force Microscopic Investigation. *J. Phys. Chem.* **1995**, *99* (35), 13257–13267. DOI: 10.1021/j100035a033.

(235) Maver, U.; Planinsek, O.; Jamnik, J.; Hassanien, A. I.; Gaberscek, M. Preparation of Atomically Flat Gold Substrates for AFM Measurements. *Acta Chim. Slov.* **2012**, *59* (1), 212–219. DOI: 10.1002/9781118170229.rh1.

(236) Dietz, H.; Berkemeier, F.; Bertz, M.; Rief, M. Anisotropic deformation response of single protein molecules. *Proc. Natl. Acad. Sci. USA* **2006**, *103* (34), 12724–12728. DOI: 10.1073/pnas.0602995103.

(237) Schlierf, M.; Rief, M. Temperature softening of a protein in single-molecule experiments. *J. Mol. Biol.* **2005**, *354* (2), 497–503. DOI: 10.1016/j.jmb.2005.09.070.

(238) Sulchek, T. A.; Friddle, R. W.; Noy, A. Strength of multiple parallel biological bonds. *Biophys. J.* **2006**, *90* (12), 4686–4691. DOI: 10.1529/biophysj.105.080291.

(239) Bizzarri, A. R.; Cannistraro, S. The application of atomic force spectroscopy to the study of biological complexes undergoing a biorecognition process. *Chem. Soc. Rev.* **2010**, *39* (2), 734–749. DOI: 10.1039/b811426a.

(240) Li, N.; Guo, S.; Akhremitchev, B. B. Apparent dependence of rupture force on loading rate in single-molecule force spectroscopy. *ChemPhysChem* **2010**, *11* (10), 2096–2098. DOI: 10.1002/cphc.201000251.

(241) Ohtaki, H.; Radnai, T. Structure and dynamics of hydrated ions. *Chem. Rev.* **1993**, *93* (3), 1157–1204. DOI: 10.1021/cr00019a014.

(242) Mandado, M.; Cordeiro, M. Natália D. S. On the stability of metal-aminoacid complexes in water based on water-ligand exchange reactions and electronic properties: Detailed study on iron-glycine hexacoordinated complexes. *J. Comput. Chem.* **2010**, *31* (15), 2735–2745. DOI: 10.1002/jcc.21567.

(243) Ishida, T.; Yamamoto, S.; Mizutani, W.; Motomatsu, M.; Tokumoto, H.; Hokari, H.; Azehara, H.; Fujihira, M. Evidence for Cleavage of Disulfides in the Self-Assembled Monolayer on Au(111). *Langmuir* **1997**, *13* (13), 3261–3265. DOI: 10.1021/la962022y.

(244) Stolberg, L.; Morin, S.; Lipkowski, J.; Irish, D. E. Adsorption of pyridine at the Au(111)-solution interface. *J. Electroanal. Chem.* **1991**, *307* (1-2), 241–262. DOI: 10.1016/0022-0728(91)85552-Z.

(245) Mollenhauer, D.; Gaston, N.; Voloshina, E.; Paulus, B. Interaction of Pyridine Derivatives with a Gold (111) Surface as a Model for Adsorption to Large Nanoparticles. *J. Phys. Chem. C* **2013**, *117* (9), 4470–4479. DOI: 10.1021/jp309625h.

(246) Paik, W.-k.; Han, S.; Shin, W.; Kim, Y. Adsorption of Carboxylic Acids on Gold by Anodic Reaction. *Langmuir* **2003**, *19* (10), 4211–4216. DOI: 10.1021/la026836s.

(247) Andon, R. J. L.; Cox, J. D. 896. Phase relationships in the pyridine series. Part I. The miscibility of some pyridine homologues with water. *J. Chem. Soc.* **1952**, 4601. DOI: 10.1039/jr9520004601.

(248) Ninković, D. B.; Janjić, G. V.; Zarić, S. D. Crystallographic and ab Initio Study of Pyridine Stacking Interactions. Local Nature of Hydrogen Bond Effect in Stacking Interactions. *Crystal Growth & Design* **2012**, *12* (3), 1060–1063. DOI: 10.1021/cg201389y.

(249) Pápai, I.; Jancsó, G. Hydrogen Bonding in Methyl-Substituted Pyridine−Water Complexes: A Theoretical Study. *J. Phys. Chem. A* **2000**, *104* (10), 2132–2137. DOI: 10.1021/jp994094e.

(250) Mootz, D.; Wussow, H.-G. Crystal structures of pyridine and pyridine trihydrate. *J. Chem. Phys.* **1981**, *75* (3), 1517. DOI: 10.1063/1.442204.

(251) Born, M.; Mootz, D.; Schaefgen, S. Tautomere Wasserschichten. Bildung und Struktur tiefschmelzender Trihydrate von Triethylamin und 4-Methylpyridin. *Z. Naturforsch. B* **1995**, *50* (1), 101–105.

(252) Rablen, P. R.; Lockman, J. W.; Jorgensen, W. L. Ab Initio Study of Hydrogen-Bonded Complexes of Small Organic Molecules with Water. *J. Phys. Chem. A* **1998**, *102* (21), 3782–3797. DOI: 10.1021/jp980708o.

(253) Piacenza, M.; Grimme, S. Van der Waals interactions in aromatic systems: structure and energetics of dimers and trimers of pyridine. *ChemPhysChem* **2005**, *6* (8), 1554–1558. DOI: 10.1002/cphc.200500100.

(254) Tomasik, P.; Klingsberg, E.; Ratajewicz, Z. *Pyridine metal complexes: Pyridine and its derivatives*; The chemistry of heterocyclic compounds 14,6,A; Interscience Publ: New York, NY, 1985.

(255) Williams, P. M. Analytical descriptions of dynamic force spectroscopy: Behaviour of multiple connections. *Anal. Chim. Acta* **2003**, *479* (1), 107–115. DOI: 10.1016/S0003-2670(02)01569-6.

(256) Sulchek, T. A.; Friddle, R. W.; Langry, K. C.; Lau, E. Y.; Albrecht, H.; Ratto, T. V.; DeNardo, S. J.; Colvin, M. E.; Noy, A. Dynamic force spectroscopy of parallel individual Mucin1-antibody bonds. *Proc. Natl. Acad. Sci. USA* **2005**, *102* (46), 16638–16643. DOI: 10.1073/pnas.0505208102.

(257) Guo, S.; Ray, C.; Kirkpatrick, A.; Lad, N.; Akhremitchev, B. B. Effects of multiple-bond ruptures on kinetic parameters extracted from force spectroscopy measurements: revisiting biotin-streptavidin interactions. *Biophys. J.* **2008**, *95* (8), 3964–3976. DOI: 10.1529/biophysj.108.133900.

(258) Kühner, F.; Erdmann, M.; Sonnenberg, L.; Serr, A.; Morfill, J.; Gaub, H. E. Friction of single polymers at surfaces. *Langmuir* **2006**, *22* (26), 11180–11186. DOI: 10.1021/la061704a.

(259) Linegar, K. L.; Adeniran, A. E.; Kostko, A. F.; Anisimov, M. A. Hydrodynamic radius of polyethylene glycol in solution obtained by dynamic light scattering. *Colloid J.* **2010**, *72* (2), 279–281. DOI: 10.1134/S1061933X10020195.

(260) Ratto, T. V.; Langry, K. C.; Rudd, R. E.; Balhorn, R. L.; Allen, M. J.; McElfresh, M. W. Force Spectroscopy of the Double-Tethered Concanavalin-A Mannose Bond. *Biophys. J.* **2004**, *86* (4), 2430–2437. DOI: 10.1016/S0006-3495(04)74299-X.

(261) Welk, M. E.; Norquist, A. J.; Stern, C. L.; Poeppelmeier, K. R. The Structure-Directing Properties of [VOF 5] 2-. *Inorg. Chem.* **2000**, *39* (18), 3946–3947. DOI: 10.1021/ic000416d.

(262) Bruehlman, R. J.; Verhoek, F. H. The Basic Strengths of Amines as Measured by the Stabilities of Their Complexes with Silver Ions. *J. Am. Chem. Soc.* **1948**, *70* (4), 1401–1404. DOI: 10.1021/ja01184a033.

(263) Zocher, M.; Bippes, C. A.; Zhang, C.; Müller, D. J. Single-molecule force spectroscopy of G-protein-coupled receptors. *Chem. Soc. Rev.* **2013**, *42* (19), 7801. DOI: 10.1039/c3cs60085h.

(264) Jun, Y.; Tripathy, S. K.; Narayanareddy, B. R.; Mattson-Hoss, M. K.; Gross, S. P. Calibration of Optical Tweezers for In Vivo Force Measurements: How do Different Approaches Compare? *Biophys. J.* **2014**, *107* (6), 1474–1484. DOI: 10.1016/j.bpj.2014.07.033.

(265) Hao, X.; Zhu, N.; Gschneidtner, T.; Jonsson, E. Ö.; Zhang, J.; Moth-Poulsen, K.; Wang, H.; Thygesen, K. S.; Jacobsen, K. W.; Ulstrup, J.; Chi, Q. Direct measurement and modulation of single-molecule coordinative bonding forces in a transition metal complex. *Nat. Commun.* **2013**, *4*, 2121. DOI: 10.1038/ncomms3121.

(266) Kersey, F. R.; Yount, W. C.; Craig, S. L. Single-molecule force spectroscopy of bimolecular reactions: system homology in the mechanical activation of ligand substitution reactions. *J. Am. Chem. Soc.* **2006**, *128* (12), 3886–3887. DOI: 10.1021/ja058516b.

(267) Kudera, M.; Eschbaumer, C.; Gaub, H. E.; Schubert, U. S. Analysis of Metallo-Supramolecular Systems Using Single-Molecule Force Spectroscopy. *Adv. Funct. Mater.* **2003**, *13* (8), 615–620. DOI: 10.1002/adfm.200304359.

(268) Scheibe, C.; Wedepohl, S.; Riese, S. B.; Dernedde, J.; Seitz, O. Carbohydrate-PNA and Aptamer-PNA Conjugates for the Spatial Screening of Lectins and Lectin Assemblies. *ChemBioChem* **2013**, *14* (2), 236–250. DOI: 10.1002/cbic.201200618.

(269) Neuert, G.; Albrecht, C.; Pamir, E.; Gaub, H. E. Dynamic force spectroscopy of the digoxigenin-antibody complex. *FEBS Lett.* **2006**, *580* (2), 505–509. DOI: 10.1016/j.febslet.2005.12.052.

(270) Best, R. B.; Fowler, S. B.; Toca Herrera, J. L.; Steward, A.; Paci, E.; Clarke, J. Mechanical Unfolding of a Titin Ig Domain: Structure of Transition State Revealed by Combining Atomic Force Microscopy, Protein Engineering and Molecular Dynamics

Simulations. *J. Mol. Biol.* **2003**, *330* (4), 867–877. DOI: 10.1016/S0022-2836(03)00618-1.

Articles in Peer Reviewed Journals

1. Weber, C.; Liebig, T.; Gensler, M.; Zykov, A.; Pithan, L.; Rabe, J. P.; Hecht, S.; Bléger, D.; Kowarik, S. “Cooperative Switching in Nanofibers of Azobenzene Oligomers” *Scientific reports*. **2016**, *6*, 25605. doi:10.1038/srep25605
2. Barucker, C.; Bittner, H. J.; Chang, P. K.-Y.; Cameron, S.; Hancock, M. A.; Liebsch, F.; Hossain, S.; Harmeier, A.; Shaw, H.; Charron, F. M.; Gensler, M.; Dembny, P.; Zhuang, W.; Schmitz, D.; Rabe, J. P.; Rao, Y.; Lurz, R.; Hildebrand, P. W.; McKinney, R. A.; Multhaup, G. “Aβ42-oligomer Interacting Peptide (AIP) neutralizes toxic amyloid-β42 species and protects synaptic structure and function” *Scientific reports*. **2015,** *5,* 15410. doi:10.1038/srep15410
3. Gensler, M.; Eidamshaus, C.; Taszarek, M.; Reissig, H.-U.; Rabe, J. P. “Mechanical stability of bivalent transition metal complexes analyzed by single-molecule force spectroscopy” *Beilstein J. Org. Chem.* **2015,** *11,* 817–827. doi:10.3762/bjoc.11.91
4. Gensler, M.; Eidamshaus, C.; Galstyan, A.; Knapp, E.-W.; Reissig, H.-U.; Rabe, J. P. “Mechanical Rupture of Mono- and Bivalent Transition Metal Complexes in Experiment and Theory” *J. Phys. Chem. C*. **2015,** *119* (8), 4333–4343. doi:10.1021/jp511104m
5. Weber, C.; Liebig, T.; Gensler, M.; Pithan, L.; Bommel, S.; Bléger, D.; Rabe, J. P.; Hecht, S.; Kowarik, S. “Light-Controlled “Molecular Zippers” Based on Azobenzene Main Chain Polymers” *Macromolecules*. **2015,** *48* (5), 1531–1537. doi:10.1021/ma502551b
6. Beyer, P.; Breuer, T.; Ndiaye, S.; Zykov, A.; Viertel, A.; Gensler, M.; Rabe, J. P.; Hecht, S.; Witte, G.; Kowarik, S. “Lattice matching as the determining factor for molecular tilt and multilayer growth mode of the nanographene hexa-peri-hexabenzocoronene” *ACS Applied Materials & Interfaces* **2014,** *6* (23), 21484–21493. doi:10.1021/am506465b
7. Joseph, V.; Gensler, M.; Seifert, S.; Gernert, U.; Rabe, J. P.; Kneipp, J. “Nanoscopic Properties and Application of Mix-and-Match Plasmonic Surfaces

for Microscopic SERS” *J. Phys. Chem. C*. **2012,** *116* (12), 6859–6865. doi:10.1021/jp212527h

Degree Theses Supervised

1. Fenger, R. “Kraftspektroskopie” *Forschungsbericht*, Humboldt-Universität zu Berlin, **2009**.
2. Goldenbogen, B. “Tether Formation via Force Spectroscopy on Planar Lipid Bilayers Containing Embedded Transmembrane Peptides” *Diplomarbeit*, Humboldt-Universität zu Berlin, **2012**.
3. Knoll, C. “Analyse von Fluor-Fluor-Interaktionen durch Einzelmolekül-Kraftspektroskopie” *Masterarbeit*, Freie Universität Berlin, **2013**.

Danksagung

Diese Dissertation ist Höhepunkt und Abschluss einer spannenden und vielseitigen Zeit. Im Laufe der vergangenen Jahre haben mich viele Wegbegleiter unterstützt, denen ich an dieser Stelle danken möchte: Allen voran Prof. Jürgen P. Rabe für die Bereitstellung des Themas und die Möglichkeit, meine Forschungen an der Humboldt-Universität zu Berlin durchzuführen. Im Betreuungsteam mit Prof. Hans-Ulrich Reißig standen mir zwei Mentoren zur Seite, die mit fachlichem Rat und Motivation maßgeblich zum Gelingen der Arbeit beigetragen haben. Der Sonderforschungsbereich 765 mit integriertem Graduiertenkolleg war ein ausgezeichneter Rahmen zum offenen Austausch von Ideen und Möglichkeiten. Natürlich soll auch die finanzielle Ausstattung durch den SFB 765 nicht ungedankt bleiben.

Mein Projekt wäre nicht möglich gewesen ohne die enge Zusammenarbeit mit unseren Kooperationspartnern. Ich danke Christian Eidamshaus für die Synthese der gemeinsam entworfenen Moleküle sowie Artur Galstyan und Prof. Ernst-Walter Knapp für zahlreiche Diskussionen und die theoretischen Berechnungen zum Reißmechanismus der Komplexverbindungen. Außerdem haben mich Hendrik Eberhard und Prof. Oliver Seitz mit besten Kräften bei der Synthese endfunktionalisierter ds-DNA unterstützt. Zu schade, dass wir dieses Projekt nicht weiter verfolgen konnten. Gleich zu Beginn meiner Dissertation konnte ich gemeinsam mit Robert Fenger während seines Fortgeschrittenenpraktikums erste Schritte in Richtung Einzelmolekül-Kraftspektroskopie unternehmen. Später habe ich mit Björn Goldenbogen im Rahmen seiner Diplomarbeit die mechanischen Eigenschaften von Lipiddoppelschichten untersucht und konnte im Gegenzug viele Erkenntnisse in mein eigenes Projekt einfließen lassen. Mit Freude denke ich an die vielen Stunden zurück, die wir im gemeinsamen Büro am Whiteboard diskutiert und philosophiert haben. Besonders dankbar bin ich auch über die Kooperationsprojekte „über den Tellerrand hinaus“: Die Masterarbeit von Christian Knoll, zur anderen Hälfte betreut durch Olaf Wagner und Prof. Rainer Haag, ermöglichte mir neue Einsichten in hydrophobe Wechselwirkungen. Von Susanne Liese und Prof. Roland Netz habe ich viel über die mechanischen Eigenschaften von PEG gelernt, Nikolai Severin hat mir die Präparation von Graphen beigebracht.

Allen Mitgliedern der Arbeitsgruppe Physik von Makromolekülen möchte ich für eine großartige Atmosphäre danken: wissenschaftlich und darüber hinaus. In loser

Reihenfolge seien hier aufgeführt: Stefan Kirstein, Tobias Liebig, Caroline Falk, Egon Steeg, Liang Hua, Marco Kraft, Martin Bogner, Omar Al-Khatib, José Gonzalez, Katherine Herman, Fardin Gholami, Hendrik Glowatzki und Stefan Eilers. Mein besonderer Dank gilt Valentin Reiter-Scherer, der ebenfalls Einzelmolekül-Kraftspektroskopie betreibt. Mit ihm konnte ich wunderbar fachsimpeln und unser Teilprojekt auf diversen Veranstaltungen des SFB 765 präsentieren und verteidigen. In der anstrengenden Endphase meiner Dissertation hat er viele Querschnittsaufgaben rund um unsere Rasterkraftmikroskope übernommen. Christian Seifert konnte mir viele nützliche Tipps zur apparativen Optimierung geben. An langen gemeinsamen Messtagen im Labor hatten wir zahlreiche Gespräche über die unterschiedlichen Modelle, mit denen Physiker oder Chemiker wissenschaftliche Phänomene beschreiben. Mit Jörn-Oliver Vogel und Philipp Lange hatte ich eine schöne Zeit im gemeinsamen Büro. Einen besonderer Dank für die technische und organisatorische Unterstützung möchte ich Evi Poblenz, Sabine Schönherr, Lothar Geyer und Michael Happ aussprechen.

Ich bin sehr dankbar für sachkundige Korrekturen dieser Arbeit, in verschiedenen Teilen gründlich gelesen von Jens Petersen, Gunnar Schwarz, Björn Goldenbogen, Daniel Trawny, Susanne Liese, Katherine Herman und Anton Zykov.

Einen ganz wesentlichen Beitrag zum Gelingen der Arbeit hatten auch all jene, die mich in den vergangenen Jahren kontinuierlich unterstützt und motiviert haben: meine Familie und guten Freunde. Meine Frau Janika hatte stets ein offenes Ohr für mich und Verständnis, wenn mich die Forschung auch zu Hause beschäftigte oder mal wieder ein Wochenende in Labor oder Büro notwendig war. Meine Mutter fand stets die richtigen Worte zur Motivation und Aufmunterung. Mein Sohn Laurin besitzt die wunderbare Fähigkeit, mir in jeder Lage in Lächeln auf das Gesicht zu zaubern. Euch allen herzlichen Dank!

Selbständigkeitserklärung

Ich erkläre, dass ich die Dissertation selbständig und nur unter Verwendung der von mir gemäß § 7 Abs. 3 der Promotionsordnung der Mathematisch-Naturwissenschaftlichen Fakultät, veröffentlicht im Amtlichen Mitteilungsblatt der Humboldt-Universität zu Berlin Nr. 126/2014 am 18.11.2014, angegebenen Hilfsmittel angefertigt habe.

Datum Unterschrift Doktorand/in